

**The Synthesis of Inorganic Semiconductor Nanocrystalline Materials  
For the Purpose of Creating Hybrid Organic/Inorganic Light-Emitting  
Devices**

by

**Jonathan S. Steckel**

B.A. in Theater and High Honors in Chemistry  
Oberlin College  
Oberlin, Ohio  
2001

Submitted to the Department of Chemistry  
in Partial Fulfillment of the Requirements for the Degree of

**DOCTOR OF PHILOSOPHY**


at the

**MASSACHUSETTS INSTITUTE OF TECHNOLOGY**

February 2006

© 2006 MASSACHUSETTS INSTITUTE OF TECHNOLOGY  
All Rights Reserved

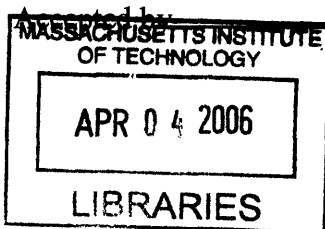
Signature of Author \_\_\_\_\_

^  


Department of Chemistry  
January 27, 2006

Certified by \_\_\_\_\_

Moungi G. Bawendi  
Professor of Chemistry  
Thesis Supervisor




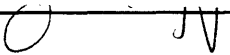
Robert W. Field  
Chairman, Department Committee on Graduate Students

**ARCHIVES**

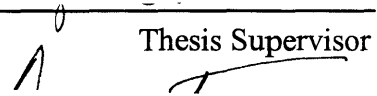


This doctoral thesis has been examined by a committee of the Department of Chemistry as follows:

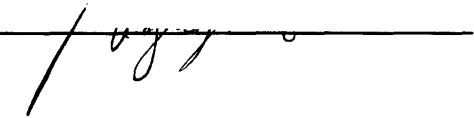
Professor Daniel Nocera

  
\_\_\_\_\_  
 Chairman

Professor Mounji G. Bawendi

\_\_\_\_\_  
 Thesis Supervisor

Professor Vladimir Bulović

\_\_\_\_\_  






# **The Synthesis of Inorganic Semiconductor Nanocrystalline Materials For the Purpose of Creating Hybrid Organic/Inorganic Light-Emitting Devices**

by

Jonathan S. Steckel

Submitted to the Department of Chemistry on February 3, 2006 in Partial Fulfillment of  
the Requirements for the Degree of Doctor of Philosophy in Chemistry

## **ABSTRACT**

Colloidal semiconductor nanocrystals (NCs) or quantum dots (QDs) can be synthesized to efficiently emit light from the ultraviolet, across the entire visible spectrum, and into the near infrared. This is now possible due to the continual development of new core and core-shell NC structures to meet specific color needs in areas as diverse as optoelectronic devices to biological imaging. Core-shell semiconductor NCs are unique light emitters. They are more stable overtime to photobleaching compared to organic dyes. Their emission is efficient and their spectral full width at half maximum remains highly narrow as their size is synthetically changed to provide desired peak wavelengths of emission to within plus or minus a couple of nanometers. They can be purified and manipulated in solution and their chemical interaction with the environment is the same for all sizes and can be modified using chemical techniques. These unique properties make semiconductor NCs ideal for use in light emitting devices (QD-LEDs). This work shows how electroluminescence can be extended into the near infrared region of the spectrum by employing infrared emitting NCs as well as into the blue region of the spectrum by designing and synthesizing NCs specifically for this application. Once efficient and color saturated electroluminescence at the visible spectrum's extremes had been realized it was a natural extension to begin exploring the potential of QD-LED devices to satisfy the technological requirements of flat panel displays and imaging applications. This led to the synthesis of a new green-emitting core-shell NC material to meet the specific color needs for flat panel display applications. At the same time we developed a new QD-LED device fabrication method to allow the patterning of the NC monolayer in our devices. Micro-contact printing the NC monolayer instead of using phase separation provided efficient and highly color saturated QD-LEDs in the red, green, and blue, and allowed us to pattern these monolayers towards the development of pixelated QD-LEDs such as needed for flat panel display applications. Along the way, the synthesis of colloidal NCs was studied to allow for more control in synthesizing higher quality materials in the future. The simple synthesis of PbSe NCs was used as a model system to begin to understand the mechanism of how the molecular precursors are reduced in solution to produce solid crystalline material in the presence of phosphorous containing molecules.

Thesis Supervisor: Mounji G. Bawendi, Ph.D.

Title: Professor of Chemistry



**For my wife and best friend Francesca and my mother and father Rose and Bill**



## TABLE OF CONTENTS

Title Page	1
Signature Page	3
Abstract	5
Dedication	7
Table of Contents	9
List of Figures	13
List of Tables	15
<b>Chapter 1: Introduction</b>	<b>17</b>
1.1 Colloidal Semiconductor Nanocrystals	17
1.1.1 Quantum Confinement and Optical Properties	17
1.1.2 The Nanocrystal Surface and Quantum Efficiency	24
1.1.3 Historical Perspective of Nanocrystal Synthesis	28
1.1.4 Core and Core-Shell Nanocrystal Synthesis	31
1.1.5 The Isolation and Purification of Nanocrystals	36
1.2 Organic Light Emitting Devices	39
1.2.1 Historical Perspective and Advantages	39
1.2.2 Fabrication and Patterning	41
1.2.3 Device Structure and Operation	44
1.3 Hybrid Organic/Inorganic Nanocrystal Light Emitting Devices	48
1.3.1 Motivation and Historical Perspective	48
1.3.2 Device Structure and Design	51
1.3.3 Device Operation	54
1.4 Overview of Thesis	61
1.5 References	62
<b>Chapter 2: PbSe Nanocrystals</b>	<b>67</b>
2.1 Introduction	67
2.2 PbSe Nanocrystal Synthesis and Characterization	69
2.2.1 Background	69
2.2.2 Diphenyl Ether Based Synthesis (TEM, XRD, WDS)	69
2.2.3 Squalene and Octadecene Based Syntheses	78
2.2.4 TOP Based Synthesis and <sup>31</sup> P NMR Analysis of TOP	80
2.2.5 Reaction Yield	86
2.2.6 Stability and Quantum Yield	90
2.2.7 Absorption Cross Section	93
2.3 On the Chemical Mechanism of Precursor Reduction during PbSe Nanocrystal Formation	95
2.3.1 Characterization of the Lead Precursor	95
2.3.2 Proposed Mechanism and Supporting Data	98
2.4 Conclusions	108
2.5 References	109

<b>Chapter 3: (CdS)ZnS and (CdS)Cd<sub>x</sub>Zn<sub>1-x</sub>S core-shell Nanocrystals</b>	112
3.1 Introduction and Motivation	112
3.2 (CdS)ZnS core-shell Nanocrystals	115
3.2.1 Discussion of Results and Characterization	115
3.2.2 Experimental Details	124
3.3 (CdS)Cd <sub>x</sub> Zn <sub>1-x</sub> S core-shell Nanocrystals	127
3.3.1 Second-Generation CdS Core Preparation	127
3.3.2 Cd <sub>x</sub> Zn <sub>1-x</sub> S Shell Growth	129
3.4 Blue Nanocrystal Lasing and Intravital Imaging	131
3.4.1 Blue Nanocrystal ASE and Lasing	132
3.4.2 Intravital Imaging in the Blue	136
3.5 Conclusions	139
3.6 References	139
<b>Chapter 4: (Cd<sub>x</sub>Zn<sub>1-x</sub>Se)Cd<sub>y</sub>Zn<sub>1-y</sub>S core-shell Nanocrystals</b>	143
4.1 Introduction and Motivation	143
4.2 Synthesis of (Cd <sub>x</sub> Zn <sub>1-x</sub> Se)Cd <sub>y</sub> Zn <sub>1-y</sub> S core-shell Nanocrystals	145
4.3 Characterization of Cd <sub>x</sub> Zn <sub>1-x</sub> Se and (Cd <sub>x</sub> Zn <sub>1-x</sub> Se)Cd <sub>y</sub> Zn <sub>1-y</sub> S	146
4.4 Conclusions	153
4.5 References	153
<b>Chapter 5: Phase Separation and QD-LEDs Made Using Phase Separation</b>	156
5.1 Introduction	156
5.2 Investigation of Phase Separation	160
5.2.1 Control of Organic Underlayer Film Thickness	160
5.2.2 Control of Monolayer Surface Coverage	160
5.2.3 Control of Packing Order and Grain Sizes	162
5.2.4 Solvent	165
5.2.5 Observation of Two Dimensional Crystal Defects	168
5.2.6 Role of Organic Underlayer	170
5.2.7 Experimental Details	171
5.3 Near Infrared Emitting QD-LEDs	172
5.3.1 Introduction and Motivation	172
5.3.2 Device Fabrication	173
5.3.3 Device Characterization	174
5.4 Blue Emitting QD-LEDs	180
5.5 Red Emitting QD-LEDs	183
5.6 Conclusions	186
5.7 References	186
<b>Chapter 6: QD-LEDs Made Using Micro-Contact Printing</b>	189
6.1 Introduction and Motivation	189
6.2 Nanocrystal Micro-Contact Printing Process	191
6.3 Micro-Contact Printing of QD-LEDs	195
6.3.1 Red, Green, and Blue Emitting QD-LEDs	195
6.3.2 Patterning of Nanocrystals, Towards QD-LED Displays	201

6.4 Conclusions	203
6.5 References	204
Curriculum Vitae	205
Acknowledgements	210





## LIST OF FIGURES

Fig. 1.1 Colloidal Semiconductor nanocrystals	18
Fig. 1.2 Illustration of quantum confinement	20
Fig. 1.3 Illustration of the effect of confinement on semiconductor to nanocrystals	21
Fig. 1.4 Illustration of energy diagrams (E versus k)	22
Fig. 1.5 Absorption spectra of a size series of CdSe nanocrystals	23
Fig. 1.6 Cartoon showing the stages of nucleation and growth of nanocrystals	32
Fig. 1.7 Cartoon of a vacuum thermal evaporator	43
Fig. 1.8 Cross-sectional diagram of a general double-heterojunction OLED	45
Fig. 1.9 Electroluminescence of Alq <sub>3</sub> and Alq <sub>3</sub> doped with DCM2 and PtOEP	47
Fig. 1.10 Basic QD-LED structure	52
Fig. 1.11 The two possible electroluminescence pathways for nanocrystals	55
Fig. 1.12 Typical normalized QD-LED electroluminescence spectra	56
Fig. 1.13 Energy diagram of a typical QD-LED	56
Fig. 1.14 Electroluminescence spectra of two QD-LED devices	57
Fig. 1.15 Graphic representation of exciton generation process within the QD-LED	58
Fig. 1.16 Normalized electroluminescence spectra from a DCM2 doped OLED	60
Fig. 2.1 Cartoon of the apparatus used to synthesize PbSe NCs	71
Fig. 2.2 HRTEM Image of 4.0 ± 0.5 nm diameter PbSe particles	72
Fig. 2.3 Typical diphenylether based PbSe NC absorption spectrum	73
Fig. 2.4 Absorption spectra of a size series of PbSe nanocrystals	74
Fig. 2.5 Powder X-ray diffraction pattern of 5.5 nm diameter PbSe nanocrystals	75
Fig. 2.6 Absorption spectra PbSe NC preparations (dioctyl vs diphenylether)	76
Fig. 2.7 Absorption spectra PbSe NC preparations (squalene vs diphenylether)	77
Fig. 2.8 Absorption spectra of two octadecene based PbSe NC preparations	79
Fig. 2.9 TOP based PbSe NC absorption and photoluminescence	83
Fig. 2.10 <sup>31</sup> P NMR spectrum of 90 % TCI / Alfa Aesar TOP mixture	85
Fig. 2.11 <sup>31</sup> P NMR spectrum of 97 % Strem TOP taken in CHCl <sub>3</sub>	87
Fig. 2.12 Outline of a stability study done on PbSe nanocrystals	91
Fig. 2.13 Plot of the saturation of the photoluminescence of 4.5 nm diameter PbSe	95
Fig. 2.14 FT-IR spectra of oleic acid and lead oleate	97
Fig. 2.15 <sup>31</sup> P NMR spectra of 4 neat growth solutions of PbSe NCs	100
Fig. 2.16 Proposed mechanism of TOPSe reacting with Pb(oleate) <sub>2</sub>	101
Fig. 2.17 Results of PbSe NC reactions run in the NMR machine at 150°C	103
Fig. 2.18 <sup>31</sup> P NMR spectrum of PbSe growth solution (diphenylphosphine)	105
Fig. 2.19 Proposed mechanism of diphenylphosphine reacting with Pb(oleate) <sub>2</sub>	106
Fig. 3.1 The blue NTSC and HDTV display standard CIE color coordinates	113
Fig. 3.2 Absorption spectra of a size-series of large CdS nanocrystals	116
Fig. 3.3 TEM images of CdS core and (CdS)ZnS core-shell nanocrystals	117
Fig. 3.4 Normalized PL spectra of bare CdS and (CdS)ZnS core-shell nanocrystals	118
Fig. 3.5 Stability of PL from CdS core versus (CdS)ZnS core-shell	119
Fig. 3.6 Absorption spectra of core CdS and core-shell (CdS)ZnS nanocrystals	121
Fig. 3.7 Absorption and emission spectra of (CdS)ZnS core-shell nanocrystals	122
Fig. 3.8 XRD patterns of bare CdS and ZnS overcoated samples	123

Fig. 3.9 The absorption spectra of two samples of CdS cores	128
Fig. 3.10 Three sizes of (CdS)Cd <sub>x</sub> Zn <sub>1-x</sub> S core-shell nanocrystals	130
Fig. 3.11 Tunable fluorescence and ASE of (CdS)Cd <sub>x</sub> Zn <sub>1-x</sub> S core-shell NCs	134
Fig. 3.12 Lasing spectra from (CdS)Cd <sub>x</sub> Zn <sub>1-x</sub> S NC-microspheres	135
Fig. 3.13 Image of the blood vessels in a mouse brain using intravital microscopy	138
Fig. 4.1 Absorption and emission spectra of core Cd <sub>x</sub> Zn <sub>1-x</sub> Se NCs over time	147
Fig. 4.2 TEM images of Cd <sub>x</sub> Zn <sub>1-x</sub> Se and (Cd <sub>x</sub> Zn <sub>1-x</sub> Se)Cd <sub>y</sub> Zn <sub>1-y</sub> S core-shell NCs	148
Fig. 4.3 Absorption and emission spectra of (Cd <sub>x</sub> Zn <sub>1-x</sub> Se)Cd <sub>y</sub> Zn <sub>1-y</sub> S NCs	149
Fig. 5.1 Illustration of the Fabrication of organic/NC bilayers via phase separation	158
Fig. 5.2 Effect of solution concentration on the phase separation process	161
Fig. 5.3 Effect of NC size distribution on the degree of packing order	163
Fig. 5.4 Depiction of the effect of surface roughness on the resolution of AFM	164
Fig. 5.5 The effect of NC aspect ratio on degree of ordering	165
Fig. 5.6 AFM images showing the effect of solvent on grain size and structure	167
Fig. 5.7 AFM images of crystal defects in two-dimensional NC colloidal crystals	169
Fig. 5.8 EL spectra of a series of QD-LEDs tuned through the near infrared	175
Fig. 5.9 The EL spectra of (CdS)ZnS core-shell NCs embedded in a QD-LED	181
Fig. 5.10 External quantum efficiency versus current density plot	182
Fig. 5.11 Structure and performance of a red emitting QD-LED	184
Fig. 6.1 A flow chart of the fabrication of QD-LEDs using micro-contact printing	192
Fig. 6.2 Detailed flow diagram of steps 3 and 4 shown in Figure 6.1	193
Fig. 6.3 AFM images of the surface relief after step 4 in Figure 6.1	194
Fig. 6.4 Red, green, and blue QD-LED device luminescence characteristics	197
Fig. 6.5 Electrical performance data of the micro-contact printed QD-LEDs	200
Fig. 6.6 Photographs of working, patterned QD-LED devices	202
Fig. 6.7 An illustration of the deposition of stripes of red, green, and blue NCs	203

## LIST OF TABLES

Table 2.1 List of phosphorous based molecules and their $^{31}\text{P}$ NMR chemical shifts	84
Table 2.2 Table showing the results of three batch PbSe NC preparations	108
Table 4.1 Experimental and calculated data for three $(\text{Cd}_x\text{Zn}_{1-x}\text{Se})$ aliquots	150
Table 4.2 Sizes of $(\text{Cd}_x\text{Zn}_{1-x}\text{Se})$ NCs during growth determined from TEM	151
Table 5.1 Examples of materials compatible with the phase separation process	159



# Chapter 1

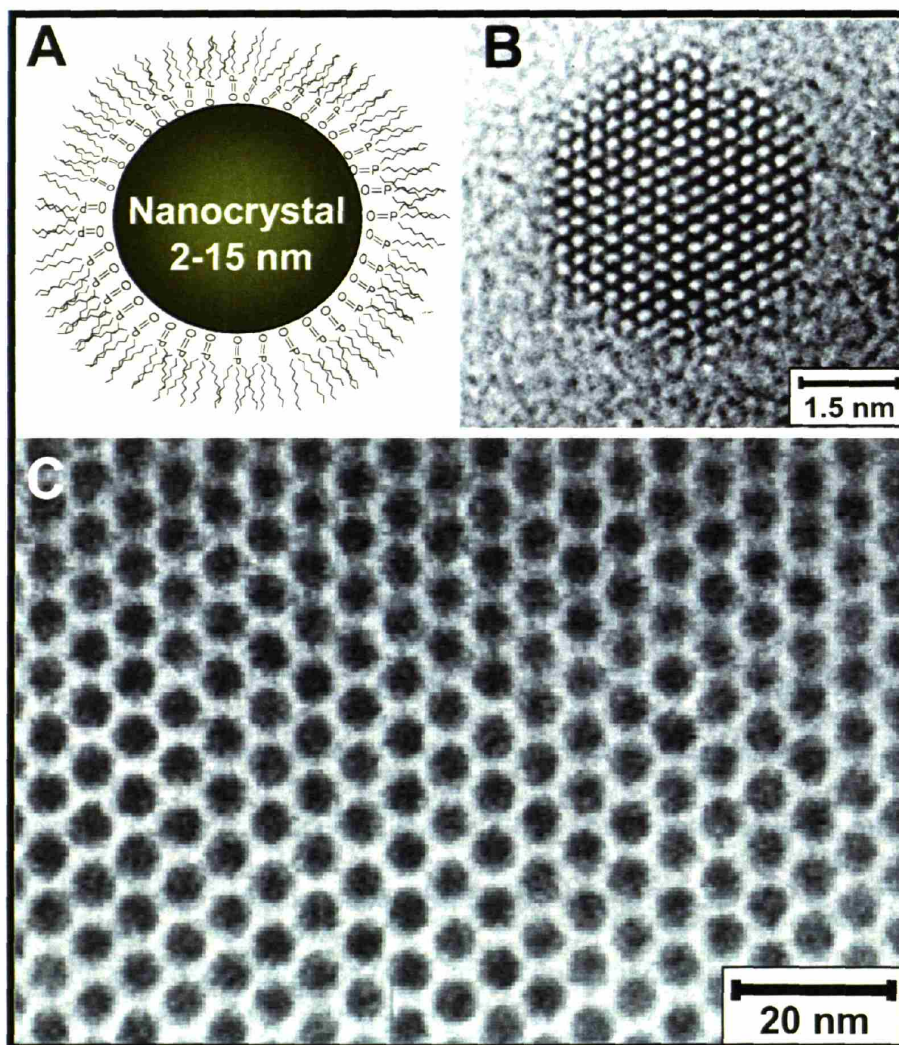
## Introduction

### 1.1 Colloidal Semiconductor Nanocrystals

#### 1.1.1 Quantum Confinement and Optical Properties

Colloidal semiconductor nanocrystals (NCs) or quantum dots (QDs) are nanometer sized, crystalline, chunks of semiconductor material that can be manipulated in solution due to molecules bound to the NCs surface maintaining favorable NC/solvent interactions (Figure 1.1). The smallest NCs (< 1 nm in diameter) are nearly molecular (< 100 atoms), while the largest (> 20 nm in diameter) are made up of over 100,000 atoms. This size regime between molecular and bulk semiconductor material is characterized by a particular change in optical properties of the semiconductor due to quantum mechanical effects<sup>[1]</sup>. The origin of this effect, known as quantum confinement, comes about when the dimensions of the chunk of semiconductor become so small that the photoexcited carriers feel the boundaries.

The first size dependent effects of quantum confinement were seen in the 1970's when the advent of molecular beam epitaxy made it possible to form very thin layers of semiconductor materials known as quantum wells<sup>[2,3]</sup>. These structures are referred to as two dimensional (2D), because the electrical carriers are confined in a 2D plane region (Figure 1.2). These electrical carriers are bound electron-hole pairs, or excitons, that have a particular size associated with them known as the exciton Bohr radius. When the thickness of the 2D plane is made to be on the same order of size as the exciton Bohr



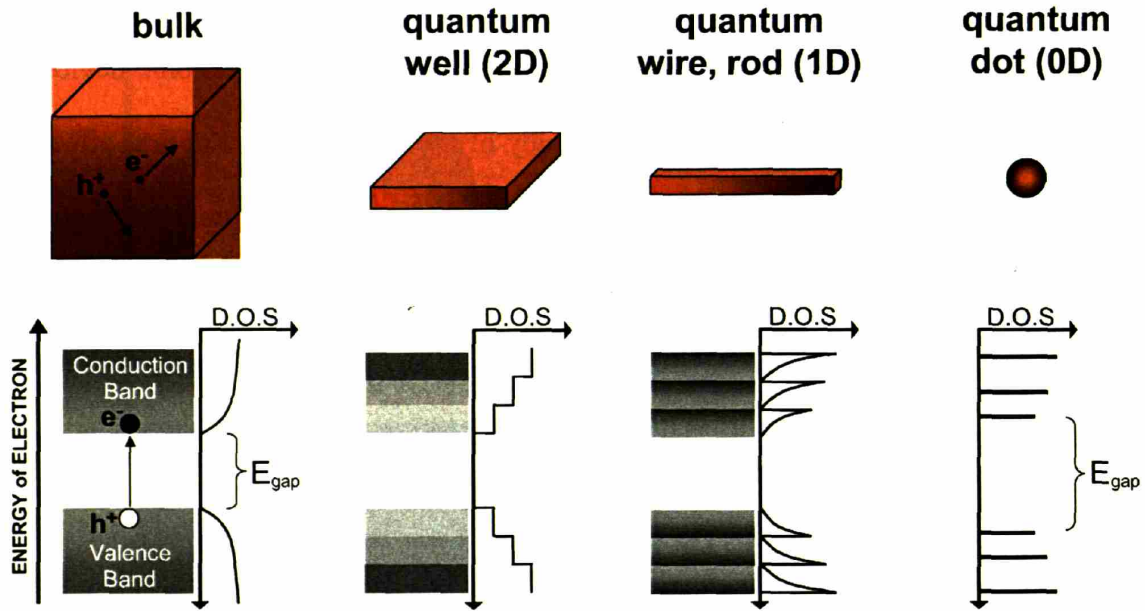
**Figure 1.1** Colloidal Semiconductor nanocrystals. (A) Cartoon of a nanocrystal with a monolayer of organic molecule capping groups associated with the surface. (B) High resolution transmission electron micrograph of a CdSe nanocrystal, where actual atom columns can be seen. (C) A low resolution transmission electron micrograph of CdSe nanocrystals that are hexagonally close packed, demonstrating their narrow size distribution and how the presence of the capping groups keep each nanocrystal a fixed distance from the next when they pack together.

radius, the exciton becomes confined, which modifies the density of states such that there are fewer band edge states and the oscillator strength of optical absorption is shifted to the blue (shorter wavelengths). Because the optical properties of quantum wells can be tuned by changing their thickness and composition and because the reduced

dimensionality leads to improved optical performance by increasing the probability of electron-hole recombination, they form the basis of most of the optoelectronic devices available today. The theoretical and physical study of the size dependent optical effects in quantum wells in time lead to the concept of quantum wires and quantum dots. Figure 1.2 illustrates the transition from bulk semiconductor to quantum well (2D) to quantum wire (1D) and finally to three-dimensionally confined materials (0D) along with the associated change in basic electronic structure and density of states that accompanies the reduction of material size.

The size of colloidal semiconductor NCs (2-15 nm in diameter) are on the order of the size of the Bohr radius of the bulk exciton (5.6 nm for CdSe<sup>[4]</sup> and 46 nm for PbSe<sup>[5]</sup>). Photoexcitation or electrical excitation of the NCs creates an electron-hole pair that is confined to and delocalized over the entire volume of the NC, which confines the exciton in all three dimensions causing the continuous density of states of the bulk solid to collapse into discrete electronic states (Figure 1.2 and 1.3). Through modeling the electronic structure of semiconductor NCs using simple effective mass theory<sup>[6]</sup>, the size effect of quantum confinement can be understood. In the strong confinement regime, the electron and hole can be treated independently as particles in a sphere bound at the NC surface by an infinite potential, which gives rise to each carrier in the NC being described by hydrogenic wavefunctions that occupy discrete electronic energy levels. The nanometer sized semiconductor NC quantizes the allowed k values and as the diameter of the NC decreases, the first state shifts to larger k values and increases the separation between states (Figure 1.3 and 1.4). This is seen spectroscopically for a series of CdSe NC samples as a blue shift in the absorption edge and band edge emission and a larger



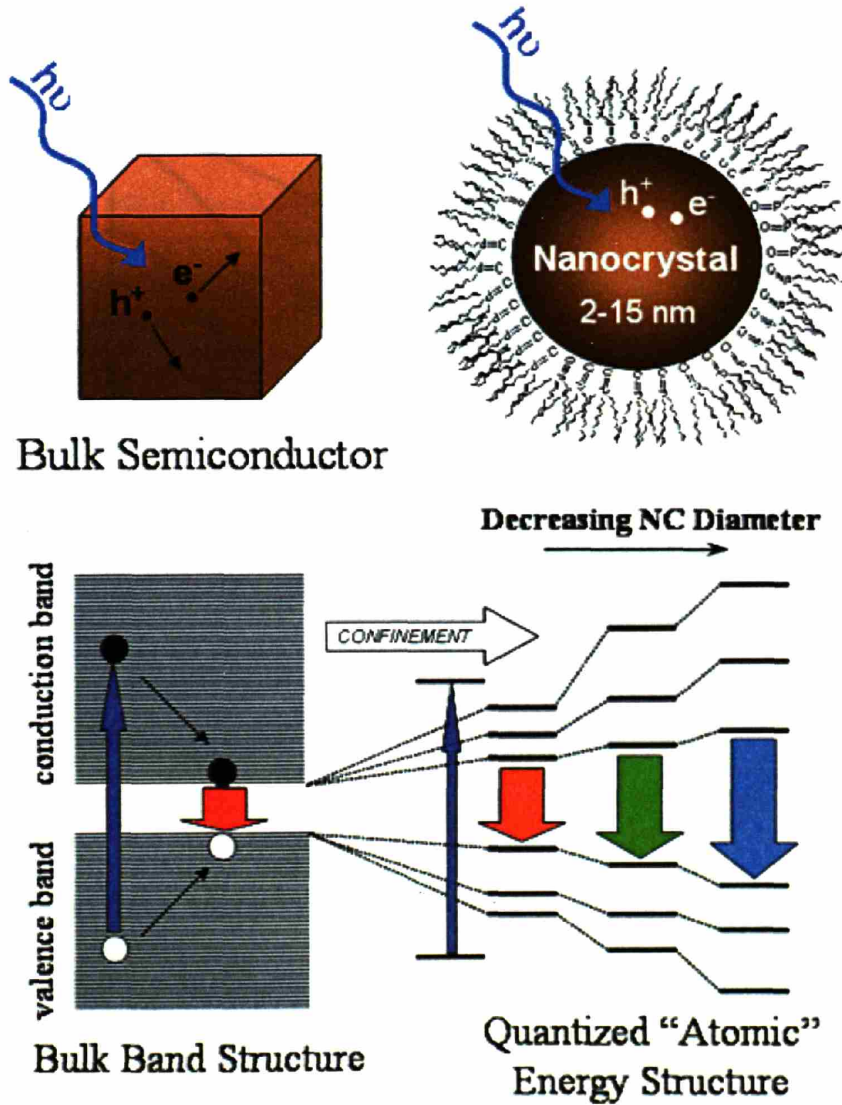


**Figure 1.2** Illustration of quantum confinement going from bulk semiconductor to quantum wells to wires or rods and finally to quantum confinement in all three dimensions in quantum dots or nanocrystals. The unrestricted motion of carriers in bulk semiconductor is associated with a band structure with a density of states proportional to  $E^{1/2}$  for each band. In thin films (quantum wells), motion of the carriers is restricted to two dimensions leading to a constant density of states for each band. In quantum wires or rods the carriers are confined in all but one dimension and the density of states begins to sharpen and nanocrystals confine the carriers in all three dimensions and atomic like states result.

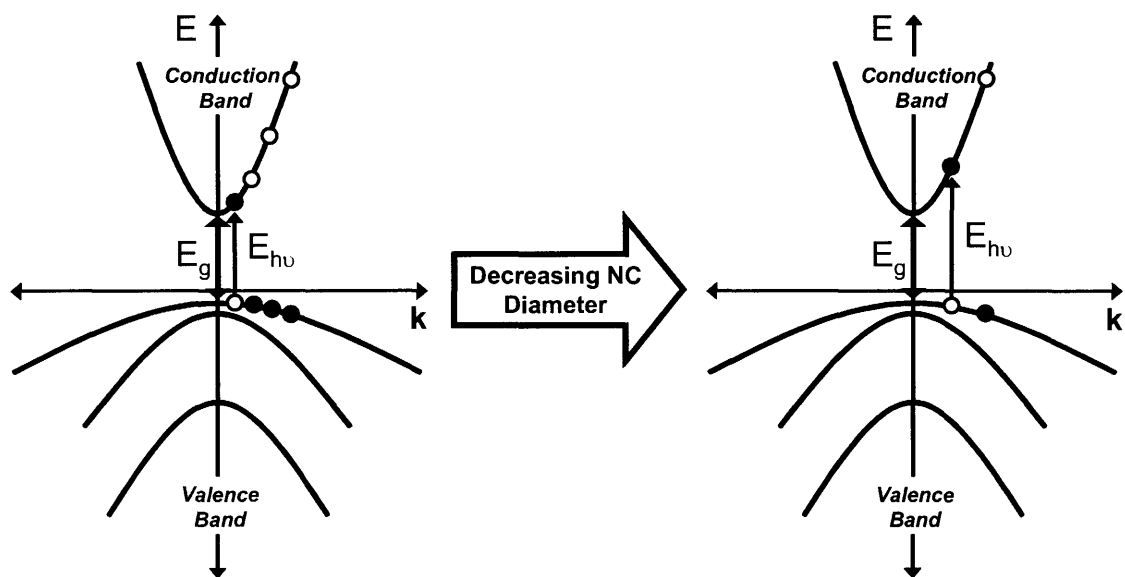
separation between electronic transitions with decreasing NC diameter<sup>[7]</sup> (Figure 1.5(a)). Semiconductor NCs are very much like “artificial atoms”<sup>[8]</sup> because of their quantized electron and hole states, which is very different compared to bulk semiconductor materials that have energy bands. This means that not only are the absorption and emission spectra of NCs blue-shifted from the bulk, but they also are no longer featureless. Both effects, blue-shifting as well as energy quantization, can be seen in Figure 1.5. The absorption spectrum of the 15 nm in diameter CdSe NCs in Figure 1.5(a) appears quite similar to bulk CdSe, being quite broad and featureless, as it experiences very little additional confinement from the bulk. Sharp transitions as well as a significant



blue-shift are quite evident in the absorption spectra for the CdSe NCs with diameters of less than 12 nm (the bulk exciton Bohr diameter).



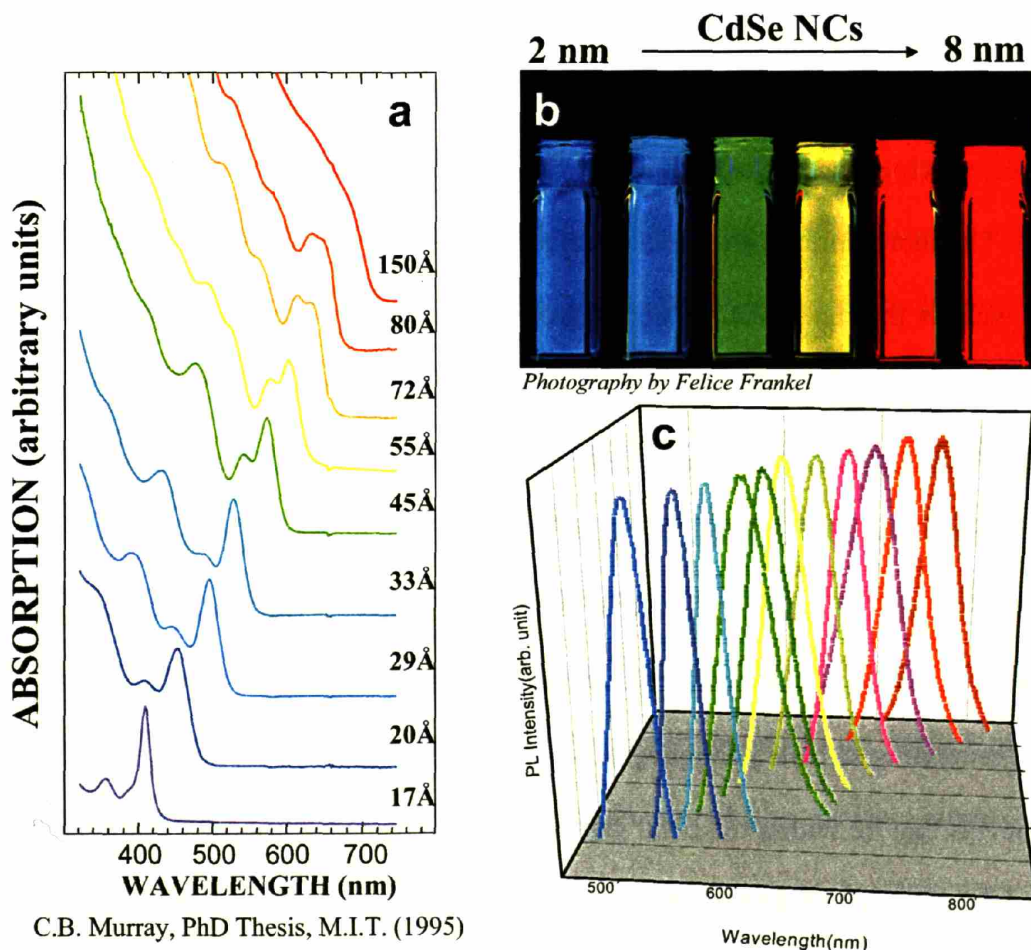
**Figure 1.3** Illustration of the effect of confinement, going from bulk semiconductor to nanocrystals, on electronic states at the conduction and valence band edge. In nanocrystals electrons occupy quantum-confined states of the conduction band while the holes occupy states of the valence band. As the diameter of the nanocrystal decreases the electron and hole wave functions are confined more and the states at the band edge split apart further, allowing the emission of the nanocrystals to be tuned based on their physical size.



**Figure 1.4** Illustration of energy diagrams ( $E$  versus  $k$ ) of the bulk conduction and valence bands for semiconductors, which are assumed to be parabolic in the effective mass approximation. The quantum confinement of the carriers in all three dimensions in a nanocrystal quantizes the allowed  $k$  values and decreasing nanocrystal diameter shifts the first state to larger values of  $k$  and increases the separation between states (diagram on the right). This increase in separation between states is seen spectroscopically as a blue shift (shorter wavelength) in the absorption and emission spectrum, as seen in Figure 1.5, and a larger separation between electronic transitions as the nanocrystal diameter decreases.

The emission properties of colloidal semiconductor NCs are also quite unique. Like the absorption shown in Figure 1.5(a) for CdSe NCs, the emission can be tuned based on the diameter of NCs synthesized as well (Figure 1.5(b) and (c)). CdSe with a bulk band gap of 1.73 eV (716 nm)<sup>[7]</sup> can be made to emit across the entire visible spectrum as seen in Figure 1.5(b), where roughly 2 nm diameter CdSe NCs emit in the blue and 8 nm particles emit in the red. When a different semiconductor with a different band gap is used to synthesize NCs, the region of the electromagnetic spectrum in which the NCs can be tuned changes. This is seen in Figure 1.5(c), where the smaller band gap CdTe (1.5 eV, 827 nm)<sup>[7]</sup> semiconductor when made into NCs can access deeper red colors than CdSe. When PbSe with a band gap of 0.26 eV (4769 nm) is used to make

NCs, the tuning range shifts out into the near infrared region of the spectrum (see Chapter 2).



**Figure 1.5** (a) Absorption spectra of a size series of CdSe nanocrystals ranging from 2 to 15 nm in diameter, demonstrating the ability to tune the optical properties of the nanocrystals with size. The multiple features and the sharpness of each feature demonstrate the narrow size distribution of each sample. (b) Vials of different sized CdSe nanocrystals (2 to 8 nm in diameter) dispersed in solution and fluorescing different colors solely due to a difference in size. (c) Emission spectra of different sized CdSe nanocrystals up to roughly 650 nm and CdTe nanocrystal emission spectra beyond 650 nm. The emission spectra of CdSe nanocrystals have very narrow linewidths making them ideal for most light emission applications.

Single CdSe NCs have been shown to have ultra-narrow homogeneous linewidths of emission, but due to differences in size, shape, and local environment, the ensemble emission linewidth is significantly broadened<sup>[9]</sup>. Typical linewidths (full widths at half

maximum (FWHM)) of high-quality semiconductor CdSe NCs are 20-30 nm. The more uniform in size and shape each NC in an ensemble is to one another, the less the FWHM is broadened compared to a single NC. As a result the FWHM of the emission spectrum for a given material becomes a good guide for the size distribution of the sample. The absorption spectrum serves as a guide to the size distribution of a sample in the same manner. The more uniform in size and shape a NC sample is, the more features will be seen as well as the more distinct and sharp each feature will appear in the absorption spectrum.

### **1.1.2 The Nanocrystal Surface and Quantum Efficiency**

Semiconductor NCs, such as CdSe, are covalently bonded solids, with four bonds per atom, which have been shown to retain the bulk crystal structure and lattice parameter<sup>[10]</sup>. At the surface of a crystal, the outermost atoms do not have neighbors to bond to, generating so called dangling bonds, which give rise to surface states of different energy levels that lie within the band gap of the semiconductor. Surface rearrangements take place during crystal formation to minimize the energy of these dangling bonds, but because such a large percentage of the atoms that make up a NC are on the surface (>75% to <0.5% for NCs <1 nm to >20 nm in diameter, respectively)<sup>[11]</sup>, the effect of these dangling bonds on the emission properties of semiconductor NCs is quite large. The surface states lead to non-radiative relaxation pathways, and thus a reduction in the efficiency of emission. The effect is made more pronounced the smaller the NC diameter, where the surface to volume ratio is larger. Radiative recombination can occur from these surface states as well and because they reside in energy levels in the band gap of the semiconductor, the emission is broad and located to the red of the band edge

emission. This emission is referred to as deep trap emission because these surface states are low energy levels in which carriers can fall into and be trapped for some period of time before leaving the NC or relaxing radiatively or non-radiatively. Deep trap emission is seen particularly in very small NC samples where the majority of atoms are located on the surface and in NC systems in which the surface is poorly passivated.

Colloidal Semiconductor NCs are grown in the presence of stabilizing agents to prevent aggregation and precipitation, as discussed further in the next section. These stabilizing agents are typically organic molecules made up of a functional head, like a nitrogen, phosphorous, or oxygen atom, and a long hydrocarbon chain. The functional head of the molecules attach to the NC surface as a monolayer through covalent, dative, or ionic bonds and are referred to as capping groups (Figure 1.1(a)). This surface capping is analogous to the binding of ligands to metal centers in more traditional coordination chemistry. When molecules are chemically bound to the surface of a NC, they are in part satisfying the bonding requirements of the surface atoms, which eliminates many of the surface traps or surface electronic states and therefore some of the non-radiative relaxation pathways. The direct result of this is that NC samples with good surface passivation have a higher quantum efficiency or quantum yield (QY) than samples with poor surface passivation. Using the right mixture of capping groups during NC synthesis, for example tri-n-octylphosphine and a long chain alkyl amine, provides very good passivation of the surface states and as a result high QYs. When NCs lose their capping molecules, which will be discussed in detail in the next section, the QY decreases dramatically. These high boiling organic molecules not only serve to passivate

the surface electronic states, but also to mediate NC growth and sterically stabilize the NCs in solution.

A shell of a different semiconductor can be grown onto NCs to passivate the surface electronic states to a greater extent than what organic molecules can achieve. When a shell of a larger band gap material is grown onto a core NC, for example ZnS (band gap of 3.7 eV) onto CdSe, the majority of the surface electronic states are passivated and a 2 to 4 fold increase in QY is observed<sup>[12]</sup>. A core-shell type composite rather than organically passivated NCs are desirable for incorporation into solid-state structures, like a solid state QD-LED device, due to their enhanced photoluminescence (PL) and electroluminescence (EL) quantum efficiencies and greater tolerance to processing conditions necessary for device fabrication<sup>[12-15]</sup>. When the radial probabilities of the electron and hole in the lowest energy eigenstates are calculated and analyzed for bare (NCs with no shell) CdSe NCs passivated with organic molecules versus CdSe NCs passivated with a ZnS shell, it is seen that for the bare NCs the wave function of the lighter electron spreads over the entire particle and tunnels only slightly into the surrounding organic molecule matrix, while the heavier hole has a higher probability at the center of the NC and does not extend into the surrounding organic molecule matrix<sup>[12]</sup>. In the case of the (CdSe)ZnS core-shell structure, the electron wave function tunnels into the ZnS shell while the hole wave function has a negligible probability of spreading into the ZnS shell. The increased delocalization of the electron in the (CdSe)ZnS core-shell structure, lowers its confinement energy and therefore the energy of the excited state, which explains why a red shift in the absorption and emission spectrum is observed when a shell of a larger band gap semiconductor is grown onto a

sample of NCs. Because the electron still tunnels out into the ZnS shell, the surface electronic states on the ZnS need to be passivated as well, but due to the energy barrier the effect of surface passivation plays less of a role compared to the bare cores.

When designing new core-shell NC material systems, one critical issue is the crystal structure of the core and shell material as well as the lattice parameter mismatch between the two. The lattice mismatch between CdSe and ZnS is 12%<sup>[12]</sup>, which is considerably large, but because only a couple of atomic layers (1 to 6 monolayers) of ZnS is grown onto CdSe the lattice strain is tolerated. The lattice strain between the two materials becomes greater and greater the thicker the shell grows and eventually a shell too thick will break off of the core. Doping the ZnS shell with Cd can relieve some of this strain and thicker shells of CdZnS can be grown. The effect is similar to transitioning more gradually from CdSe to CdS to ZnS (lattice mismatch between CdSe and CdS is about 4% and that between CdS and ZnS is about 8%), which provides more uniform and thicker shells and therefore better NC core surface passivation and higher quantum efficiencies.

The presence of a shell of a different semiconductor on the core protects the core from degradation. The quantum efficiency of core-shell NCs decreases significantly slower over time compared to bare NCs (NCs with no shell) and organic dyes (which photobleach readily), when they are illuminated over long periods of time in the presence of water and oxygen (ambient conditions)<sup>[16]</sup>. The combination of high efficiency and stability, emission color tunability down to a couple of nanometers of any desired wavelength from the ultra violet to the near infrared region of the spectrum, and narrow emission spectra of core-shell NCs, makes them ideal “dye molecules” for almost any

light emission application. The work done in this thesis focuses on the optimization of the light emission of core and core-shell NCs for use in quantum dot light emitting devices (QD-LEDs). The very narrowband emission of NCs not only produces QD-LEDs with high color saturation, but also allows for the creation of high luminous efficiency LEDs in the blue and red, where otherwise light would be lost to the ultraviolet and infrared respectively.

Another physical phenomenon that influences the process of NC light emission and quantum efficiency is Auger recombination<sup>[17-19]</sup>. Auger recombination is important because of the dominant role it plays in quenching emission from excitons whenever lone electrons or holes in a charged NC or constituent carriers in other excitons are present. The Auger mechanism renders charged NCs non-luminescent and is thought to be responsible for off states in the fluorescence intermittency or blinking of single nanocrystals<sup>[20]</sup>. The process of Auger recombination involves the transfer of an exciton's energy of relaxation to another excited, delocalized carrier in the NC. The carrier (electron or hole) is excited to higher energy after accepting the energy of the exciton and ultrafast intraband relaxation brings it back to the band-edge<sup>[21,22]</sup>. The Auger relaxation process is very fast (10-100ps<sup>[23,24]</sup>) compared to the NC radiative lifetime ( $\tau \sim 10\text{-}20$  ns) and because a charged NC is a dark NC, balancing charge injection into NCs in a QD-LED device is a concern.

### **1.1.3 Historical Perspective of Nanocrystal Synthesis**

Semiconductor NCs have been synthesized in many different ways, but many of these methods do not allow for the manipulation of the NCs after growth for use in practical applications. Most applications of semiconductor NCs (especially use in QD-



LEDs), require the NCs to have narrow size distributions ( $\sigma = 5-10\%$ ) and high quantum efficiencies ( $> 20\%$ ) as well as be easy to process and manipulate in solution. The ability to easily tune the final size of the NCs through synthesis techniques is important as well.

Semiconductor NCs were first synthesized fortuitously in glass matrices by glass workers who added cadmium, zinc, sulfur, and selenium containing compounds to create glasses with colorful hues. Later scientists used this method of NC synthesis deliberately to create better sized distributions of PbSe, PbS, CuBr, CuCl, CdS, and CdSe semiconductor NCs for study<sup>[25-29]</sup> by fine tuning the concentration of precursors in the melt, the temperature of the melt, and the time at which the melt was kept at high temperature. These NCs were highly crystalline due to the high temperatures at which they were formed and the size distributions of some samples were as low as 10%. Because the NCs were embedded in a glass matrix, it was not only impossible to manipulate them for use in practical applications, but hard to study and characterize as well.

Another interesting and early method for the formation of nanometer sized semiconductor particles is the Stranski-Krastanow method of growth<sup>[30,31]</sup>, where sub-monolayers of epitaxially grown thin films of one semiconductor are deposited on a substrate of another semiconductor material with a significant lattice mismatch. The lattice mismatch is relieved by the balling up of the thin film of semiconductor into islands known as SK dots or epitaxial quantum dots. These islands of semiconductor are typically only a couple of nanometers thick and of larger dimension (as much as 100 nm in diameter) in the plane of the layer, which results in less quantum confinement than is

seen in colloiddally grown NCs. Additionally, it is challenging to have all of the droplets form into the same size, and hence the size distribution of these epitaxially grown quantum dots is broad, even though the surface passivation is typically better compared to colloidal NCs because they are fabricated under ultra clean growth conditions and are embedded in a larger band gap semiconductor.

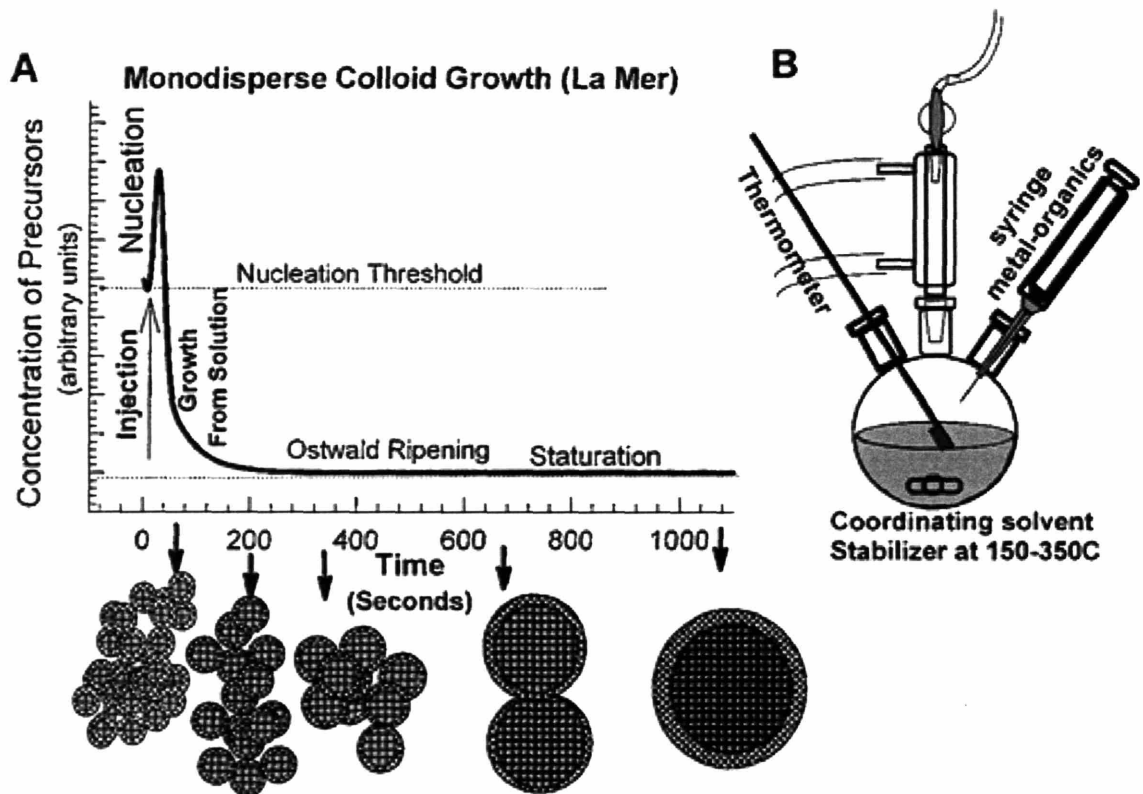
Several solution based techniques were later developed for the synthesis of semiconductor NCs, which include syntheses using metal salts in aqueous solutions<sup>[32-34]</sup>, biosynthesis<sup>[35-37]</sup>, NC formation in inverse micelles<sup>[38,39]</sup>, the pyrolysis of organometallic species in coordinating solvents<sup>[7,40]</sup>, and finally the reduction of metal salts in coordinating and non-coordinating solvents<sup>[41-44]</sup>.

NCs synthesized in aqueous solutions generally have lower quantum efficiencies, due to the presence of species that oxidize the particles, like water and oxygen, as well as poor crystallinity due to the formation of the NCs at low temperatures. The inverse micelle approach proved to produce NCs with better stability as well as allow post synthesis manipulation and surface treatment of the NCs, but provided size distributions of 15-20 % as well as NCs with poor crystallinity due to the low temperature of formation. In 1993 a significant breakthrough in the synthesis of semiconductor NCs was made by Murray and co-workers<sup>[7]</sup>, which produced high-quality NCs that were easy to process and manipulate in solution. This synthesis technique has now been adopted by most for the production of not only all types of binary and tertiary semiconductor nanocrystals, but for metal and metal oxide particles as well. This technique of rapid introduction of precursors into a high boiling solvent at elevated temperature has paved

the way for the synthesis of new shapes<sup>[45-50]</sup> of NCs, including nanorods<sup>[51,52]</sup> and tetrapods<sup>[53]</sup>.

#### **1.1.4 Core and Core-Shell Nanocrystal Synthesis**

The rapid injection of precursors into a hot solvent (300-360° C) to form NCs was used by Murray and co-workers<sup>[7]</sup> to synthesis II-VI semiconductor NCs by high-temperature pyrolysis of organometallic precursors (dimethylcadmium) in coordinating solvents (tri-n-octylphosphine (TOP) and tri-n-octylphosphine oxide (TOPO)). This work was based on the seminal colloidal work by LaMer and Dinegar<sup>[54]</sup>, who introduced the idea that lyophobic colloids grow in solution via a temporally discrete nucleation event followed by controlled growth on the existing nuclei (Figure 1.6). This is usually achieved by an abrupt increase in reagent concentration resulting in supersaturation, which is relieved by the formation of nuclei and subsequent growth of these nuclei. The initial size distribution is determined by the time over which the nuclei form and grow based on the fact that the growth of any one NC is similar to all others. Focusing of the size distribution can occur over time if the percentage of NC growth during the nucleation period is small compared with subsequent growth<sup>[55]</sup>. Another distinct growth phase known as Ostwald ripening is exhibited by many systems at later times during the reaction<sup>[56,57]</sup>. This process involves the dissolution of small NCs due to their high surface energy and the deposition of this material onto the larger NCs. The average NC diameter increases overtime with a compensating decrease in NC number. Taking advantage of Ostwald ripening has proven beneficial for the preparation of a size series of NCs using the organometallic route described by Murray and co-workers.



**Figure 1.6** (a) Cartoon showing the stages of nucleation and growth of nanocrystals based on the LaMer and Dinegar model that describes how lyophobic colloids grow in solution via a temporally discrete nucleation event followed by controlled growth on the existing nuclei. This is shown in the plot of concentration of precursors versus time of reaction, which depicts how a sudden increase in concentration of precursors causes the nucleation of many tiny particles which then grow over time. (b) Cartoon of the typical apparatus used to synthesize nanocrystals, which consists of a round bottom flask with a magnetic stir bar, a condenser connected to a Schlenk line, a temperature probe (depicted as a thermometer), and a rubber septum through which the syringe is inserted when the precursors are rapidly injected into the hot solvent. This picture was taken from C. B. Murray, C. R. Kagan, M. G. Bawendi, *Annu. Rev. Mater. Sci.* **2000**, *30*, 545.

Currently organometallic reagents or, more commonly, inorganic metal salts along with the complementary molecular precursors are rapidly injected into the hot reaction vessel containing one or several high boiling organic solvents, which results in a burst of homogeneous nucleation. The depletion of the reagents through nucleation and the sudden temperature drop due to the introduction of the room temperature solution of reagents minimizes further nucleation. After the injection the dispersion in some cases is

reheated up to a growth temperature to allow for slow growth and annealing of the crystallites.

As discussed in the previous section, the surface of the NCs is passivated by a capping molecule with functionality at one end that allows it to associate itself with the surface through a dative bond and typically an alkyl chain on the other that interacts with the solvent, for example oleic acid, TOP, TOPO, oleylamine, phosphonic acid or phosphinic acid. In some cases the capping molecule is added (when non-coordinating solvents such as octadecene or squalene are used) and in others the organic solvent itself is the capping molecule. The ability to control and separate both the nucleation and growth environments is provided by the choice of organic solvent and capping molecule used. The capping molecules present a steric barrier to the addition of material to the surface of a growing crystallite, which significantly slows the growth kinetics. It is desirable to have enough capping molecules present to prevent uncontrolled nucleation and growth, but not so much that growth is completely suppressed. This synthetic procedure for the synthesis of semiconductor NCs provides a great deal of control and as a result the synthesis can be optimized to give the desired peak wavelength of emission as well as a narrow size distribution. This degree of control is based on the ability to change the temperature of injection, the growth time, the concentration of precursors in solution, the ratio of precursors in solution, and the concentration and type of capping molecules. By changing one or more of these parameters the size of the NCs can be tuned across a large range while maintaining good size distributions.

Due to the high reactivity and toxicity of organometallic species, metal salts such as acetates, hydroxides, acetylacetonates, and oxides have been employed. The

organometallic route provides size distributions ranging from 10 to 15 %, which can be narrowed down to 5 % through size-selective precipitation and quantum efficiencies of 5-10%. Present metal salt based procedures typically provide size distributions of 5-10 % directly with quantum efficiencies ranging from 20-40 %. These metal salts are typically converted in-situ into the species that actually react to form the NCs. For example lead acetate and cadmium hydroxide are converted into lead and cadmium oleate when degassed in the presence of oleic acid and it is the metal oleate species which react with the tri-n-octylphosphine selenide (TOPSe) to form the PbSe and CdSe NCs.

In most cases the metal salts provide metal species in an oxidated state, which need to be reduced before reaction with TOPSe (Se is formally selenium zero in TOPSe) can occur. The addition of mild reducing agents such as 1,2-hexadecanediol and dodecanal provide rapid nucleation in the beginning of the cadmium acetylacetonate based CdSe reaction producing good separation between nucleation and growth. The result is the synthesis of NCs with very good size distributions ( $\sigma = 5-10\%$ ) and high quantum efficiencies compared to the organometallic based synthesis (N. E. Stott, PhD Thesis, M.I.T. (2004)). Stronger reducing agents such as diphenylphosphine, when used in small quantities provide the right degree of reactivity in the nucleation event to increase reaction yields while maintaining good size distributions ( $\sigma = 5-10\%$ ) (see Chapter 2). When no additional reducing agents are added to the synthesis and only very mild reducing agents such as TOP are present, the result is very low reaction yields.

As discussed in the previous section, the growth of a larger band gap semiconductor shell onto the NC core provides very good surface passivation and protection from oxidation, which leads to significantly higher quantum efficiencies as

well as increased stability for use in practical applications such as solid state devices and biological imaging. The technique for growing a shell of a different semiconductor onto core NCs is very general and has been applied to many material systems. The first high-quality NC core-shell system that was made and fully characterized was a shell of ZnS grown onto CdSe, referred to here as (CdSe)ZnS core-shell NCs<sup>[12,14]</sup>. The technique employed was to first isolate the core NCs and redisperse them in a fresh solution of solvent and stabilizers, followed by the slow addition of the shell precursors at temperatures ranging from 140 to 220°C to allow the shell precursors to heterogeneously nucleate on the seed (core) NCs. The homogeneous nucleation of ZnS in solution was controlled by not letting the ZnS precursor concentration in solution reach the threshold for nucleation. The slow addition of the ZnS precursors achieved this by keeping the rate of precursor addition lower than the rate of deposition of the ZnS precursors onto the CdSe NC seeds (cores). Presently the same procedure is generally used with slight modifications for some material systems, for example introducing the shell precursors directly into the growth solution of the NC cores has been successful in recent work in our lab with growing shells on III-V materials. Another interesting change has been to use syringe pumps to add the shell precursors into the NC core solutions at very slow rates (30-50  $\mu\text{L}/\text{min}$ ), which has provided continuous and uniform shell growth. This has increased quantum efficiencies by almost two fold in some cases compared to the use of an addition funnel, which allows only drops of solution at a time to be introduced into the flask.

Three main criteria that are important when synthesizing semiconductor core-shell materials are: The core NCs onto which the shell will be grown must withstand the

conditions under which the shell is deposited (temperature and stabilizing agents should be right such to avoid core NC size and size distribution changes via Ostwald ripening); The core NC semiconductor material and the shell material must not readily interdiffuse under the deposition conditions (core-shell materials have been deliberately heated at high temperatures for long periods of time to induce alloying)<sup>[58]</sup> (see Chapter 4); And lastly, the surface energies of the two semiconductor materials must be sufficiently similar so that the barrier for nucleation of the shell material on the core NCs (heterogeneous nucleation) is lower than that for the nucleation of the shell material in solution (homogeneous nucleation). Using these principles numerous high-quality core-shell NC material systems have been synthesized, some of which include (CdSe)CdS<sup>[59,60]</sup> core-shell, (CdSe)ZnSe<sup>[61]</sup> and the inverse<sup>[62,63]</sup>, (CdSe)CdS/ZnS and (CdSe)ZnSe/ZnS<sup>[64]</sup>, (CdSe)ZnTe/ZnS<sup>[65]</sup>, (CdSe)Zn<sub>x</sub>Cd<sub>1-x</sub>S and (CdSe)CdS/Zn<sub>x</sub>Cd<sub>1-x</sub>S/ZnS<sup>[16]</sup>, (CdS)ZnS<sup>[66]</sup> and (CdS)Cd<sub>x</sub>Zn<sub>1-x</sub>S (see Chapter 3), (Cd<sub>x</sub>Zn<sub>1-x</sub>Se)Cd<sub>y</sub>Zn<sub>1-y</sub>S (see Chapter 4), (CdTe)CdSe and (CdSe)ZnTe<sup>[67]</sup>, (ZnTe)CdSe<sup>[68]</sup>, (ZnSe)ZnS and (ZnSe)ZnSe<sub>x</sub>S<sub>1-x</sub><sup>[69]</sup>, (InAs<sub>x</sub>P<sub>1-x</sub>)InP/ZnSe<sup>[70]</sup>, and (InAs)InP and (InAs)CdSe<sup>[71]</sup>.

### 1.1.5 The Isolation and Purification of Nanocrystals

Colloidally grown semiconductor core and core-shell NCs can be processed and manipulated in solution for practical applications as well as for characterization and study. This is possible due to the capping molecules, discussed earlier in great detail, associated with the surface of the particles. These capping molecules serve to sterically stabilize the NCs in solution as well as to mediate NC growth and passivate surface states. The molecules that are present in the growth solution are typically high boiling organic molecules, which have a functional head that associates with the NC surface and



a long alkyl chain tail that associates with the solvent. The NCs are in a sense covered in an oily ball of molecules and as a result can be dispersed in non-polar solvents like hexane, chloroform, and toluene. If it is desirable to disperse the NCs in polar solvents like ethanol or water, or change the length of capping group, the hydrophobic capping groups in which the NCs were synthesized can be exchanged with more polar or smaller capping molecules<sup>[7,11,72-75]</sup>. This is referred to as cap exchange and consists of repeated exposure of the NCs to an excess of competing capping molecules. The NCs are then removed from solution to isolate them and the cycle is repeated to allow more complete ligand exchange. Cap exchange however, is not ideal for NCs used in light emission applications because the quantum efficiency of the NCs suffers greatly.

Core and core-shell NCs need to be isolated and purified from their growth solutions in order to be used in applications such as solid state device fabrication. The capping groups on the NCs provide a repulsive force in solution that is sufficient in strength and range to counteract the inherent van der Waals attraction between NCs, which keeps them from aggregating. This repulsive force is however, strongly dependent on the energy of mixing between the tethered capping molecules and the solvent. When a nonsolvent (typically butanol/methanol), miscible with the solvent in which the NCs are dispersed (typically hexane or growth solution), is added, the NC dispersion is destabilized and the NCs aggregate and precipitate. The aggregated NC dispersions are typically centrifuged, which isolates the NCs as a powder, leaving in solution many of the synthetic by-products. The resulting NC solids can then be redispersed in a variety of different solvents (typically non-polar solvents such as alkanes, aromatics, long-chain alcohols, chlorinated solvents, and organic bases like amines, pyridines, furans, and

phosphines). Repeated flocculation and dispersion of the NCs into fresh solvent provides NCs solutions that are pure and ready for use in device fabrication. The NCs solutions are typically flocculated twice and then filtered with a 0.2  $\mu\text{m}$  syringe filter to remove any unwanted aggregates or particulates before being used in device fabrication.

Each cycle of NC flocculation and dispersion causes more and more capping groups on the surface to be removed and if this is done too many times the NCs will aggregate permanently and not go back into solution. If this occurs, excess capping molecules such as TOPO or octylamine can be added to the solution and the NCs will often be restabilized after some mixing. Upon each successive precipitation the quantum efficiency decreases as well. The decrease in quantum efficiency is more pronounced with core NCs than with core-shell NCs. When the nonsolvent is added gradually into the NC dispersions (titrated), partial flocculation can be achieved and this is known as size-selective precipitation. The largest NCs in solution flocculate before the smaller ones due to their larger attractive van der Waals forces and as the larger NC aggregates form they exclude the smaller ones. When this partially flocculated NC dispersion is centrifuged, the solid that precipitates is enriched in the larger NCs, while the smaller ones are left in solution. Size-selective precipitation is a powerful technique when working with samples with larger size distributions, for example the NCs made using the pyrolysis of organometallic precursors that typically give size distributions of 10-15 %. Size-selective precipitation can provide NC dispersions with size distributions below 5 %. The metal salt based syntheses typically give size distributions of 5-10 % directly and no size-selective precipitation is required.

## 1.2 Organic Light Emitting Devices

### 1.2.1 Historical Perspective and Advantages

In 1987, the first vacuum-deposited organic light emitting device made from thin (few hundred angstroms) amorphous organic small molecule films with low operating voltages ( $< 20$  V) was reported by Tang and VanSlyke<sup>[76]</sup>. The potential of this technology was quickly recognized. The devices were efficient (close to 1 % external quantum efficient) and they were made using materials and a growth technique that was cheap compared to crystalline semiconductor devices (epitaxially grown inorganic light emitting devices). Shortly after this demonstration of vacuum deposited molecular materials, Burroughes and co-workers<sup>[77]</sup> made thin films of polymeric materials and showed that they could be used in efficient electroluminescent devices.

The field of organic light emitting devices (OLEDs) began to advance rapidly when it was realized that bright and efficient OLED-based flat panel displays were achievable with this technology<sup>[78,79]</sup>. Now OLEDs can be found in their transparent<sup>[80]</sup>, flexible<sup>[81]</sup>, metal-free<sup>[82]</sup>, or phosphorescent<sup>[83,84]</sup> forms and are commercially available in digital cameras (Figure 1.8(d)), personal digital assistants, car stereo systems, cell phones, head-up displays in aircraft, and displays inside high-end sports cars. Much work has gone into improving the external quantum efficiency (EQE)<sup>[85-87]</sup> of OLEDs, narrowing their emission spectra<sup>[88]</sup>, increasing device lifetime<sup>[89,90]</sup>, lowering operating voltages<sup>[91,92]</sup>, and understanding how they operate<sup>[93]</sup>. Significant effort has been placed on developing new means of depositing<sup>[94,95]</sup> and patterning<sup>[96]</sup> organic materials for OLED displays as well. The OLED technology has matured to the point where 40 inch polymer based flat panel displays with lifetimes of  $\sim 10,000$  hours have been fabricated

(by Samsung and Epson), but will not be available for purchase until 2007 (Figure 1.8(c)). Initial commercial displays had EQEs of near 1 %, while current laboratory pixels have been demonstrated with EQEs of ~20 % corresponding to an internal quantum efficiency of ~100 %<sup>[84]</sup>.

One of the major advantages OLEDs have over traditional flat panel display technologies is based on the ability to deposit the organic materials over large areas in a more scalable manufacturing process making it potentially more cost effective. This is much more applicable to the polymer materials that can be inkjet printed than the small molecule organics that are typically deposited using vacuum thermal evaporation. Because the pixels in OLED displays are emissive and are either on or off, the contrast ratios are much better than liquid crystal displays (LCDs). The light in LCDs is generated by a white fluorescent back-light, which is then polarized and filtered to create red, green, and blue pixels. The liquid crystals function as a voltage driven light valve, allowing light to pass or not depending on the voltage applied across the cell. When the crystals are oriented such that the polarized light is being blocked, the pixel is off. The LCD pixels are, however, incapable of showing true black due to some light always leaking through.

The OLED technology also has better color saturation and range of accessible colors in the display (based on the linewidth of the red, green, and blue emission and their respective CIE chromaticity diagram color coordinates compared to those of an LCD display) than LCD or plasma displays as well as higher brightness and viewing angle based on each pixel directly emitting light. OLEDs use considerably less power compared to LCDs as well (only the active pixels are switched on in OLEDs compared

to LCDs where the backlight is on continuously and much of the light is lost due to pixels being off, filtering, and polarization), which makes them ideal for mobile applications. Lastly, the fact that OLEDs can be fabricated on flexible substrates opens the door to new applications such as roll-up displays or displays embedded in clothing.

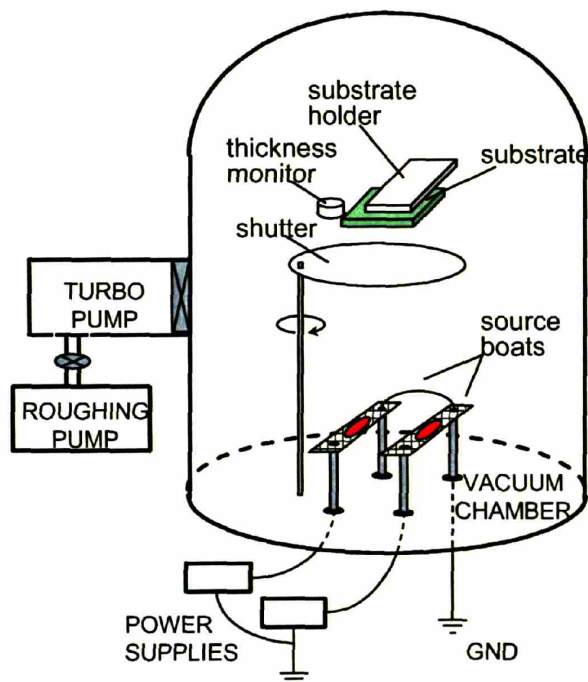
### **1.2.2 Fabrication and Patterning**

The focus of this section is on the fabrication and operating principles of small molecule OLEDs given that this thesis is based on the incorporation of semiconductor nanocrystals (NCs) into small organic molecule devices, not polymer based OLEDs. Both small molecule and polymer OLEDs have been combined with semiconductor NCs, see section 1.3.1 for details, and both OLED technologies have their advantages and disadvantages. Polymer OLEDs have the flexibility and diversity of polymer design as well as the low cost of wet deposition techniques which do not require the use of vacuum equipment, while small molecule OLEDs have the higher purity of available materials, the reproducibility and thickness control of vacuum evaporation, and ultimately the higher performance metrics that have been achieved compared to polymer OLEDs. We have the advantage of being able to combine semiconductor NCs with both sets of deposition techniques and materials and thus can pursue the technology that seems more promising.

Small molecule organics are most commonly deposited in thin films for OLED fabrication by vacuum thermal evaporation (VTE) in contrast to inkjet printing or spin-casting used to create polymer OLEDs. Small molecules used in OLEDs such as aluminum *tris*(8-hydroxyquinoline) ( $\text{Alq}_3$ ) are generally not soluble enough in concentrations necessary to fabricate thin films using spin-casting or inkjet printing,

while polymers would decompose before reaching temperatures high enough to evaporate them due to their high molecular weights. VTE of small organic molecules is a reproducible and ultra clean method for depositing large area, homogenous amorphous thin films. In a low pressure (typically  $10^{-6}$  torr) vacuum chamber a resistive metal boat (typically tungsten, molybdenum, or tantalum), containing the organic material, is heated by the passage of electrical current (Figure 1.7). The organic material evaporates or sublimates when the temperature is high enough and the material travels at some initial speed and direction that is not changed until it hits the substrate or chamber wall, which are cold enough to cause it to condense on contact. The substrate onto which the organic material is being deposited is typically rotated to reduce non-uniformities in one direction. 70-99% (depending on throw distance) of the material in the boat is deposited on the walls of the vacuum chamber, rather than the substrate<sup>[97]</sup>. Film thickness is observed using a quartz crystal thickness monitor and when the desired film thickness is reached, the growth can be shuttered off to stop film growth abruptly (Figure 1.7). Not only are all of the organic layers in small molecule OLEDs deposited using VTE, but the top metal cathode as well.

Patterning of the cathode as well as the emissive layers in VTE is most commonly achieved using a shadow mask. Typically a thin metal foil with the desired pattern cut out of it is used. The shadow mask is suspended as close as possible to the substrate and the organic or low melting metal (i.e. Ag) material is deposited on the substrate in the desired pattern as the material passes through the holes in the mask. The material that does not pass through the mask is deposited onto the mask (like a spray-paint stencil). This patterning technique is very simple and valuable, but has serious problems when it is



**Figure 1.7** Cartoon of a vacuum thermal evaporator used to deposit thin films of organic small molecules and low melting metals for the fabrication of OLEDs. The metal source boats, shown in red, are resistively heated until the organic or low melting metal material begins to evaporate. The gas phase materials travel unimpeded in vacuum until they collide with the substrate, shown in green, or the chamber wall and condense. When the desired film thickness on the substrate is reached (determined by the quartz crystal thickness monitor), growth is abruptly stopped by closing the shutter located just below the substrate. Picture courtesy of S. Coe-Sullivan, PhD Thesis, M.I.T. (2005).

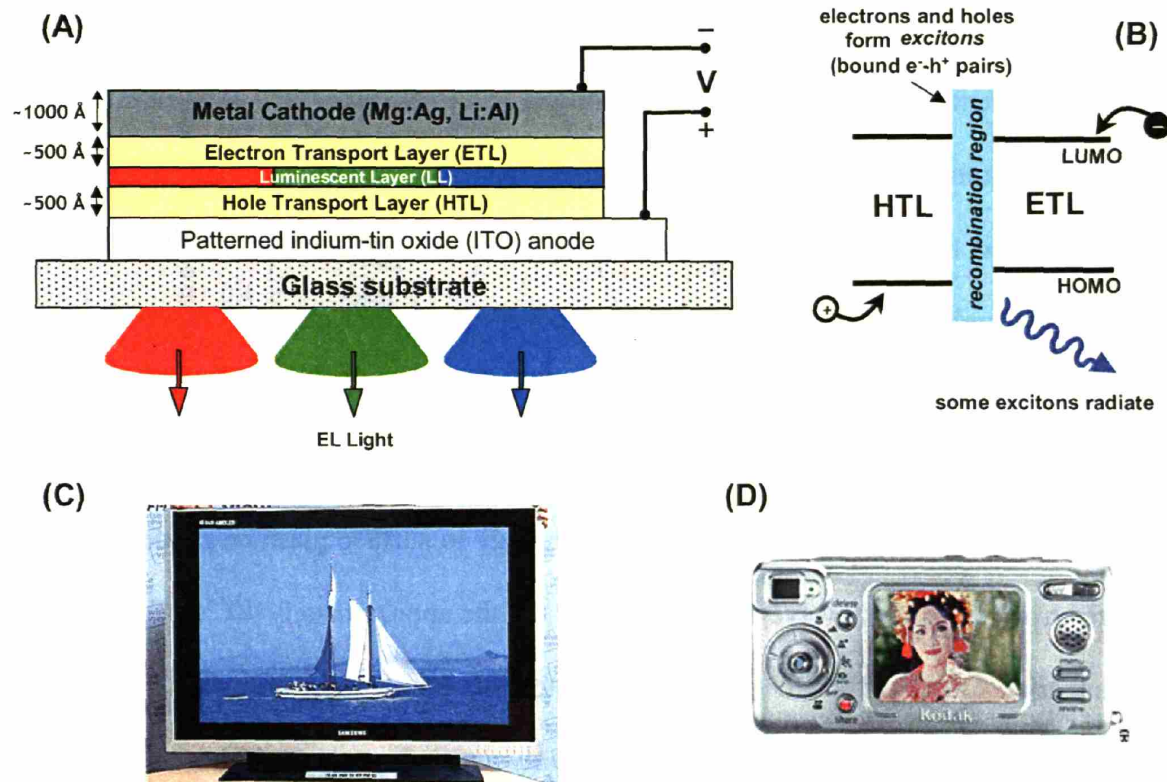
employed in large scale manufacturing of OLED displays. Scaling up to substrates larger than four inches in diagonal has proven difficult because the thin foil shadow mask sags in the middle when stretched over considerable distances and produces non-uniform patterned films. Too much tension on the foil mask will tear it and if the mask is made too thick the uniformity of the deposited organic film suffers. Another problem is the organic material buildup on the shadow mask and the chamber walls that occurs overtime. The organic and metal buildup on these surfaces becomes a source of impurity and particulates in the chamber, reducing yields of subsequent runs, and requiring the

masks and the chambers to be cleaned. Shadow masking wastes material, which further decreases the material utilization rate and increases the cost to manufacture.

### 1.2.3 Device Structure and Operation

The device structure and operating principles of hybrid organic/inorganic quantum dot light-emitting devices (QD-LEDs) and OLEDs are very similar. As a result, understanding how OLEDs function is important to this body of work. The first small molecule OLEDs with low operating voltages, made by Tang and VanSlyke<sup>[76]</sup>, were based on aluminum *tris*(8-hydroxyquinoline) ( $\text{Alq}_3$ ) / N,N'-diphenyl-N,N'-bis(3-methylphenyl)-(1,1'-biphenyl)-4,4'-diamine (TPD) single heterostructures, where  $\text{Alq}_3$  served as both the electron transport layer (ETL) and the luminescent layer (LL), while TPD functioned as the hole transport layer (HTL). Figure 1.8(a) shows a cross-sectional diagram of a general double-heterojunction OLED, where the functions of the ETL, HTL, and LL are performed by separate organic materials. When a bias is applied across the  $\text{Alq}_3$  – TPD single heterostructure, holes are injected from the transparent anode (indium-tin oxide (ITO)) into the TPD and are transported via hopping from one molecule to the next through the TPD to the TPD-  $\text{Alq}_3$  interface, where they buildup at the band edge mismatch (Figure 1.8(b)). At the same time, electrons are injected from the low work function metal cathode (typically Mg:Ag or Li:Al alloys) into the  $\text{Alq}_3$  and are transported via hopping through the  $\text{Alq}_3$  thin film to the TPD-  $\text{Alq}_3$  interface where they also accumulate. In the vicinity of the ETL-HTL interface, holes and electrons meet on TPD and  $\text{Alq}_3$  molecules to form a tightly bound electron-hole pair (Frenkel exciton). The excitons live for approximately 1-10 ns (exciton lifetime), before they radiatively recombine generating light or nonradiatively recombine to generate heat. This region of



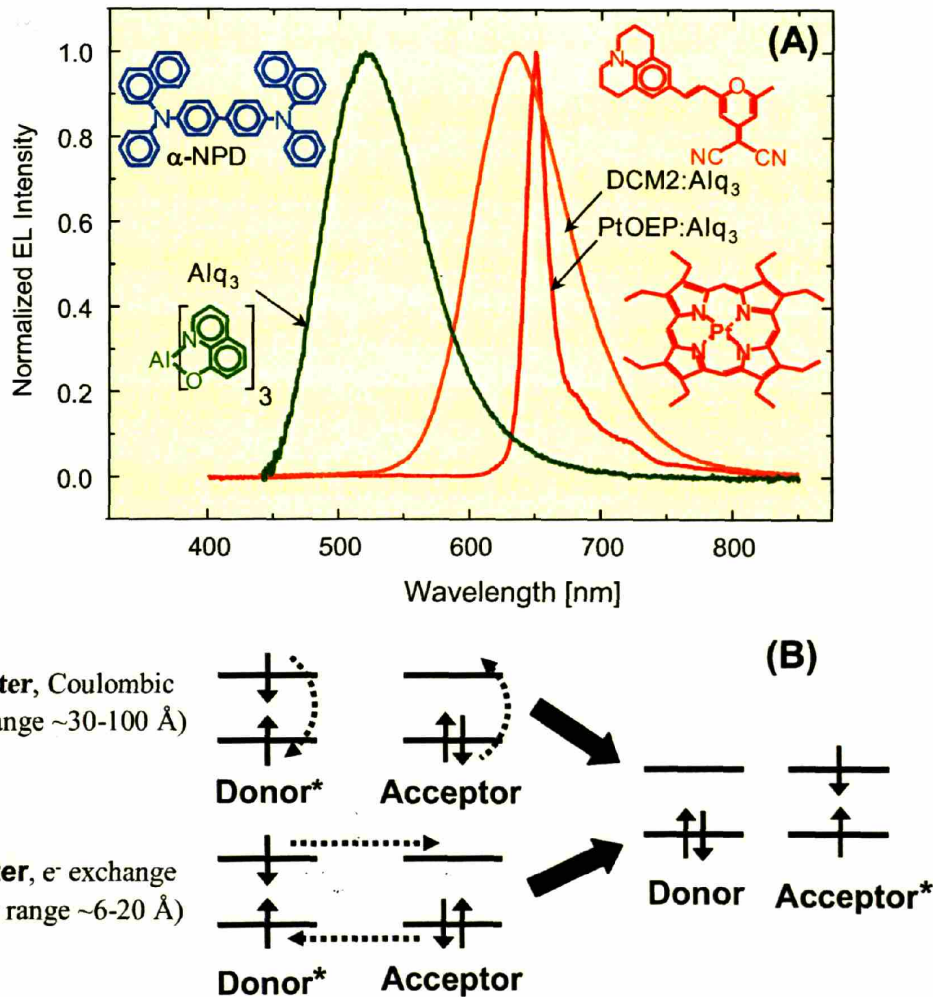


**Figure 1.8** (A) Cross-sectional diagram of a general double-heterojunction OLED, where the functions of the ETL, HTL, and LL are performed by separate organic materials to create red pixels next to green pixels next to blue pixels for full color OLED displays. (B) Principle of operation of a typical OLED, where electrons and holes in their respective transport layers travel towards the recombination region created by the interface between the two films. In this region, an electron and hole may combine on a molecule to create an exciton, which can then recombine radiatively generating a photon of light at the characteristic wavelength of that molecule. (C) 40 inch diagonal polymer based OLED display recently fabricated by Samsung (not available for purchase until 2007). (D) small molecule based OLED display currently available for purchase in Kodak digital cameras.

the device where the excitons are generated and relax is known as the “recombination zone”, whose width is determined by the diffusion length of carriers and excitons in the emitting material (Figure 1.8(b)). Excitons can diffuse from one molecule to another via energy transfer processes before they relax and as a result all of the excitons in the TPD-Alq<sub>3</sub> device transfer their energy to the Alq<sub>3</sub> molecules prior to relaxing. This is evident by the fact that no TPD emission is observed in these devices.

Injected electrons and holes are presumed to be uncorrelated in the process of electroluminescence (EL) and can form both singlet and triplet excitons. Approximately one singlet exciton is created for every three triplet excitons<sup>[98]</sup> in OLEDs (based on their multiplicity) and because the ground state is typically spin-antisymmetric (like singlet excitons), only relaxations of singlet excitons conserve spin and generate fluorescence, while the energy in triplet excitons is wasted. Studies on Alq<sub>3</sub>-based OLEDs indicate that 60 % of the carriers injected into the device do not form excitons, or form excitons that are rapidly quenched at defects or transfer their energy to surface plasmon modes in the metal electrode or to lossy waveguide modes<sup>[99]</sup>. Of the approximately 40 % of injected carriers that do form excitons that can contribute to a luminescent process, only 22 ± 3 % are singlet states<sup>[98,99]</sup>. To make matters worse, only approximately 20 % of the photons generated make it out of the device through the glass substrate. All of these effects combine to give an external quantum efficiency (EQE) (the number of electrons injected versus the number of photons observed by a detector external to the device) of roughly 1% for the “conventional” Alq<sub>3</sub>-diamine OLED. The EQE ( $\eta_{\text{ex}}$ ) can be expressed in the following way:  $\eta_{\text{ex}} = \chi \cdot \eta_{\text{PL}} \cdot \eta_r \cdot \eta_e$ , where  $\chi$  is the fraction of charge carrier recombinations resulting in singlet excitons,  $\eta_{\text{PL}}$  is the photoluminescence efficiency of the material in the solid state,  $\eta_r$  is the fraction of injected electrons that form excitons, and  $\eta_e$  is the fraction of emitted photons that are coupled out of the device<sup>[83]</sup>.

The emission color and efficiency of the conventional Alq<sub>3</sub>-diamine OLED structure was quickly improved upon after its first demonstration in 1987 by doping the active layers with high-quantum-efficiency luminescent dyes<sup>[100]</sup>. When a luminescent guest molecule is embedded in a donor host material, the excited donor molecule



**Figure 1.9** (A) Electroluminescence of Alq<sub>3</sub> electron transport layer, and Alq<sub>3</sub> doped with fluorescent DCM2 and phosphorescent PtOEP. The chemical formula for these organic materials is shown as well as  $\alpha$ -NPD, which was used as the HTL in these devices instead of TPD. Picture courtesy of S. Coe-Sullivan, PhD Thesis, M.I.T. (2005). (B) A pictorial representation of Förster and Dexter processes in singlet-singlet energy transfer, which enables increased luminescence efficiency, color saturation, and color tunability in doped OLEDs as shown in (A).

(Donor\*) can transfer its energy (exciton) to the luminescent acceptor molecule in the ground state (Acceptor). The two possible mechanisms for exciton energy transfer in OLEDs are Förster or Dexter energy transfer as shown pictorially in Figure 1.9(b)<sup>[101]</sup>. The luminescent guest molecules can also be directly excited (exciton formation directly on the guest molecules) if the energy level structure of the guest molecules relative to the

host molecules causes electrons or holes to be trapped as the carriers are traveling through the host. In some doped organic thin films, exciton energy transfer can increase the luminescence of the guest molecules, while quenching that of the host molecules completely. Less than 1 % doping of guest molecules into the electrically pumped host layer is sufficient to quench the host luminescence. Low dopant concentrations provide highly efficient luminescence due to the reduction in exciton-exciton quenching when the guest molecules are separated from one another by relatively large distances. Figure 1.9(a) shows some examples of doped Alq<sub>3</sub> OLEDs. For comparison, the luminescence spectrum of undoped Alq<sub>3</sub> is also shown. Förster energy transfer in Alq<sub>3</sub>:(2%) DCM2 ([2-methyl-6-[2-(2,3,6,7-tetrahydro-1H, 5H-benzo [ij] quinolizin-9-yl) ethenyl]-4H-pyran-4-ylidene]propane-dinitrile) OLEDs leads to orange EL with forward external emission efficiency of ~ 0.5 % photons per injected carrier<sup>[100,102]</sup>. Dexter energy transfer in Alq<sub>3</sub>:(6%) PtOEP (2,3,7,8,12,13,17,18-octaethyl-21H,23H-porphine platinum (II)) OLEDs leads to highly efficient, ~ 4%, saturated red phosphorescence when triplet excitons as well as singlet excitons contribute to the luminescence<sup>[83]</sup>.

## 1.3 Hybrid Organic/Inorganic Nanocrystal Light Emitting Devices\*

### 1.3.1 Motivation and Historical Perspective

OLEDs are a great technology that has already made it into the market place for many display applications, but it is slowly becoming clear that there are several basic physical problems that will continue to be difficult to overcome with any organic material. Currently, the largest problem is that of OLED device lifetime. The lifetimes

---

\* Much of this section has appeared in print (S. Coe-Sullivan *et al*, *Org. Electr.* **2003**, 4, 123)

of OLEDs have been extended by using new chemistry to prevent crystallization, and more sophisticated packaging schemes<sup>[103]</sup> to prevent water and oxygen from degrading the emitting molecules, but this has only taken the lifetimes of small area commercial displays into the range of 10,000 hours<sup>[104]</sup>. Also, the packaging methods are difficult to use with flexible substrates, which is partly why flexible displays are not yet available. Semiconductor nanocrystals (NCs) in contrast are much more stable to degradation overtime in the presence of oxygen and water than organic molecules making them very interesting as the emitters (dopant) in OLED devices.

Blue and red OLEDs that have lifetimes long enough to use in large area commercial displays are a particular problem based on the fact that blue and red OLEDs have to be run at higher intensities compared to green devices to be perceived as the same brightness by the human eye. This is true because the human perception of luminous intensity peaks sharply in the green and drops off dramatically as we move to the blue and red side of the visible spectrum. Broadband blue emitting devices will either look green-blue to the human eye or emit a large amount of UV light, which we cannot perceive at all; therefore the creation of efficient emitters at the visible spectrum's extremes requires a narrowband source. The emission spectra of organic molecules are fundamentally broader than semiconductor NCs. NC emission spectra are typically half as broad as most organic molecule spectra (NCs on average have full widths at half maximum (FWHM) of 30 nm) making them very suitable to create efficient and saturated in color LEDs in the red and blue.

Another problem that small molecule OLED manufacturers are dealing with is how to laterally pattern red, green and blue materials on a substrate to create large area

full color displays in a truly manufacturable process. As discussed in section 1.2.2, shadow masking has size limitations as well as material utilization and impurity problems, which will require the development of a new patterning technique for the manufacture of large area small molecule OLED displays. The use of NCs as the emitter in OLED displays would require the patterning of only the NC layer, alleviating the need to pattern the organics. As discussed in Chapter 6, we have adopted a method to pattern and deposit dry thin films of NCs for device fabrication, which shows promise as a technique to manufacture large area NC based OLED displays. In addition to these advantages NCs have over organic molecules for use as the emitter in OLED displays, the emission spectrum of NCs can be tuned to plus or minus 5 nm of any desired color of visible emission as well as into the near infrared and near ultraviolet portions of the electromagnetic spectrum.

Many of the factors discussed above contributed to the initial motivation for researchers to create NC light emitting devices or quantum dot light emitting devices (QD-LEDs). The first QD-LED made using colloiddally grown NCs was a bilayer device utilizing a polymer hole transporting layer and a 15-25 nm thick NC (CdSe cores with no ZnS shell) film (5 NC monolayers of 3-5 nm diameter) as the electron transporting layer<sup>[105]</sup>. This device structure required the transport of electrons from NC to NC through the multilayers of NCs located near the cathode. Around the same time, a QD-LED structure was fabricated incorporating NCs within a semiconducting polymer matrix in a single layer sandwiched between the cathode and the anode<sup>[13]</sup>. This device structure involved the NCs (CdSe cores with no ZnS shell) in both electron and hole transport and likely resulted in charged NCs, which are much less efficient emitters due to the Auger

process discussed in section 1.1.2. While the external EL quantum efficiency reported in both papers was low ( $\eta_{\text{ex}} < 0.01 \%$ ), the studies demonstrated that electrically generated NC EL was possible, alluding to the technological potential of QD-LEDs.

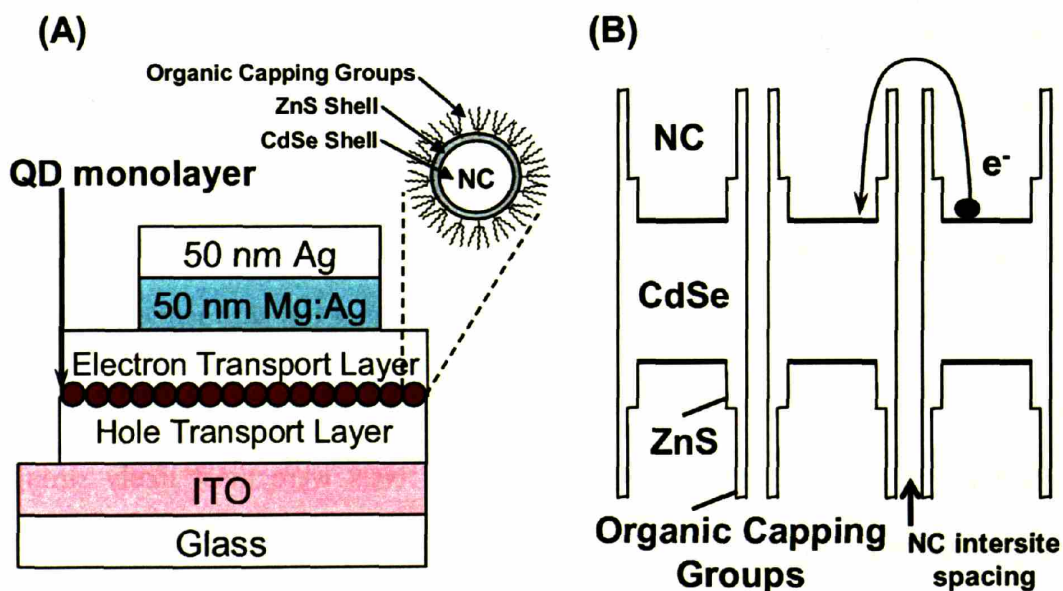
Subsequent papers explored the benefits of combining these two approaches<sup>[106]</sup>, as well as the use of (CdSe)ZnS core-shell<sup>[107]</sup> and (CdSe)CdS core-shell NCs<sup>[108]</sup>. Development of these devices yielded  $\eta_{\text{ex}}$  as high as 0.22 %<sup>[108]</sup> but with response times in excess of several seconds. (InAs)ZnSe core-shell NCs were used to generate efficient EL in the near infrared, by blending films of NCs and polymers between opposing electrodes<sup>[109]</sup>. External quantum efficiencies of as high as 0.5 % were reported in this work. This was followed by the demonstration of  $\eta_{\text{ex}} = 0.5 \%$  visible emitting QD-LEDs that incorporate a single layer of (CdSe)ZnS core-shell NCs in a molecular organic structure by Coe and Woo<sup>[110]</sup>. Extensions upon this have since yielded  $\eta_{\text{ex}} = 1.1 \%$ <sup>[15]</sup> and most recently  $\eta_{\text{ex}} = 2 \%$ <sup>[111]</sup>. The fast response time and higher EQEs of these latest devices matches that of fluorescent OLEDs.

### **1.3.2 Device Structure and Design**

Looking back at the two major categories of devices fabricated prior to 2002 it is possible to analyze the shortcomings of these devices. For devices in which NCs were homogeneously distributed in a polymer matrix, the NCs were most likely strongly influencing the film morphology and charge conduction through the polymer layer. Rough surface morphology, typical of thick (more than a few monolayers) NC films likely contributed to the observed low device yields and allowed little freedom in optimizing charge injection, transport and position of the exciton recombination region. In the devices in which NCs were deposited as thick, neat films, the NCs functioned as



both lumophores and charge transport layers. NC photoconductivity experiments provide direct evidence of the poor conduction properties of thick NC films relative to organic semiconductors<sup>[112]</sup>. Neat NC films are essentially insulating due to carriers having to overcome large energy barriers created by the organic capping molecules as they hop from one NC to the next (Figure 1.10(b)). In addition, thin films that have both charge and excitons present often undergo quenching mechanisms such as polaron-exciton quenching or Auger recombination<sup>[113]</sup>. A single monolayer of NCs, sandwiched between two thin films of molecular organic semiconductors allows the NCs to function exclusively as lumophores (Figure 1.10(a)). In small molecule OLEDs, charge injection, transport, and light emission are controlled using separate layers optimized for these



**Figure 1.10** (A) Basic QD-LED structure, where a monolayer of NCs is resides between a small organic molecule electron transport layer and a hole transport layer, which removes the need for the NCs to participate in charge transport while using them solely for their light emission properties. (B) Energy band diagram showing the difficulty of conducting electrons from one NC to another due to the large energy barrier created by the organic capping molecules on the NCs.



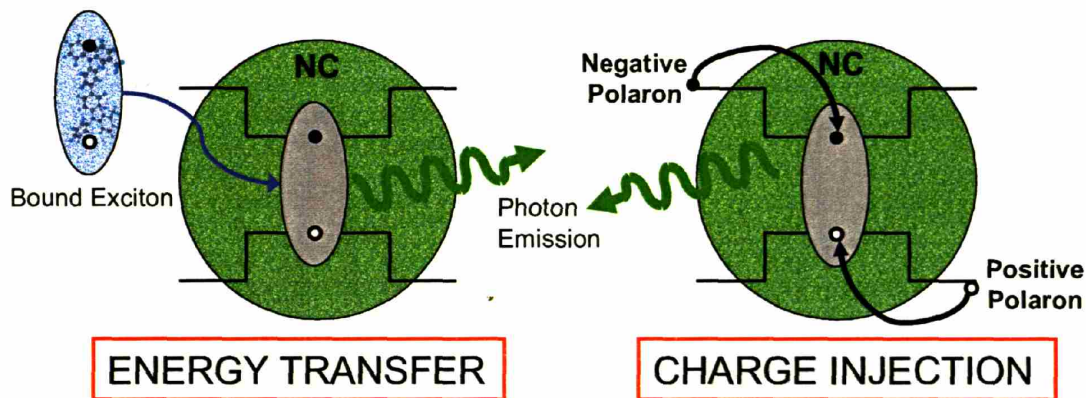
functions. The ability to create layered structures of distinct materials is one of the principle advantages small molecule OLEDs have over polymer OLEDs and in part explains the higher device efficiencies that have been achieved by small molecule OLEDs. All previous work attempting to create efficient QD-LEDs focused on using polymers as the NC matrix, but it wasn't until small molecule organics were employed that distinct layered structures were made to isolate the function of the NCs. The result of incorporating NCs into small molecule OLEDs was QD-LED devices that are both more efficient and easier to optimize.

The basic QD-LED structure shown in Figure 1.10(a) is made in the following manner<sup>[15]</sup>. The HTL and NC monolayer bilayer film is first deposited from a solution of N, N'-diphenyl-N, N'-bis(3-methylphenyl)-(1, 1'-biphenyl)-4, 4'-diamine (TPD) and (CdSe)ZnS core-shell NCs in chloroform that is spin coated onto a cleaned ITO coated glass substrate. Phase separation (discussed in detail in Chapter 5) occurs as the solvent dries during this process forming the TPD/NC (40 nm total thickness) bilayer. The relative amount of TPD can be varied to control the TPD layer thickness, and the NC concentration in solution is used to optimize the NC monolayer coverage. A 30 nm thick film of tris-(8-hydroxyquinoline) aluminum (Alq<sub>3</sub>) is then thermally evaporated on top of the NC monolayer followed by an evaporated Mg:Ag/Ag electrode (50:1 Mg:Ag by weight), which is patterned using a contact shadow mask. The spin-on deposition of the HTL-NC bilayer is done within a controlled nitrogen environment (< 5 ppm O<sub>2</sub>, H<sub>2</sub>O) and the evaporator base pressure is  $5 \times 10^{-8}$  Torr.

### 1.3.3 Device Operation

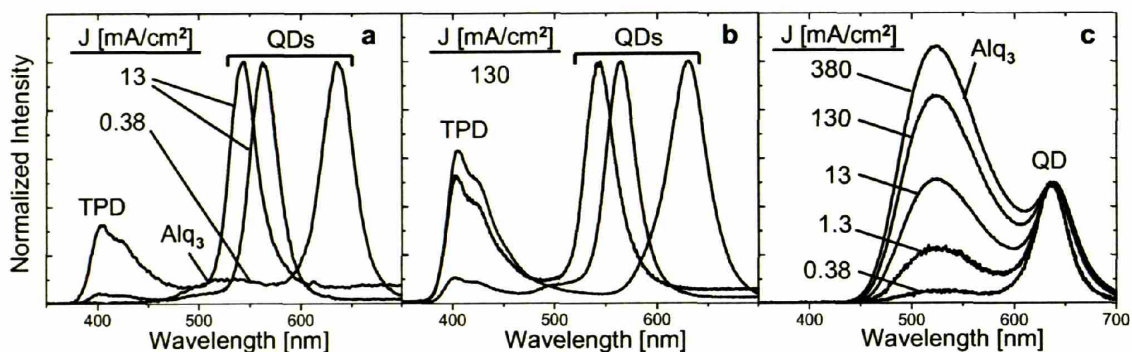
As shown in Figure 1.10(a), the QD-LED device structure is essentially a single heterojunction small molecule OLED device with a monolayer of NCs located exactly at the HTL-ETL interface (recombination region). When electrons are injected into the ETL from the cathode and holes into the HTL from the anode they meet in the recombination zone as they would in a regular OLED device and create excitons on the ETL and HTL molecules as well as on the NCs. Two possible mechanisms were proposed for how the NCs in these devices are excited to create electroluminescence and in fact both mechanisms are possible depending on the device structure made. Figure 1.11 graphically depicts both of these processes, exciton energy transfer and direct charge injection. In exciton energy transfer, as discussed in section 1.2.3 and shown pictorially in Figure 1.9(b), an exciton created on neighboring organic molecules of higher exciton energy can transfer its energy, either through Dexter or Förster energy transfer, to the NCs. This is analogous to energy transfer from a host molecule to a dopant molecule in doped small molecule OLED devices discussed in section 1.2.3. Direct charge injection occurs when an electron and hole (negatively and positively charge polaron) are introduced directly into the NCs as they are moving through the device to create an exciton on the NCs. Because Dexter energy transfer occurs over very short distances (6-20 Å) compared to Förster energy transfer (30-100 Å) the energy transfer mechanism that would dominate in QD-LEDs is Förster energy transfer.

As shown in Figure 1.12, the EL spectrum of these devices contain both NC emission as well as organic molecule emission. In the energy transfer picture, the organic emission can be attributed to the recombination of excitons in the organic molecules

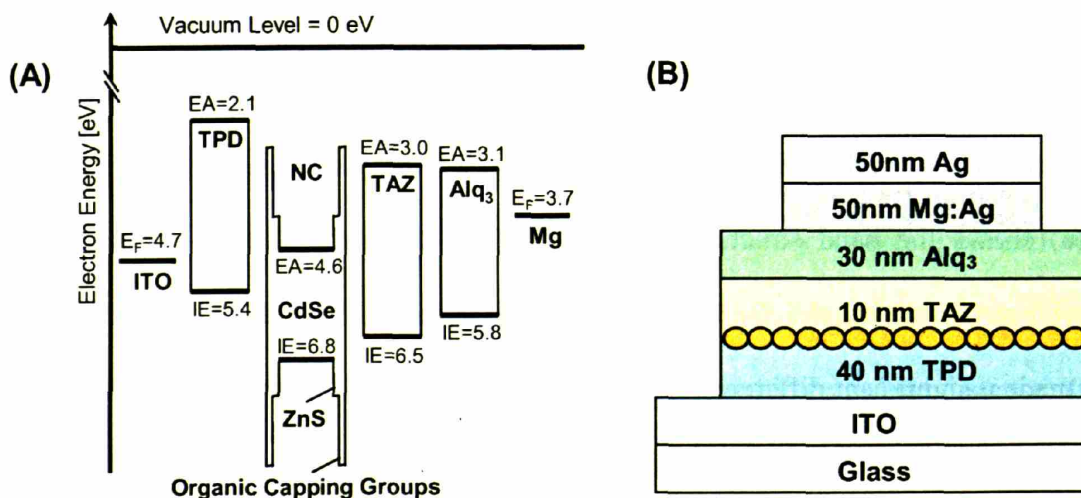


**Figure 1.11** Two possible electroluminescence pathways for nanocrystals embedded in a small molecule OLED. The organic molecules can energy transfer their excitons to the NCs, shown on the left, or the electron and hole (negatively and positively charge polaron) can be directly injected into the NCs, shown on the right to create an exciton that can radiatively recombine to produce light.

which are at a distance greater than the Förster energy transfer radius from the nearest NC. Therefore, at lower currents, either all excitons have energy transferred from organic molecules to NCs, or alternatively, they are initially formed by direct charge injection on the NC sites. It was found that inserting a hole blocking layer (HBL) between the NC monolayer and the ETL ( $\text{Alq}_3$ ) served to limit the number of excitons generated on  $\text{Alq}_3$  molecules by blocking holes from getting into the  $\text{Alq}_3$  layer. Figure 1.13(a) shows the band structure for a QD-LED with the HBL 3-(4-Biphenyl)-4-phenyl-5-tert-butylphenyl-1, 2, 4-triazole (TAZ) inserted between the NCs and the ETL. This made a significant difference in the ratio of NC EL to organic EL in these devices. As seen in Figure 1.14 the percentage of organic emission seen in the devices decreases significantly when TAZ is used. Because a significant percentage of holes are being blocked from reaching the  $\text{Alq}_3$  molecules by the TAZ, the  $\text{Alq}_3$  EL decreases and a small amount of emission is seen from the TPD.

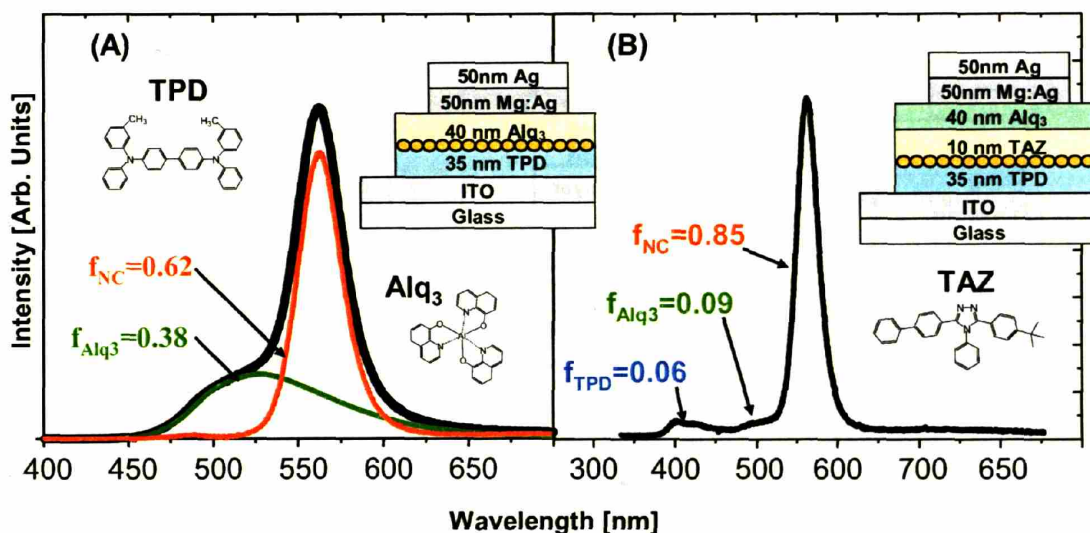


**Figure 1.12** Typical normalized QD-LED electroluminescence spectra of three different sized NC samples measured at (a) low current levels (0.38-13 mA/cm<sup>2</sup>), where most (> 70 % in all cases) of the emission is from the NCs in the device, with only small spectral contributions from either Alq<sub>3</sub> (when TAZ layer is omitted) or TPD (when TAZ layer is present) (b) moderate current levels (130 mA/cm<sup>2</sup>), where two of the three spectra have a large fraction of EL from TPD (c) and a progression of currents for a single device (from 0.38 mA/cm<sup>2</sup> to 380mA/cm<sup>2</sup>). Note that the devices emitting at 540 nm and 560 nm are the same in (a) and (b). At low currents, a larger portion of the excitons are created within a Förster energy transfer radius of the NC monolayer. For all devices, 0.2 % < EQE < 0.5 %.



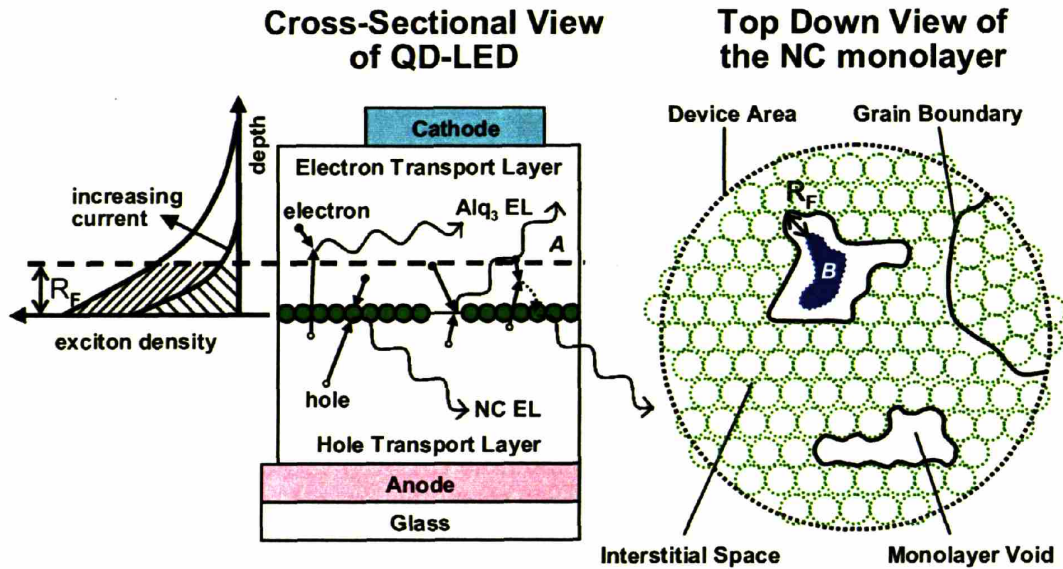
**Figure 1.13** (A) Energy diagram for QD-LEDs of the type shown in the cross-sectional diagram in (B). The highest occupied molecular orbital (HOMO) and lowest unoccupied molecular orbital (LUMO) band energies were determined from photoemission spectroscopy and inverse photoemission spectroscopy measurements<sup>[115]</sup>, while the NC energy structure has been calculated<sup>[107]</sup>.





**Figure 1.14** Electroluminescence spectra of two devices made with the same NCs, where (A) is simply an Alq<sub>3</sub>-NC-TPD device and (B) is the same device with the hole blocking layer TAZ grown between the Alq<sub>3</sub> and the NC monolayer. Spectral peaks at wavelengths of 562 and 400 nm, and the broader shoulder centred at 530 nm, are attributed to emission from NCs, TPD and Alq<sub>3</sub>, respectively. The green and orange lines in (A) show the decomposition of the electroluminescence spectra into Alq<sub>3</sub>, TPD, and NC contributions, which are quantified in terms of an emission fraction ( $f_x$ ). The respective device cross-sections are shown for comparison as insets as well as the molecular structure of the small organic molecules TPD, Alq<sub>3</sub>, and TAZ.

Figure 1.12(a) shows the EL spectra of different QD-LEDs operated at low current density (0.38-13 mA/cm<sup>2</sup>). The spectra demonstrate the ability to fabricate devices which yield highly monochromatic EL that is tunable from 540 nm to 635 nm, corresponding to the PL spectrum of each NC starting solution. The EL of these devices has greater than 70% NC emission. The remaining organic (Alq<sub>3</sub> or TPD) EL is due to the presence of voids, grain boundaries, and interstitial spaces in the NC monolayers that allow the creation of excitons on organic sites as depicted in Figure 1.15. For example, excitons generated in region A, deep within the electron transporting layer, are more than the Förster energy transfer radius ( $R_F$ ) away from the nearest NC, resulting in organic EL. Similarly, excitons in region B, within the monolayer void, will result in organic EL.



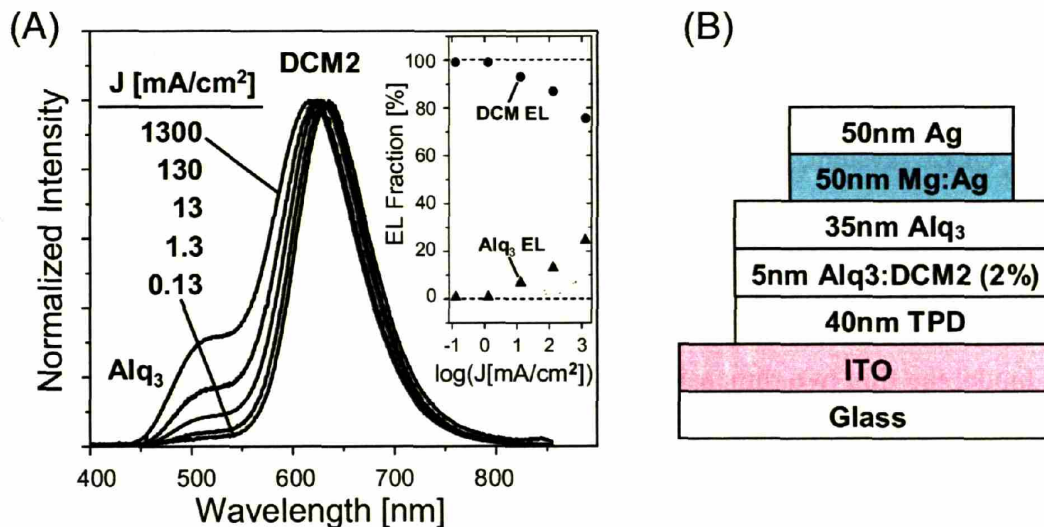
**Figure 1.15** Graphic representation of exciton generation process within the QD-LED structure. At high currents the width of the exciton generation region is expected to exceed the organic-NC Förster energy transfer radius ( $R_F$ ) (region *A* in the figure), resulting in an increased contribution of organic ( $Alq_3$  or TPD) luminescence to the EL spectrum. Excitons created at voids (region *B* in the figure), interstitial spaces and grain boundaries of the NC monolayer may also be farther than  $R_F$  away from the nearest NC.

Figure 1.12(b) shows the EL spectra of QD-LEDs operated at higher current density ( $130 \text{ mA/cm}^2$ ). Comparing to Figure 1.12(a), it is clear that the fraction of emission coming from organic lumophores has increased. Figure 1.12(c) demonstrates this same effect for a single QD-LED operated over 3 decades of current densities, from  $0.38 \text{ mA/cm}^2$  to  $380 \text{ mA/cm}^2$ . This change in ratio of NC to organic EL signifies a notable change in the exciton generation process. At the current density of  $130 \text{ mA/cm}^2$ , at most  $10^6$  electrons per second arrive at each NC site so that the rapid NC exciton relaxation (thin film CdSe NC exciton lifetime is less than  $10 \text{ ns}^{[114]}$ ) keeps the NC exciton density at less than 1%. Such a low NC exciton population should not modify the organic-NC exciton transfer rate, and consequently the change in the NC emission fraction with current could be due to a change in the exciton recombination region width.

As was seen in an earlier study<sup>[99]</sup>, it was proposed that the exciton recombination region of QD-LEDs broadens with increasing current, which was confirmed by using an archetype OLED system, DCM2 doped into a TPD/Alq<sub>3</sub> structure. The OLED cross-section is shown in Figure 1.16(b), with the red laser dye DCM2 used in place of NCs. The dye is doped at low concentration (2% by weight) in a 5 nm thick Alq<sub>3</sub> layer, to closely model the thin two-dimensional NC sheet that makes up the emissive layer of the QD-LED structures. With this device the performance of a very thin and extensively characterized lumophore layer was studied, eliminating NCs as a performance modifier. The spectral dependence on current density was then measured over 4 decades of current. From the normalized EL spectra in Figure 1.16(a) it is clear that the ratio of Alq<sub>3</sub> to DCM2 emission rises with increasing current density. The observed changes in Figure 1.16(a) are consistent with the spectral changes of the QD-LED in Figure 1.12(c). Equivalently, the organic emission in the QD-LED devices is a consequence of the very thin NC lumophore layer, suggesting the need for better confinement of excitons near the NCs. To date, however, fabrication of an effective exciton confinement structure has been complicated by the difficulty in depositing a uniform thin (< 10 nm) aromatic film on top of an alkane capped NC monolayer, as morphological studies have explored<sup>[110]</sup>.

Recent studies<sup>[97]</sup> indicate that efficient Förster energy transfer occurs from phosphorescent organic molecules to NC monolayers when they are located adjacent to one another. If Förster energy transfer is the mechanism for efficient EL in these hybrid organic/inorganic QD-LED devices, then changing the organic molecules located next to the NCs from fluorescent to phosphorescent species is expected to quadruple the observed EL external quantum efficiency. Repeated attempts at this experiment (in





**Figure 1.16** Normalized electroluminescence spectra from the DCM2 doped OLED structure shown in (B). The five curves are at five different current levels, each an order of magnitude higher than the previous. At the lowest current density ( $0.13 \text{ mA/cm}^2$ ) the device is nearly monochromatic, emitting only from DCM2 sites. As the current is increased, a larger fraction of the emission is from the  $\text{Alq}_3$  sites. Inset is a plot of emission fraction versus current density for  $\text{Alq}_3$  and DCM2 EL.

various device structures) have failed to demonstrate an efficiency increase. Instead it is usually coupled to an efficiency decrease despite the far greater EQE that is achieved in these phosphorescent OLEDs which do not include a NC monolayer. Further studies<sup>[97]</sup> indicate that the NCs trap electrons during device operation. As mentioned earlier, the Auger process most likely quenches excited NCs that are charged, so an exciton that is energy transferred to a charged NC will probably be quenched before radiatively recombining. This suggests that the efficient emission process in these QD-LEDs is most likely direct injection of charge (both holes and electrons) into the NC to create neutral excitons which can then recombine radiatively before an additional electron is injected. The creation of more efficient devices operating by this mechanism requires a finely balanced injection of electrons and holes into the NCs, which the QD-LED device band diagram (Figure 1.13(a)) suggests will be challenging.



## 1.4 Overview of Thesis

The fabrication of QD-LEDs consists of first synthesizing the semiconductor nanocrystals (NCs) with the desired properties followed by the incorporation of these NCs into OLED based device structures. Along this theme, this thesis is divided into two major sections. The first being the synthesis and characterization of the NC materials, Chapters 2, 3, and 4, followed by the fabrication and characterization of the resulting QD-LEDs, Chapters 5 and 6. Chapter 2 introduces the semiconductor PbSe and discusses in detail the synthesis, characterization, and properties of PbSe NCs, as well as how the simple PbSe NC synthesis can be used as a platform to look in depth at the mechanism for how molecular precursors are reduced to form solid crystalline NCs in solution in the presence of phosphorous containing molecules. Chapters 3 and 4 discuss the synthesis and characterization of new blue and green emitting NCs optimized for QD-LED display applications as well as, in the case for the blue emitting NCs, how they were also useful in NC lasing and biological imaging. Chapter 5 discusses the study of phase separation, the first technique developed to produce NC monolayers for efficient QD-LED fabrication, as well as the recent near infrared, blue, and red QD-LEDs fabricated using this method from the materials discussed in Chapters 2 and 3. Chapter 6 finishes off the thesis with the introduction of a new technique for patterning and depositing NC monolayers for QD-LED fabrication, known as micro-contact printing, as well as demonstrates its potential as a QD-LED fabrication technique for the creation of color saturated red, green, and blue patterned devices towards full color QD-LED displays.

## 1.5 References

1. L. E. Brus, *J. Chem. Phys.* 1983, 79, 5566.
2. D. S. Chemla, *Physics Today*, **1993**, 46.
3. D. S. Chemla and D. A. B. Miller, *J. Opt. Soc. Am. B* 2, **1985**, 1155.
4. K. H. Hellwege, *Landolt-Bornstein Numerical Data and Functional Relationships in Science and Technology* (Springer-Verlag, Berlin, 1982).
5. F. W. Wise, *Acc. Chem. Res.* **2000**, 33, 773.
6. Al. L. Efros, M. Rosen, *Annu. Rev. Mater. Sci.* **2000**, 30, 475.
7. C. B. Murray, D. J. Norris, M. G. Bawendi, *J. Am. Chem. Soc.* **1993**, 115, 8706.
8. M. A. Kastner, *Physics Today* **1993**, 46, 24.
9. S. A. Empedocles, M. G. Bawendi, *Acc. Chem. Res.* **1999**, 32, 389.
10. M. G. Bawendi, A. R. Kortan, M. L. Steigerwald, L. E. Brus, *J. Chem. Phys.* **1989**, 91, 7282.
11. C. B. Murray, C. R. Kagan, M. G. Bawendi, *Annu. Rev. Mater. Sci.* **2000**, 30, 545.
12. B. O. Dabbousi, J. Rodriguez-Viejo, F. V. Mikulec, J. R. Heine, H. Mattoussi, R. Ober, K. F. Jensen, M. G. Bawendi, *J. Phys. Chem. B* **1997**, 101, 9463.
13. B. O. Dabbousi, O. Onitsuka, M. G. Bawendi, M. F. Rubner, *Appl. Phys. Lett.* **1995**, 66, 1316.
14. M. A. Hines, P. Guyot-Sionnest, *J. Phys. Chem.* **1996**, 100, 468.
15. S. Coe-Sullivan, W. K. Woo, J. S. Steckel, M. G. Bawendi, V. Bulović, *Org. Electron.* **2003**, 4, 123.
16. R. Xie, U. Kolb, J. Li, T. Basche, A. Mews, *J. Am. Chem. Soc.* **2005**, 127, 7480.
17. D. I. Chepic, A. L. Efros, A. I. Ekimov, M. G. Ivanov, V. A. Kharchenko, I. A. Kudriavtsev, T. V. Yazeva, *Journal of Luminescence* **1990**, 47, 113.
18. A. L. Efros, in Archives (Naval Research Laboratory, **2002**).
19. V. A. Kharchenko and M. Rosen, *Journal of Luminescence* **1996**, 70, 158.
20. A. L. Efros, *Phys. Rev. Lett.* **1997**, 78, 1110.
21. V. I. Klimov, D. W. McBranch, C. A. Leatherdale, M. G. Bawendi, *Phys. Rev. B* **1999**, 60, 13740.
22. V. I. Klimov, A. A. Mikhailovsky, D. W. McBranch, C. A. Leatherdale, M. G. Bawendi, *Phys. Rev. B* **2000**, 61, 13349.
23. V. I. Klimov, *J. Phys. Chem. B* **2000**, 104, 6112.
24. V. I. Klimov, A. A. Mikhailovsky, D. W. McBranch, C. A. Leatherdale, M. G. Bawendi, *Science* **2000**, 287, 1011.
25. A. Lipovskii, E. Kolobkova, V. Petrikov, I. Kang, A. Olkhovets, T. Krauss, M. Thomas, J. Silcox, F. Wise, Q. Shen, S. Kycia, *Appl. Phys. Lett.* **1997**, 71, 3406.
26. A. I. Ekimov, A. A. Onushchenko, V. A. Tsekhomskii, *Fizika i Khimiya Stekla* **1980**, 6, 511.
27. A. I. Ekimov, A. A. Onushchenko, *Pis'ma v Zhurnal Eksperimental'noi i Teoreticheskoi Fiziki* **1981**, 34, 363.
28. A. Ekimov, *Journal of Luminescence* **1996**, 70, 1.
29. L. E. Brus, *J. Chem. Phys.* **1983**, 79, 5566.
30. I. N. Stranski, L. Krastanow, *Akademische Wissenschaft Literatur, Mainz Abh Math. Naturwiss. Kl.* **1939**, 146, 767.

31. B. A. Joyce, D. D. Vvedensky, *Materials Science and Engineering Reviews - Reports* **2004**, *46*, 127.
32. R. Rossetti, L. Brus, *J. Phys. Chem.* **1982**, *86*, 4470.
33. A. Fojtik, H. Weller, U. Koch, A. Henglein, *Berichte der Bunsen-Gesellschaft* **1984**, *88*, 969.
34. A. Henglein, *Chem. Rev.* **1989**, *89*, 1861.
35. C. T. Dameron, R. N. Reese, R. K. Mehra, A. R. Kortan, P. J. Carroll, M. L. Steigerwald, L. E. Brus, D. R. Winge, *Nature* **1989**, 338 596.
36. C. T. Dameron, B. R. Smith, D. R. Winge, *J. Bio. Chem.* **1989**, *264*, 17355.
37. K. K. W. Wong, S. Mann, *Adv. Mater.* **1996**, *8*, 928.
38. M. L. Steigerwald, A. P. Alivisatos, J. M. Gibson, T. D. Harris, R. Kortan, A. J. Muller, A. M. Thayer, T. M. Duncan, D. C. Douglass, L. E. Brus, *J. Am. Chem. Soc.* **1988**, *110*, 3046.
39. J. G. Brennan, T. Siegrist, P. J. Carroll, S. M. Stuczynski, L. E. Brus, M. L. Steigerwald, *J. Am. Chem. Soc.* **1989**, *111*, 4141.
40. D. V. Talapin, A. L. Rogach, A. Kornowski, M. Haase, H. Weller, *Nano Lett.* **2001**, *1*, 207.
41. M. G. Bawendi, N. E. Stott, *U. S. Patent Number 6,576,291: USA*, **2003**.
42. B. K. H. Yen, N. E. Stott, K. F. Jensen, M. G. Bawendi, *Adv. Mater.* **2003**, *15*, 1858.
43. L. Qu, Z. A. Peng, *Nano Lett.* **2001**, *1*, 333.
44. Z. A. Peng, X. Peng, *J. Am. Chem. Soc.* **2001**, *123*, 183.
45. L. Manna, E. C. Scher, A. P. Alivisatos, *J. Am. Chem. Soc.* **2000**, *122*, 12706.
46. L. Manna, E. C. Scher, A. P. Alivisatos, *J. Cluster Sci.* **2002**, *13*, 521.
47. Z. A. Peng, X. Peng, *J. Am. Chem. Soc.* **2002**, *124*, 3343.
48. X. Peng, *Adv. Mater.* **2003**, *15*, 459.
49. W. W. Yu, Y. A. Wang, X. Peng, *Chem. Mater.* **2003**, *15*, 4300.
50. D. J. Milliron, S. M. Hughes, Y. Cui, L. Manna, J. Li, L.-W. Wang, A. P. Alivisatos, *Nature* **2004**, *430*, 190.
51. X. Peng, U. Manna, W. Yang, J. Wickham, E. Scher, A. Kadavanich, A. P. Alivisatos, *Nature* **2000**, *404*, 59.
52. Z. A. Peng, X. Peng, *J. Am. Chem. Soc.* **2001**, *123*, 1389.
53. L. Manna, D. J. Milliron, A. Meisel, E. C. Scher, A. P. Alivisatos, *Nat. Mater.* **2004**, *2*, 382.
54. V. K. LaMer, R. H. Dinegar, *J. Am. Chem. Soc.* **1950**, *72*, 4847.
55. H. Reiss, *J. Chem. Phys.* **1951**, *19*, 482.
56. Y. De Smet, L. Deriemaeker, R. Finsy, *Langmuir* **1997**, *13*, 6884.
57. H. Grätz, *Scr. Mater.* **1997**, *37*, 9.
58. Zhong, X.; Han, M.; Dong, Z.; White, T. J.; Knoll, W. *J. Am. Chem. Soc.* **2003**, *125*, 8589.
59. X. Peng, M. C. Schlamp, A. V. Kadavanich, A. P. Alivisatos, *J. Am. Chem. Soc.* **1997**, *119* 7019.
60. D. V. Talapin, R. Koeppel, S. Götzinger, A. Kornowski, J. M. Lupton, A. L. Rogach, O. Benson, J. Feldmann, H. Weller, *Nano Lett.* **2003**, *3*, 1677.
61. P. Reiss, J. Bleuse, A. Pron, *Nano Lett.* **2002**, *2*, 781.

62. S. A. Ivanov, J. Nanda, A. Piryatinski, M. Achermann, L. P. Balet, I. V. Bezel, P. O. Anikeeva, S. Tretiak, V. I. Klimov, *J. Phys. Chem. B* **2004**, *108*, 10625.
63. X. Zhong, R. Xie, Y. Zhang, T. Basche, W. Knoll, *Chem. Mater.* **2005**, *17*, 4038.
64. D. V. Talapin, I. Mekis, S. Götzinger, A. Kornowski, O. Benson, H. Weller, *J. Phys. Chem. B* **2004**, *108*, 18826.
65. C.-T. Cheng, C.-Y. Chen, C.-W. Lai, W.-H. Liu, S.-C. Pu, P.-T. Chou, Y.-H. Chou, H.-T. Chiu, *J. Mater. Chem.* **2005**, *15*, 3409.
66. J. S. Steckel, J. P. Zimmer, S. Coe-Sullivan, N. E. Stott, V. Bulovic, M. G. Bawendi, *Angew. Chem. Int. Ed.* **2004**, *43*, 2154.
67. S. Kim, B. R. Fisher, H.-J. Eisler, M. G. Bawendi, *J. Am. Chem. Soc.* **2003**, *125*, 11466.
68. R. Xie, X. Zhong, T. Basche, *Adv. Mater.* **2005**, *17*, 2741.
69. H.-S. Chen, B. Lo, J.-Y. Hwang, G.-Y. Chang, C.-M. Chen, S.-J. Tasi, S.-J. J. Wang, *J. Phys. Chem. B* **2004**, *108*, 17119.
70. S.-W. Kim, J. P. Zimmer, S. Ohnishi, J. B. Tracy, J. V. Frangioni, M. G. Bawendi, *J. Am. Chem. Soc.* **2005**, *127*, 10526.
71. Y.-W. Cao, U. Banin, *Angew. Chem. Int. Ed.* **1999**, *38*, 3692.
72. M. Kuno, J. K. Lee, B. O. Dabbousi, F. V. Mikulec, M. G. Bawendi, *J. Chem. Phys.* **1997**, *106*, 9869.
73. C. B. Murray, C. R. Kagan, M. G. Bawendi, *Science* **1995**, *270*, 1335.
74. Y. Chan, J. P. Zimmer, M. Stroh, J. S. Steckel, R. K. Jain, M. G. Bawendi, *Adv. Mater.* **2004**, *16*, 2092.
75. S.-W. Kim, S. Kim, J. B. Tracy, A. Jasanoff, M. G. Bawendi, *J. Am. Chem. Soc.* **2005**, *127*, 4556.
76. C. W. Tang, S. A. VanSlyke, *Appl. Phys. Lett.* **1987**, *51*, 913.
77. J. H. Burroughes, D. D. C. Bradley, A. R. Brown, R. N. Marks, K. MacKay, R. H. Friend, P. L. Burn, A. B. Holmes, *Nature* **1990**, *347*, 539.
78. N. C. Greenham, R. H. Friend, *Solid State Phys.* **1995**, *49*, 1.
79. J. R. Sheets, H. Antoniadis, M. Hueschen, W. Leonard, J. Miller, R. Moon, D. Roitman, A. Stocking, *Science* **1996**, *273*, 884.
80. V. Bulovic, G. Gu, P. E. Burrows, M. E. Thompson, S. R. Forrest, *Nature* **1996**, *380*, 29.
81. G. Gu, P. E. Burrows, S. Venkatesh, S. R. Forrest, M. E. Thompson, *Optics Lett.* **1997**, *22*, 172.
82. G. Parthasarathy, P. E. Burrows, V. Khalfin, V. G. Kozlov, S. R. Forrest, *Appl. Phys. Lett.* **1998**, *72*, 2138.
83. M. A. Baldo, D. F. O'Brien, Y. You, A. Shoustikov, S. Sibley, M. E. Thompson, S. R. Forrest, *Nature* **1998**, *395*, 151.
84. C. Adachi, M. A. Baldo, M. E. Thompson, S. R. Forrest, *J. Appl. Phys.* **2001**, *90*, 5048.
85. C. Adachi, M. A. Baldo, S. R. Forrest, S. Lamansky, M. E. Thompson, R. C. Kwong, *Appl. Phys. Lett.* **2001**, *78*, 1622.
86. T. Yamasaki, K. Sumioka, T. Tsutsui, *Appl. Phys. Lett.* **2000**, *76*, 1243.
87. S. Moller, S. R. Forrest, *J. Appl. Phys.* **2002**, *91*, 3324.

88. S. Dirr, A. Böhler, S. Wiese, H.-H. Johannes, W. Kowalsky, *Jap. J. Appl. Phys. Part 1-Regular Papers Short Notes & Review Papers* **1998**, *37*, 1457.
89. Z. D. Popovic, H. Aziz, N.-X. Hu, A.-M. Hor, G. Xu, *Synth. Metal.* **2000**, *111*, 229.
90. J. J. Ho, *Elect. Lett.* **2003**, *39*, 458.
91. M. Ben Khalifa, D. Vaufrey, J. Tardy, *Org. Electr.* **2004**, *5*, 187.
92. G. Parthasarathy, C. Shen, A. Kahn, S. R. Forrest, *J. Appl. Phys.* **2001**, *89*, 4986.
93. C. F. Madigan, V. Bulovic, *Phys. Rev. Lett.* **2003**, *91*, 247403.
94. M. A. Baldo, V. G. Kozlov, P. E. Burrows, S. R. Forrest, V. S. Ban, B. Koene, M. E. Thompson, *Appl. Phys. Lett.* **1997**, *71*, 3033.
95. M. Shtein, H. F. Gossenberger, J. B. Benziger, S. R. Forrest, *J. Appl. Phys.* **2001**, *89*, 1470.
96. M. Shtein, P. Peumans, J. B. Benziger, S. R. Forrest, *J. Appl. Phys.* **2003**, *93*, 4005.
97. S. Coe-Sullivan, PhD Thesis, M.I.T. (2005).
98. M. A. Baldo, D. F. O'Brien, M. E. Thompson, S. R. Forrest, *Phys. Rev. B* **1999**, *60*, 14422.
99. V. Bulovic, V. B. Khalfin, G. Gu, P. E. Burrows, D. Z. Garbuzov, S. R. Forrest, *Phys. Rev. B* **1998**, *58*, 3730.
100. C. W. Tang, S. A. VanSlyke, C. H. Chen, *J. Appl. Phys.* **1989**, *65*, 3610.
101. V. Bulovic, P. E. Burrows, S. R. Forrest, *Semiconductors and Semimetals* **2000**, *64*, 255.
102. V. Bulovic, V. G. Kozlov, V. B. Khalfin, S. R. Forrest, *Science* **1998**, *279*, 553.
103. L. Ke, R. S. Kumar, K. Zhang, S. J. Chua, A. T. S. Wee, *Synth. Metals* **2004**, *140*, 295.
104. L. Mizuho Securities Co., "Organic EL Industry", 2004.
105. V. L. Colvin, M. C. Schlamp, A. P. Alivisatos, *Nature* **1994**, *370*, 354.
106. H. Mattoussi, L. H. Radzilowski, B. O. Dabbousi, D. E. Fogg, R. R. Schrock, E. L. Thomas, M. F. Rubner, M. G. Bawendi, *J. Appl. Phys.* **1999**, *86*, 4390.
107. H. Mattoussi, L. H. Radzilowski, B. O. Dabbousi, E. L. Thomas, M. G. Bawendi, M. F. Rubner, *J. Appl. Phys.* **1998**, *83*, 7965.
108. M. C. Schlamp, X. G. Peng, A. P. Alivisatos, *J. Appl. Phys.* **1997**, *82*, 5837.
109. N. Tessler, V. Medvedev, M. Kazes, S. Kan, U. Banin, *Science* **2002**, *295*, 1506.
110. S. Coe, W.-K. Woo, M. Bawendi, V. Bulovic, *Nature* **2002**, *420*, 800.
111. S. Coe-Sullivan, J. S. Steckel, W.-K. Woo, M. G. Bawendi, V. Bulovic, *Adv. Funct. Mater.* **2005**, *15*, 1117.
112. C. A. Leatherdale, C. R. Kagan, N. Y. Morgan, S. A. Empedocles, M. A. Kastner, M. G. Bawendi, *Phys. Rev. B* **2000**, *62*, 2669.
113. V. I. Klimov, D. W. McBranch, *Phys. Rev. Lett.* **1998**, *80*, 4028.
114. C. R. Kagan, C. B. Murray, M. G. Bawendi, *Phys. Rev. B* **1996**, *54*, 8633.
115. I. G. Hill, A. Kahn, *J. Appl. Phys.* **1999**, *86*, 4515.



# Chapter 2

## PbSe Nanocrystals

### 2.1 Introduction

PbSe is a IV-VI binary semiconductor with a bulk band gap of 0.26 eV (4769 nm). It has a very large exciton Bohr radius (46 nm)<sup>[1]</sup> compared to most semiconductors and as a result, PbSe nanocrystals (NCs) with diameters in the synthetically accessible range of 2-16 nm exhibit strong quantum confinement. In contrast CdSe has an exciton Bohr radius of 6 nm<sup>[1]</sup> and like most other II-VI and III-V semiconductors, has a hole Bohr radius of  $\sim 1$  nm<sup>[1,2]</sup>, due to the large hole mass. PbSe has similarly small electron and hole masses, resulting in electron and hole Bohr radii of 23 nm<sup>[1]</sup>. The result of these large confinement energies in PbSe NCs in the particle size regime of 2-16 nm is a band gap tuning range of  $\sim 2500$  nm<sup>[3,4]</sup>, compared to a tuning range of  $\sim 250$  nm (2-15 nm in diameter) for CdSe<sup>[5]</sup>. PbSe crystallizes in the cubic sodium chloride structure in the bulk as well as in the NC regime, whereas CdSe and most other II-VI and III-V semiconductors take on the wurtzite or zinc-blende crystal structure. This difference in crystal structure between PbSe and most other II-VI and III-V semiconductors has led to the great difficulty encountered in trying to overcoat the PbSe NCs with a larger band gap semiconductor in order to increase its stability and efficiency for use in solid state devices. Not many large band gap semiconductors or for that matter semiconductors in general adopt the rock salt crystal structure and those that over the years have become most common in NC core-shell preparation all adapt the wurtzite or zinc-blende crystal

structure. Typically very ionic materials such as NaF, KCl, FeCl, CuI, HgCl, CaS, AgCl, etc. adopt the rock salt crystal structure, but unfortunately these materials are for the most part not stable to water and oxygen. This instability to water and oxygen applies to interesting large band gap semiconductor materials such as MgS and MgSe (both adopt the rock salt crystal structure) as well. Attempts to overcoat PbSe with CdSe, ZnSe, and ZnS were made by me and others (V. Klimov's group), but a true core-shell structure has not been realized to date. Two literature reports claim to have overcoated PbSe NCs with PbS<sup>[6,7]</sup> (bulk band gap is 0.37 eV and crystallizes in the rock salt structure with a lattice mismatch of only ~3% from PbSe), but because of the extremely small difference in band gap energy between PbSe and PbS, this effectively does nothing to maintain exciton confinement in the PbSe core, leading to what is essentially a larger PbSe particle. PbS, however, may be less susceptible to oxidation compared to PbSe and therefore provide a slight increase in NC stability. Other much less common materials such as SnSe, InSe, or GaSe may prove to be more suitable for the successful growth of a larger band gap semiconductor shell onto PbSe NCs.

PbSe NCs have been synthesized and used for many different applications. Because the very simple PbSe NC growth procedure, first described by Murray and co-workers<sup>[8]</sup>, can be made to produce very narrow size distributions, PbSe NCs have been used to form highly ordered close packed NC films over large areas in complex systems<sup>[9]</sup> as well as simple hexagonally close packed systems<sup>[10]</sup>. And because their optical properties address the near-infrared (NIR) portion of the wavelength spectrum, they have been used to fabricate large area NIR-emitting QD-LEDs<sup>[3]</sup>, films that exhibit NIR optically pumped amplified spontaneous emission<sup>[11]</sup>, PbSe containing polymeric



waveguides<sup>[12]</sup>, and PbSe NC based efficient passive Q-switches in NIR pulsed lasers<sup>[13]</sup>. Lastly, PbSe NCs have enabled the observation of both hole and electron injection into quantum confined states of colloidal NCs<sup>[14]</sup> for the first time, as well as the observation that impact ionization (the inverse of Auger recombination) occurs with high efficiency in semiconductor NCs<sup>[15]</sup>. These observations were possible for the first time due to the small band gap of PbSe and the high degree of quantum confinement obtainable using this material.

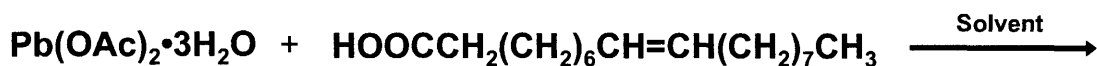
## **2.2 PbSe Nanocrystal Synthesis and Characterization**

### **2.2.1 Background**

PbSe nanocrystals (NCs) with size distributions narrow enough to measure structured absorption spectra were first synthesized and characterized by Lipovskii and co-workers<sup>[16]</sup>. This was achieved through phase decomposition of a PbSe solid solution in a phosphate glass host. The NCs made using this method were then trapped in the glass host and as a result could not be manipulated for more in depth study and characterization or used in fabrication of active devices. It was not until Murray and co-workers<sup>[8]</sup> developed a colloidal synthesis of high-quality PbSe NCs that the scientific community could begin to study in more depth and use PbSe NCs for practical applications.

### **2.2.2 Diphenyl Ether Based Synthesis (TEM, XRD, WDS)**

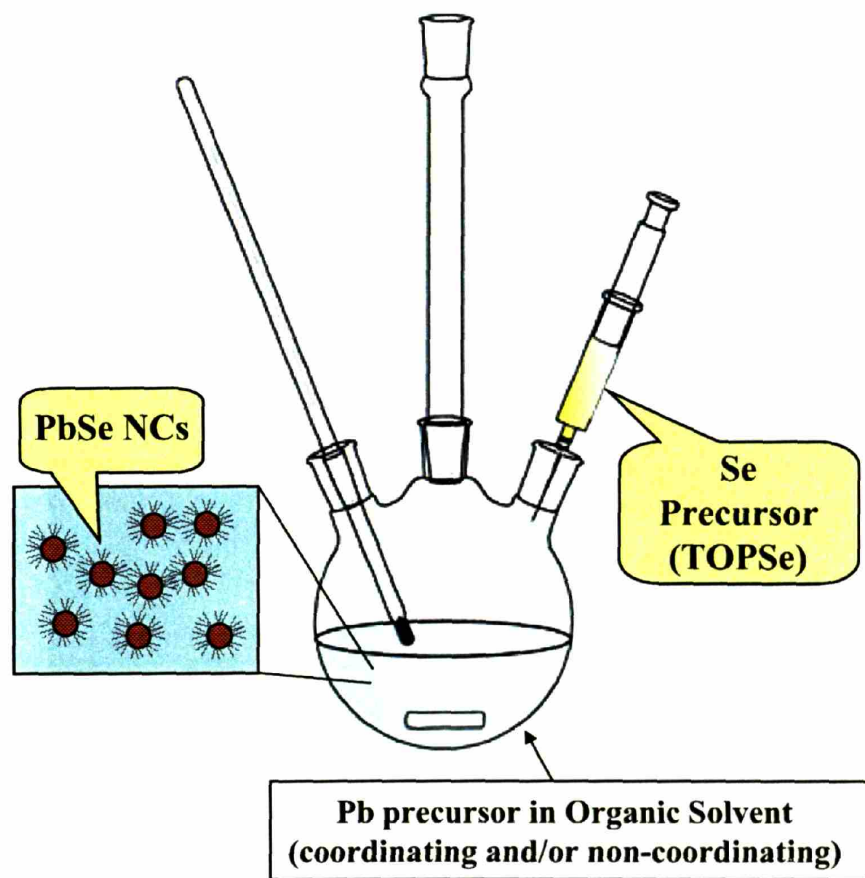
Based on this brief, non detailed colloidal synthesis by Murray and co-workers<sup>[8]</sup>, this PbSe NC synthesis was optimized and enhanced to yield high-quality PbSe NCs with very narrow size distributions in the size regime of 2 nm to 10 nm (corresponding to



**Reaction Scheme 2.1** General reaction scheme for the growth of PbSe NCs. Lead acetate is mixed with oleic acid in a solvent to form the lead precursor. Then TOPSe is injected into the solution containing the lead precursor to form the PbSe NCs.

absorption peaks  $\lambda = 1.0 \mu\text{m}$  (1.2 eV) to  $\lambda > 2.4 \mu\text{m}$  (<0.5 eV), respectively). The basic synthesis scheme is shown in Reaction Scheme 2.1 and pictorially in Figure 2.1. Pb acetate is degassed in the presence of oleic acid to form Pb oleate (Pb precursor). This can be done in many different solvents. The solvent used by Murray and co-workers was diphenyl ether (DPE), which is also the solvent used here initially. I found that other solvents such as squalene, tri-n-octylphosphine (TOP), dioctyl ether (DOE), and octadecene (ODE) can be used as well, which will be discussed shortly. Tri-n-octylphosphine selenide (TOPSe) is then injected into the hot flask of Pb oleate in solution to form the PbSe NCs (see Figure 2.1).

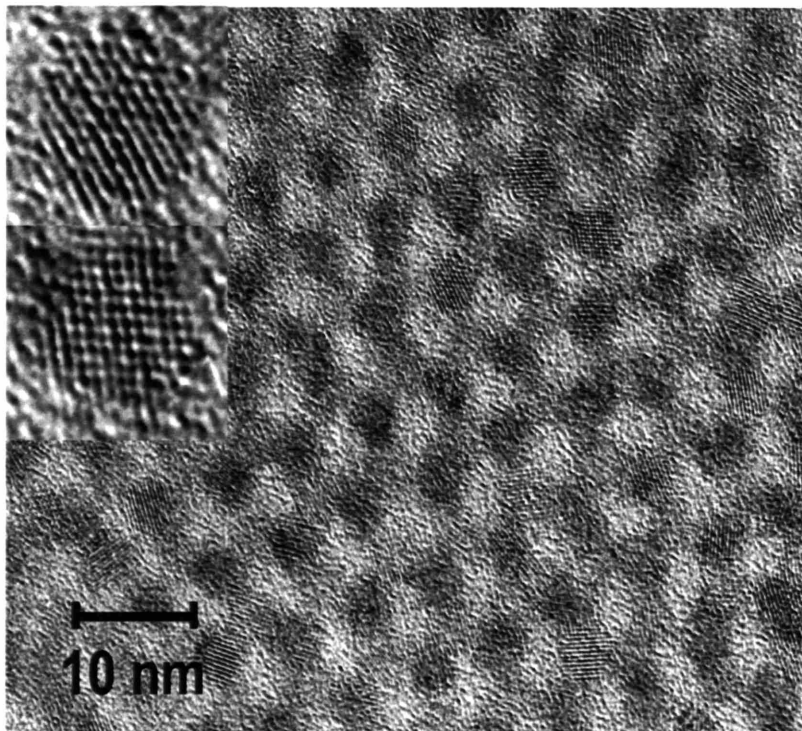
The detailed description of the DPE based synthesis that was found to produce good particles goes as follows: 5 mL of 1M TOPSe (TOPSe was made by dissolving selenium shot (Alfa Aesar) in TOP (early work used 90 % TCI or Alfa Aesar and later work used 97 % Strem) and stirring overnight) was injected into a round bottom flask containing stirring, degassed (pulled vacuum for 2 hrs. at 85°C) DPE (99 % Alfa Aesar) (15-25 mL), oleic acid (99 % TCI) (1-2 mmol), and lead (II) acetate trihydrate (99.999 % Aldrich) (1 mmol), under argon, at a temperature of 100-180°C. After injection, the nucleated particles were grown for 0-5 minutes while the temperature was ramping back



**Figure 2.1** Cartoon of the apparatus used to synthesize the PbSe NCs. A three neck round bottom flask equipped with a magnetic stir bar, condenser, and temperature readout is shown. The TOPSe is injected into the flask via a syringe pierced through a rubber septum and PbSe NCs form in the solution.

up to the injection temperature. After the growth time, the heating mantle was removed, allowing the solution to cool to room temperature. No size selection was needed after growth because the synthesis was optimized to give very narrow size distributions directly. Particle sizes were tuned by changing the temperature of injection, the growth time, and the concentration of precursors in the solution. These three parameters were explored extensively and it was found that an increase in the concentration of selenium and lead, while keeping their relative concentrations the same, yields smaller NCs and

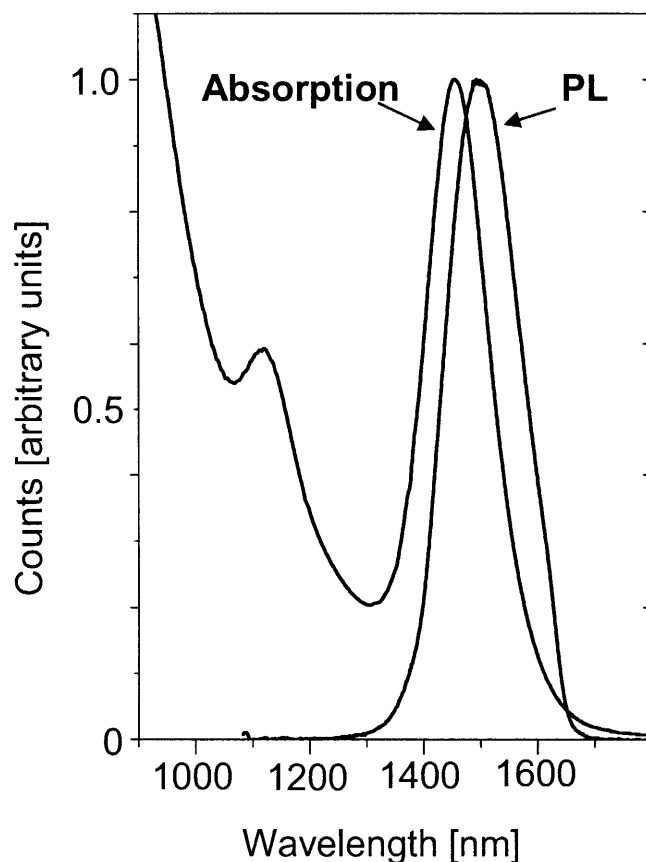
vice versa, an increase in injection temperature gives larger particles and vice versa, and an increase in growth time produces larger NCs and vice versa.



**Figure 2.2** HRTEM Image of  $4.0 \pm 0.5$  nm diameter PbSe particles with two enlarged images (inset).

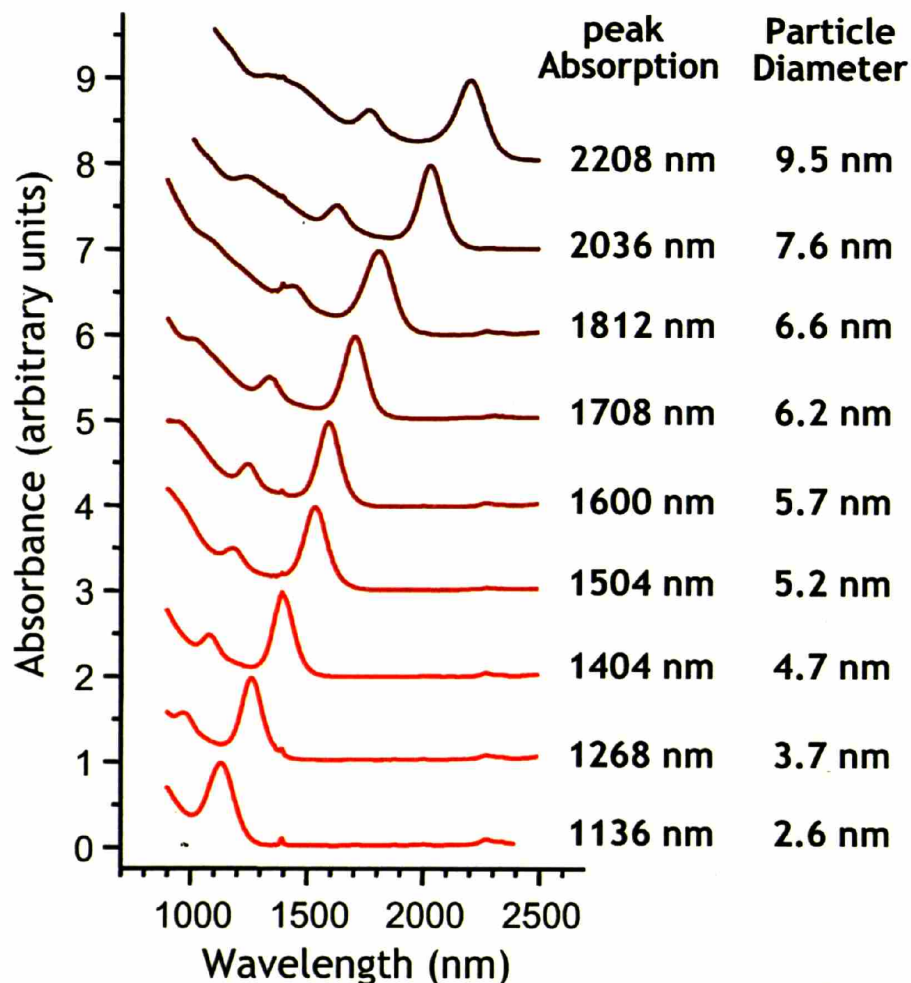
The PbSe NCs were removed from growth solution and purified in the following manner (when purifying particles for use in devices everything was done in the glove box using anhydrous solvents): (Note: This procedure is used for the DPE based PbSe NC preparation) Excess methanol is added to the growth solution and the particles are isolated via centrifugation (spun at 3900 rpm for 5 minutes). They are then redispersed in 1,1,2-trichlorotrifluoroethane and precipitated once more with methanol (a small amount of methanol,  $\sim 1$  mL, is needed to flocculate the particles in 1,1,2-trichlorotrifluoroethane). After centrifugation (3900 rpm for 5 minutes) the NCs are

rinsed with methanol and any excess solvents left behind are pulled off using vacuum. The PbSe NCs were typically stored as dry powders under nitrogen because this was found to lead to the least amount of degradation over time (oxidation of the surface). PbSe NC degradation is discussed later in this chapter.



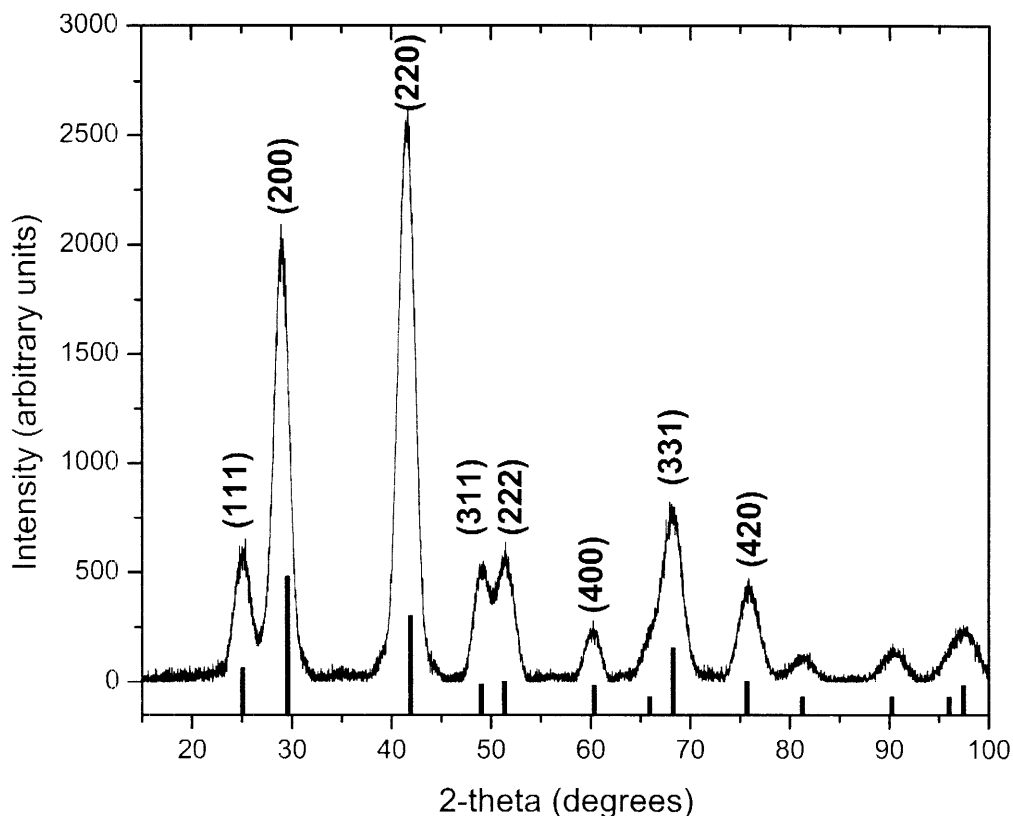
**Figure 2.3** Typical diphenyl ether based PbSe NC absorption (peak at  $\lambda = 1456$  nm) (FWHM = 125 nm / 73 meV) and photoluminescence (PL) (peak at  $\lambda = 1500$  nm) (FWHM = 130 nm / 72 meV) spectra.

Figure 2.2 depicts an ordered layer of  $4.0 \pm 0.5$  nm diameter PbSe NCs imaged by high resolution transmission electron microscopy (HRTEM), showing in the inset an enlarged view of the atomic planes from two NCs. The HRTEM was performed on a JEOL-2010 electron microscope operated at 200kV by Michael Frongillo. Figure 2.3



**Figure 2.4** Absorption spectra of a size series of PbSe NCs ranging from 2.6 to 9.5 nm in diameter. Peak absorption corresponds to the wavelength of absorption of the first absorption feature. Core sizes were measured from TEM images such as in Figure 2.2. The uncertainty in measuring the particle diameters is  $\pm 10\%$ .

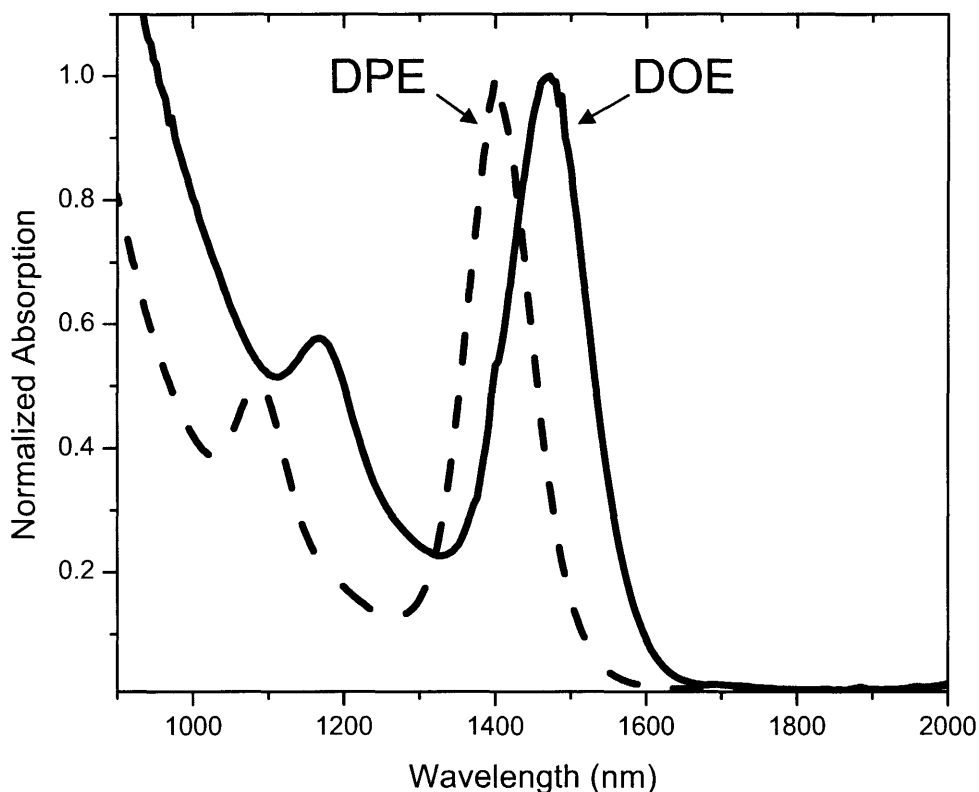
shows typical absorption and emission spectra for  $5.0 \pm 0.5$  nm diameter PbSe NCs. The optical absorption spectra of the PbSe NCs dispersed in 1,1,2-trichlorotrifluoroethane were taken on a Carry 5E, UV-Vis-NIR spectrophotometer and the NIR photoluminescence spectra were acquired using an InGaAs photodiode array cooled to 173 K (Roper Scientific OMA V) and monochromator (the NC solutions were excited using a portable helium neon gas laser).



**Figure 2.5** Powder X-ray diffraction pattern of 5.5 nm diameter PbSe NCs. The bulk PbSe pattern is shown as solid lines and the respective lattice planes are indicated above each peak.

These PbSe NCs were made using the following recipe: A solution of 1mmol of lead acetate trihydrate (Aldrich, 99.99 %) and 2mmol of oleic acid (TCI America, 99 %) in 21 mL of diphenyl ether (99 % Alfa Aesar) was degassed for 2 hours at 85°C. 5mL of 1M TOPSe (TOP used was 97 % Strem) was injected at 155°C and grown for 3.5 min while the temperature was ramping back up to ~155°C. After the growth time, the heating mantle was removed, allowing the solution to cool to room temperature. PbSe NC preparations such as the one outlined above can be modified slightly to yield smaller or larger particles depending on what parameters are changed. As mentioned earlier, simply by changing the temperature of injection, the growth time, and the concentration

of precursors in the solution, one can tune through a very large NC size range as depicted in Figure 2.4.

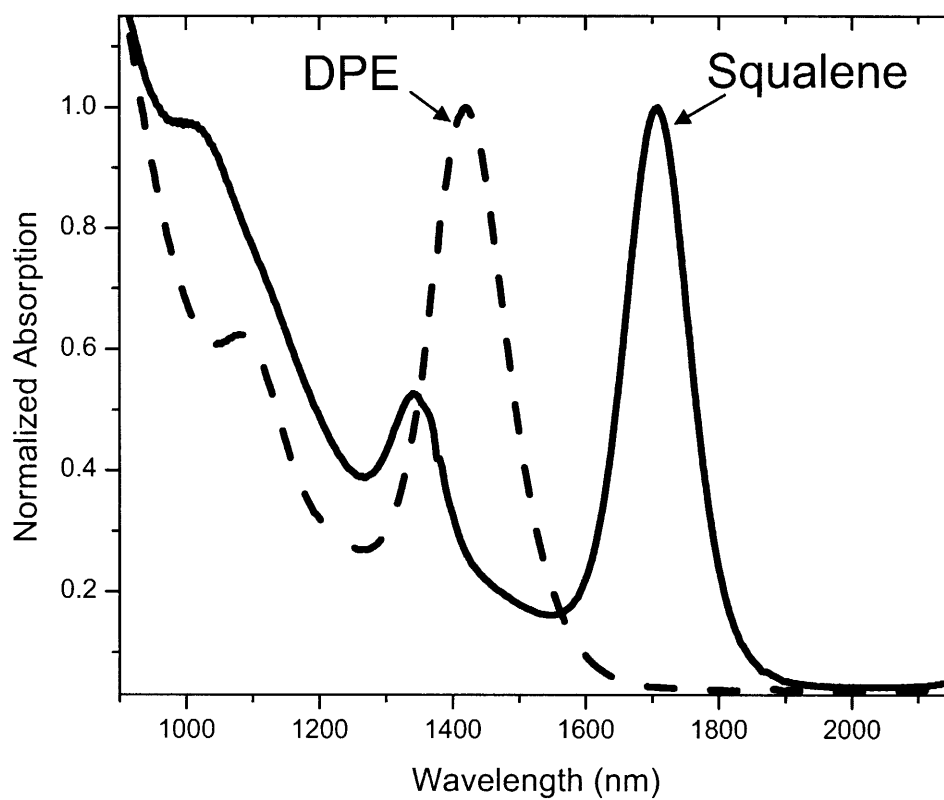


**Figure 2.6** Absorption spectra of two PbSe NC preparations, identical to one another except for the direct substitution of dioctyl ether (DOE) (solid) (peak at  $\lambda = 1472$  nm and FWHM = 116 nm / 67 meV) for diphenyl ether (DPE) (dashed) (peak at  $\lambda = 1407$  nm and FWHM = 94 nm / 59 meV).

Using this procedure, good size distributions can be maintained from 2.6 to 9.5 nm diameter particles, which corresponds to a wavelength tuning range of 1100 nm to 2200 nm in absorption. To confirm that the PbSe NCs were crystallizing in the rock salt crystal structure, powder X-ray diffraction (XRD) was performed on thick drop cast films of the NCs. The powder patterns were obtained on a Rigaku Ru300 X-ray diffractometer. Figure 2.5 shows the powder pattern of 5.5 nm diameter PbSe NCs. It is seen that the pattern matches that of the bulk rock salt PbSe crystal powder pattern indicated by the



solid lines. Elemental analysis of the PbSe NCs was done using wavelength dispersive spectroscopy (WDS) on a JEOL JXA-733 Superprobes. The samples were prepared by drop-casting thick films of purified NCs onto the shiny side of silicon. The average of several measurements yielded a ratio of Pb to Se of 52:48, which is very close to 1:1.



**Figure 2.7** Absorption spectra of two PbSe NC preparations, identical to one another except for the direct substitution of squalene (solid) (peak at  $\lambda = 1706$  nm and FWHM = 105 nm / 45 meV) for diphenyl ether (DPE) (dashed) (peak at  $\lambda = 1420$  nm and FWHM = 135 nm / 83 meV).

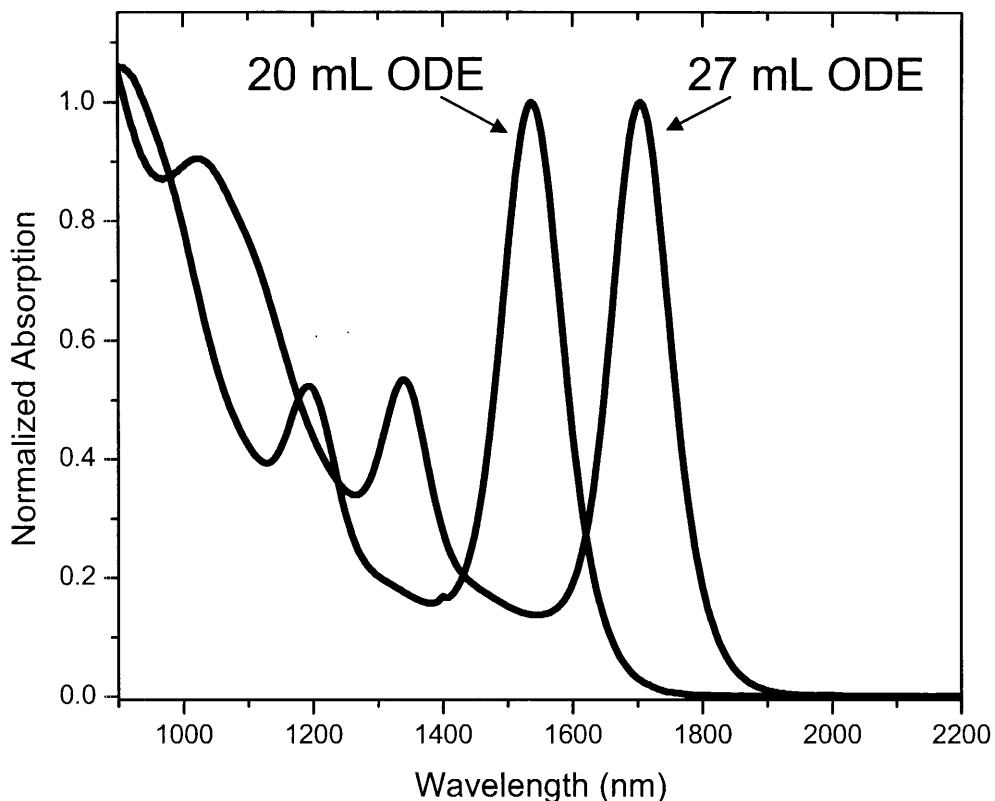
In place of diphenyl ether, dioctyl ether can be used. When a direct substitution is made and all other parameters are left the same, the DOE preparation yields PbSe NCs that are slightly larger with a poorer size distribution (PbSe NC size distribution can be assessed from the absorption spectrum by looking at how defined the second absorption feature is as well as looking at the FWHM of the first absorption feature). This

comparison is shown in Figure 2.6 for the following synthesis: A solution of 1mmol of lead acetate trihydrate (Aldrich, 99.99 %) and 2mmol of oleic acid (TCI America, 99 %) in 20 mL of diphenyl ether (99 % Alfa Aesar) versus 20 mL of dioctyl ether (TCI) was degassed for 2 hours at 85°C. 5mL of 1M TOPSe (TOP used to make the TOPSe was from TCI America and was run once through a column of basic activated aluminum oxide before being used to make the TOPSe) was injected at 140°C and grown for 5 minutes while the temperature was ramping back up to ~140°C. After the growth time, the heating mantle was removed, allowing the solution to cool to room temperature.

### **2.2.3 Squalene and Octadecene Based Syntheses**

Squalene and octadecene are high-boiling organic solvents that are considered to be non-coordinating solvents in NC preparation compared to species like TOP. One would therefore presume that larger PbSe NCs would result when using these non-coordinating solvents due to much less chemical interaction (and therefore less inhibition of NC growth) between the solvent, and the molecular precursors and growing NC surface. This is indeed the case as is shown below. Diphenyl ether is a smelly and high-melting point solvent (~26.8°C), and as a result is not pleasant to work with (It is often a solid at lab temperature and needs to be heated up to use as a liquid). As a result other solvents were explored and two that gave good results were squalene and octadecene.

When a direct substitution of squalene is made for diphenyl ether and all other parameters are left the same, the squalene preparation yields PbSe NCs that are significantly larger with very good size distributions. This comparison is shown in Figure 2.7 for the following synthesis: A solution of 1mmol of lead acetate trihydrate (Aldrich, 99.99 %) and 2mmol of oleic acid (TCI America, 99 %) in 22.5 mL of diphenyl



**Figure 2.8** Absorption spectra of two octadecene (ODE) based PbSe NC preparations. The synthesis was exactly the same for each, apart from the volume of ODE used, which is indicated for each. 20 mL ODE has a peak absorption at  $\lambda = 1536$  nm and a FWHM = 106 nm / 56 meV and the 27 mL ODE preparation has an absorption peak at  $\lambda = 1704$  nm and a FWHM = 103 nm / 44 meV.

ether (99 % Alfa Aesar) versus 22.5 mL of squalene (J.T. Baker, 99 %) was degassed for 2 hours at 85°C. 5mL of 1M TOPSe (TOP used to make the TOPSe was from TCI America and was run once through a column of basic activated aluminum oxide before being used to make the TOPSe) was injected at 160°C and grown for 4 minutes while the temperature was ramping back up to ~160°C. After the growth time, the heating mantle was removed, allowing the solution to cool to room temperature. The NCs were precipitated out of squalene using a four fold (by volume relative to the growth solution volume) excess of butanol and after centrifugation were redispersed in 1,1,2-trichlorotrifluoroethane.

Octadecene (ODE) when used as the solvent, like squalene, gives very good size distributions. Squalene and ODE are very similar to one another in terms of how they behave in this PbSe NC synthesis however, squalene under the same conditions tends to give larger sizes than ODE (this implies that squalene interacts less with the molecular precursors and growing NC surface than ODE, in very simple terms). Figure 2.8 shows two absorption spectra of two different ODE based PbSe NC preparations, which were made under the same conditions except for the volume of ODE used. One can see that the trend described earlier for the diphenyl ether preparation holds here as well. An increase in the concentration of selenium and lead (smaller solvent volume), while keeping their relative concentrations the same, yields smaller NCs and vice versa. The details of the two ODE based PbSe NC preparations go as follows: A solution of 1mmol of lead acetate trihydrate (Aldrich, 99.99 %) and 2mmol of oleic acid (TCI America, 99 %) in 20 mL of octadecene (97 % Fluka) versus 27 mL of octadecene was degassed for 2.5 hours at 100°C. 5mL of 1M TOPSe (TOP used to make the TOPSe was 97 % Strem) was injected at 180°C and grown for 6 minutes while the temperature was ramping back up to ~180°C. After the growth time, the heating mantle was removed, allowing the solution to cool to room temperature. The NCs were precipitated out of ODE using a four fold (by volume relative to the growth solution volume) excess of butanol and after centrifugation were redispersed in 1,1,2-trichlorotrifluoroethane.

#### **2.2.4 TOP Based Synthesis and <sup>31</sup>P NMR Analysis of TOP**

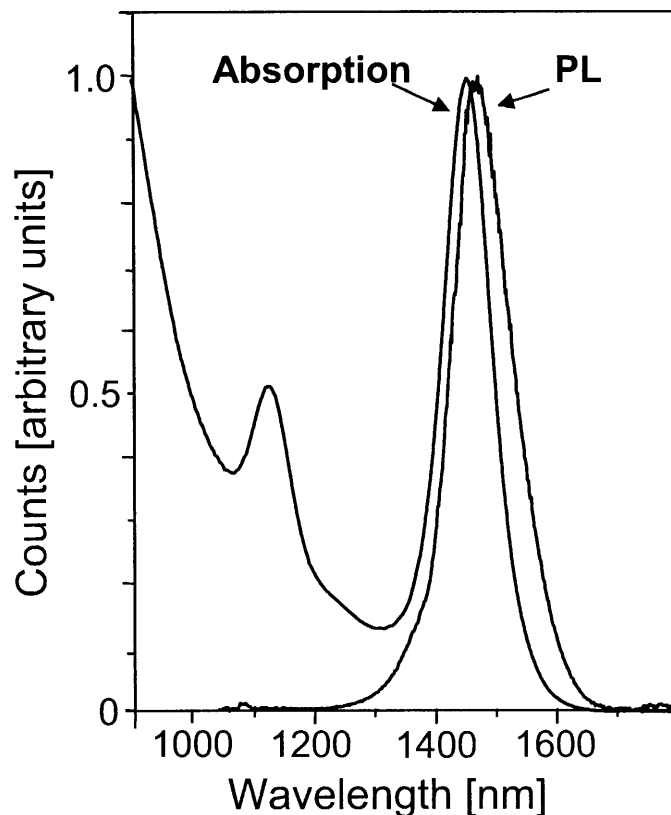
Tri-n-octylphosphine (TOP) is considered to be a coordinating solvent in NC synthesis, due to the phosphorous being able to donate its lone electron pair to species such as the Pb oleate complex and the Se and Pb atoms on the surface of the growing

NCs. TOP is unfortunately hard to purify and as a result the most pure TOP available for purchase to date is 97 % from Strem Chemicals. Several years ago only 90 % TOP was available for purchase and many NC syntheses were developed based on this purity<sup>[5]</sup>. When using 90 % TOP it was clearly seen that the final size and size distribution of the NCs was affected dramatically upon going from one manufacturer to another and even from one lot number to another from the same manufacturer. This same dependency on the purity of TOP was seen even for the 97 % Strem, going from one lot number to another. There has been much speculation over the years as to what the impurities are that modify so extensively the final NC size and size distributions. The current thought in the community is that species such as phosphonic (-PO(OH)<sub>2</sub>) and phosphinic (-PO(OH)) acids act as growth inhibitors by binding strongly to the molecular precursors<sup>[17]</sup> as well as to the growing NC surface. Dialkyl phosphines could also be present, which act as good reducing agents, causing accelerated nucleation in the early stages of the reaction.

Many attempts to purify TOP have been made here in our lab. Several years ago we started running the TOP through a column of basic activated aluminum oxide, which supposedly served to neutralize the phosphonic and phosphinic acids. Significant differences in NC size and size distribution were in fact seen when the filtered TOP was used relative to the original TOP. Attempts at distilling the 97 % Strem have modified the mixture based on <sup>31</sup>P NMR spectra, but have not diminished the total concentration of impurities seen compared to the original TOP. This would suggest that many of these impurities have very similar boiling points to that of TOP and as a result can not be removed via this route and when exposed to high temperatures are chemically modified.

Many organic syntheses, most likely including that of TOP, are carried out using metal based catalysts. These metal based catalysts could very well still be present in the TOP and could not only play a role in the NC syntheses, but also account for the fact that when TOP is heated to high temperatures new peaks appear and others go away or diminish in intensity in the  $^{31}\text{P}$  NMR spectra. The thought being that the metal catalysts would be responsible for the chemical transformation of some impurities into others.

When PbSe NCs first started being synthesized using TOP as the solvent, it was naively believed that the synthesis was not sensitive to the manufacturer and lot number of TOP used, and as a result, a batch of 90 % TCI was mixed with a batch of 90 % Alfa Aesar and passed through a column of basic activated aluminum oxide. This TOP mixture was used in many of the early PbSe syntheses to make the TOPSe. When this batch was almost finished, this TOP mixture was used as the solvent instead of diphenyl ether and it made some of the tightest size distributions of PbSe NCs than ever before or after. Figure 2.9 shows the absorption and emission spectra of one of these TOP based PbSe NCs preparations, which was made in the following manor: A solution of 1mmol of lead acetate trihydrate (Aldrich, 99.99 %) and 2mmol of oleic acid (TCI America, 99 %) in 12 mL of tri-n-octylphospine (TCI America/Alfa Aesar, run once through a column of basic activated aluminum oxide) was degassed for 2 hours at 100°C. 5mL of 1M TOPSe (the TOP used to make the TOPSe was the same as above) was injected at 130°C and grown for 3.5 min while the temperature was ramping back up to ~130°C. After the growth time, the heating mantle was removed, allowing the solution to cool to room temperature. The NCs were precipitated out of TOP using butanol and excess methanol and after centrifugation were redispersed in 1,1,2-trichlorotrifluoroethane.



**Figure 2.9** TOP based PbSe NC absorption (peak at  $\lambda = 1452$  nm) (FWHM = 90 nm / 53 meV) and photoluminescence (PL) (peak at  $\lambda = 1470$  nm) (FWHM = 105 nm / 60 meV) spectra.

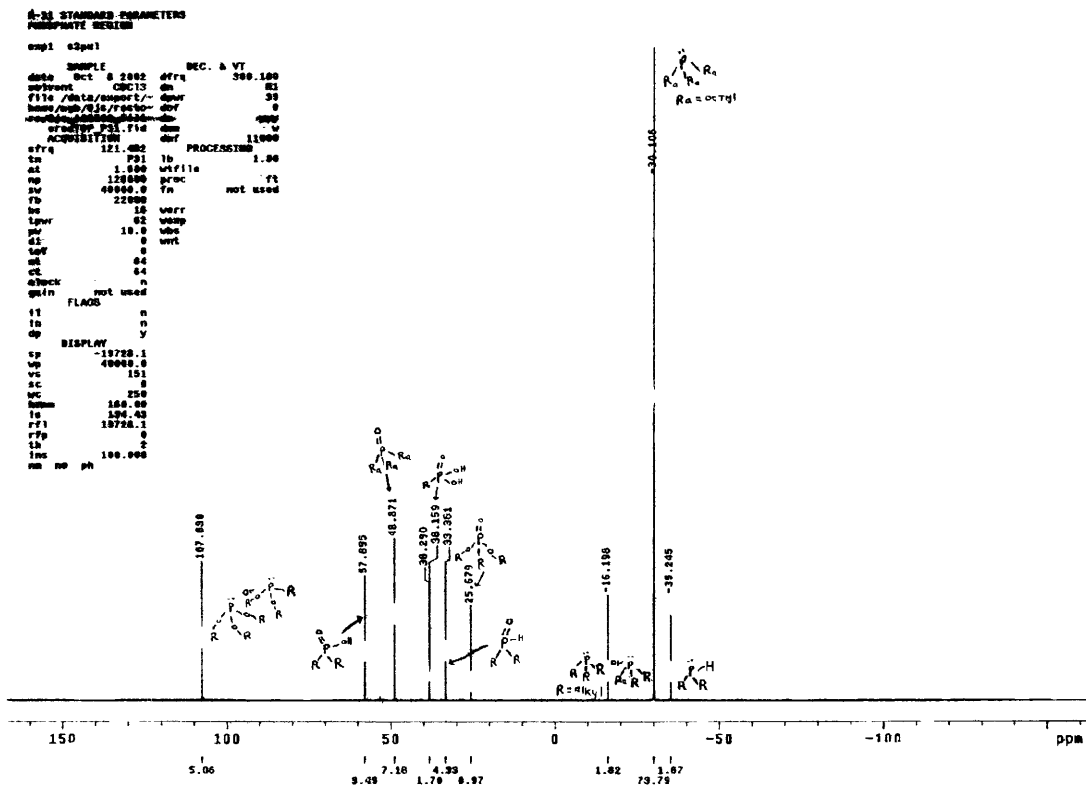
There are very few reports in the literature on the analysis of TOP and its impurities. One report found, uses reversed-phase high performance liquid chromatography to investigate the impurities in tri-n-octylphosphine oxide (TOPO), which is very similar to TOP<sup>[18]</sup>. When this special mixture of TOP that gave very good size distributions of PbSe NCs (Figure 2.9) was finished, it was necessary to turn to 97 % Strem and other batches of 90 % TCI and Alfa Aesar. Never again were PbSe NCs with the same extremely narrow size distributions made. Investigations began using <sup>31</sup>P NMR to help elucidate what species were present in the TCI/Alfa Aesar TOP that were not

present in the new batches.  $^{31}\text{P}$  NMR spectra of the old TOP batches and new ones were acquired and compared. There were differences, but the identity of each peak was unknown. The  $^{31}\text{P}$  NMR spectra for many different phosphorous compounds were either acquired or looked up in the hope of beginning to assign chemical species to peaks.

Chemical Name	Chemical Formula	Chemical Shift in $\text{CHCl}_3$ (ppm)
Diphenylphosphine	$\text{P}(\text{phenyl})_2\text{H}$	-39 to -40
Tri-n-butyl/tri-n-octyl phosphine	$\text{PR}_3$	-30 to -31
Triphenylphosphine	$\text{P}(\text{phenyl})_3$	-4 to -5
Phosphoric acid	$\text{P}(\text{OH})_3\text{O}$	0
Phosphoric acid-Tris(2-ethylhexyl) Ester	$\text{P}(\text{OR})_3\text{O}$	0 to 1
Mono-n-dodecyl phosphate	$\text{P}(\text{OR})(\text{OH})_2\text{O}$	0 to 2
Bis(2-ethylhexyl) phosphate	$\text{P}(\text{OR})_2(\text{OH})\text{O}$	1 to 2
Di-n-butyl phosphite	$\text{P}(\text{OR})_2\text{HO}$	8 to 9
Triphenylphosphine oxide	$\text{P}(\text{phenyl})_3\text{O}$	29 to 30
3-Diethylphosphono propionic acid	$\text{PR}(\text{OR})_2\text{O}$	30 to 31
Tri-n-alkylphosphine selenide	$\text{PR}_3\text{Se}$	35 to 36
Dioctylphosphine oxide	$\text{PR}_2\text{HO}$	35 to 36
n-Tetradecyl/n-decyl/n-hexyl/ phosphonic acid	$\text{PR}(\text{OH})_2\text{O}$	37 to 39
Tri-n-alkylphosphine oxide	$\text{PR}_3\text{O}$	49 to 50
Dimethylphosphinic acid	$\text{PR}_2(\text{OH})\text{O}$	53 to 54
Bis(2,4,4-trimethylpentyl) phosphinic acid	$\text{PR}_2(\text{OH})\text{O}$	59
Dioctylphosphinic acid	$\text{PR}_2(\text{OH})\text{O}$	61
Phosphorous acid-Tris(2-ethylhexyl)Ester	$\text{P}(\text{OR})_3$	140

**Table 2.1** List of many relevant phosphorous based molecules and their  $^{31}\text{P}$  NMR chemical shifts acquired in  $\text{CHCl}_3$  and ordered by increasing chemical shift.





**Figure 2.10** <sup>31</sup>P NMR spectrum of 90% TCI/Alfa Aesar TOP mixture, run once through a column of basic activated aluminum oxide, taken in CDCl<sub>3</sub>. This TOP mixture was used to make the PbSe NC sample shown in Figure 9. The chemical shift in ppm is shown above each peak, the integration of each peak relative to one another is shown below each peak, and the hand drawn molecules are the assignments.

Left to right: Peak at 107.630 ppm was assigned to a phosphorous acid-tris ester or a phosphorous acid-bis ester with an alkyl group; 57.895 ppm: phosphinic acid; 48.871 ppm: tri-n-octylphosphine oxide (TOPO); 38.290-38.159 ppm: phosphonic acid; 33.361 ppm: dialkylphosphine oxide; 25.679 ppm: phosphorous acid-tris ester oxide; -16.198 ppm: trialkylphosphine (not octyl); -30.106 ppm: tri-n-octylphosphine (TOP); -35.245 ppm: dialkylphosphine or trialkylphosphine (not octyl, possibly propyl).

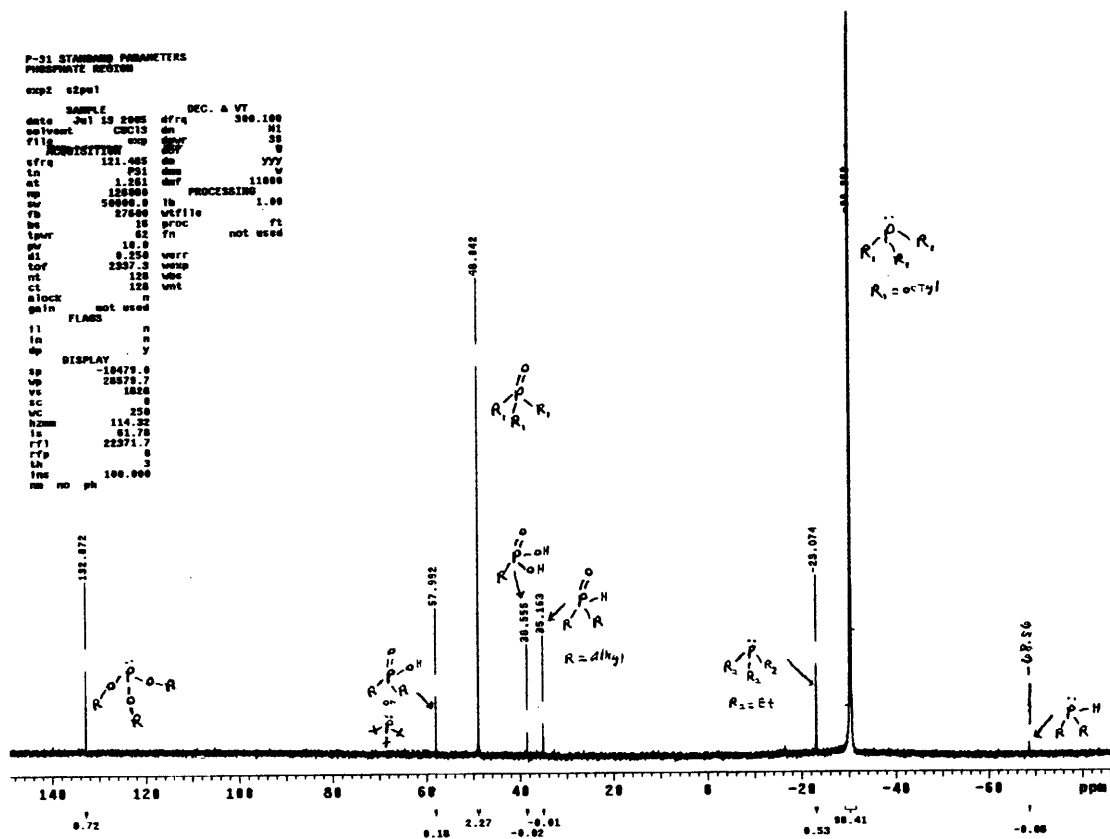
Table 2.1 lists the chemical name, chemical formula, and shift in ppm seen in the <sup>31</sup>P NMR spectrum for the relevant compounds analyzed. With this information in hand and with the help of published tables of phosphorous chemical shift data, it was possible to identify with confidence the majority of the phosphorous compounds that we consider to be impurities in our TOP. Figure 2.10 shows the <sup>31</sup>P NMR spectrum of the original TCI/Alfa Aesar mixture of TOP used to make the PbSe NCs shown in Figure 2.9, along

with the phosphorous species corresponding to each peak. Some of these assignments could be mistaken and could be phosphorous species bound to a metal center (residual metal catalyst left in solution from the making of the TOP), but most should be correct. This is not to say either that all of the impurities in TOP are identified here. There could be other impurities in the TOP that affect NC growth, which do not contain phosphorous and as a result are not seen using  $^{31}\text{P}$  NMR.  $^1\text{H}$  and  $^{13}\text{C}$  NMR were used as well to look at these different TOPs, but due to the long alkyl groups these spectra are very complex and as a result make it hard to distinguish one species from another.

The TOP shown in Figure 2.10 is not very pure. The integration shows that there is only 74 % TOP and 7 % TOPO relative to all of the other species present (19 % impurities). This is dramatically different compared to the 97 % Strem TOP shown in Figure 2.11. Based on the relative integrations shown in the  $^{31}\text{P}$  NMR spectrum of the 97 % Strem TOP we see that there is 96.4 % TOP and 2.3 % TOPO versus 1.3 % impurities. This difference in TOP purity that we see using  $^{31}\text{P}$  NMR is also seen very clearly in a NC synthesis when 90 % versus 97 % TOP is used. In the PbSe NC synthesis when TOP is used as the solvent, 97 % TOP yields much larger NCs compared to the 90 % (actually ~70-80 %) TOP due to the significant difference in concentration of species that inhibit NC growth. These species are the phosphonic and phosphinic acids (5.2 % in the TCI/Alfa Aesar mixture versus ~0.2 % in the 97 % TOP).

### 2.2.5 Reaction Yield

The reaction yield of PbSe NCs, using the general reaction scheme shown in Reaction Scheme 2.1, is significantly lower than that typically seen for CdSe. Most CdSe NC syntheses give reaction yields of 60 % to almost 100 %<sup>[19,20]</sup>. Determining NC



**Figure 2.11**  $^{31}\text{P}$  NMR spectrum of 97 % Strem TOP, taken in  $\text{CHCl}_3$ . The chemical shift in ppm is shown above each peak, the integration of each peak relative to one another is shown below each peak, and the hand drawn molecules are the assignments. Left to right: Peak at 132.872 ppm was assigned to a phosphorous acid-tris ester; 57.992 ppm: phosphinic acid or tritertbutylphosphine; 48.942 ppm: tri-n-octylphosphine oxide (TOPO); 38.555 ppm: phosphonic acid; 35.163 ppm: dialkylphosphine oxide ( $R = \text{dialkyl}$ ); -23.074 ppm: trialkylphosphine (not octyl, possibly ethyl); -30.353 ppm: tri-n-octylphosphine (TOP); -68.56 ppm: dialkylphosphine.

reaction yields by simply weighing the purified, dry, NC powder introduces significant error into the final number. The error arises from material loss during purification and most significantly from the fact that each NC contains a monolayer or more of organic molecules on the surface. When the weighing method is used to determine the PbSe NC reaction yield, numbers from 30-50 % are measured. Major differences in reaction yield were not observed when comparing different solvent based PbSe NC syntheses (TOP vs. squalene vs. diphenyl ether vs. octadecene).

Another, much more accurate way of measuring the reaction yield for this system is to use flame atomic absorption spectrometry. This technique was used to look at the reaction yield of the TOP and octadecene based PbSe NC syntheses. In the first case (TOP based synthesis), the entire growth solution was centrifuged after having added butanol and methanol, resulting in complete separation of PbSe NCs from solution. An aliquot of the supernatant was digested in nitric acid, which forms lead nitrate very rapidly (Note: It was important to have a high enough concentration of water in the solution in order to solubilize completely the lead nitrate that formed). This aqueous solution of lead nitrate was then analyzed for the concentration of lead using NIOSH method 7082, flame atomic absorption spectrometry (FAA), at MIT's environmental health and safety office. This method of analysis gave a reaction yield of 12 %. The second measurement, taken on the octadecene based PbSe NC synthesis, consisted of isolating an aliquot of the growth solution via centrifugation and then dissolving the actual PbSe NCs in nitric acid and measuring the concentration of lead in the aqueous solution using FAA. This analysis gave a reaction yield of 15 %, which compares nicely to the reaction yield measured by looking at the concentration of lead left in solution after the reaction (description above). As expected, we see that the reaction yields measured by FAA gave much lower numbers compared to those found when weighing the dry NCs. All of the following reaction yields reported were determined by FAA.

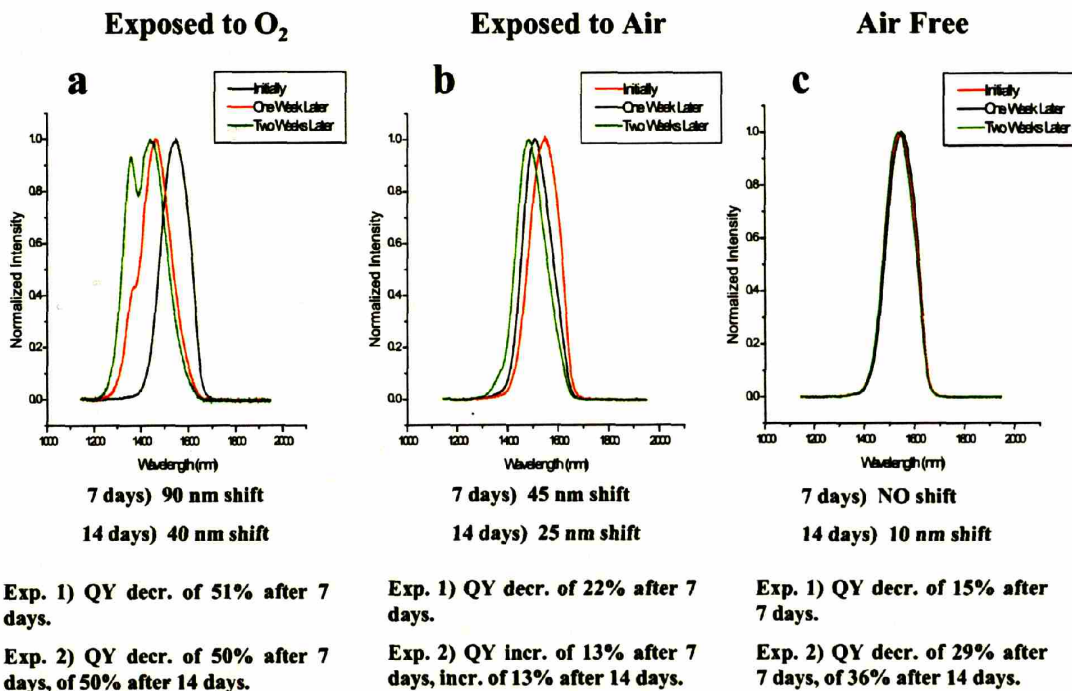
As mentioned in section 2.2.4, reducing agents can cause accelerated nucleation and provide a larger number of nuclei to form in the beginning of the reaction. And when added to the reaction during the growth stage one would expect to see an increase in growth depending on the conditions of the reaction. Dialkylphosphines are known to be

good reducing agents and as we saw in section 2.2.4, they are also present to some extent in the TOP we use. When we use a controlled amount of a dialkylphosphine in the PbSe NC reaction, a significant increase in reaction yield is observed. It was observed that when a small amount (~1 % relative to the volume of TOP used) of diphenylphosphine (DPP) is used in the PbSe NC synthesis, the reaction yield can be made to increase by as much as 8 fold (see section 2.3.2). When larger amounts of the DPP was used the size distribution suffered. Weaker reducing agents such as TOP can have a significant effect on the reaction yield as well. A 2.24M TOPSe solution (all TOP molecules have been made into TOPSe) was made and used to study the PbSe NC reaction, which is discussed in detail in section 2.3.2. This solution was compared to the normal 1M TOPSe solution in a PbSe NC synthesis (octadecene based preparation), while maintaining all other parameters the same, and only a small decrease (from 2.8 % to 2.5 %) (reactions were scaled down by a factor of four and a ratio of 1:1 Pb:Se was used instead of the normal 1:5 ratio, which accounts for the 2.8 % reaction yield compared to the normal 10-15 % yields) in the reaction yield was observed for the 2.24M TOPSe synthesis. TOP (1mmol of TOP was added and 0.25 mmol of Pb and Se were present) was then added half way through the reaction of the 2.24M based synthesis and a 2.5 fold increase in reaction yield was measured (2.5 % to 6.2 %). When TOP was added to a normal (1:5, Pb:Se ratio) octadecene based PbSe NC preparation large red shifts in absorption were observed as well (~300 nm). The effect that TOP has on the reaction yield could be based on one or both of two possibilities. First, the TOP could be acting as a mild reducing agent and pushing the PbSe nucleation and/or growth (Reaction Scheme 2.1) forward, and two could be simply stabilizing the Pb oleate complex as well as the PbSe clusters in solution,

thereby allowing the reaction to proceed in the forward direction by lowering the activation energy barrier as well as the final energy of the product.

### **2.2.6 Stability and Quantum Yield**

The measured absolute photoluminescence (PL) efficiency (Quantum Yield (QY)) of our PbSe NC solutions ranges from 6 to 20 % and is reduced to 0.5 to 1.5 % when the NCs are in a thin film, in contrast to relative QYs of 10 to 80 % for PbSe NCs in solution reported by others.<sup>[21,22]</sup> The lack of convenient luminescent standards in the NIR spectral range could be responsible for the differences in quantum yield measurements reported in the literature. The Absolute PL quantum efficiency in both the solution and solid state was measured using a  $\lambda = 405$  nm laser as the excitation source. The absorbed power was quantified using a Newport 818-UV-C/M Silicon detector. The NIR signal was detected 15° off of the front face normal, 10 cm distant from the sample, with a Silicon filter in place to block all reflected visible emission. The solid angle bisected by the 3 mm diameter Germanium detector was taken into account when calculating the total NIR emission. The solution samples were measured in a 2 mm path length quartz cuvette, and the solid state samples were measured from drop-cast films that were isolated from oxygen to prevent photo-oxidation during the measurement. Relative PL QY experiments reveal no dependence on excitation wavelength throughout the analyzed range of  $\lambda = 400$  to 900 nm.



**Figure 2.12** Outline of a stability study done on PbSe NCs, where solutions of NCs were exposed to oxygen (a), regular air (b), and only nitrogen (c). The spectra shown are emission spectra corresponding to experiment two. Below each spectrum is a brief description of the shifts to longer wavelengths observed as well as an outline of the changes in quantum yields (QY) seen.

The results of a detailed study on the stability of the PbSe NCs are summarized in Figure 2.12. Studying and understanding the stability of the PbSe NCs showed that the oxidation of the PbSe surface has a profound effect that can shift the emission maximum to higher energies by as much as 90 nm over a period of a week. Interestingly no emission peak shift was found for PbSe NCs exposed to air in the solid state over two days. The accepted explanation for these shifts in emission is that as the PbSe surface oxidizes to form lead oxide and selenium oxide, the particles decrease in size and as a result the emission shifts to longer wavelengths. It appears that this process of oxidation occurs much more readily in solution than in solid thin film form. If the oxide layer on

the surface of the particles forms at a slow enough rate, it is possible to observe an increase in the QY due to the oxide layer passivating the core PbSe NCs (Figure 2.12b). This is naturally accompanied by a decrease in the core diameter of the particle because the lead and selenium atoms on the surface are now associated with oxygen and are no longer part of the core PbSe NC. The oxide will keep forming and eventually break due to lattice strain and leave the surface, thereby causing the particle size to decrease as well as leave an unpassivated surface behind leading to a decrease in QY. The QY, over a period of seven days, decreased by 15-29 % (accompanied by no shift in emission peak maximum) of its initial value for a dilute sample of PbSe NCs in degassed hexane stored under a positive pressure of inert gas (Figure 2.12c). When stored in hexane under air after bubbling oxygen through the solution for 1 minute, the quantum yield decreased by 50 % (accompanied by a 90 nm shift to longer wavelengths in emission peak maximum) (Figure 2.12a) and those exposed to air for a week only decreased by 22 % and in some cases increased in QY by 13 %. After the same samples sat for 14 days, the air-free sample showed a 36 % decrease in QY with an emission peak maximum shift to shorter wavelengths of only 10 nm, while the sample exposed to oxygen showed the same 50 % decrease in QY but with a shift in the emission peak maximum to shorter wavelengths of 130 nm. The sample exposed to air again showed an increase of 13 % after the second week.

As demonstrated in Figure 2.12, there was and still is a strong need to overcoat (grow a shell of inorganic semiconductor onto) PbSe with a large band gap inorganic semiconductor to passivate it and make it more efficient and stable. Several attempts were made using CdSe, ZnSe, ZnS, and MgSe, but with no success. There was, however,



a difference seen in PbSe NC stability when CdSe was attempted. In this case, the PbSe NCs were synthesized in octadecene and after 5 minutes of growth, dimethylcadmium in TOP was dripped directly into the PbSe NC growth solution at 130°C. The cleaned up particles showed no decrease in QY or shift in emission after sitting in hexane in air for a day. After the introduction of the cadmium the growth solution with the PbSe present was stable to mild heating (60-70°C) overnight. Usually a shift in absorption and emission was seen as well as a broadening of the size distribution when the particles were left in growth solution for too long. XRD showed no significant difference from the usual PbSe powder pattern except for the peak at ~40 degrees (220 plane) was higher in intensity than would be seen in normal PbSe NCs and as would be seen in bulk PbSe (See Figure 2.5, which is the spectrum of the PbSe NCs that were exposed to Cd (Notice the line heights for the bulk PbSe peaks shown below the spectrum)). Four out of five samples showed a very small amount of Cd present relative to Pb and Se when characterized with WDS. Cadmium percentages ranging from ~ 0.25 to ~ 0.28 were seen from the WDS experiments and it was concluded that percentages so low would correspond to a fraction of a monolayer of CdSe and that indeed the PbSe NCs were not overcoated with CdSe. One possibility, however, is that many of the Se atoms on the surface of the PbSe NCs are associated with a Cd oleate molecule, forming a cadmium oleate protective layer around each PbSe NC. This could account for the increase in stability that was observed.

### **2.2.7 Absorption Cross Section**

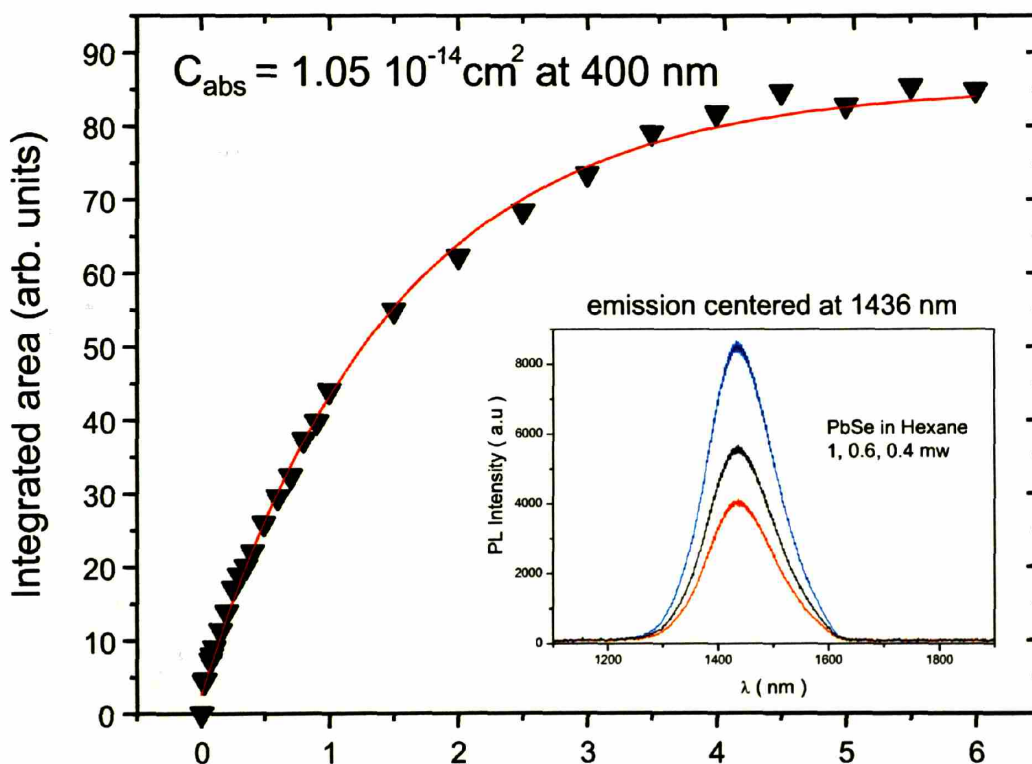
The absorption cross section  $C_{\text{abs}}$  (in  $\text{cm}^2$ ) for PbSe NCs was calculated using equation 2.1. Equation 2.1 is a rearrangement of equations taken from the work by

Leatherdale and co-workers<sup>[19]</sup>.  $C_{\text{abs}}$  is proportional to the product of the bulk semiconductor absorption coefficient ( $2n_1k_1$ ) and a local field factor that is equal to the ratio of the applied electric field to the electric field inside the NC. The  $n$  and  $k$  values for bulk PbSe were found in the *Handbook of Optical Constants of Solids*, Academic Press, Inc., 1985, pg. 520. Calculations were performed for two different wavelengths, 400 nm and 620 nm. These wavelengths chosen were dictated by the wavelengths that corresponded to the  $n$  and  $k$  values reported. The calculated per particle absorption cross section (in  $\text{cm}^2$ ) for PbSe at 400 nm was found to be  $C_{\text{abs}} = (6.552 \times 10^5)a^3 \text{ cm}^{-1}$  and that at 620 nm was  $C_{\text{abs}} = (3.755 \times 10^5)a^3 \text{ cm}^{-1}$ .

$$C_{\text{abs}} = \frac{2\pi}{m_3 \lambda} 9m_3^4 \frac{2n_1k_1}{(n_1^2 - k_1^2 + 2m_3^2)^2 + 4(n_1k_1)^2} \frac{4}{3} \pi a^3$$

**Equation 2.1** Equation used to calculate the absorption cross section  $C_{\text{abs}}$  of PbSe NCs, where  $m_3$  = refractive index of the solvent (assume no absorption of excitation photons by solvent (hexane at  $\lambda = 400$  and  $620$  nm)),  $\lambda$  = wavelength of excitation (400 and 620 nm),  $n$  and  $k$  = refractive index values for bulk PbSe at  $\lambda = 400$  and  $620$  nm,  $a$  = average NC radius.

The absorption cross section (at 400 nm) of 4.5 nm diameter PbSe NCs was determined experimentally by Jean-Michel Caruge, by fitting the saturation curve of the photoluminescence and from that fit backing out the absorption cross section (Figure 2.13). The experimental value obtained from the fit is  $C_{\text{abs}}$  or  $\sigma = 1.05 \times 10^{-14} \text{ cm}^2$ . When the radius of  $2.25 \times 10^{-7} \text{ cm}$  (4.5 nm diameter), the size of PbSe NCs used in the experiment shown in Figure 2.13, is plugged into  $C_{\text{abs}} = (6.552 \times 10^5)a^3 \text{ cm}^{-1}$ , we get a calculated absorption cross section at 400 nm of  $C_{\text{abs}} = 7.46 \times 10^{-15} \text{ cm}^2$ , which is very close to the experimental value of  $C_{\text{abs}} = 1.05 \times 10^{-14} \text{ cm}^2$ .



**Figure 2.13** Plot of the saturation of the photoluminescence of 4.5 nm diameter PbSe NCs that has been fitted, red line, in order to extract out the absorption cross section of the PbSe NCs. The excitation wavelength was 400 nm. The inset shows three emission curves of the PbSe NCs in hexane at pump powers of 1, 0.6, and 0.4 mW, whose emission was centered at 1436 nm.

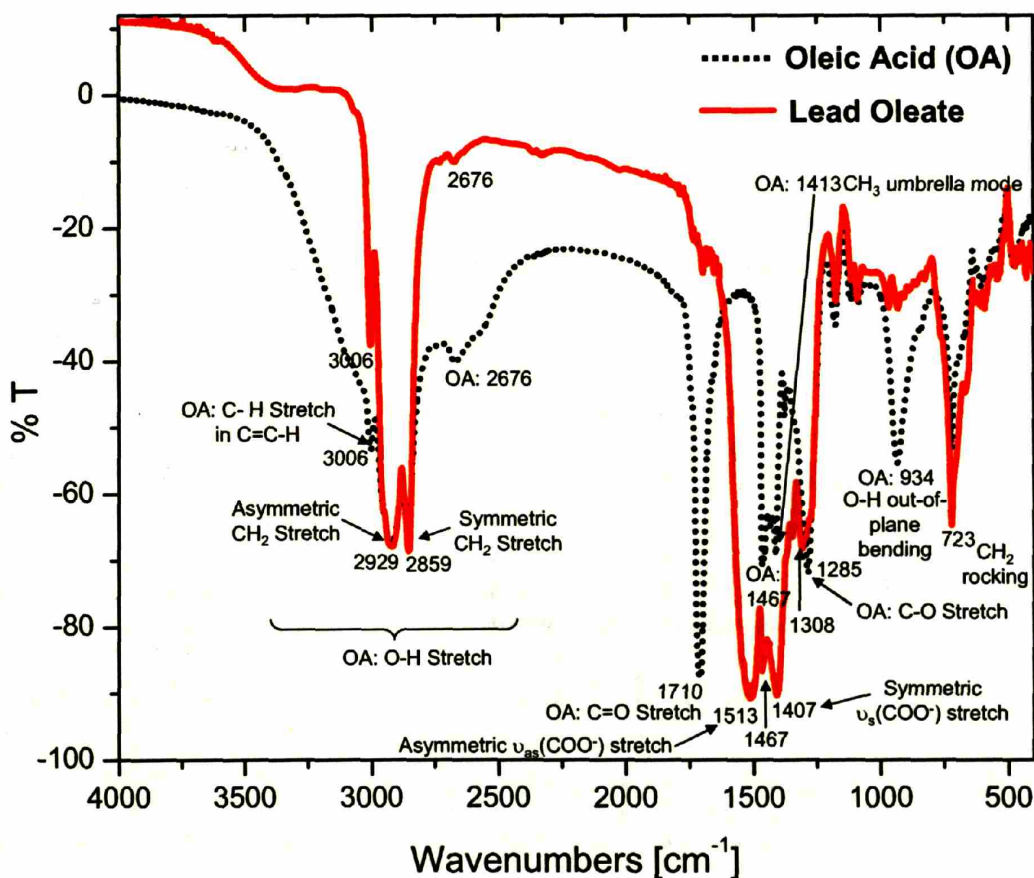
## 2.3 On the Chemical Mechanism of Precursor Reduction during PbSe Nanocrystal Formation

### 2.3.1 Characterization of the Lead Precursor

When the lead acetate tri-hydrate is degassed in the presence of oleic acid, acetic acid is pulled off. This has been confirmed by smelling the acetic acid left in the trap as well as by analysis of this solution left in the trap by  $^1\text{H}$  NMR. In all solvents (diphenylether (DPE), octadecene (ODE), dioctylether (DOE), and squalene) except tri-n-octylphosphine (TOP), a white waxy precipitate forms overtime as the degassed solution

is left to sit at room temperature. This white waxy precipitate can then be isolated from the solvent and rinsed in hexane to remove excess solvent. When the precipitate is cooled down to room temperature after being placed in an oven ( $\sim 120^{\circ}\text{C}$ ), it forms a white waxy film which can be solvated in non-polar solvents, for example TOP, chloroform, dichloromethane, and toluene. When as much of this white solid was collected after rinsing and separating from the solvent and weighed, 630 mg was found corresponding to (0.82 mmol of Pb, assuming this solid is Pb oleate). If all of the lead acetate were converted over to lead oleate, we would expect 770 mg (1 mmol of Pb). When the supernatant (solvent left behind after the lead oleate was centrifuged to remove it from solution) was analyzed for its lead content using flame atomic absorption spectrometry, only 2.2  $\mu\text{mol}$ s were detected. This indicates that there is almost complete conversion of the lead acetate into lead oleate within error.

Mass spectrometry, elemental analysis, as well as fourier transform infrared spectroscopy (FT-IR) were done to confirm the identity of the white waxy solid as being lead oleate. The mass spectrum of the white solid showed the appropriate peak at 771 ( $[\text{M}+\text{H}]^+$ ) corresponding to lead oleate as well as many peaks corresponding to species with less mass assigned as fragments. Several peaks corresponding to species with more mass than lead oleate were seen as well, some of which were assigned to oxidized species of lead oleate based on their regular incremental increase in mass by roughly 16. Elemental analysis gave very similar percentages as to those calculated for lead oleate ( $\text{C}_{36}\text{H}_{66}\text{O}_4\text{Pb}$ , FW. 770.13 g/mol). The calculated percentages for carbon, proton, and lead were 56.2, 8.6, and 26.9 respectively, while the measured percentages were 55.1, 8.7, and 24.2 respectively.



**Figure 2.14** FT-IR spectra of oleic acid and lead oleate with the relevant assigned IR bands for each<sup>[23,24]</sup>. Both oleic acid and the lead oleate were placed onto disposable PTFE FT-IR cards to acquire the spectra.

Figure 2.14 shows the FT-IR spectrum of oleic acid in comparison to the white waxy solid taken by smearing the waxy solid onto a PTFE disposable FT-IR card. The broad O-H stretch ( $\sim 3000\text{ cm}^{-1}$ ) and the O-H out-of-plane bending ( $934\text{ cm}^{-1}$ ) seen in the oleic acid spectrum are not present in that of the white solid. The oleic acid C=O stretch disappears and we see instead two new stretches at  $1513$  and  $1407\text{ cm}^{-1}$ . When the head of a carboxylic acid is associated with a metal atom, the interaction is categorized as four types: monodentate, bridging bidentate, chelating bidentate, and ionic; and the wavenumber separation ( $\Delta$ ) between the symmetric  $\nu_s(\text{COO}^-)$  stretch and the asymmetric

$\nu_{\text{as}}(\text{COO}^-)$  stretch IR bands can be used to diagnose the type of interaction. Large  $\Delta$  (200-300  $\text{cm}^{-1}$ ) correspond to a monodentate interaction, medium  $\Delta$  (140-190  $\text{cm}^{-1}$ ) correspond to a bridging bidentate interaction, and small  $\Delta$  ( $< 110 \text{ cm}^{-1}$ ) correspond to a chelating bidentate interaction<sup>[23]</sup>. When this analysis is performed here we see a difference of 106  $\text{cm}^{-1}$  ( $\Delta = 1513-1407 = 106 \text{ cm}^{-1}$ ) corresponding to a chelating bidentate species as we would expect in lead oleate.

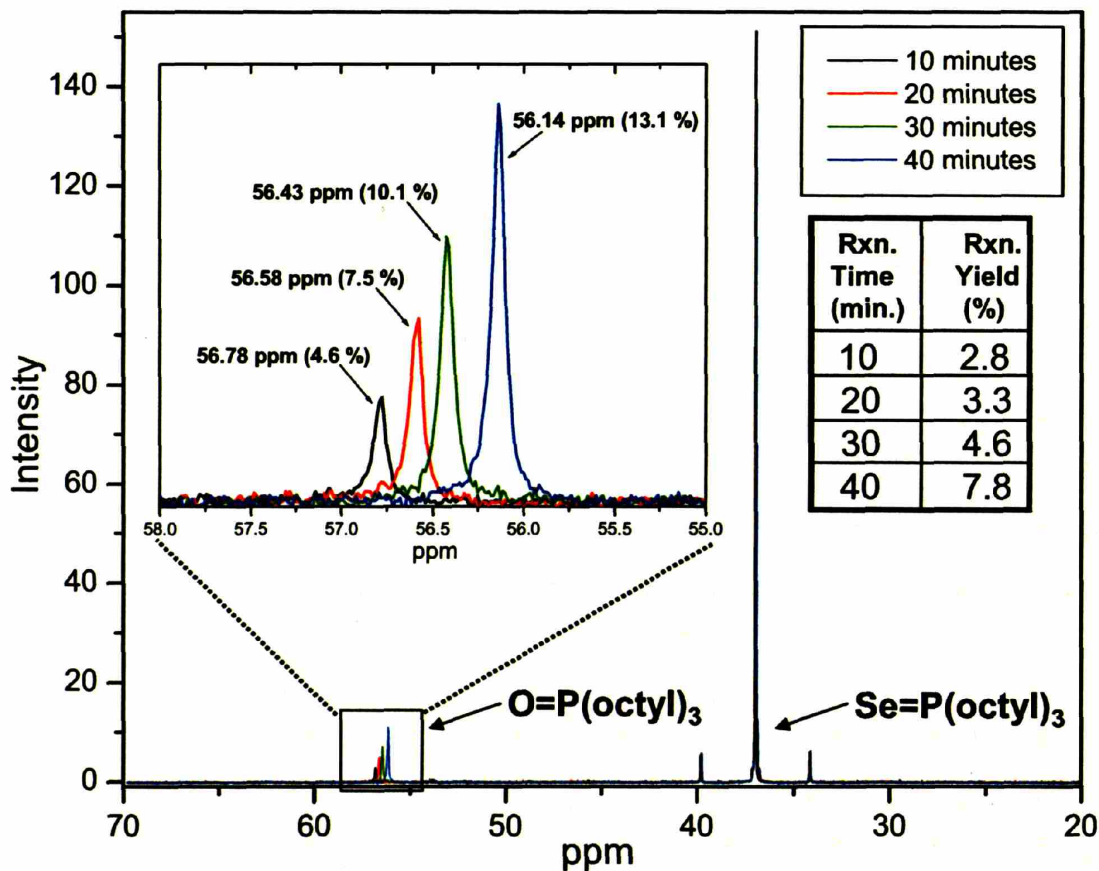
### 2.3.2 Proposed Mechanism and Supporting Data

Once the species that is reacting with the tri-*n*-octylphosphine selenide (TOPSe) was confirmed to be lead oleate, we could begin to study the chemistry in more detail. The PbSe system used in these studies was very simple. The non-coordinating solvent octadecene (ODE) was used and the initial system consisted of lead oleate, TOPSe, and ODE. In a normal batch preparation of PbSe NCs, as discussed in section 2.2, 1 M TOPSe is used and is made by mixing selenium shot (elemental selenium) and tri-*n*-octylphosphine (TOP) and stirring overnight. The selenium dissolves into the TOP to form TOPSe ( $\text{Se}=\text{P}(\text{R})_3$ , where  $\text{R} = \text{octyl}$ ), where the selenium is formally considered to be selenium zero ( $\text{Se}^0$ ). 5 mL of 1 M TOPSe contains roughly 6 mmols of TOP that is not associated with Se and the  $^{31}\text{P}$  NMR spectrum shows a peak for TOP at around -30 ppm and a triplet for TOPSe at around +35 ppm (the triplet is due to the 7.63 % spin  $\frac{1}{2}$   $^{77}\text{Se}$  splitting the 100 %  $^{31}\text{P}$  spin  $\frac{1}{2}$  phosphorous signal). To remove the role of the TOP from the chemistry and to simplify the system under study even more, a solution of TOPSe was made where every TOP is bound to a Se. This solution is a 2.24 M TOPSe solution and it shows only the triplet at +35 ppm in the  $^{31}\text{P}$  NMR spectrum, corresponding to the TOPSe. A similar solution can be made using tri-*n*-butylphosphine

(TBP), where all TBP molecules have a Se bound to them corresponding to a 4.04 M TBPSe solution showing the same triplet in the  $^{31}\text{P}$  NMR spectrum at around +35 ppm.

This simplified system, consisting of ODE as the solvent, 2.24M TOPSe, and  $\text{Pb}(\text{oleate})_2$ , shows the production of tri-n-octylphosphine oxide (TOPO) overtime and solid PbSe NCs. Figure 2.15 shows the  $^{31}\text{P}$  NMR spectra acquired on the neat growth solution at intervals of 10 minutes up to 40 minutes. It is seen that the intensity of the TOPO signal increases overtime (10-40 minutes). Because the TOPSe signal is so much larger in intensity and the change in concentration (reaction yield is small) is small, very little change in peak height is seen. Both the TOPSe and TOPO signal shift slightly overtime to smaller ppm due to the magnetic susceptibility changing overtime as the concentration of PbSe NCs in solution increases (PbSe NCs were left in solution during measurement so as not to remove TOPO in equilibrium with the PbSe NC surfaces). Under these conditions, small reaction volumes (0.8 mL), high Pb and Se concentrations (0.089 mmols each), and long reaction times (10-40 minutes) compared to the normal batch preparation (section 2.2), the quality of the resulting PbSe NCs is very poor (very broad size distributions, poor passivation in solution). These conditions however, are necessary in order to detect the presence of TOPO with good signal to noise in the  $^{31}\text{P}$  NMR spectra under reasonable data acquisition times. The table inset in Figure 2.15 shows the reaction yields corresponding to each  $^{31}\text{P}$  NMR spectrum over the 40 minute reaction time. These percentages were determined based on the digestion of the PbSe NCs, produced at each time interval, in nitric acid to form lead nitrate, whose concentration is then measured using flame atomic absorption spectrometry. The reaction yield, and hence the mmols of Pb and Se being consumed in the reaction, is seen



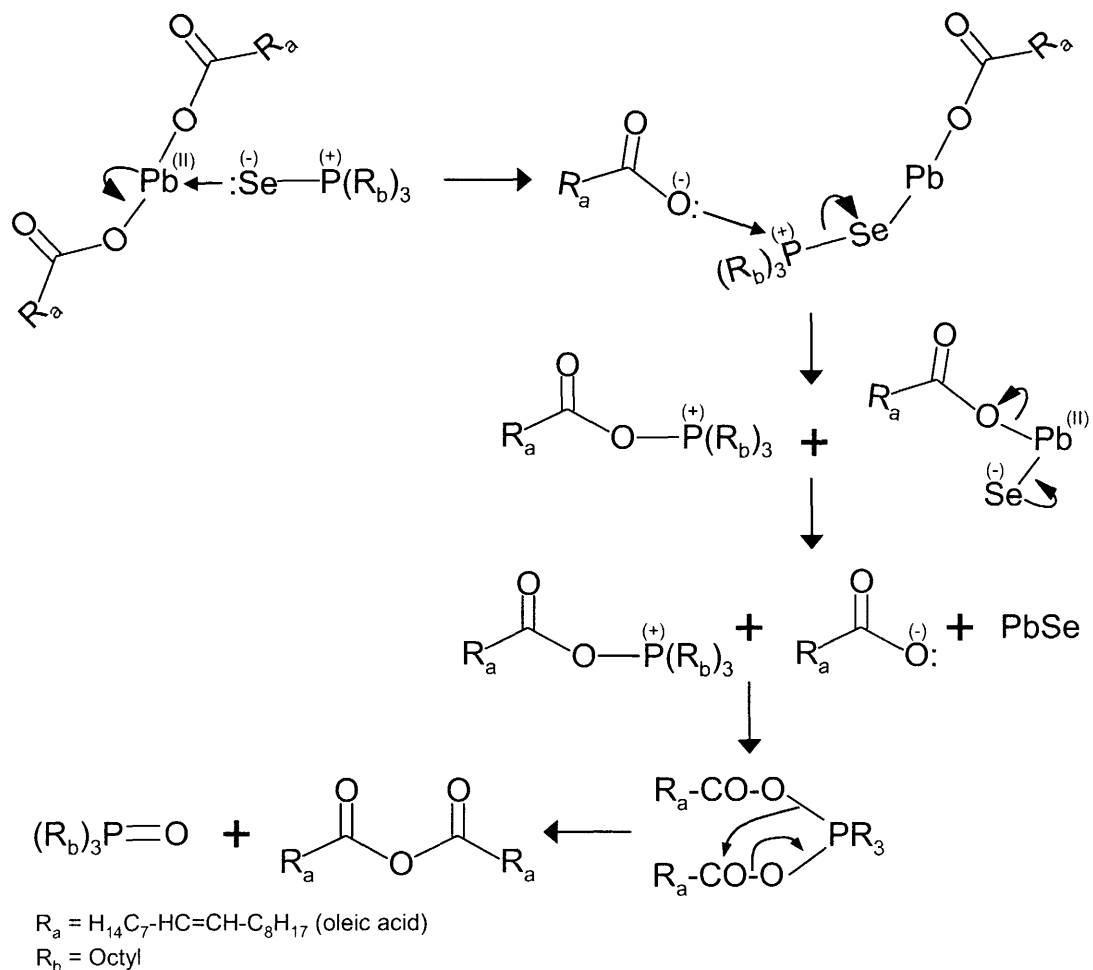


**Figure 2.15**  $^{31}\text{P}$  NMR spectra of 4 neat growth solutions of PbSe NCs taken at 10, 20, 30, and 40 minutes of growth. All solutions were run in NMR tubes placed in an oil bath at  $170^\circ\text{C}$  and left to react for their respective times. Each tube contained 0.089 mmols of Pb and 0.082 mmol of Se in a total volume of 0.5 mL of ODE. At the end of the reaction 0.3 mL of anhydrous  $\text{CHCl}_3$  was added to each tube to solvate the TOPO (TOPO is not soluble in ODE) before the NMR spectra were taken. 256 transients were acquired for each spectrum. No other peaks were seen except those shown, in the region of acquisition (+200 to -200 ppm). The peak at  $\sim 56$  ppm was confirmed to be TOPO by the addition of 99% TOPO to one of the solutions and seeing the intensity increase. The detail view of the four TOPO peaks shows the ppm shift as well as the percentage of peak area relative to the TOPSe peak area determined from integration. The inset on the right is a table of the corresponding reaction yields determined by flame atomic absorption spectrometry.

to increase regularly overtime as that of the TOPO concentration (shown in the  $^{31}\text{P}$  NMR spectra detail view in the left hand inset in Figure 2.15).



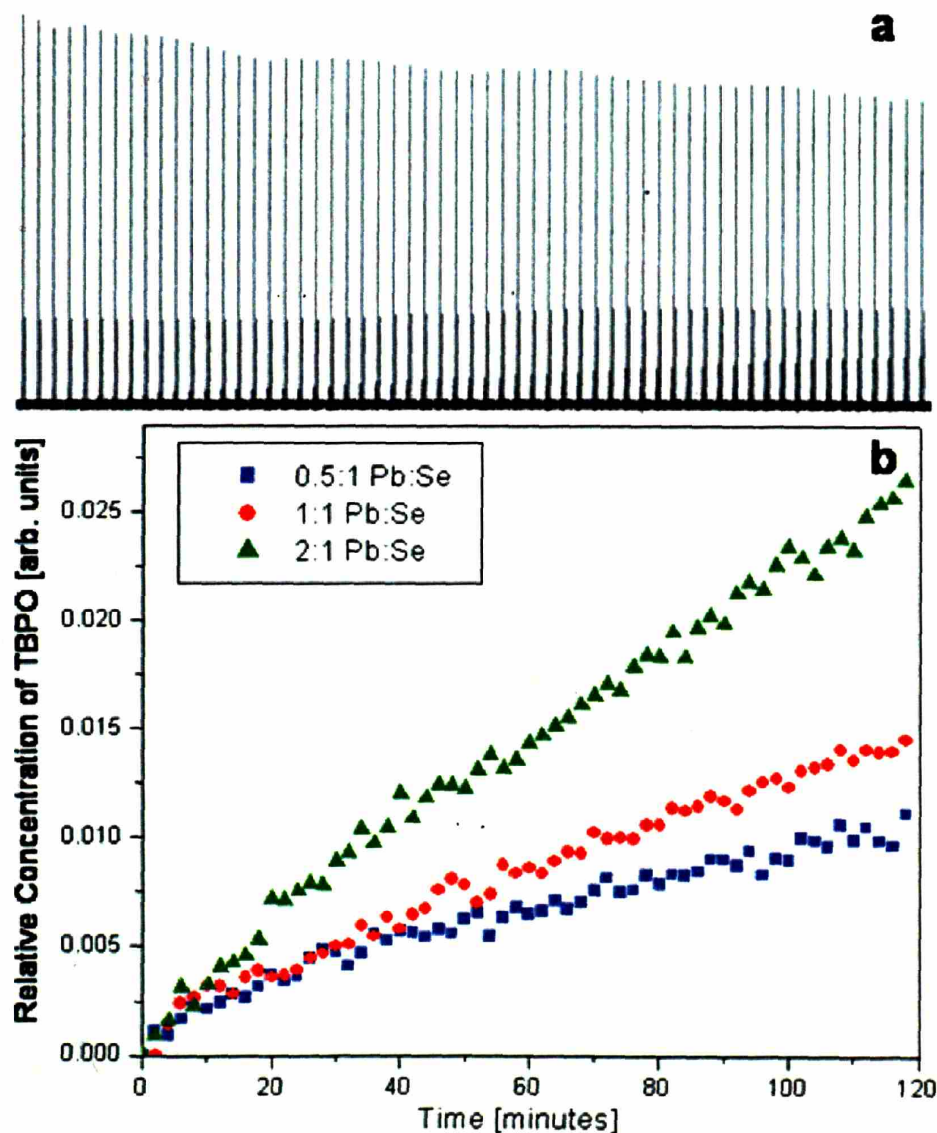




**Figure 2.16** Proposed mechanism of how TOPSe reacts with  $Pb(\text{oleate})_2$  to form PbSe NCs and TOPO. The Pb remains as  $Pb^{(II)}$  throughout the reaction, while the Se is reduced from  $Se^{(0)}$  in TOPSe to  $Se^{(-2)}$  in PbSe and the phosphorous is oxidized from  $P^{(+3)}$  in TOPSe to  $P^{(+5)}$  in TOPO. The other product of the reaction is the oleate anhydride, which despite attempts was never seen using FT-IR due to the large overlap of the alkyl chain IR bands of the solvent with those of the anhydride.

Reaction 1 summarizes the chemistry we believe to be occurring in this simplified PbSe NCs system, while Figure 2.16 shows in more detail the mechanism we are proposing. The TOPSe reacts with the Pb center to eventually produce TOPO, an oleate anhydride, and PbSe. The Pb center remains  $Pb^{(II)}$ , while the phosphorous is oxidized from  $P^{(+3)}$  ( $((\text{octyl})_3P=Se$ ) to  $P^{(+5)}$  ( $((\text{octyl})_3P=O$ ) and the Se is reduced from  $Se^{(0)}$

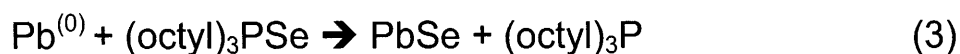
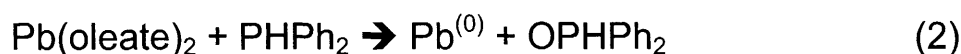
$((\text{octyl})_3\text{P}=\text{Se})$  to  $\text{Se}^{(-2)}$  ( $\text{PbSe}$ ). This reaction was also run in an NMR tube (at  $150^\circ\text{C}$  inside of NMR) while  $^{31}\text{P}$  NMR spectra were acquired during the reaction every two minutes over 120 minutes (total of 60 spectra were acquired). The Se source in this case was 4.04M TBPSe (each TBP is bound to a Se) instead of 2.24M TOPSe due to the higher reaction yields observed when using TBPSe (larger concentration of TBPO observed compared to TOPO and therefore more oxide signal). The ratio of Pb to Se was varied from 0.5, 1, 2, to 1. Figure 2.17(a) shows the 60 spectra for the 2:1 Pb:Se reaction plotted side by side. The middle sized peak is a standard (phosphoric acid in a microcapillary tube inside of the NMR tube) and is seen to not be changing in intensity overtime. The largest peak is TOPSe and is clearly seen to be slowly decreasing, while the smallest peak is TOPO and is seen to be increasing regularly over the course of the reaction. Figure 2.17(b) is a plot of the relative concentrations of the TOPO generated in the three different experiments varying the ratio of Pb to Se. The raw signal of TOPO for each spectrum was integrated and compared to a known quantity of TOPO added in at the end of the experiment to get a relative concentration for each point. Although  $^{31}\text{P}$  NMR is not quantitative in terms of absolute integration, we can get a relative qualitative comparison, which shows the regular increase overtime of the TOPO concentration in each case as well as the fact that more TOPO is generated in the 2:1 regime compared to the 0.5:1 Pb:Se regime. This type of analysis for the TOPSe signal is meaningless because such small changes in a large concentration are full of fluctuation and error even though by eye we can see in Figure 2.17(a) that the intensity of the TOPSe signal is decreasing overtime.



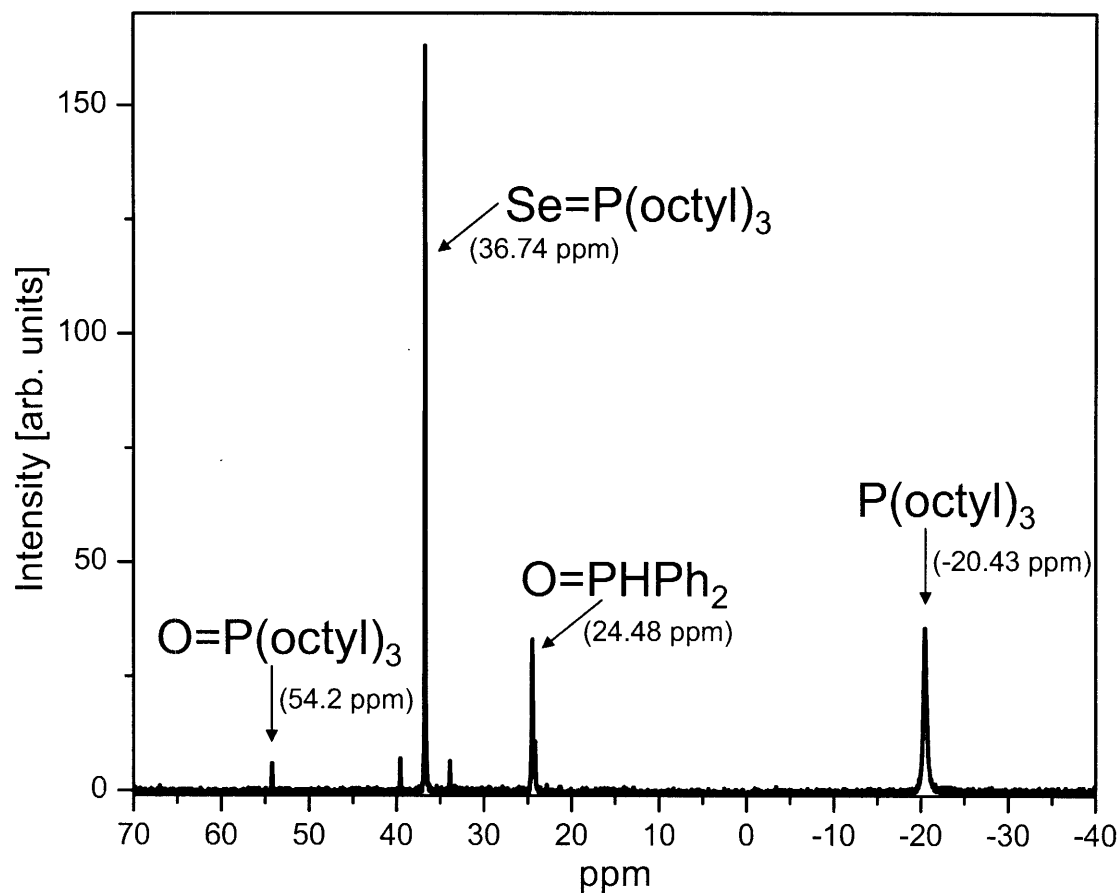
**Figure 2.17** Results of PbSe NC reactions run in the NMR machine at 150°C. (a) 60 spectra side by side, taken one every two minutes as the reaction ran inside the NMR machine for a total of 120 minutes. The ratio of Pb:Se was 2:1 (0.16 mmol Se) in a volume of 0.8 mL of ODE. TBPSe was the Se precursor in these experiments (a) and (b). Middle sized peak is the phosphoric acid standard in sealed a microcapillary tube inside the NMR tube. The largest sized peak is the TOPSe signal and the smallest peak is the TOPO signal. (b) The TOPO peaks in each 60 spectra (a) are integrated relative to the standard and plotted versus time for three different ratios of Pb:Se. The 2:1 data shown in (a) is the same data plotted in (b). The three sets of data were normalized to one another by adding a known quantity of TOPO to each tube at the end of the experiment to relate each TOPO peak intensity to the known quantity added.

Studies done by Amatore and co-workers<sup>[25]</sup> found that triphenylphosphine (PPh<sub>3</sub>) reduces divalent palladium to zerovalent in the complex Pd(OAc)<sub>2</sub>(PPh<sub>3</sub>)<sub>2</sub> by an intramolecular reaction and is oxidized to triphenylphosphine oxide. In their proposed mechanism the Pd(OAc)<sub>2</sub>(PPh<sub>3</sub>)<sub>2</sub>, through reductive elimination, produces “Pd<sup>(0)</sup>(PPh<sub>3</sub>)”, OAc<sup>-</sup>, and AcO-PPh<sub>3</sub><sup>+</sup> and then the AcO-PPh<sub>3</sub><sup>+</sup> is converted to either AcOH and O=PPh<sub>3</sub> in the presence of H<sub>2</sub>O or to Ac<sub>2</sub>O (acetic anhydride) and O=PPh<sub>3</sub> in the presence of AcO<sup>-</sup>. When we tried to reduce Pb(oleate)<sub>2</sub> with excess TOP, TBP, and PPh<sub>3</sub>, in solution, no Pb solid was seen until temperatures of 250-320°C were reached, which are far above standard PbSe NC reaction temperatures (150-170°C). The stronger reducing agent, diphenylphosphine (DPP), however did reduce Pb(oleate)<sub>2</sub> to solid Pb metal at around 180°C. The <sup>31</sup>P NMR spectrum of the final solution showed DPP and diphenylphosphine oxide (DPPO).

Based on the mechanism described above, we would expect that TOPSe reacting with a zerovalent Pb center would produce PbSe and TOP. In fact, when DPP is added to the same reaction as that described above for 2.24M TOPSe and Pb(oleate)<sub>2</sub>, we see the complete oxidation of the DPP to DPPO, a large increase in PbSe NCs reaction yield, and the production of TOP and a small amount of TOPO as shown in the <sup>31</sup>P NMR spectrum



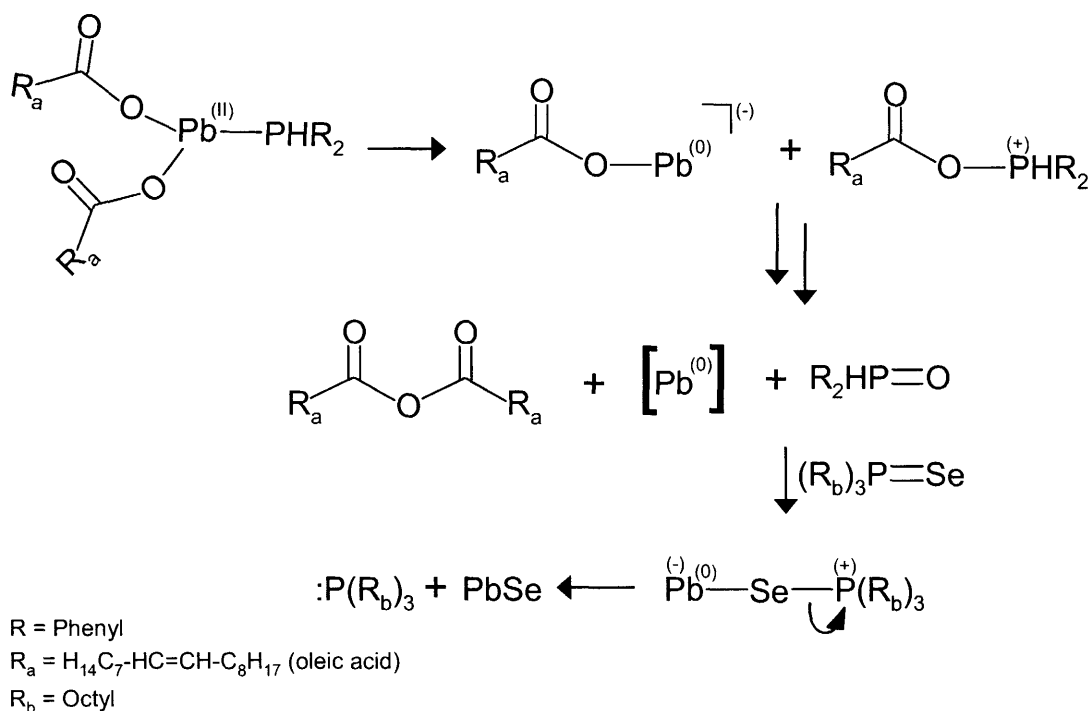
in Figure 2.18. The TOP and DPPO peak are very similar in intensity as we would expect based on reactions 2 and 3. The presence of the TOPO peak indicates that the mechanism described above and shown in Figure 2.16 is happening to some extent as well. Figure 2.19 describes reaction 2 and 3 in more detail. The Pb<sup>(II)</sup> in the form of



**Figure 2.18**  $^{31}\text{P}$  NMR spectrum of the growth solution of PbSe NCs that were made using diphenylphosphine (DPP) doped into the TOPSe solution. A 1:1 Pb:Se ratio was used (0.089 mmol of each) in a volume of 0.5 mL in an NMR tube in an oil bath at 170°C inside the glove box. 0.027 mmols of DPP (30%) was added to the 2.24M TOPSe solution used. The reaction went for 10 minutes and then 0.3 mL of anhydrous  $\text{CHCl}_3$  was added. TOP usually appears at -30 ppm, but due to the chemical environment shifted to -20 ppm, which was confirmed by adding 97% TOP to the reaction afterward to and seeing the TOP peak increase in intensity. A control experiment (exactly the same except no  $\text{Pb}(\text{oleate})_2$  was added) showed DPP and TOPSe with minute amounts of TOPO and DPPO.

$\text{Pb}(\text{oleate})_2$  is reduced by the diphenylphosphine to give a  $\text{Pb}^{(0)}$  species and diphenylphosphine oxide (Figure 2.18). The  $\text{Pb}^{(0)}$  species reacts with the  $\text{Se}^{(0)}$  in the form of TOPSe to liberate TOP (Figure 2.18) and form PbSe NCs. The  $^{31}\text{P}$  NMR spectrum shown in Figure 2.18 was the result of doping the TOPSe solution with 30 % DPP (1:1:3 Pb:Se:DPP, 0.089, 0.089: 0.027 mmol) and growing for 10 minutes at 170°C (exactly

same conditions as that shown in Figure 2.15), which gave roughly a 20 fold increase in reaction yield (2.8 %, no DPP (table inset in Figure 2.15), to 54 %).



**Figure 2.19** Proposed mechanism of how a reducing agent, in this case diphenylphosphine (PHR<sub>2</sub>), reacts with Pb(oleate)<sub>2</sub> to generate a zerovalent Pb species that then reacts with TOPSe to liberate TOP and form PbSe NCs. The divalent Pb (Pb<sup>II</sup>) in Pb(oleate)<sub>2</sub> is reduced by the DPP to form zerovalent Pb (Pb<sup>0</sup>), diphenylphosphine oxide (R<sub>2</sub>HP=O), and oleate anhydride. The Pb<sup>0</sup> species then reacts with Se<sup>0</sup> in TOPSe ((R<sub>b</sub>)<sub>3</sub>P=Se) to form the PbSe NCs and liberate free TOP (P(R<sub>b</sub>)<sub>3</sub>).

As mentioned in the beginning of this section, all regular batch preparations of Se based semiconductor NCs use 1 or 1.5 M TOPSe or TBPSe, which consists of a large amount of free TOP or TBP. Most NC preparations also use excess Se to provide good size distributions, for example 1:5 Pb:Se in the PbSe batch preparations discussed in section 2.2 and 1:3 or 1:5 Cd:Se typical of most CdSe NC preparations. In these batch NC preparations this corresponds to ratios of metal to free TOP of roughly 1:2 to 1:6. Even though TOP and TBP are weak reducing agents, simply due to their large excess in

solution, it is likely that these species are reducing the metal precursors to some extent from divalent to zerovalent as shown in Figure 2.19. We therefore believe that both of the two proposed mechanisms (Figure 2.16 and 2.19) are happening simultaneously in batch NC preparations where TOPSe or TBPSe are employed. As discussed in section 2.2.4, TOP is not pure and there can be significant quantities of phosphorous species (dialkylphosphines) that are good reducing agents, which affect the reaction yield, size distribution, and average size of all NC preparations. These species influence on the physical properties of the NCs is due to their affect on the chemistry as we see for diphenylphosphine (Figure 2.19). Now that we have an understanding of how each species in the reaction contributes to the chemistry, we can begin to modify the results of these reactions. Table 2.2 shows the results of three regular batch preparations of PbSe NCs (similar to those described in section 2.2), where diphenylphosphine was added to the 5 mL of 1M TOPSe before injection into the hot (135°C) Pb(oleate)<sub>2</sub> containing solution (1 mmol Pb, and 20 mL of diphenylether). When no DPP was added a reaction yield of 2.3 % was obtained. When 0.08 and 0.15 mmol of DPP were added, the reaction yield increased to 11.6 % and 16.2 % respectively and the size distribution remained tight. The presence of the DPP gave a 7 fold increase in reaction yield, which is not only due to the increased rate of growth, seen by the fact that the final particle sizes were larger, but also to the formation of more nuclei in the beginning of the reaction, seen in Table 2.2 as an increase in the number of NCs. This makes perfect sense based on the mechanism proposed in Figure 2.19. The DPP increases the reactivity of the Pb by reducing it from divalent to zerovalent in the presence of the TOPSe, which results in the formation of more nuclei during the nucleation event.

DPP/Pb	Rxn. Yield (%)	# of NCs	1 <sup>st</sup> Abs. Peak (nm)
0	2.3	$1.81 \times 10^{16}$	1358
0.08	11.6	$3.09 \times 10^{16}$	1736
0.15	16.2	$4.53 \times 10^{16}$	1716

**Table 2.2** Table showing the results of three batch PbSe NC preparations. The three preparations were done with 1) no diphenylphosphine (DPP) doped into the 5 mL of 1M TOPSe, 2) 0.08 mmols, and 3) 0.15 mmols of DPP. The corresponding reaction yields, number of NCs made, and the first absorption peak are shown. All three preparations were done exactly the same: 1mmol Pb in 20 mL of diphenylether; TOPSe was injected into the Pb(oleate)<sub>2</sub> solution at 135°C and the particles were grown for 2 minutes after injection. The reaction yield and number of NCs were calculated from the absorption of a dilute solution of PbSe NCs, the known NC size from the first absorption peak, and the absorption cross-section at 400 nm from section 2.2.7.

## 2.4 Conclusions

PbSe NCs are the material of choice for light emission applications in the 1 to 3  $\mu\text{m}$  region of the spectrum. Large area emitters in the near infrared have been identified as technologically useful for chemical spectroscopy and sensing, night vision applications, and could be incorporated into on-chip optoelectronic integrated circuits. The colloidal synthesis of semiconductor PbSe NCs was optimized and enhanced to yield high-quality PbSe NCs with very narrow size distributions in the size regime of 2 to 10 nm (corresponding to emission peaks  $\lambda = 1.1 \mu\text{m}$  to  $\lambda > 2.4 \mu\text{m}$ , respectively). The stability of light emission and quantum efficiency under an inert atmosphere are good, but the growth of a protective shell (which has proven to be difficult) is needed in order to use these materials for practical applications in the presence of oxygen and water. The synthesis was extended to other solvent systems that provided extremely narrow size distributions as well as a model system on which to study the chemical mechanism of NC



formation. This simple PbSe synthesis allowed us to study how the molecular precursors in NC syntheses are reduced to form solid crystalline materials in the presence of phosphorous containing molecules. Two mechanisms are proposed to occur simultaneously in the batch synthesis based on our experimental results, which has led to the better understanding of this system as well as many others which employ metal salts and phosphorous containing molecules (which are numerous at this point). One practical example of this understanding is our ability to increase the reaction yield of the PbSe synthesis by almost ten fold (while maintaining the size distribution) simply by addition of a stronger reducing agent (diphenylphosphine), which increases the initial number of nuclei during the nucleation event.

## 2.5 References

1. F. W. Wise, *Acc. Chem. Res.* **2000**, *33*, 773.
2. H. Du, C. Chen, R. Krishnan, T. D. Krauss, J. M. Harbold, F. W. Wise, M. G. Thomas, J. Silcox, *Nano Lett.* **2002**, *2*, 1321.
3. J. Steckel, S. Coe-Sullivan, V. Bulovic, M. G. Bawendi, *Adv. Mater.* **2003**, *15*, 1862.
4. J. M. Pietryga, R. D. Schaller, D. Werder, M. H. Stewart, V. I. Klimov, J. A. Hollingsworth, *J. Am. Chem. Soc.* **2004**, *126*, 11752.
5. C. B. Murray, D. J. Norris, M. G. Bawendi, *J. Am. Chem. Soc.* **1993**, *115*, 8706.
6. A. Sashchiuk, L. Langof, R. Chaim, E. Lifshitz, *J. Crystal Growth* **2002**, *240*, 431.
7. M. Brumer, A. Kigel, L. Amirav, A. Sashchiuk, O. Solomesch, N. Tessler, E. Lifshitz, *Adv. Funt. Mater.* **2005**, *15*, 1111.
8. F. Chen, K. L. Stokes, W. Zhou, J. Frang, C. B. Murray, *Mater. Res. Soc. Symp. Proc.* **2001**, *691*,G10.2.
9. F. X. Redl, K.-S. Cho, C. B. Murray, S. O'Brien, *Nature* **2003**, *423*, 968.
10. S. Coe-Sullivan, J. S. Steckel, W.-K. Woo, M. G. Bawendi, V. Bulovic, *Adv. Funt. Mater.* **2005**, *15*, 1117.
11. R. D. Schaller, M. A. Petruska, V. I. Klimov, *J. Phys. Chem. B* **2003**, *107*, 13765.
12. Y. K. Olsson, G. Chen, R. Rapaport, D. T. Fuchs, V. C. Sundar, J. S. Steckel, M. G. Bawendi, A. Aharoni, U. Banin, *Appl. Phys. Lett.* **2004**, *85*, 4469.

13. A. Kigel, M. Brumer, A. Sashchiuk, M. Sirota, E. Galun, E. Lifshitz, *Proc. of SPIE* **2005**, 5929, 5929OF-1.
14. B. L. Wehrenberg, P. Guyot-Sionnest, *J. Am. Chem. Soc.* **2003**, 125, 7806.
15. R. D. Schaller, V. I. Klimov, *Phys. Rev. Lett.* **2004**, 92, 186601.
16. A. Lipovskii, E. Kolobkova, V. Petrikov, I. Kang, A. Olkhovets, T. Krauss, M. Thomas, J. Silcox, F. Wise, Q. Shen, S. Kycia, *Appl. Phys. Lett.* **1997**, 71, 3406.
17. X. Peng, L. Manna, W. Yang, J. Wickham, E. Scher, A. Kadavanich, A. P. Alivisatos, *Nature* **2000**, 404, 59.
18. M. Kolosky, J. Vialle, T. Cotel, *J. Chromatogr.* 1984, 299, 436.
19. C. A. Leatherdale, W.-K. Woo, F. V. Mikulec, M. G. Bawendi, *J. Phys. Chem. B* **2002**, 106, 7619.
20. B.K.H. Yen, N.E. Stott, K.F. Jensen, M.G. Bawendi, *Adv. Mater.* **2003**, 15, 1858.
21. H. Du, C. Chen, R. Krishnan, T. D. Krauss, J. M. Harbold, F. W. Wise, M. G. Thomas, J. Silcox, *Nano Lett.* **2002**, 2, 1321.
22. B. L. Wehrenberg, C. Wang, P. Guyot-Sionnest, *J. Phys. Chem. B* **2002**, 106, 10634.
23. N. Wu, L. Fu, M. Su, M. Aslam, K. C. Wong, V. P. Dravid, *Nano Lett.* **2004**, 4, 383.
24. L. Robinet, M.-C. Corbeil, *Studies in Conservation* **2003**, 48, 23.
25. C. Amatore, A. Jutand, M. A. M'Barki, *Organometallics* **1992**, 11, 3009.



# Chapter 3

## (CdS)ZnS and (CdS)Cd<sub>x</sub>Zn<sub>1-x</sub>S core-shell Nanocrystals

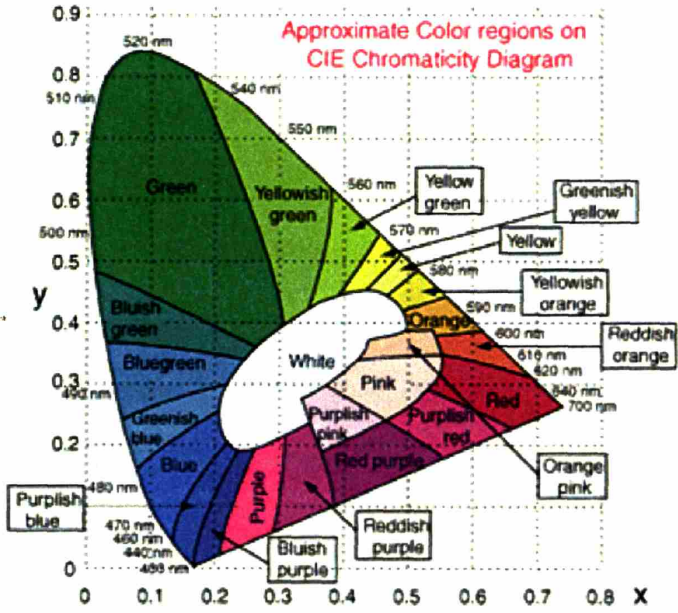
### 3.1 Introduction and Motivation

The ability to synthesize semiconductor nanocrystals (NCs) or quantum dots (QDs) with narrow size-distributions and high luminescent efficiencies has made these materials an attractive alternative to organic molecules in applications such as optoelectronic devices<sup>[1,2]</sup> and biological fluorescence labeling<sup>[3-5]</sup>. As is described in detail in the introduction and chapter 6 of this thesis, NCs are particularly interesting as the active materials in large area (cm<sup>2</sup>) hybrid organic/inorganic QD-light emitting devices (QD-LEDs)<sup>[6-8]</sup> and have become interesting as a viable alternative flat panel display technology. At the time, when the work described in this chapter was carried out, all of the QD-LED demonstrations utilized the well developed (CdSe)ZnS core-shell NC material system, and while this yielded proof of concept demonstrations of high performance devices it did not demonstrate the crucial element of an efficient blue emitter<sup>[9]</sup>. Blue QD-LEDs had remained elusive due to a lack of blue emitting NC core-shell material. In order to fill this gap, first the appropriate blue target wavelength for a blue emitting QD-LED pixel for a display application had to be chosen and then a suitable semiconductor material to provide the blue emission.

Display Standard	CIE(x)	CIE(y)
NTSC (CRT)	0.155	0.07
HDTV	0.15	0.06

$\lambda$ [nm]	Relative Sensitivity [human eye]	CIE Coord. [x,y]
380	0.00004	
400	0.0004	
420	0.004	
440	0.023	0.16, 0.014
460	0.06	0.14, 0.035
480	0.139	0.11, 0.13
500	0.323	0.047, 0.46



**Figure 3.1** The NTSC and HDTV display standard CIE color coordinates for blue emission (upper left table) are shown along with the Commission International d’Eclairage (CIE) Chromaticity Diagram for reference, which has the color regions and wavelengths labeled. The relative sensitivity of the human eye and the corresponding CIE color coordinates for several blue wavelengths (bottom left table) are tabulated to show how the human eye’s sensitivity decreases dramatically when seeing shorter wavelengths versus how the CIE color coordinates of the longer wavelengths lie inside the coordinates of the display standard coordinates (NTSC and HDTV). The blue wavelength chosen for QD-LED display applications (FWHM = 30 nm) is 460–470 nm (CIE coordinates highlighted in red), which provides color coordinates that lie to the outside of the display standard coordinates (more color saturated) and at the same time maximized perceived power.

The ideal blue emission spectrum of an LED for a flat panel display application would have a narrow bandwidth and a wavelength such that its coordinates on the Commission International d’Eclairage (CIE) Chromaticity Diagram would lie to the outside of the current National Television System Committee (NTSC) standard color triangle. For a gaussian emission spectrum with a full width at half maximum (FWHM) of 30 nm and a maximized perceived power, the ideal wavelength of blue emission for display applications is ~465 nm. This choice represents a trade off between the perceived power of the emission, and the perceived blueness of the emission, as shown in Figure

3.1. Wavelengths bluer than 460-470 nm become difficult for the human eye to perceive, while those redder than 460-470 nm have coordinates that lie inside the standard NTSC color triangle.

The best-characterized semiconductor QD system to date is CdSe, whose optical tuning range spans the visible region of the spectrum<sup>[10]</sup>. Blue emission can be obtained from CdSe particles smaller than 2 nm, which are to date difficult to synthesize with narrow size-distributions and good quantum efficiencies. They are difficult to process, manipulate, and overcoat with a higher band gap inorganic semiconductor, all of which are necessary for incorporation into solid-state structures. A core-shell type composite rather than organically passivated QDs are desirable in a solid state QD-LED device due to their enhanced photoluminescence (PL) and electroluminescence (EL) quantum efficiencies and greater tolerance to processing conditions necessary for device fabrication<sup>[2,11-13]</sup>. In addition, QDs < 2 nm in diameter have a small absorption cross-section, which leads to a small Förster energy transfer radius. All of these factors combine to make CdSe a poor choice for blue QD-LEDs.

The largest high-quality ZnSe (ZnSe has a room temperature bulk band gap of 2.7 eV (460 nm)) NCs recently reported exhibit band-edge fluorescence up to 440 nm, which is too blue<sup>[14,15]</sup>. Both ZnTe and CdS have appropriate band gaps (ZnTe and CdS have room temperature bulk bands gaps of 2.39 eV (519 nm) and 2.42 eV (512 nm) respectively). To date, it has been difficult to grow large (>4.5 nm diameter) particles of ZnTe with narrow size distributions and as a result CdS was chosen.

A recent report has detailed the synthesis of high-quality bare CdS QDs<sup>[16]</sup>. However, bare CdS cores tend to emit deep-trap white luminescence that overwhelms the

blue emission and as mentioned above these cores need to be overcoated with a larger band gap semiconductor such as ZnS. The high-quality CdS NCs described in the article mentioned above are made using oleic acid and to date we have had very little success attempting to overcoat NCs made in the presence of oleic acid. After this work was completed several reports appeared in the literature describing the synthesis of alloyed  $\text{Cd}_x\text{Zn}_{1-x}\text{Se}$  NCs<sup>[17]</sup> and what was claimed to be (CdSe)ZnSe core-shell NCs<sup>[18,19]</sup>, which have narrow size distributions and high quantum efficiencies, making these materials another great candidate for QD-LED display applications.

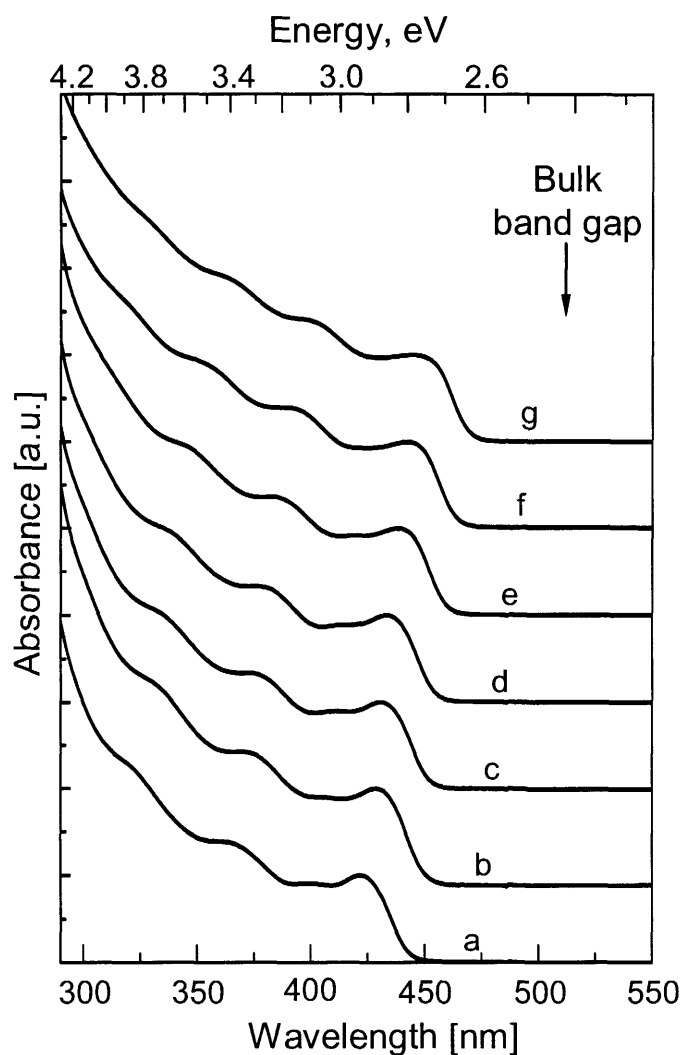
## 3.2 (CdS)ZnS core-shell Nanocrystals\*

### 3.2.1 Discussion of Results and Characterization

The synthesis of the (CdS)ZnS core-shell nanocrystals (NCs) is a two-step procedure. The CdS cores are synthesized and processed from growth solution, and the shell of ZnS is grown onto the CdS cores in a separate reaction. The synthesis of the CdS NC core material is based on the well established colloidal methods of preparing NCs, in which the precursors are rapidly injected at high temperatures into a flask of high-boiling organic solvents<sup>[10]</sup>. Here the cadmium and sulfur precursors are injected into a mixture of oleylamine and trioctylphosphine in the presence of a dialkyl phosphinic acid, providing controlled growth, which leads to large particles with narrow size distributions.

---

\* Much of this section has appeared in print (J. S. Steckel *et al*, *Angew. Chem. Ed. Int.* **2004**, *43*, 2154)

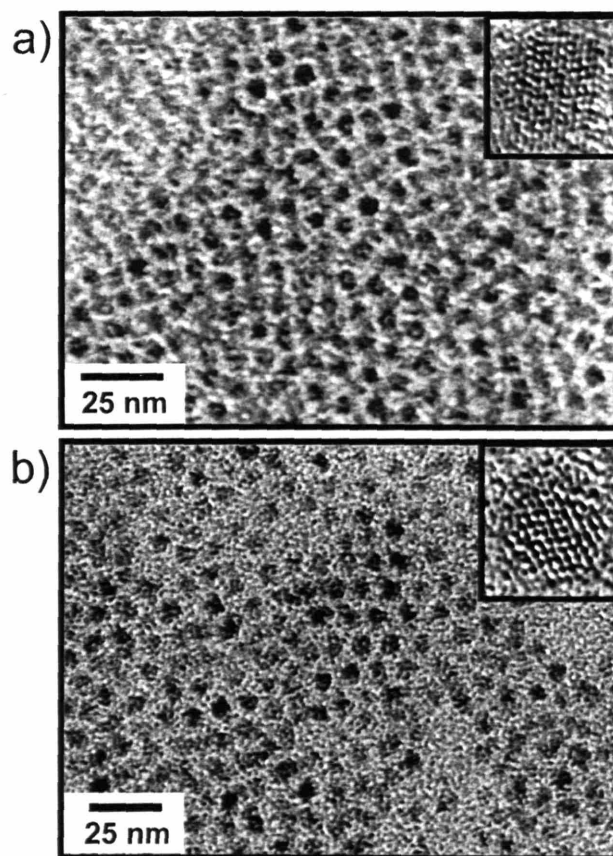


**Figure 3.2** Absorption spectra of a size-series of large CdS nanocrystals ranging from  $3.7 \pm 0.4$  nm to  $5.2 \pm 0.4$  nm in diameter. The longest wavelength absorption feature for spectrum (a) occurs at  $\lambda = 422$  nm, (b) 427 nm, (c) 432 nm, (d) 435 nm, (e) 439 nm, (f) 444 nm, and (g) 448 nm.

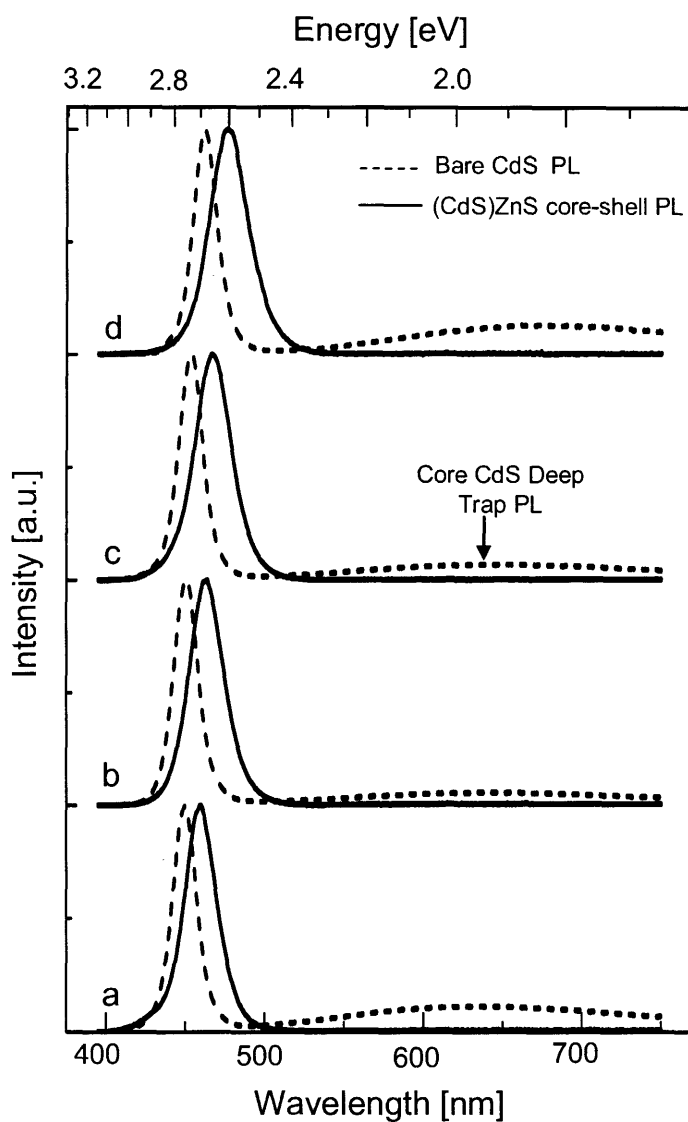
Figure 3.2 shows the optical absorption spectra for a size series of CdS cores, demonstrating their narrow size distributions. The largest particles with a first absorption feature at 448 nm (core diameter  $5.2 \pm 0.4$  nm) still exhibit secondary and even tertiary absorption features. The crystallinity of the core material is seen clearly in the inset of



Figure 3.3a, in which the HRTEM micrograph shows the atom columns of a  $\sim 4.9$  nm particle. The low resolution TEM image (Figure 3.3a) illustrates the relatively good size-distribution and morphology of the particles. PL quantum efficiencies for these CdS core NCs after processing were 3-6 %. The PL of the CdS core NCs contains a noticeable quantity of deep trap emission (Figure 3.4), giving the core materials a violet appearance when excited with a UV lamp.

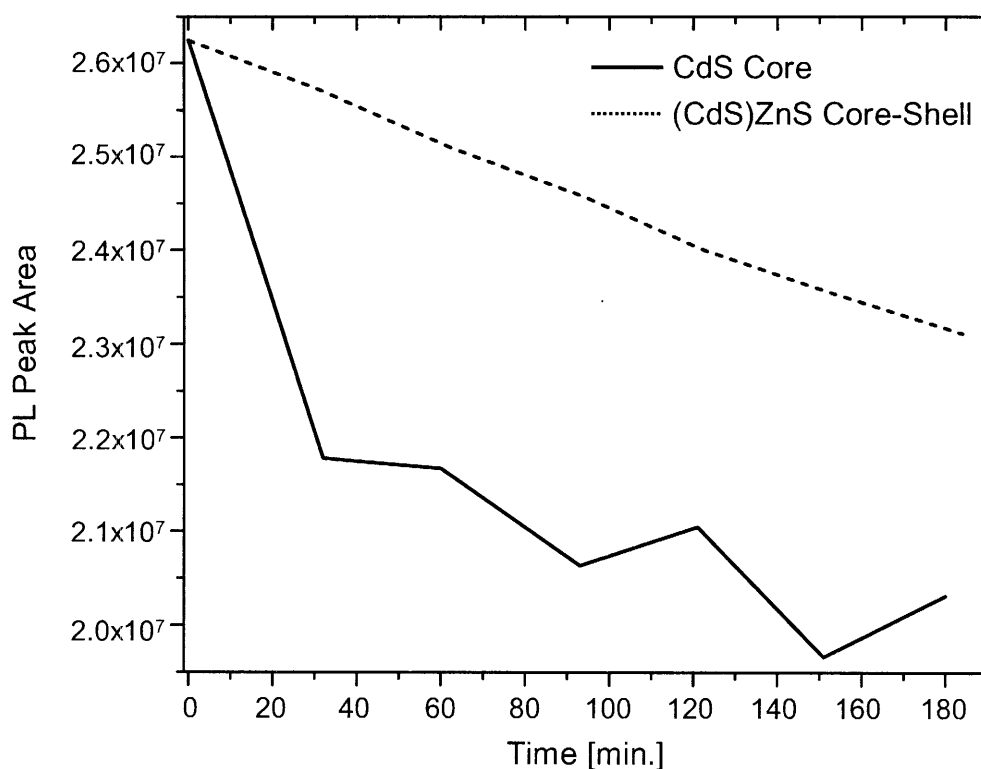


**Figure 3.3** TEM images of CdS core and (CdS)ZnS core-shell nanocrystals. Micrograph (a) shows bare,  $4.9 \pm 0.4$  nm CdS nanocrystals with a HRTEM image inset and image (b) depicts the same nanocrystal sample overcoated with  $\sim 3$  monolayers ( $3.1 \text{ \AA}$  per monolayer) of ZnS with a HRTEM image inset.



**Figure 3.4** Normalized PL spectra of bare CdS nanocrystals (dotted lines) and the corresponding PL of the (CdS)ZnS core-shell nanocrystals (solid lines). (a) Bare CdS nanocrystals emitting at 450 nm ( $4.7 \pm 0.4$  nm diameter core, FWHM = 18 nm) and overcoated with  $\sim 2$  monolayers emitting at 460 nm (FWHM = 24 nm), (b) Bare CdS nanocrystals emitting at 450 nm ( $4.7 \pm 0.4$  nm diameter core, FWHM = 18 nm) and overcoated with  $\sim 3$  monolayers emitting at 465 nm (FWHM = 25 nm), (c) Bare CdS nanocrystals emitting at 454 nm ( $4.9 \pm 0.4$  nm diameter core, FWHM = 18 nm) and overcoated with  $\sim 3$  monolayers emitting at 469 nm (FWHM = 27 nm), and (d) Bare CdS nanocrystals emitting at 463 nm ( $5.2 \pm 0.4$  nm diameter core, FWHM = 18 nm) and overcoated with  $\sim 4.5$  monolayers emitting at 480 nm (FWHM = 28 nm).

Growth of the ZnS shell is based on the prior overcoating procedure for (CdSe)ZnS core-shell NCs.<sup>[12,13]</sup> ZnS was chosen as the shell material because of its large band gap (3.7 eV corresponding to  $\lambda = 335$  nm), which aids confinement of the exciton on the CdS core, accompanied by the relatively small, 8 % lattice mismatch between CdS and ZnS. As the zinc and sulfur precursors are added, the weak violet fluorescence changes gradually over the course of the overcoating process to a bright blue emission.

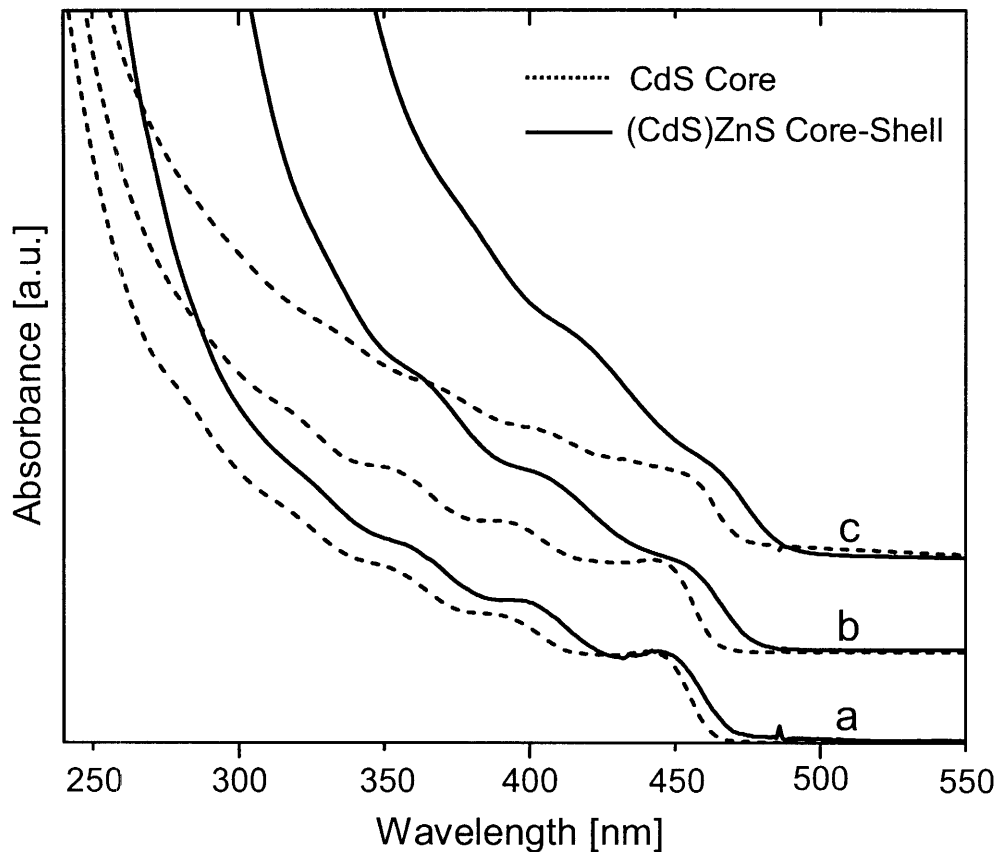


**Figure 3.5** Stability of PL from CdS core versus (CdS)ZnS core-shell. Core and core-shell material were precipitated out of solution two times and dropcast from hexane onto a glass slide. Each slide sat in open air for a total of 180 minutes and a scan was acquired every 30 minutes.

Figure 3.4 shows the emission spectra of CdS cores before overcoating and the corresponding (CdS)ZnS core-shell emission spectrum after overcoating. Consistent with previous overcoating studies, suppression of deep trap emission is achieved with the

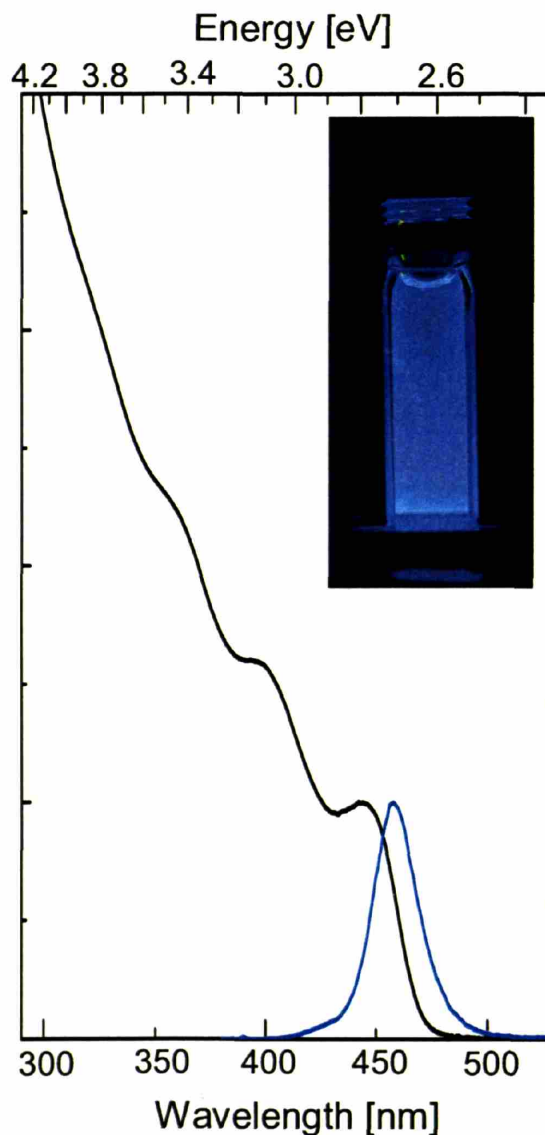
growth of the ZnS shell, as well as increased PL stability (Figure 3.5). The relatively good size-distribution and crystallinity of the (CdS)ZnS core-shell NCs is seen in Figure 3.3b.

The core-shell NCs exhibit quantum efficiencies of 20-30 %. The NC PL quantum efficiencies were determined by comparing the integrated emission of a given NC sample in dilute hexane solution with an optical density of 0.1 with that of the laser dye Coumarin 102 (Lambda Physik) in ethanol. The quantum efficiency peaks at an average ZnS shell thickness of  $\sim 3$  monolayers ( $3.1 \text{ \AA}$  per monolayer). No change in the quantity of deep trap emission from the cores was seen in the presence of amine. We believe that the amine enables the controlled growth of the ZnS shell based on the fact that in the absence of amine in the overcoating solution not all of the deep trap emission is suppressed<sup>[20]</sup>. These observations make it difficult to distinguish how the amine independently affects shell thickness (amine concentration was always held constant) and quantum yield. As thicker shells of ZnS are grown onto the core CdS NCs, an expected increase in the emission FWHM occurs. The band-edge emission FWHM of the CdS core particles is 17-19 nm. After overcoating with 2-3 monolayers the FWHM increases to about 24-26 nm accompanied by red shifts of about 10 nm in emission and about 5 nm for the first absorption feature (Figure 3.6). Similar red shifts in absorption have been observed for the overcoating of CdSe with ZnS and are due to the leakage of the exciton into the shell<sup>[13]</sup>.



**Figure 3.6** Absorption spectra of core CdS and core-shell (CdS)ZnS nanocrystals. (a) Bare  $4.7 \pm 0.4$  nm CdS (dotted line) and the corresponding (CdS)ZnS core-shell nanocrystals (solid line) with an average ZnS shell thickness of  $\sim 2$  monolayers. (b) Bare  $4.9 \pm 0.4$  nm CdS (dotted line) and the corresponding (CdS)ZnS core-shell nanocrystals (solid line) with an average ZnS shell thickness of  $\sim 3$  monolayers. (c) Bare  $5.2 \pm 0.4$  nm CdS (dotted line) and the corresponding (CdS)ZnS core-shell nanocrystals (solid line) with an average ZnS shell thickness of  $\sim 4.5$  monolayers.

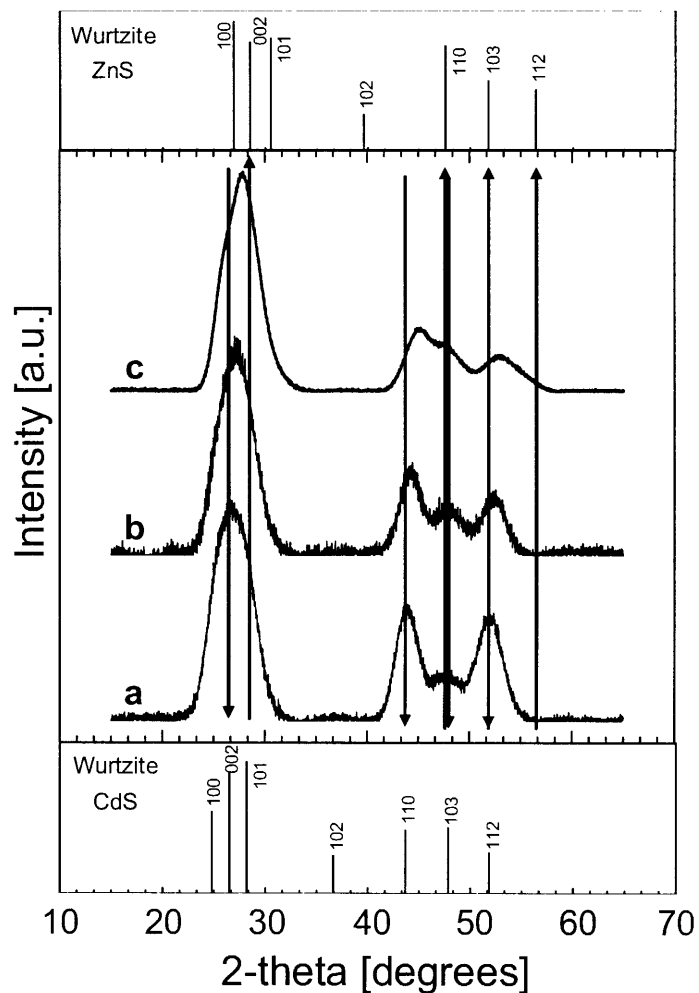
Wavelength dispersive spectroscopy (WDS) was used to confirm the thickness of the ZnS shell for the NC sample shown in Figures 3.3b and 3.8c, giving an average element weight percent of  $21.6 \pm 0.9$  % for Cd,  $32.2 \pm 0.5$  % for Zn, and  $46.2 \pm 0.7$  % for S. These values correspond to a 0.77 nm (2.5 monolayers) thick theoretical ZnS shell, which is consistent with the average experimental thickness obtained from TEM. Figure 3.7 shows the absorption and emission of  $5.4 \pm 0.4$  nm (CdS)ZnS core-shell NCs.



**Figure 3.7** Absorption and emission spectra of (CdS)ZnS core-shell nanocrystals. The (CdS)ZnS core-shell nanocrystals have a  $4.7 \pm 0.4$  nm diameter core, with a ZnS shell thickness of  $\sim 2$  monolayers. The emission peaks at 459 nm with a FWHM of 24 nm and the first absorption feature is at 445 nm.

Figure 3.8a shows the X-ray powder pattern for  $4.9 \pm 0.4$  nm bare CdS NCs, which appears to be a wurtzite structure with zinc-blende stacking faults along the [002] direction<sup>[10]</sup>. The X-ray powder patterns of core-shell NCs with ZnS coverages of  $\sim 2$  monolayers (Figure 3.8b) and  $\sim 3$  monolayers (Figure 3.8c) show a noticeable influence

of the wurtzite ZnS shell on the overall diffraction pattern. Little evidence of small ZnS particles was seen with TEM or optical spectroscopy, but nonetheless care was taken during sample preparation to ensure that no ZnS particles were present for the XRD and WDS measurements.



**Figure 3.8** XRD patterns for (a)  $4.9 \pm 0.4$  nm bare CdS nanocrystals and ZnS overcoated samples with coverages of (b)  $\sim 2$ , and (c)  $\sim 3$  monolayers. The powder patterns for wurtzite CdS and ZnS are shown for comparison in the bottom and top insets, respectively. The lines with arrows are included to help guide the eye to the respective bulk material powder peaks.

### 3.2.2 Experimental Details

A two-step synthetic route was employed to prepare (CdS)ZnS core-shell nanocrystals (NCs). In the first step, the CdS cores were prepared by rapidly injecting the precursor solution into a round bottom flask containing degassed (under vacuum at 100°C for 1 hour) oleylamine (7 mL, 98% Pfaltz & Bauer Inc.)<sup>[21]</sup> and trioctylphosphine (TOP) (8 mL, 97% Strem) stirring rapidly at 250-280°C and then growing at 250°C for 15 to 30 minutes. The precursor solution was made by mixing a degassed (under vacuum at 100°C for 1 hour) mixture of cadmium acetate hydrate (1-2 mmol), TOP (6 mL), and Bis(2,4,4-trimethylpentyl) phosphinic acid (BTMPPA) (1-2 mmol, Cyanex<sup>+</sup> 272 Extractant, Cytec Canada Inc.)<sup>[22]</sup> with a degassed (under vacuum at room temperature for 1 hour) solution of elemental sulfur (1-2 mmol) in oleylamine (3 mL). The size was tuned by changing the injection temperature, growth time, and concentration of precursors, while maintaining the sulfur to cadmium to BTMPPA ratio at 1:1:1. This procedure gives reaction yields of 11-12%.

Before overcoating, the CdS cores were precipitated out of growth solution and then one more time out of hexane to remove unreacted precursors and excess capping ligands. The particles were flocculated from growth solution by adding 0.4 volumes of hexane, 0.8 volumes of butanol, and 3.0 volumes of methanol to 1.0 volume of growth solution and centrifuging for 5 minutes. The particles were then dispersed in 0.15 volumes of hexane and flocculated by adding 1 drop of butanol per 1 volume of original growth solution and 0.5 volumes of methanol and centrifuging for 5 minutes.

In the second step, the ZnS shell was grown. Trioctylphosphine oxide (TOPO) (8-14g, 99 % Strem), oleylamine (3 mL), hexadecylamine (2 g, 98 % Aldrich), and



BTMPPA (0.3-2.0 mmol) were degassed under vacuum for 2 hours in a four-necked flask at 100°C. The CdS cores dispersed in hexane were then added to the degassed solution and the hexane was pulled off at 80°C under vacuum. Under a flow of argon, the NC solution was heated to 180°C and the ZnS shell precursor solution (diethyl zinc (min. 95 % Strem) and hexamethyldisilthiane (>97 % Fluka) dissolved in TOP (7 mL)) was introduced into the flask by dropwise addition (~1 drop/2 seconds). After addition was complete the solution was kept at 180°C for 5 minutes and then left stirring overnight at 75°C to promote annealing of the shell. The (CdS)ZnS core-shell NCs were obtained by precipitation using a mixture of butanol and methanol, similar to the core processing procedure.

To determine the concentration of CdS particles in solution, for overcoating and reaction yield purposes, the absorption cross section of CdS was calculated using equation 2.1 (from chapter 2 (section 2.2.7)). The n and k values were found in the same handbook as used for PbSe (see chapter 2 (section 2.2.7)) and the calculated absorption cross section at 350 nm for CdS was found to be  $C_{\text{abs}} = (5.110 \times 10^5)a^3 \text{ cm}^{-1}$ , where a = average particle radius.

Optical absorption spectra were acquired on a Hewlett-Packard 8453 diode array spectrometer. Photoluminescence spectra were acquired using a SPEX Fluorolog-2 spectrometer in a right angle collection configuration. The core CdS absorption spectra were taken with samples prepared by diluting the as-grown NC solutions in hexane, while all (CdS)ZnS core-shell optical characterization was done with samples that had been precipitated out of solution at least one time and redispersed in hexane. High-resolution transmission electron microscopy (HRTEM) done to determine the shell thickness,

crystallinity, and particle size distributions was performed on a JEOL-2010 electron microscope operated at 200kV. Low resolution TEM was done on a JEOL 2000FX operated at 200kV. Elemental analysis of the core-shell material was done using wavelength dispersive spectroscopy (WDS) on a JEOL JXA-733 Superprobes. Powder X-ray diffraction patterns were obtained on a Rigaku Ru300 X-ray diffractometer.

An example preparation is described below for cores with a first absorption peak at 438 nm (455 nm emission with a FWHM = 19 nm) and the overcoating of these cores with ZnS to give a first absorption peak at 440 nm (462 nm emission with a FWHM = 25 nm) and a quantum yield of 25 %:

The CdS cores were prepared by rapidly injecting the precursor solution into a round bottom flask containing degassed (under vacuum at 100°C for 1 hour) oleylamine (7 mL) and TOP (8 mL) stirring rapidly at 280°C and then growing at 250°C for 25 minutes. The precursor solution was made by mixing a degassed (under vacuum at 100°C for 1 hour) mixture of cadmium acetate hydrate (1 mmol, 230.5 mg), TOP (6 mL), and Bis(2,4,4-trimethylpentyl) phosphinic acid (BTMPPA) (1 mmol, 316  $\mu$ L) with a degassed (under vacuum at room temperature for 1 hour) solution of elemental sulfur (0.5 mmol, 16 mg) in oleylamine (3 mL).

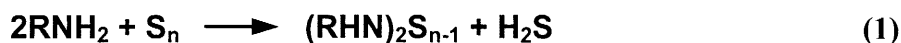
The ZnS shell was grown by first degassing, under vacuum for 2 hours in a four-necked flask at 100°C, TOPO (8g), oleylamine (2 mL), hexadecylamine (2 g), and BTMPPA (2 mmol, 632 $\mu$ L). The CdS cores dispersed in hexane were then added to the degassed solution and the hexane was pulled off at 80°C under vacuum (0.022 mmol Cd in NC form). Under a flow of argon, the NC solution was heated to 180°C and the ZnS

shell precursor solution (diethyl zinc (17 mg) and hexamethyldisilthiane (24 mg) dissolved in TOP (6 mL)) was introduced into the flask by dropwise addition (~1 drop/2 seconds).

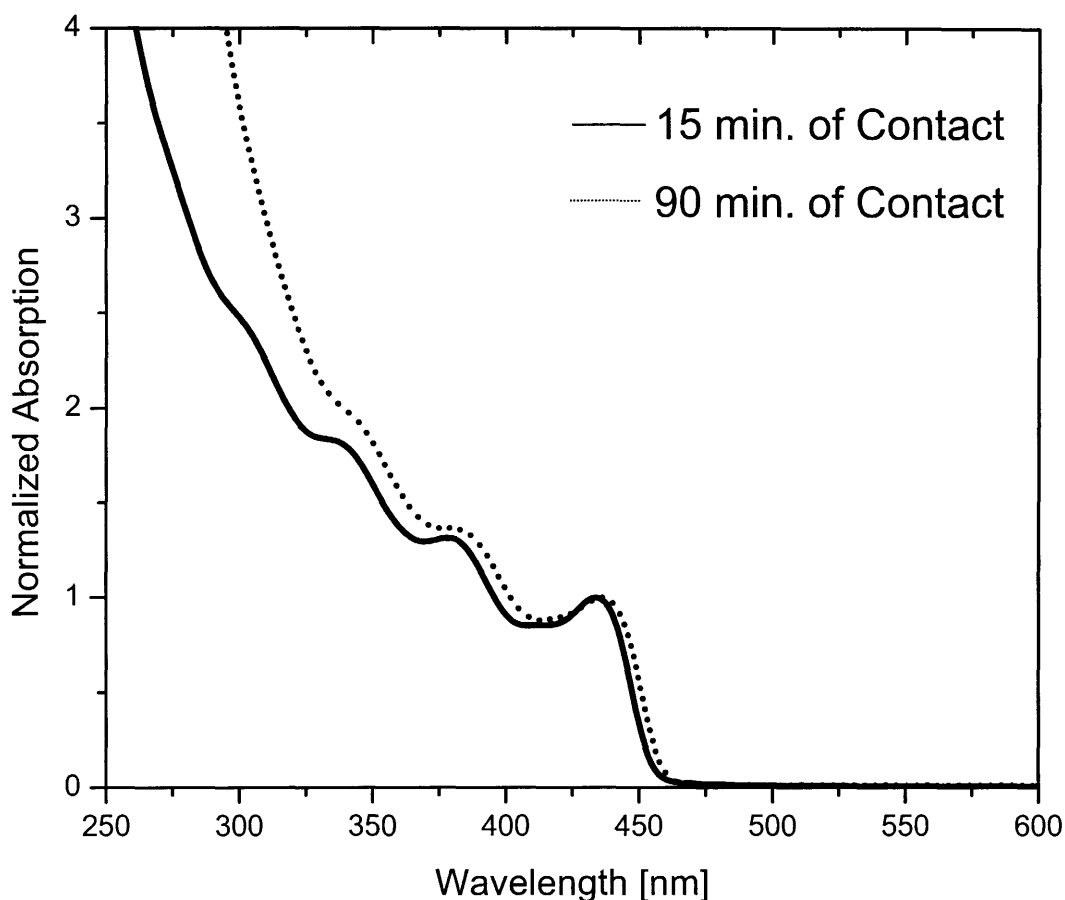
### 3.3 (CdS)Cd<sub>x</sub>Zn<sub>1-x</sub>S core-shell Nanocrystals

#### 3.3.1 Second-Generation CdS Core Preparation

It was found that when the oleylamine is degassed at room temperature in the presence of elemental sulfur for shorter amounts of time (10-20 minutes instead of 1 hour) during the preparation of CdS core NCs, the size distribution of the resulting CdS NCs is tighter. The procedure, as described above in detail (3.2.2), consists of mixing the degassed elemental sulfur and oleylamine solution with the degassed TOP/cadmium solution. When the two solutions are mixed, the dark brown/yellow color of the sulfur/oleylamine solution turns clear (the TOP/cadmium solution is clear to begin with). This suggests that the sulfur that has not dissolved completely in the oleylamine or the product of the sulfur and oleylamine reaction (see reaction (1) below), (RHN)<sub>2</sub>S<sub>n-1</sub>, is reacting with the TOP to form tri-n-octylphosphine sulfide (TOPS) or with the cadmium



complex. The less reaction (1) is pushed to the right during the degassing step, the less elemental sulfur is consumed and the better the size distribution of the resulting CdS NCs. This effect does not change the size of the resulting CdS NCs, but only the size distribution and quantum yield (QY). The QYs measured for cores made using this new method were 15-16 % compared to 3-6 % measured previously. Figure 3.9 shows the absorption spectra of two CdS core samples prepared in exactly the same way (see experimental details below) except for the time the elemental sulfur and oleylamine were



**Figure 3.9** The absorption spectra of two samples of CdS cores prepared in the same way (see experimental details below) except for the time in which the elemental sulfur was in contact with the oleylamine while degassing at room temperature. The sample in which the elemental sulfur was in contact with the oleylamine for only 15 minutes has a better size distribution (FWHM of emission spectrum = 15 nm), while that which was in contact for 90 minutes had a slightly worse size distribution (FWHM of emission spectrum = 17 nm) and lower QY (6% versus 16%).

in contact (15 minutes versus 90 minutes). It can be clearly seen that the size distribution of the sample in which the oleylamine and elemental sulfur were in contact for only 15 minutes is slightly better.

The two CdS cores samples shown in Figure 3.9 were prepared by rapidly injecting the precursor solution into a round bottom flask containing degassed (under vacuum at 100°C for 90 minutes) oleylamine (7 mL) and TOP (8 mL) stirring rapidly at 290°C and then growing at 250°C for 30 minutes. The precursor solution was made by

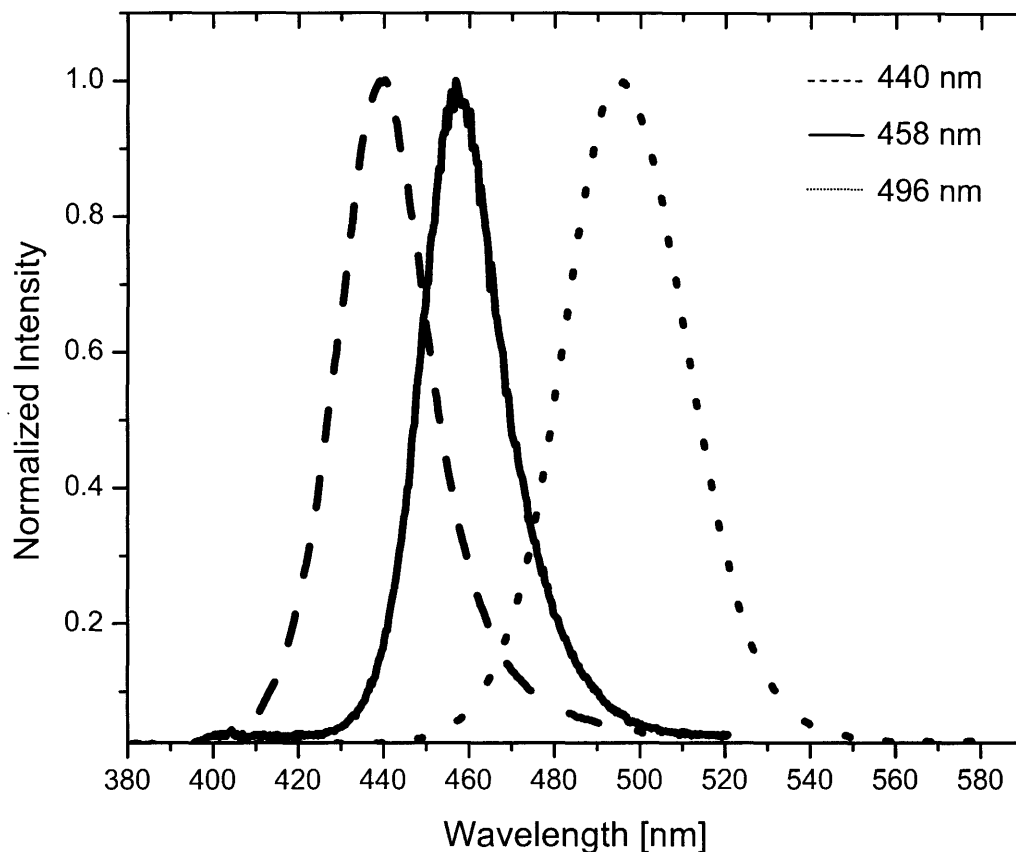
mixing a degassed (under vacuum at 100°C for 90 minutes) mixture of cadmium acetate hydrate (1 mmol, 230.5 mg), TOP (6 mL), and Bis(2,4,4-trimethylpentyl) phosphinic acid (1 mmol, 316  $\mu$ L) with a degassed (under vacuum at room temperature for 90 minutes versus 15 minutes) solution of elemental sulfur (1 mmol, 32 mg) in oleylamine (3 mL).

### 3.3.2 Cd<sub>x</sub>Zn<sub>1-x</sub>S Shell Growth

The addition of cadmium into the ZnS shell creates a graded structure at the interface as opposed to an abrupt change from CdS to ZnS. This graded interface allows for a more crystalline transition from the core to the shell and as a result less lattice strain. Thicker and more uniform shells can then be grown, which provides enhanced core surface passivation and consequently higher quantum efficiencies. Three significant changes to the ZnS overcoating procedure described in section 3.2 were also made. The shell growth solution was modified to mimic that of the CdS core growth solution (TOP/oleylamine/phosphinic acid), two to three fold excess sulfur (hexamethyldisilthiane) was used to achieve more uniform shell growth, and the shell precursors were added over 1 to 2 hours using a syringe pump compared to 5 minutes using an addition funnel. The longer addition times using a syringe pump provides smooth, continuous shell precursor addition and therefore controlled and uniform shell growth. The introduction of cadmium into the shell as well as the three changes described above provide the conditions necessary to grow thicker and more uniform shells and a two fold increase in quantum yield was observed (50 % compared to 25 % previously).

Figure 3.10 shows three different sizes of (CdS)Cd<sub>x</sub>Zn<sub>1-x</sub>S core-shell NCs. The two samples emitting at 440 nm and 496 nm were made for lasing applications (see

section 3.4), while the sample emitting at 458 nm was made for QD-LED applications. The  $(\text{CdS})\text{Cd}_x\text{Zn}_{1-x}\text{S}$  core-shell NCs emitting at 458 nm have a FWHM = 20 nm and a QY of 49% and the detailed synthesis is described below for reference.



**Figure 3.10** Three sizes of  $(\text{CdS})\text{Cd}_x\text{Zn}_{1-x}\text{S}$  core-shell NCs emitting at 440 nm (dashed) with a FWHM = 23 nm, 458 nm (solid) with a FWHM = 20 nm, and 496 nm (dotted) with a FWHM = 29 nm. The detailed description of the synthesis of the sample emitting at 458 nm can be found below. The quantum yield was measured to be 49%.

An example preparation of  $(\text{CdS})\text{Cd}_x\text{Zn}_{1-x}\text{S}$  core-shell NCs is described below for cores with a first absorption peak at 430 nm (442 nm emission with a FWHM = 17 nm) and the overcoating of these cores with  $\text{Cd}_x\text{Zn}_{1-x}\text{S}$  to give a first absorption peak at 443 nm (458 nm emission with a FWHM = 20 nm) and a quantum yield of 49% (emission spectrum shown in Figure 3.10). The CdS cores were prepared by rapidly injecting the

precursor solution into a round bottom flask containing degassed (under vacuum at 100°C for 2.5 hours) oleylamine (7 mL) and TOP (8 mL) stirring rapidly at 300°C and then growing at 250°C for 25 minutes. The precursor solution was made by mixing a degassed (under vacuum at 100°C for 2 hours) mixture of cadmium acetate hydrate (1 mmol, 230.5 mg), TOP (6 mL), and Bis(2,4,4-trimethylpentyl) phosphinic acid (BTMPPA) (1 mmol, 316 µL) with a degassed (under vacuum at room temperature for 15 minutes) solution of elemental sulfur (1 mmol, 32 mg) in oleylamine (3 mL).

The  $\text{Cd}_x\text{Zn}_{1-x}\text{S}$  shell was grown by first degassing, under vacuum for 2 hours in a four-necked flask at 100°C, TOP (5 mL), oleylamine (5 mL), and BTMPPA (1 mmol, 316 µL). The CdS cores dispersed in hexane were then added to the degassed solution and the hexane was pulled off at 70°C under vacuum (0.071 mmol Cd in NC form). Under a flow of argon, the NC solution was heated to 170°C and the two  $\text{Cd}_x\text{Zn}_{1-x}\text{S}$  shell precursor solutions (solution #1: diethyl zinc (47 mg) and dimethylcadmium (4 mg) dissolved in 3 mL of TOP and solution #2: hexamethyldisilthiane (146 mg (2 fold excess)) in 3 mL of TOP), each in separate syringes, were introduced into the flask at a rate of 33 µL/minute (90 minute addition) using a syringe pump.

### **3.4 Blue Nanocrystal Lasing and Biological Imaging**

The purpose of this section is to highlight how the synthesis of high-quality blue emitting NCs has influenced two other important areas of NC research: NC lasing and biological imaging. For more details see the respective published articles.

### 3.4.1 Blue Nanocrystal ASE and Lasing\*

Semiconductor NCs are unique as optical gain media due to their size-dependent color-tunability and chemical flexibility. Previous work on CdSe NCs has shown that both amplified spontaneous emission (ASE) and lasing at room temperature can be achieved under appropriate conditions<sup>[23-25]</sup>. Despite the fact that CdSe NCs have emission tunability over a large portion of the visible range, however, neither ASE nor lasing at blue wavelengths has been demonstrated from these NCs. This may be attributed to highly efficient non-radiative Auger relaxation processes which become dominant as the size of the nanocrystal decreases<sup>[26]</sup>. Recently, ASE at blue wavelengths was achieved by the use of Type-II NCs, but only at low temperature<sup>[27]</sup>, whereas all of our work was done at room temperature.

Much attention has been given to CdS NCs in view of their potential use as nonlinear optical materials, such as optical switches and amplifiers. From z-scan measurements elucidating the third and higher order nonlinearities<sup>[28-30]</sup>, to theoretical<sup>[31]</sup> and experimental<sup>[32]</sup> efforts determining optical gain, CdS NCs have been the subject of much fundamental study. Numerous efforts have therefore been dedicated to embedding these NCs in a host matrix. Many of these efforts, however, employ CdS NCs whose surfaces are not well passivated, resulting in significant deep trap emission<sup>[29,32,33]</sup>. This leads to a broadened emission spectral profile<sup>[33]</sup> (FWHM > 150 nm) which can overlap with the size-tunable band-edge emission, making it difficult to separate the emissive contribution from deep-trap states to the observed fluorescence. The spectrally

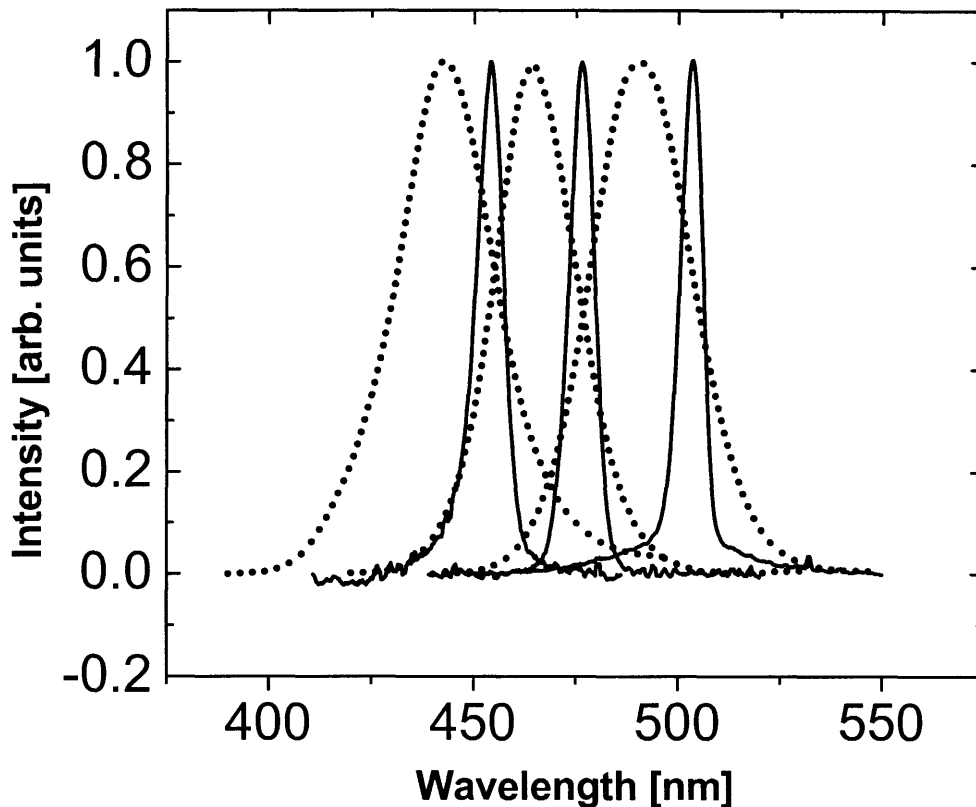
---

\* Much of this section has appeared in print (Y. Chan *et al*, *Appl. Phys. Lett.* **2005**, *86*, 073102)



broadened emission is also undesirable for optical applications that rely upon the narrow emission profiles of NCs.

Previous work on CdSe NCs established that a judicious choice of surface ligands leads to NCs that are dispersible in ethanol, allowing their incorporation into sol-gel derived matrices in volume fractions sufficiently high to observe stimulated emission<sup>[34,35]</sup>. The (CdS)Cd<sub>x</sub>Zn<sub>1-x</sub>S core-shell NCs were rendered dispersible in ethanol by treatment with oleylamine and 5-amino-1-pentanol (AP) in the presence of small amounts of tetrahydrofuran. Addition of the silica precursor [3-aminopropyltrimethoxysilane (APS)] resulted in a slightly viscous liquid that was spin coated onto a glass slide to form a thin clear film. The spin-coated film was then annealed at 100°C for ~5 minutes and then at 200°C for ~ 2 minutes to complete the condensation of the siloxane in APS, bridging the silica network. Figure 3.11 shows the emission profiles of 3 different (CdS)Cd<sub>x</sub>Zn<sub>1-x</sub>S NC-silica composite films. The narrow spectral widths of the fluorescence emission of the NCs (FWHM ~ 25-30 nm) are preserved upon incorporation into the film. No significant deep trap emission is observed, suggesting that the incorporation process does not appreciably perturb the surface quality of the overcoated NCs. ASE at room temperature was achieved by exciting the films with the frequency-doubled output of a regeneratively amplified Titanium-Sapphire (Ti-Sapph) laser system. This provided excitation centered at 400 nm with a pulsewidth of 100 fs and a repetition rate of 1 KHz. The narrower (FWHM ~ 5-7 nm) ASE counterpart of each fluorescence spectrum appears on the lower energy side of the fluorescence. The use of high-quality (CdS)Cd<sub>x</sub>Zn<sub>1-x</sub>S core-shell particles, which exhibited no deep trap

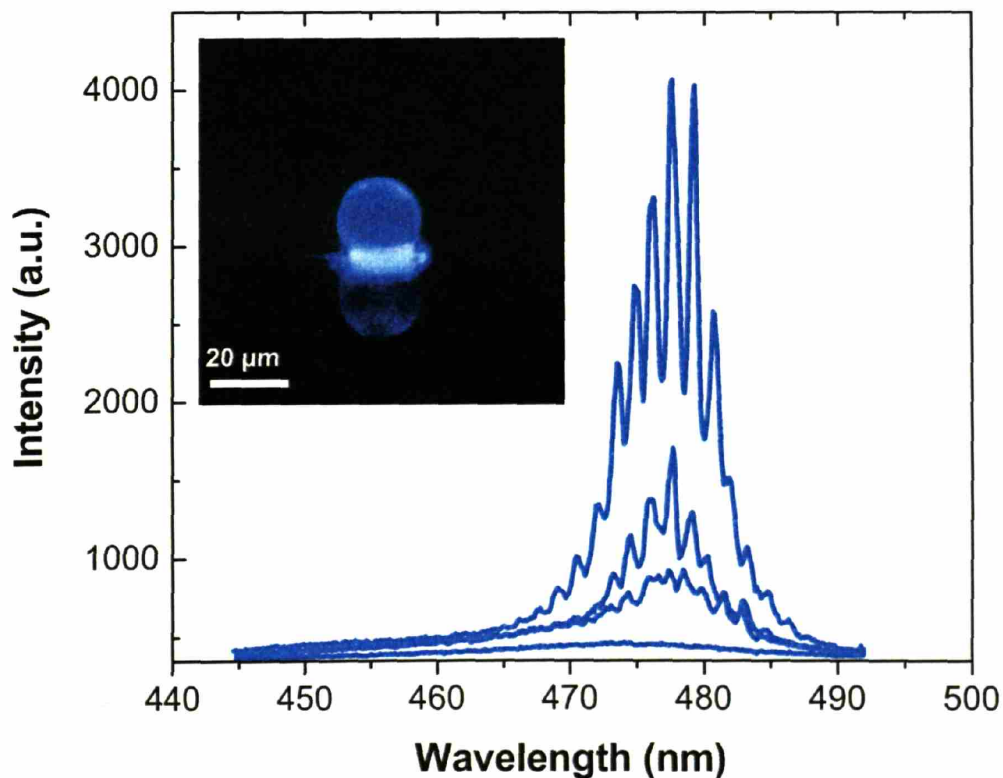


**Figure 3.11** Tunable fluorescence of  $(\text{CdS})\text{Cd}_x\text{Zn}_{1-x}\text{S}$  core-shell NCs in silica films (dotted lines). Their corresponding room temperature ASE spectra (solid lines), which occur at 454 nm, 477 nm and 503 nm, feature dramatically reduced linewidths (from  $\sim 25$  nm to  $\sim 5$  nm).

emission allowed us to determine the biexcitonic origin of the optical gain, and facilitated VSL measurements of the room temperature modal gain.

Optically pumped lasing was achieved by coupling the  $(\text{CdS})\text{Cd}_x\text{Zn}_{1-x}\text{S}$  NC-silica composite to a spherical resonator. The  $(\text{CdS})\text{Cd}_x\text{Zn}_{1-x}\text{S}$  NC-silica coated spherical resonators were produced according to a recently developed procedure<sup>[36]</sup> in which the NC-sol mixture is spin-coated in the presence of commercially available silica microspheres onto a substrate. The inset in Figure 3.12 shows a microscope image of a typical microsphere resonator under UV light excitation. A home-built imaging / dispersive far-field fluorescence microscope coupled to the frequency-doubled output of

the Ti:Sapph regenerative amplifier was used to excite and detect lasing from the microsphere-NC composites. Lasing was obtained at room temperature by exciting individual microspheres above threshold, as indicated in the spectra shown in Figure 3.12. The development of narrow (FWHM < 1 nm), evenly-spaced peaks (characteristic of whispering gallery modes<sup>[37]</sup>) within the gain spectrum of the NCs depicts the onset of



**Figure 3.12** Lasing spectra from the  $(\text{CdS})\text{Cd}_x\text{Zn}_{1-x}\text{S}$  NC-microspheres at increasing pump intensities. The inset is a fluorescence microscope images of a typical  $20\ \mu\text{m}$  diameter  $(\text{CdS})\text{Cd}_x\text{Zn}_{1-x}\text{S}$  NC-microsphere composite under UV light excitation. The bright halo is due to agglomeration of the NC-sol at the base of the sphere during spin-casting.

lasing. These blue-emitting spherical resonators open up a new spectral window, providing room temperature NC-based lasers access across the entire visible range.

### 3.4.2 Intravital Imaging in the Blue\*

Intravital microscopy has provided unmatched molecular, cellular, anatomical, and functional insight into both tumor biology and the response to treatment<sup>[38]</sup>. This technique captures fluorescence from molecules that are either injected into the host or expressed by cells<sup>[39,40]</sup> as well as intrinsic signals such as second harmonic generation emanating from collagen when multi-photon excitation is used<sup>[41,42]</sup>. Traditional fluorophores (organic molecules) hamper simultaneous imaging of the major components of a solid tumor (the cancer and host cells, the extracellular matrix, and the blood vessels that provide nourishment) because they photobleach and have relatively narrow excitation and broad emission spectra. Nanocrystals (NCs) on the other hand have the potential to overcome these limitations because they are photostable, tunable to a desired narrow emission spectrum, relatively insensitive to the wavelength of excitation light, and are especially bright fluorophores for use with multiphoton microscopy<sup>[43]</sup>.

Recent work<sup>[44]</sup> presented three studies that highlight the synergy of semiconductor NCs and multiphoton intravital microscopy for tumor pathophysiology studies: differentiating tumor vessels from both peri-vascular cells and matrix, assaying the ability of microparticles to access the tumor, and monitoring the trafficking of precursor cells. In this work we synthesized (CdS)ZnS core-shell NCs with peak emission at 470 nm, which intentionally laid nicely in between the second harmonic generation (SHG) and the green fluorescent protein (GFP) signals. As a result NCs emitting at 470 nm and 590 nm could be excited and imaged concurrently, while

---

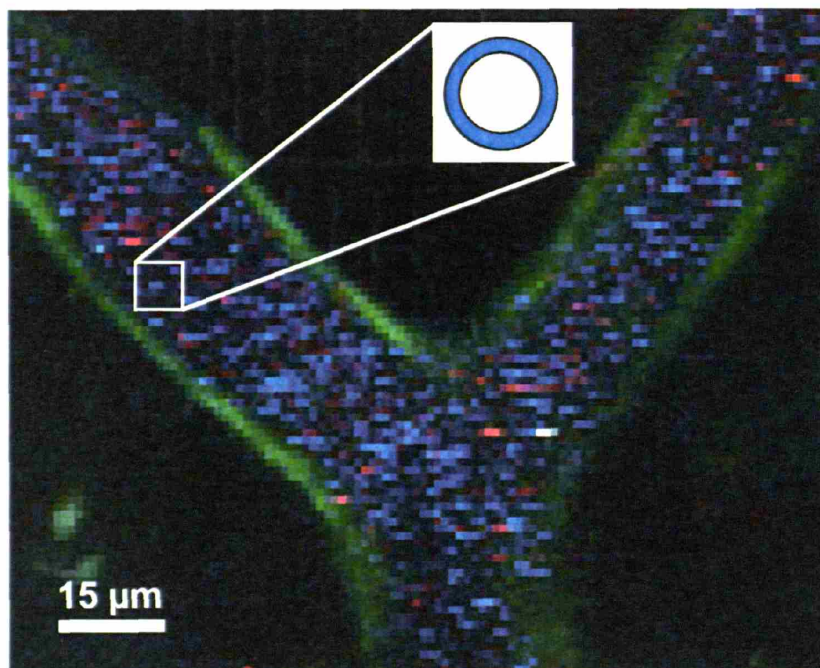
\* Much of this section has appeared in print (Y. Chan *et al*, *Adv. Mater.* **2004**, *16*, 2092)

avoiding the interference of the fluorescence of the fixed signals emanating from the tumor environment<sup>[44]</sup>.

The (CdS)ZnS core-shell NCs were also incorporated into a silica shell grown on preformed sub-micron diameter silica microspheres<sup>[45]</sup>, analogous to the method of Vrij *et al.*<sup>[46]</sup>. The strategy employed growing a shell of silica onto a silica microsphere in the presence of properly derivatized NCs. The core silica microspheres were synthesized using previously established techniques<sup>[47,48]</sup>. The native tri-n-octylphosphine oxide (TOPO) ligands on the (CdS)ZnS core-shell NC surface were cap-exchanged with 5-amino-1-pentanol (AP) and 3-aminopropyltrimethoxysilane (APS). The amino group of each ligand binds to the NC surface and the hydroxyl group of AP permits dispersion in ethanol while the alkoxy silane moiety of APS presumably allows the formation of siloxane bonds with the silica host matrix. The cap-exchanged NCs are then dispersed in a mixture of ethanol, tetraethoxysilane and bare silica microspheres and upon addition of water and ammonium hydroxide to this mixture at elevated temperatures, rapid hydrolysis of the siloxane precursor occurs, which subsequently condenses to form a thin shell of silica around each microsphere.

The inherent stability of the spheres in aqueous solvents, as well as their photostability, brightness, and spectral resolution, allows them to be used in biological applications where the size of the chromophore is key. NC-loaded silica microspheres were used in conjunction with multiphoton intravital microscopy as a new method to guide the design of particulate drug delivery vehicles<sup>[44]</sup>. More specifically, the ability of differently-sized NC-encoded microspheres was assayed to access vascular endothelial growth factor-green fluorescing protein (VEGF-GFP) peri-vascular cells using highly

uniform 100 and 500 nm silicate beads, loaded with (CdS)ZnS core-shell NCs emitting at 470 nm and (CdSe)Cd<sub>x</sub>Zn<sub>1-x</sub>S core-shell NCs emitting at 590 nm, respectively. The NC-encoded spheres were administered concurrently to a VEGF-GFP mouse bearing wild-type MCAIV tumor explant within a dorsal skinfold chamber preparation. Following a 5-hour period of extravasation, a region of the tumor was imaged to reveal the distribution of microspheres. The ability to tune the NC fluorescence from the GFP reporter protein enabled us to assess the ability of these candidates to access the peri-vascular cells.



**Figure 3.13** Image of the blood vessels in the brain of a Tie2-GFP mouse using intravital multiphoton microscopy. Blue-emitting microspheres (mean diameter 100 nm) and red-emitting microspheres (mean diameter 500 nm) are shown circulating within the blood vessels lined with GFP-expressing endothelial cells (green). More blue emission is seen due to the fact that a much higher concentration of blue microspheres was injected. The enlarged selected area shows a cartoon of a core-shell silica microsphere, where the shell appears blue due to the presence of the (CdS)ZnS core-shell NCs.

These (CdS)ZnS NC-tagged microspheres were also injected and imaged (using multiphoton intravital microscopy) in the blood vessels in the brain of a Tie2-GFP mouse for illustrative purposes<sup>[45]</sup>, Figure 3.13.

### 3.5 Conclusions

The synthesis of blue emitting (CdS)ZnS and (CdS)Cd<sub>x</sub>Zn<sub>1-x</sub>S core-shell nanocrystals (NC) was described in detail. The procedure is a two step synthesis, in which CdS core NCs are overcoated with ZnS or Cd<sub>x</sub>Zn<sub>1-x</sub>S to yield stable core-shell particles. This blue emitting core-shell material was tuned from 440 nm to 500 nm and shown to exhibit quantum efficiencies as high as 50%. Complete material characterization was achieved using absorption and emission spectrophotometry, transmission electron microscopy, X-ray powder diffraction, and wavelength dispersive spectroscopy. These core-shell NCs were also shown to exhibit greater stability to photoluminescence efficiency degradation compared to core CdS NCs. Access to the blue region of the visible spectrum has been realized with stable, processable core-shell nanocrystals, making applications such as blue QD-LEDs, blue nanocrystal lasing, and blue NC-biological fluorescence labeling possible.

### 3.6 References

1. V. L. Colvin, M. C. Schlamp, A. P. Alivisatos, *Nature* **1994**, 370, 354.
2. B. O. Dabbousi, O. Onitsuka, M. G. Bawendi, M. F. Rubner, *Appl. Phys. Lett.* **1995**, 66, 1316.
3. M. Jr. Bruchez, M. Moronne, P. Gin, S. Weiss, P. A. Alivisatos, *Science* **1998**, 281, 2013.
4. W. C. W. Chan, S. Nie, *Science* **1998**, 281, 2016.
5. H. Mattoussi, J. M. Mauro, E. R. Goldman, G. P. Anderson, V. C. Sundar, F. V.

- Mikulec, M. G. Bawendi, *J. Am. Chem. Soc.* **2000**, *122*, 12142.
6. S. Coe, W. K. Woo, M. Bawendi, V. Bulović, *Nature* **2002**, *420*, 800.
  7. N. Tessler, V. Medvedev, M. Kazes, S. H. Kan, U. Banin, *Science* **2002**, *295*, 1506.
  8. J. S. Steckel, S. Coe-Sullivan, V. Bulović, M. G. Bawendi, *Adv. Mater.* **2003**, *15*, 1862.
  9. J. S. Steckel, J. P. Zimmer, S. Coe-Sullivan, N. E. Stott, V. Bulovic, M. G. Bawendi, *Angew. Chem. Int. Ed.* **2004**, *43*, 2154.
  10. C. B. Murray, D. J. Norris, M. G. Bawendi, *J. Am. Chem. Soc.* **1993**, *115*, 8706.
  11. S. Coe-Sullivan, W. K. Woo, J. S. Steckel, M. G. Bawendi, V. Bulović, *Org. Electron.* **2003**, *4*, 123.
  12. M. A. Hines, P. Guyot-Sionnest, *J. Phys. Chem.* **1996**, *100*, 468.
  13. B. O. Dabbousi, J. Rodriguez-Viejo, F. V. Mikulec, J. R. Heine, H. Mattoussi, R. Ober, K. F. Jensen, M. G. Bawendi, *J. Phys. Chem. B* **1997**, *101*, 9463.
  14. M. A. Hines, P. Guyot-Sionnest, *J. Phys. Chem. B* **1998**, *102*, 3655.
  15. L. S. Li, N. Pradhan, Y. Wang, X. Peng, *Nano Lett.* **2004**, *4*, 2261.
  16. W. W. Yu, X. Peng, *Angew. Chem. Int. Ed.* **2002**, *41*, 2368.
  17. X. Zhong, M. Han, Z. Dong, T. J. White, W. Knoll, *J. Am. Chem. Soc.* **2003**, *125*, 8589.
  18. S. A. Ivanov, J. Nanda, A. Piryatinski, M. Achermann, L. P. Balet, I. V. Bezel, P. O. Anikeeva, S. Tretiak, V. I. Klimov, *J. Phys. Chem. B* **2004**, *108*, 10625.
  19. X. Zhong, R. Xie, Y. Zhang, T. Basche, W. Knoll, *Chem. Mater.* **2005**, *17*, 4038.
  20. D. V. Talapin, A. L. Rogach, A. Kornowski, M. Haase, H. Weller, *Nano Lett.* **2001**, *1*, 207.
  21. B. K. H. Yen, N. E. Stott, K. F. Jensen, M. G. Bawendi, *Adv. Mater.* **2003**, *15*, 1858.
  22. D. A. Zehnder, M. P. Bruchez, J. A. Treadway, J. P. Earhart, U. S. Patent Application 20020144644, 2002.
  23. V.I. Klimov, A.A. Mikhailovsky, Su Xu, A. Malko, J.A. Hollingsworth, C.A. Leatherdale, H.-J. Eisler, M.G. Bawendi, *Science* **2000**, *290*, 314.
  24. H.-J. Eisler, V.C. Sundar, M.G. Bawendi, M. Walsh, H.I. Smith, V.I. Klimov, *Appl. Phys. Lett.* **2002**, *80*, 4614.
  25. V.I. Klimov, M.G. Bawendi, *MRS Bulletin* **2001**, *26*, 998.
  26. V.I. Klimov, A.A. Mikhailovsky, D.W. McBranch, C.A. Leatherdale, M.G. Bawendi, *Science* **2000**, *287*, 1011.
  27. S.A. Ivanov, J. Nanda, A. Piryatinski, M. Achermann, L.P. Balet, I.V. Bezel, P.O. Anikeeva, S. Tretiak, V.I. Klimov, *J. Phys. Chem. B* **2004**, *108*, 10625.
  28. J. He, W. Ji, G.H. Ma, S.H. Tang, H.I. Elim, W.X. Sun, Z.H. Zhang, W.S. Chin,



- J. Appl. Phys.* **2004**, *95*, 6381.
29. H. Du, G.Q. Xu, W.S. Chin, L. Huang, W. Ji, *Chem. Mater.* **2002**, *14*, 4473.
  30. Yu.P. Rakovich, M.V. Artemyev, A.G. Rolo, M.I. Vasilevskiy, M.J.M. Gomes, *Phys. Stat. Sol.(b)* **2001**, *1*, 319.
  31. J.T. Andrews, P. Sen, *J. Appl. Phys.* **2002**, *91*, 2827.
  32. J. Butty, N. Peyghambarian, Y.H. Kao, J.D. Mackenzie, *Appl. Phys. Lett.* **1996**, *69*, 3224.
  33. K. Kang, K. Daneshvar, *J. Appl. Phys.* **2004**, *95*, 646.
  34. V.C. Sundar, H.-J. Eisler, M.G. Bawendi, *Adv. Mater.* **2002**, *14*, 739.
  35. M.A. Petruska, A.V. Malko, P.M. Voyles, V.I. Klimov, *Adv. Mater.* **2003**, *15*, 610.
  36. P.T. Snee, Y. Chan, D.G. Nocera, M.G. Bawendi, *Adv. Mater.* **2005**, *17*, 1131.
  37. V. Lefèvre-Seguin, *Opt. Mater.* **1999**, *11*, 153.
  38. R. K. Jain, L. L. Munn, D. Fukumura, *Nat. Rev. Cancer* **2002**, *2*, 266.
  39. E. B. Brown et al., *Nat. Med.* **2001**, *7*, 864.
  40. D. Fukumura et al., *Cell* **1998**, *94*, 715.
  41. W. R. Zipfel, R. M. Williams, W. W. Webb, *Nat. Biotechnol* **2003**, *21*, 1369.
  42. E. Brown et al., *Nat. Med.* **2003**, *9*, 796.
  43. D. R. Larson et al., *Science* **2003**, *300*, 1434.
  44. M. Stroh, J. P. Zimmer, D. G. Dudal, S. T. Levchenko, K. S. Cohen, D. T. Scadden, V. P. Torchilin, M. G. Bawendi, D. Fukumura, R. K. Jain, *Nat. Med.* **2005**, *11*, 678.
  45. Y. T. Chan, J. P. Zimmer, M. Stroh, J. S. Steckel, R. K. Jain, M. G. Bawendi, *Adv. Mater.* **2004**, *16*, 2092.
  46. A. van Blaaderen, A. Vrij, *Langmuir* **1992**, *8*, 2921.
  47. G.H. Bogush, M.A. Tracy, C.F. Zukoski IV, *J. Non-Cryst. Solids* **1988**, *104*, 95.
  48. W. Stöber, A. Fink, E. Bohn, *J. Colloid Interface Sci.*, **1968**, *26*, 62.



# Chapter 4

## **(Cd<sub>x</sub>Zn<sub>1-x</sub>Se)Cd<sub>y</sub>Zn<sub>1-y</sub>S core-shell Nanocrystals**

### **4.1 Introduction and Motivation**

Semiconductor nanocrystals (NCs) or quantum dots (QDs) show great promise for use in QD-LED (quantum dot light emitting device) displays, due to their unique optical properties and the continual development of new core and core-shell structures to meet specific color needs<sup>[1-10]</sup>. This in combination with the recent development of more efficient and saturated QD-LEDs as well as new QD-LED fabrication techniques<sup>[11,12]</sup>, suggests that QD-LEDs have the potential to become an alternative flat panel display technology (see Chapter 6). The ideal red, green, and blue emission spectrum of an LED for a display application would have a narrow bandwidth and a wavelength such that its color coordinates on the Commission International d'Eclairage (CIE) chromaticity diagram would lie to the outside of the current National Television System Committee (NTSC) standard color triangle. For a Gaussian emission spectrum with a full width at half maximum (FWHM) of 30 nm and a maximized perceived power, the optimal peak wavelength for display applications is  $\lambda = 610\text{-}620$  nm for red,  $\lambda = 525\text{-}530$  nm for green, and  $\lambda = 460\text{-}470$  nm for blue (see section 3.1). For the red pixels, wavelengths longer than  $\lambda = 620$  nm become difficult for the human eye to perceive, while those shorter than  $\lambda = 610$  nm have coordinates that lie inside the standard NTSC color triangle. Optimization of wavelengths for the blue pixels follows the same arguments as for the red pixels, but at the other extreme of the visible spectrum. Green is a different story

however. Green pixels emitting at  $\lambda = 525\text{-}530$  nm provide a color triangle with the largest area on the CIE chromaticity diagram (and therefore the largest number of colors accessible by a display). Wavelengths longer than  $\lambda = 530$  nm make some of the blue/green area of the triangle inaccessible. Wavelengths shorter than  $\lambda = 525$  nm compromise the yellow display emissions.

To date, efficient red-emitting QD-LEDs with a peak emission wavelength optimized for display applications have been realized using (CdSe)ZnS core-shell NCs<sup>[11,13]</sup>, while blue QD-LEDs with a peak wavelength of emission optimized for display applications have been realized with a (CdS)ZnS core-shell material<sup>[10]</sup>. To date, an efficient and stable green-emitting core-shell semiconductor NC that emits at  $\lambda = 525$  nm has not been synthesized and used to fabricate a QD-LED suitable for display applications. Previous work using (CdSe)ZnS core-shell NCs gave QD-LEDs that emit at wavelengths no shorter than  $\lambda = 540\text{-}560$  nm<sup>[13,14]</sup>. Using (CdSe)ZnS core-shell NCs to achieve  $\lambda = 525$  nm emission would require making small CdSe cores (~2.5 nm diameter), due to the significant red shifts obtained after the shell of ZnS is grown onto the CdSe cores<sup>[15,16]</sup>. Such small CdSe semiconductor NCs are difficult to synthesize with narrow size distributions and high quantum efficiencies, and are also difficult to process and overcoat with a higher band gap inorganic semiconductor, which is necessary for incorporation into solid-state structures. A core-shell type composite rather than an organically passivated NC is desirable in a solid state QD-LED device due to the former's enhanced photoluminescence and electroluminescence quantum efficiencies and greater tolerance to processing conditions necessary for device fabrication<sup>[13,15-17]</sup>. Larger NCs are also more desirable for use in QD-LEDs, because the absorption cross section of

NCs scales with size. Larger NCs with larger absorption cross sections lead to an increase in the efficiency of Förster energy transfer from organic molecules to NCs in a working QD-LED, which in turn leads to more efficient devices.

## 4.2 Synthesis of $(\text{Cd}_x\text{Zn}_{1-x}\text{Se})\text{Cd}_y\text{Zn}_{1-y}\text{S}$ core-shell Nanocrystals

In this work, we synthesized a  $\text{Cd}_x\text{Zn}_{1-x}\text{Se}$  alloy core and then grew a  $\text{Cd}_y\text{Zn}_{1-y}\text{S}$  shell to create a core-shell NC material with the ideal spectral characteristics for green emission in a QD-LED display. Our  $\text{Cd}_x\text{Zn}_{1-x}\text{Se}$  core synthesis was based on work recently published, in which Cd and Se precursors were slowly introduced into a growth solution of ZnSe NCs<sup>[1,2]</sup>. A three-step synthetic route was employed to prepare the  $(\text{Cd}_x\text{Zn}_{1-x}\text{Se})\text{Cd}_y\text{Zn}_{1-y}\text{S}$  core-shell NCs.

In the first step, ZnSe NCs were prepared by rapidly injecting 0.7 mmol diethylzinc (Strem) and 1 mL of tri-n-octylphosphine selenide (TOPSe) (1M) dispersed in 5 mL of tri-n-octylphosphine (TOP) (97 % Strem), into a round bottom flask containing 7 grams of degassed hexadecylamine (distilled from 90 % Sigma-Aldrich) at 310°C and then growing at 270°C for 90 minutes.

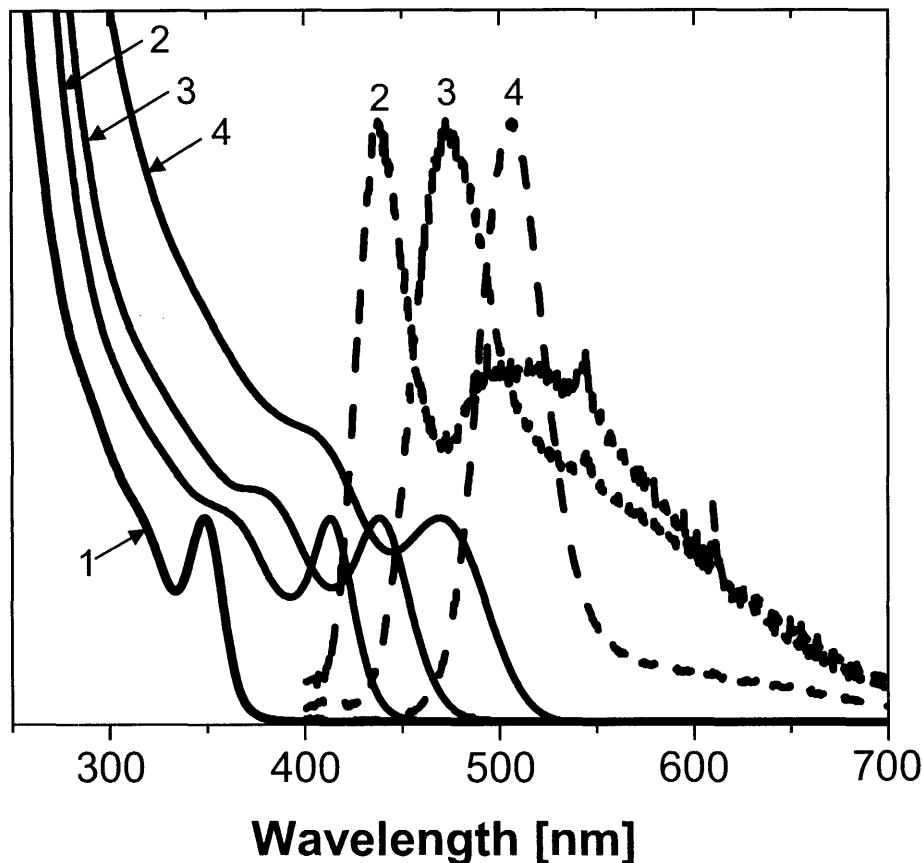
The second step consisted of transferring 8 mL of the above ZnSe NC growth solution, while at 160°C, into a degassed solution of 16 grams of tri-n-octylphosphine oxide (TOPO) (distilled from 90 % Sigma-Aldrich) and 4 mmol of hexylphosphonic acid (HPA) (Alfa Aesar), which was also at 160°C. A solution of 1.1 mmol of dimethylcadmium (Strem) and 1.2 mL of TOPSe (1M) dispersed in 8 mL of TOP (97 % Strem) was then introduced dropwise (1 drop / ~2 seconds) into the ZnSe NC growth solution/TOPO/HPA mixture, which was at 150°C. The solution was then stirred at 150°C for 46 hours. Before overcoating the  $\text{Cd}_x\text{Zn}_{1-x}\text{Se}$  cores with  $\text{Cd}_y\text{Zn}_{1-y}\text{S}$ , the

$\text{Cd}_x\text{Zn}_{1-x}\text{Se}$  cores were isolated by precipitating them out of solution twice with a miscible non-solvent.

In the third step, the  $\text{Cd}_y\text{Zn}_{1-y}\text{S}$  shell was grown by introducing dropwise a solution of dimethylcadmium (20 % of total required moles of cation) (Strem), diethylzinc (Strem), and hexamethyldisilthiane (2 fold excess of required amount) (Fluka) in 8 mL of TOP into a degassed solution of 10 grams of TOPO (distilled from 90 % Sigma-Aldrich) and 2.4 mmol of HPA (Alfa Aesar), which contained the core  $\text{Cd}_x\text{Zn}_{1-x}\text{Se}$  NCs at a temperature of  $150^\circ\text{C}$  (the  $\text{Cd}_x\text{Zn}_{1-x}\text{Se}$  cores dispersed in hexane were added to the degassed TOPO/HPA solution and the hexane was pulled off at  $70^\circ\text{C}$  under vacuum prior to the addition of the shell precursors).

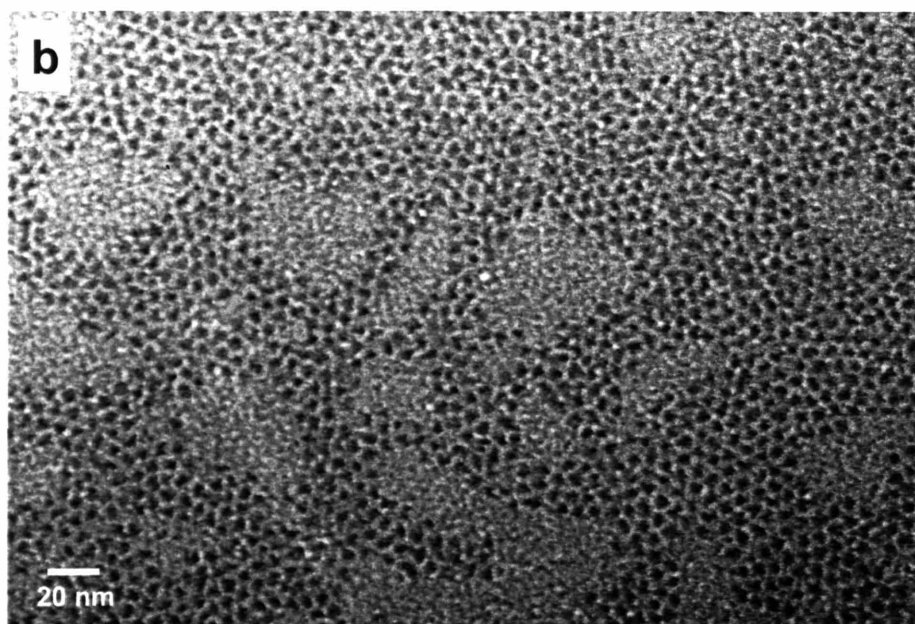
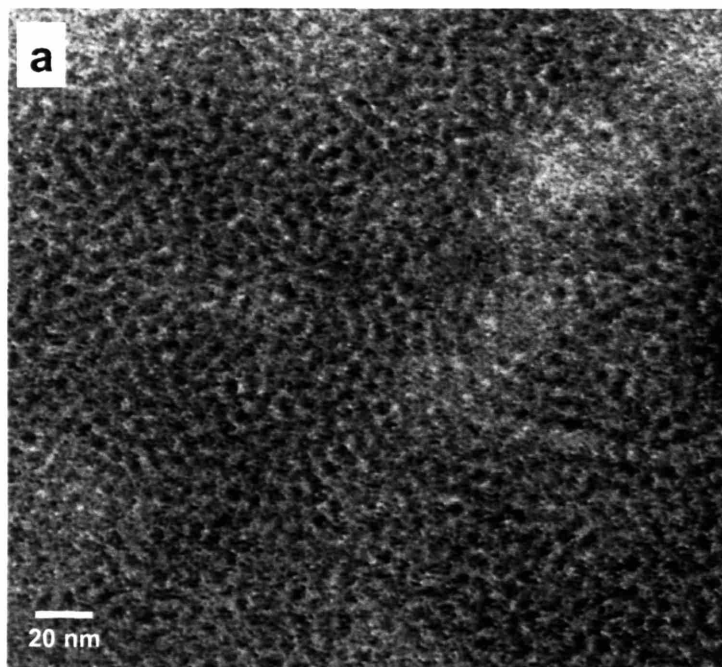
### **4.3 Characterization of $\text{Cd}_x\text{Zn}_{1-x}\text{Se}$ and $(\text{Cd}_x\text{Zn}_{1-x}\text{Se})\text{Cd}_y\text{Zn}_{1-y}\text{S}$**

To fully characterize our  $\text{Cd}_x\text{Zn}_{1-x}\text{Se}$  core material, aliquots were sampled from the growing solution at time  $t = 7, 60,$  and  $2760$  (46 hours) minutes and analyzed with transmission electron microscopy (TEM), wavelength dispersive spectroscopy (WDS), and absorption and fluorescence spectrophotometry. Figure 4.1 shows the absorption and emission spectra of these three aliquots as well as the absorption spectrum of the starting ZnSe NCs ( $2.6 \pm 0.5$  nm in diameter determined by TEM). It was seen that over time the absorption and emission spectra shifted to the red and the deep trap emission diminished after 46 hours of growth (Figure 4.1, spectrum 4), yielding particles  $\sim 3$  nm in diameter. Figure 4.2(a) shows a TEM image of the core  $\text{Cd}_x\text{Zn}_{1-x}\text{Se}$  particles after 46 hours of growth. Upon overcoating the cores of  $\text{Cd}_x\text{Zn}_{1-x}\text{Se}$  with  $\text{Cd}_y\text{Zn}_{1-y}\text{S}$ , the deep trap emission was suppressed completely, yielding an efficient (quantum yields of 50-60%),



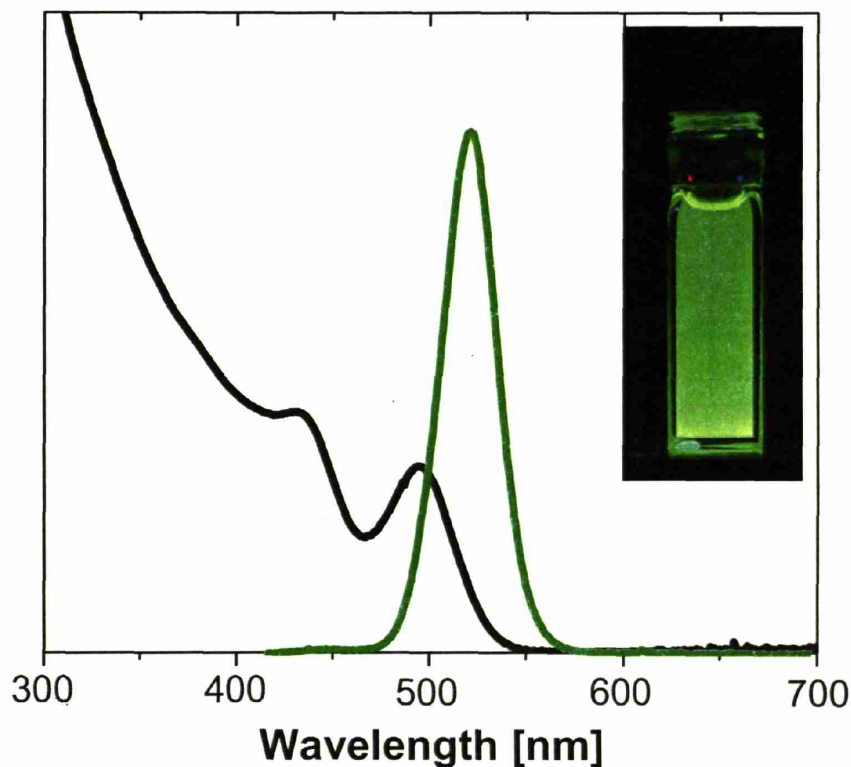
**Figure 4.1** Normalized absorption (solid) and emission (dashed) spectra of the core NCs over time: (1) Starting ZnSe NCs (first absorption peak at 350 nm); (2) Aliquot taken out after 7 minutes of growth (first absorption peak at 413 nm; emission peak at 439 nm); (3) Aliquot taken out after 60 minutes of growth (438 nm; 475 nm); (4) Aliquot taken out after 46 hours of growth (470 nm; 506 nm (FWHM = 34 nm)). All absorption and emission spectra were taken with samples prepared by diluting the as-grown NC solutions in hexane and filtering with a 0.2  $\mu\text{m}$  syringe filter.

saturated color (FWHM = 30 nm), green-emitting core-shell material suitable for QD-LED display applications (Figure 4.3). The  $(\text{Cd}_x\text{Zn}_{1-x}\text{Se})\text{Cd}_y\text{Zn}_{1-y}\text{S}$  core-shell NC morphology can be seen in Figure 4.2(b). The diameter of the core-shell particles was measured to be  $3.8 \pm 0.5$  nm from TEM. The photoluminescence quantum efficiencies were determined by comparing the integrated emission of a given NC sample in dilute hexane solution with an optical density of 0.1 with that of the laser dye Coumarin 540 in ethanol.



**Figure 4.2** TEM images of core  $\text{Cd}_x\text{Zn}_{1-x}\text{Se}$  and  $(\text{Cd}_x\text{Zn}_{1-x}\text{Se})\text{Cd}_y\text{Zn}_{1-y}\text{S}$  core-shell NCs. a) Micrograph showing bare,  $3.2 \pm 0.5$  nm in diameter  $\text{Cd}_x\text{Zn}_{1-x}\text{Se}$  NCs; b) the  $\text{Cd}_x\text{Zn}_{1-x}\text{Se}$  NCs overcoated with  $\text{Cd}_y\text{Zn}_{1-y}\text{S}$  ( $3.8 \pm 0.5$  nm in diameter).





**Figure 4.3** Absorption and emission spectra of  $(\text{Cd}_x\text{Zn}_{1-x}\text{Se})\text{Cd}_y\text{Zn}_{1-y}\text{S}$  core-shell NCs. The emission peaks at 520 nm with a FWHM of 30 nm and the first absorption feature is at 495 nm. The inset shows the bright, color saturated, green emission from the NCs while being excited with a UV lamp.

Table 4.1 shows the growth time ( $t = 7, 60,$  and  $2760$  minutes) of each aliquot, the average outer diameter determined by TEM, the Zn to Cd ratio determined by WDS, the measured first absorption peak, and the calculated alloy  $(\text{Cd}_x\text{Zn}_{1-x}\text{Se})$  and core-shell  $((\text{ZnSe})\text{CdSe}$  core-shell) wavelengths. Table 4.2 shows in more detail the size analysis of the growing NCs over time, including the number of particles measured to contribute to the average NCs diameters. We see from the raw data that as the reaction proceeds, the first absorption peak shifts to the red (Figure 4.1), the Zn to Cd ratio decreases, and the diameter of the particles increases. It is important to note that there was a relatively large increase in particle diameter from  $t = 7$  to  $t = 60$  minutes of growth, but then a very small

Growth Time (minutes) <sup>a</sup>	Outer Diameter (nm) <sup>b</sup>	Zn/Cd <sup>c</sup>	Measured Absorption (nm) <sup>d</sup>	Calculated Alloy Wavelength (nm)	Calculated Core-Shell Wavelength (nm)	Inner Diameter (nm) <sup>e</sup>
7	1.9 ± 0.3	0.33	413	324	416	0.65
60	3.1 ± 0.5	0.18	438	477	509	1.64
2760	3.2 ± 0.5	0.08	470	505	534	1.35

**Table 4.1** Experimental data for the three aliquots taken out of the growing core solution, shown along with the results of effective mass approximation calculations of the first transition energy of alloyed ( $\text{Cd}_x\text{Zn}_{1-x}\text{Se}$ ) vs. core-shell ( $\text{ZnSe}$ )CdSe NCs.

a. Time from when the Cd and Se precursors were introduced into the flask containing the ZnSe NCs to when the aliquot was removed from the flask (complete addition of the Cd and Se precursors occurred at 9.5 minutes).

b. Measured from TEM.

c. Measured from WDS. The NC samples for the WDS measurements were prepared by precipitating the NCs out of solution twice and redispersing in hexane and then drop cast onto a silicon substrate.

d. First absorption feature from absorption spectra shown in Figure 4.1.

e. Calculated from the Zn/Cd ratio and the known outer NC diameter from TEM measurements. This parameter is relevant only for the core-shell calculations while the alloy results depend only on the outer diameter.

increase in diameter from  $t = 60$  to  $t = 2760$  minutes (46 hours). This small change in diameter was accompanied by a relatively large change in the Zn to Cd ratio as well as a relatively large shift to the red of the first absorption peak. This would suggest that at  $t = 7$  minutes the structure is most likely a (ZnSe)CdSe core-shell structure and that for  $t > 7$  minutes the structure becomes a  $\text{Cd}_x\text{Zn}_{1-x}\text{Se}$  alloy, due to the migration of cations in the material<sup>[3]</sup>. It is interesting to note that we saw a decrease in particle diameter following the introduction of the neat hexadecylamine ZnSe growth solution ( $2.6 \pm 0.5$  nm in diameter) into the TOPO/phosphonic acid solution at  $160^\circ\text{C}$  after about 2/3 of the Cd and Se precursors had been added (7 minute aliquot,  $1.9 \pm 0.3$  nm in diameter). This particle etching is plausible based on the large excess of acid present in the solution.

Growth Time (minutes)	Outer Diameter (nm)	# of NCs Measured
0 (ZnSe core)	$2.60 \pm 0.50$	75
7	$1.86 \pm 0.30$	217
20	$2.62 \pm 0.43$	306
60	$3.06 \pm 0.52$	401
660	$3.09 \pm 0.51$	524
2760	$3.21 \pm 0.46$	475

**Table 4.2** Experimental data showing in more detail the size of the NCs as they grew, determined from TEM and the number of NCs measured per sample to determine the average size. The sample at 20 minutes is not shown in Table 4.1.

In order to help confirm our analysis of the NCs composition ( $\text{Cd}_x\text{Zn}_{1-x}\text{Se}$  alloy vs.  $(\text{ZnSe})\text{CdSe}$  core-shell) we performed calculations, as summarized in Table 4.1. The eigenvalues of an electron and hole within an alloyed or a core-shell semiconductor NC were calculated using the effective mass approximation as described previously<sup>[18,19]</sup>. These calculations used experimentally derived electron and hole effective masses and band gaps to determine the lowest energy at which standard radial boundary conditions for the wavefunctions are satisfied<sup>[18-21]</sup>. The following parameters were used in these calculations. The effective masses are 0.1323 for the CdSe electron and 0.45 for the hole. The effective masses for ZnSe are 0.157 for the electron and 0.64 for the hole. Band offsets for CdSe relative to ZnSe: -1.20 eV for the electron and 0.22 eV for the hole. The bulk band gaps are 1.761 eV for CdSe and 2.685 eV for ZnSe. Notice that the hole energy offset for CdSe relative to ZnSe is modeled as being positive as the holes disperse towards negative energies (and thus prefer to reside in the higher valence band material).

It was found that the calculated first transition energies for CdSe and ZnSe NCs

using this method overestimate the effect of quantum confinement. For example, CdSe NCs with a 3.2 nm diameter are calculated to have a first absorption feature at 424 nm, which is significantly blue shifted from the experimental value of 520 nm<sup>[22]</sup>. As a result, we treated the band gaps and electron effective masses as parameters to be optimized for both pure NC materials to match reported experimental results<sup>[2,22,23]</sup>. Essentially, the band gaps are slightly increased (~10%) while the electron masses are raised by a factor of 2-3<sup>[26]</sup>. Next, we performed two sets of calculations using these optimized parameters to represent an alloyed material or a strict core-shell structure. To model an alloyed NC we adjusted the optimized band gap and electron/hole effective masses via a linear interpolation of the parameters for the pure materials based upon the experimentally determined stoichiometry (i.e. Zn to Cd ratio determined by WDS, shown in Table 4.1). To model a core-shell structure, we used the measured stoichiometry to determine the core radius and calculated the lowest electron and hole energies of a material with a ZnSe core, CdSe shell, and organic capping layer which has a high band offset (5 eV) for the electron and hole. The lowest transition energy is then determined by adding the electron and hole eigenvalues to the optimized band gap along with the Coulombic binding energy of the electron and hole as determined from perturbation theory<sup>[18]</sup>. The optimized electron effective masses were 0.3727 for CdSe and 0.345 for ZnSe. The optimized bandgaps were 1.9433 for CdSe and 2.9437 for ZnSe. It was found that the deviation between the calculated first transition energy versus experiment was on the order of  $\pm 2$  nm using these parameters.

It can be seen that the calculated first transition energy for a core-shell structure is a good match for the NC material after the initial (7 minute aliquot) exposure to the Cd

and Se precursors. After prolonged (>1 hour) exposure, an alloyed structure matches the experimental results while a core-shell material has a first absorption that is too low in energy. These results suggest that an alloy better represents the electronic structure of the core materials made here.

#### 4.4 Conclusions

$\text{Cd}_x\text{Zn}_{1-x}\text{Se}$  alloy core nanocrystals (NCs) were synthesized and characterized using absorption and emission spectrophotometry, transmission electron microscopy, and wavelength dispersive spectroscopy. Based on the experimental data and calculations, it was determined that the  $\text{Cd}_x\text{Zn}_{1-x}\text{Se}$  NCs are best described as alloyed particles. The  $\text{Cd}_x\text{Zn}_{1-x}\text{Se}$  NCs were overcoated with  $\text{Cd}_y\text{Zn}_{1-y}\text{S}$  to create high-quality, efficient  $(\text{Cd}_x\text{Zn}_{1-x}\text{Se})\text{Cd}_y\text{Zn}_{1-y}\text{S}$  core-shell NCs with the precise emission peak required for QD-LED display applications.

#### 4.5 References

1. S. A. Ivanov, J. Nanda, A. Piryatinski, M. Achermann, L. P. Balet, I. V. Bezel, P. O. Anikeeva, S. Tretiak, V. I. Klimov, *J. Phys. Chem. B* **2004**, *108*, 10625.
2. X. Zhong, R. Xie, Y. Zhang, T. Basche, W. Knoll, *Chem. Mater.* **2005**, *17*, 4038.
3. X. Zhong, M. Han, Z. Dong, T. J. White, W. Knoll, *J. Am. Chem. Soc.* **2003**, *125*, 8589.
4. R. E. Bailey, S. Nie, *J. Am. Chem. Soc.* **2003**, *125*, 7100.
5. X. Zhong, Y. Feng, W. Knoll, M. Han, *J. Am. Chem. Soc.* **2003**, *125*, 13559.
6. R. Xie, X. Zhong, T. Basche, *Adv. Mater.* **2005**, *17*, 2741.
7. J. J. Li, Y. A. Wang, W. Guo, J. C. Keay, T. D. Mishima, M. B. Johnson, X. Peng, *J. Am. Chem. Soc.* **2003**, *125*, 12567.
8. D. V. Talapin, R. Koeppel, S. Gotzinger, A. Kornowski, J. M. Lupton, A. L. Rogach, O. Benson, J. Feldmann, H. Weller, *Nano Lett.* **2003**, *3*, 1677.
9. P. Reiss, J. Bleuse, A. Pron, *Nano Lett.* **2002**, *2*, 781.
10. J. S. Steckel, J. P. Zimmer, S. Coe-Sullivan, N. E. Stott, V. Bulovic, M. G. Bawendi, *Angew. Chem. Int. Ed.* **2004**, *43*, 2154.

11. S. Coe-Sullivan, J. S. Steckel, W.-K. Woo, M. G. Bawendi, V. Bulovic, *Adv. Funct. Mater.* **2005**, *15*, 1117.
12. S. Coe-Sullivan, J. S. Steckel, L. A. Kim, M. G. Bawendi, V. Bulovic, *Proc. of SPIE* **2005**, *5739*, 108.
13. S. Coe-Sullivan, W.-K. Woo, J. S. Steckel, M. G. Bawendi, V. Bulović, *Org. Electron.* **2003**, *4*, 123.
14. S. Coe, W.-K. Woo, M. G. Bawendi, V. Bulović, *Nature* **2002**, *420*, 800.
15. M. A. Hines, P. Guyot-Sionnest, *J. Phys. Chem.* **1996**, *100*, 468.
16. B. O. Dabbousi, J. Rodriguez-Viejo, F. V. Mikulec, J. R. Heine, H. Mattoussi, R. Ober, K. F. Jensen, M. G. Bawendi, *J. Phys. Chem. B* **1997**, *101*, 9463.
17. B. O. Dabbousi, O. Onitsuka, M. G. Bawendi, M. F. Rubner, *Appl. Phys. Lett.* **1995**, *66*, 1316.
18. D. Dorfs, H. Henschel, J. Kolny, A. Eychmuller, *J. Phys. Chem. B* **2004**, *108*, 1578.
19. K. Chang, J.-B. Xia, *Phys. Rev. B* **1998**, *57*, 9780.
20. W. R. Frensley, H. Kroemer, *Phys. Rev. B* **1977**, *16*, 2642.
21. Landolt-Börnstein, New Series, Group III: Crystal and Solid State Physics, Volume 17, Subvolume b, Physics of II-VI and I-VII Compounds, Semimagnetic Semiconductors, Editor in Chief: K.-H. Hellwege, Editors: O. Madelung, M. Schule, and H. Weiss, Springer-Verlag Berlin-Heidelberg, New York, 1982.
22. C. B. Murray, D. J. Norris, M. G. Bawendi, *J. Am. Chem. Soc.* **1993**, *115*, 8706.
23. M. A. Hines, P. J. Guyot-Sionnest, *J. Phys. Chem. B* **1998**, *102*, 3655.



# Chapter 5

## Phase Separation and QD-LEDs Made Using Phase Separation

### 5.1 Introduction

We investigate a new method for forming large area ( $> \text{cm}^2$ ), ordered monolayers of colloidal semiconductor nanocrystals (NCs) or quantum dots (QDs). The NC thin films are formed in a single step by spin-casting a mixed solution of aromatic organic materials and aliphatic-capped NCs. The two different materials phase separate during solvent drying, and for a predefined set of conditions the NCs can assemble into hexagonally close packed crystalline domains. We demonstrate the robustness and flexibility of this phase separation process, as well as how the properties of the resulting films can be controlled in a precise and repeatable manner. Solution concentration, solvent ratio, QD size distribution and QD aspect ratio affect the morphology of the cast thin film structure. Controlling all of these factors allows the creation of colloidal crystal domains that are square microns in size, containing tens of thousands of individual NCs per grain. Such fabrication of large area, engineered layers of nanoscale materials brings the beneficial properties of inorganic NCs into the realm of nanotechnology. For example, this technique has already enabled significant improvements in the performance of QD light emitting devices (QD-LEDs)<sup>[1]</sup>.

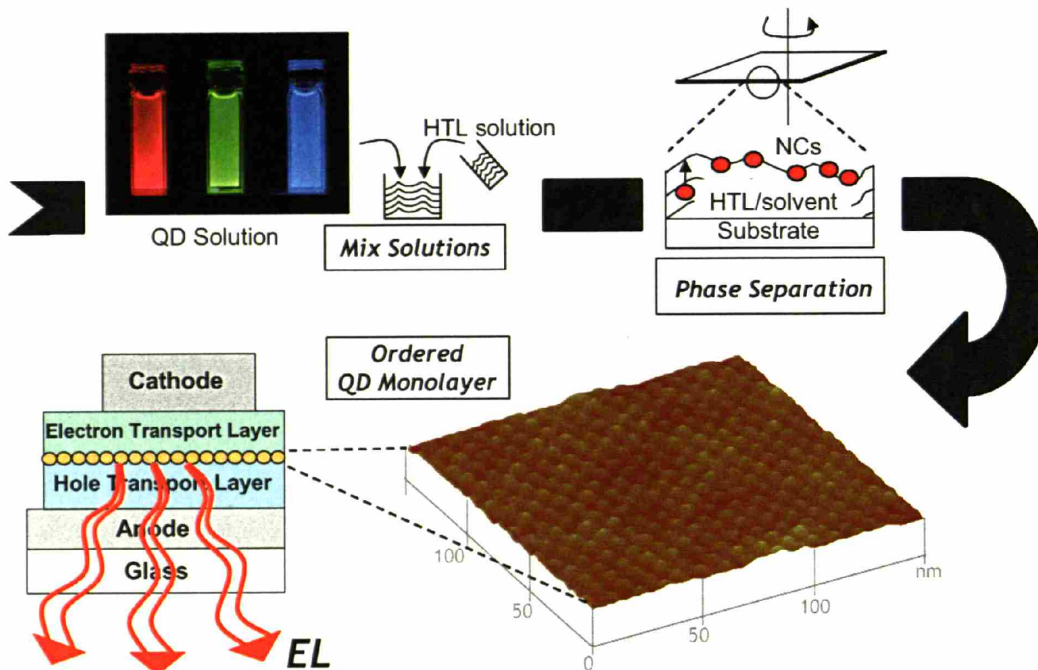
The colloidal synthesis of inorganic NCs<sup>[2-5]</sup> enables tuning of NC material properties with atomic level precision. Research on devices that harness these properties can be divided into two distinct classes: point-contact devices that utilize a countable



number of NCs, or large area devices that utilize great numbers of NCs. In both cases, controlling the placement of the NCs within the active device structure presents the greatest challenge to device fabrication. Many of the earlier studies dedicated to assembling 2D and 3D superlattices of NCs on solid substrates<sup>[6-10]</sup> present techniques that require long preparation times and precise control of surface interactions to achieve ordered assembly, making the incorporation of such techniques into a working device structure challenging.

The present work investigates the phase separation during spin-casting process, capable of arranging NCs over large areas ( $\text{cm}^2$ ) in two-dimensional sheets within layered structures. This process simultaneously yields NC monolayers self-assembled into hcp arrays and places this monolayer on top of a co-deposited contact. We describe the NC phase separation and self-assembly processes and how to controllably tune the resulting film properties. The technique has already been used in the structuring of efficient quantum dot light emitting devices (QD-LEDs)<sup>[1,11-13]</sup>, but as a general and flexible fabrication technique this method could enable fabrication of a wide variety of large area nanostructured heterostructures. NC monolayers arranged onto organic thin films are a unique platform for the study of basic physical properties of materials, for example allowing investigation of coarsening mechanisms on the individual adatom (in this case a single NC) level<sup>[14,15]</sup>.

The fabrication of a monolayer sheet of close-packed NCs by phase separation during spin-casting is in essence a very simple process, as depicted in Figure 5.1. The process relies upon the solvation of both the organically capped semiconductor NCs and the organic material to be used as an underlayer in a compatible solvent system. During



**Figure 5.1** Graphical description of the fabrication of organic/NC bilayers through phase separation during spin-casting: TPD (*N,N'*-diphenyl-*N,N'*-bis(3-methylphenyl)-(1,1'-biphenyl)-4,4'-diamine) exemplifies the organic material (hole transport layer (HTL)). The entire process can be completed on the time scale of seconds, differentiating it from other NC self-assembly techniques. This fabrication process enables the creation of efficient QD-LED structures<sup>[1]</sup>, depicted in the bottom left of the figure.

solvent drying, the NCs phase separate from the organic underlayer material, and rise towards the surface of the film. When drying is complete, the organic material is in the form of a homogenous thin film, which is coated by a layer of NCs. For typical solvent systems, the film is dry well before equilibrium is achieved, and thus the film formation is arrested in a non-equilibrium condition. The exact structure and composition of the layer is completely determined by the composition of the spin-casting solution (for a fixed set of processing conditions). Hence, the material purity of the NC sample is of critical importance to the phase separation process (see 5.2.7 Experimental Details). As an example, the fabrication can be continued resulting in a complete light emitting device.

While it is impossible for any thin film fabrication method to be universally applicable, we demonstrate that within the extent of this study the phase separation process is not critically dependant on any one component of the system. We observe phase separation and assembly of NC monolayer sheets for a number of substrates, solvents, organic underlayer materials, NC core materials, NC organic capping groups, NC diameters, NC size aspect ratios, spin-casting parameters, and environmental conditions. Table 1 lists the materials used to demonstrate the generality of this process. The only known constraints on the phase separation process are 1) that there is a solvent or solvent system which dissolves both NCs and organics in the needed concentrations, and 2) that the solvent and organic layer wet the substrate surface.

Organic hosts	TPD, NPD, poly-TPD, CBP, Alq <sub>3</sub> , polycarbonate
Solvents	Chloroform, chlorobenzene, toluene, benzene, pyridine
QD core materials	PbSe, CdSe, and (CdSe)ZnS, (CdS)ZnS, Au
QD capping molecules	Oleic acid, pyridine, TOPO, dodecane thiol
QD core diameter	3-10nm
QD size aspect ratio	1:1 (spherical), 5:2, 5:1 (nano-rod)
Substrates	Silicon, glass, ITO, parylene-C, 'Eponate 12' epoxy

**Table 5.1** Examples of materials compatible with the phase separation process: A list of materials that have been incorporated successfully into the phase separation process. This list is not meant to be exhaustive, but rather representative of the materials that are compatible. TPD = N,N'-diphenyl-N,N'-bis(3-methylphenyl)-(1,1'-biphenyl)-4,4'-diamine; NPD = 4,4-bis[N-(1-naphthyl)-N-phenylamino]biphenyl; poly-TPD = Poly(N,N'-bis(4-butylphenyl)-N,N'-bis(phenyl)benzidine; CBP = 4,4'-N,N'-dicarbazolyl-biphenyl; Alq<sub>3</sub> = tris-(8 hydroxyquinoline)aluminum; TOPO = Trioctylphosphine oxide; Eponate 12 = trade name of epoxy available from Ted Pella Inc; ITO = indium tin oxide.

## 5.2 Investigation of Phase Separation\*

### 5.2.1 Control of Organic Underlayer Film Thickness

Perhaps the simplest film property to control in this process is the underlayer organic film thickness. It is well known that the thickness of spin-cast organic thin films may be controlled by varying the solution concentration while fixing the spin parameters. For example, for a fixed set of spin conditions, the phase separation process remains unaffected when the TPD (N,N'-diphenyl-N,N'-bis(3-methylphenyl)-(1,1'-biphenyl)-4,4'-diamine, an archetypical organic) concentration in the solution is changed from 2 mg/ml (resulting in 12 nm underlayer film thickness) to 94 mg/mL (440 nm underlayer film thickness). Figure 5.2(f, inset) shows that the relationship between the TPD concentration in a chloroform solution and the resulting underlayer film thickness is linear. Atomic force microscopy (AFM) images of these surfaces reveal that phase separation is still present in all samples, and that the fraction of NC surface coverage is completely independent of underlayer film thickness. This separation of parameters facilitates optimization of device performance in fabricated structures.

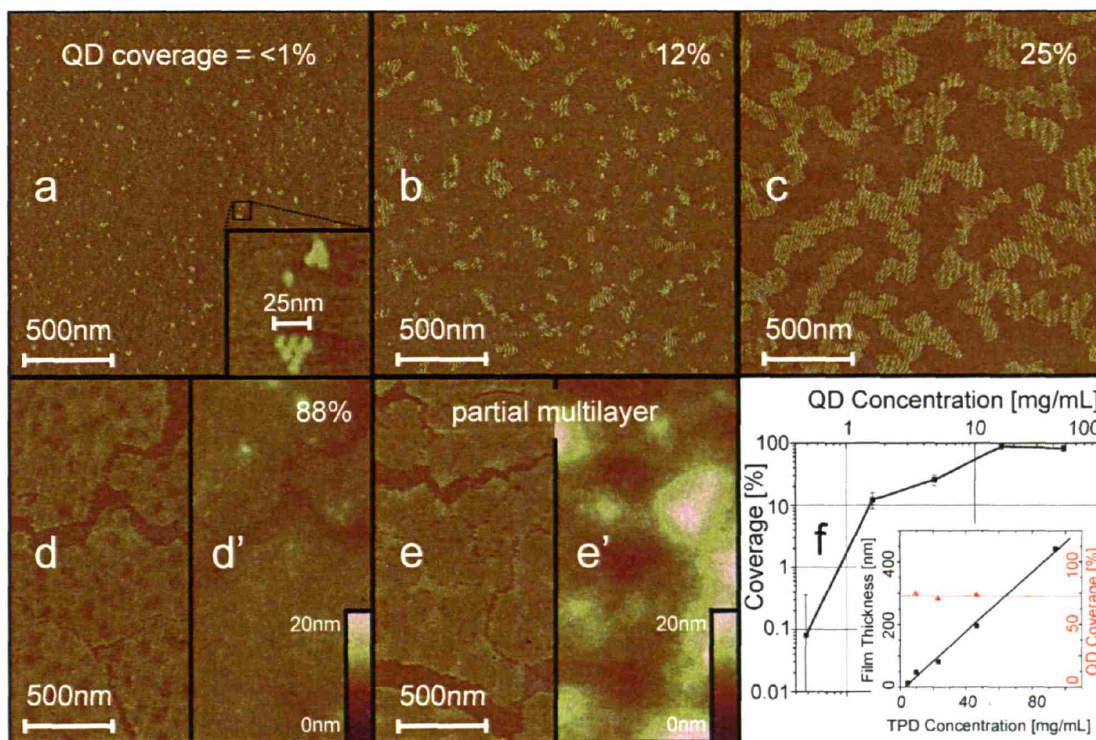
### 5.2.2 Control of Monolayer Surface Coverage

The concentration of NCs in the spin-casting solution may also be tuned, with predictable effects on the resulting bilayer. For very low NC concentrations, the bilayer film (see Figure 5.2(a)) contains a countable number of QDs distributed homogeneously on the organic surface. The NCs can be imaged individually, or in close-packed groupings of two or more crystals. As the solution NC concentration is increased, the number of NCs on the surface of the film increases (see Figures 5.2(b)-5.2(d)). Figure

---

\* Much of this section appeared in print (S. Coe-Sullivan *et al.*, *Adv. Funct. Mater.* **2005**, *15*, 1117)

5.2(f) plots the observed percent coverage versus NC concentration in the spin-casting solution.



**Figure 5.2** Effect of solution concentration on the phase separation process: Tapping mode AFM images of NCs assembled on an organic surface. As the concentration of NCs in the spin-casting solution is increased, the surface coverage of NCs is increased. The images show NC partial monolayers (a-d) with various coverages, and a partial multilayer that results from even higher NC solution concentrations (e). Figures (a-e) are phase images, while Figures (d', e') are the corresponding height images which demonstrate the increase in surface roughness for multilayer NC films. NC concentrations are Figure (a) 0.48 mg/mL, (b) 1.6 mg/mL, (c) 4.8 mg/mL, (d) 16mg/mL, and (e) 48 mg/mL. Figure (f) shows the dependence of NC monolayer surface coverage on concentration of NCs in the spin-casting solution. The inset plots the linear dependence of organic film thickness on the concentration of organic in the spin-casting solution (TPD in chloroform). The parameters that are varied in the two plots are completely independent, allowing organic layer thickness to be tuned independent of NC surface coverage fraction. The NCs in this figure are 6.5 nm diameter PbSe cores, prepared as described in chapter 2, section 2.2.4.

As the NC solution concentration is increased, a nearly complete coverage of NCs on the organic surface is observed. If the concentration of NCs in the spin-casting solution is further increased, the result is a breakdown of the flat, uniform morphology



shown in the other AFM images in this work. As more NCs than can fit try to pack, they are forced to break out of the plane of the monolayer and seek lower energy conformations. In some cases the NCs pile up into three dimensional stacks, leaving exposed regions of the organic underlayer. In other cases the first layer coverage remains high, but a buildup of regions of NC multilayers occurs (Figure 5.2(e)). Within this work we do not study such multilayer structures, but instead focus on the more controllable process of generating ordered monolayer and sub-monolayer coverage.

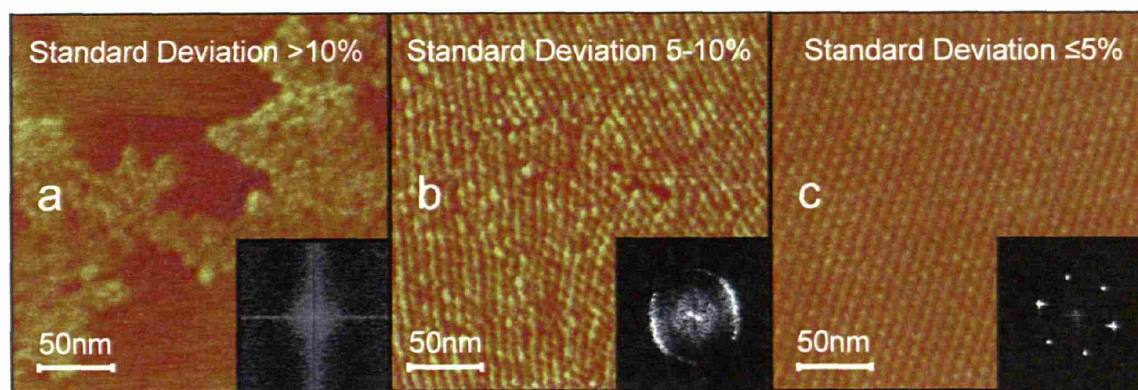
### 5.2.3 Control of Packing Order and Grain Sizes

The degree of hexagonal packing that is observed on a NC monolayer is directly related to the polydispersity of NC diameter. Figure 5.3 shows three partial NC monolayers, spin-cast from solutions formulated from three different NC samples. Figure 5.3(a) shows an example of a largely disordered film, made from a NC sample with size distribution standard deviation ( $\sigma_{SD}$ ) of  $>10\%$ . Although the film stack is determined by the phase separation process, the self-assembly into an hcp array of particles has been prevented by the size dispersion.

Figure 5.3(b) shows a bilayer formed from a NC sample with  $\sigma_{SD} = 5-10\%$ . While it is clear that the NCs have assembled into the hcp monolayer structure, the ordered domains, or grains, remain small, containing at most a few hundred NCs per grain. It is noted that this size distribution is narrow enough to form high coverage monolayers which are of high enough quality for the fabrication of monochromatic emitting QD-LEDs.

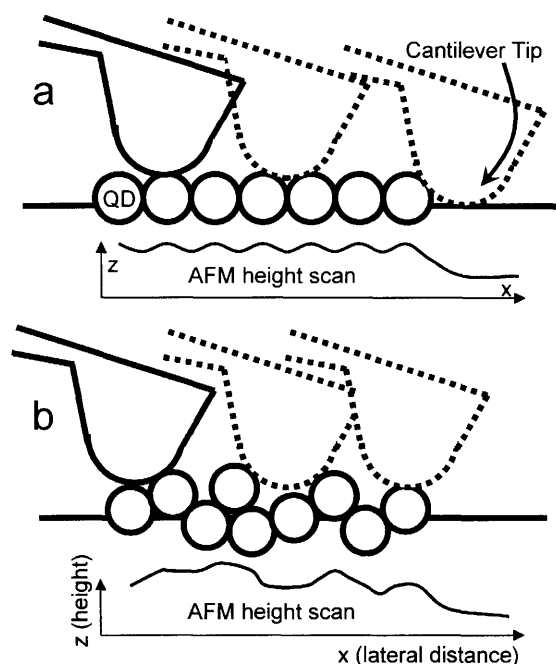
By careful control of NC synthetic techniques,  $\sigma_{SD} < 5\%$  is achievable (see Chapter 2, section 2.2.4). Figure 5.3(c) shows an AFM image of an hcp bilayer created

with such a sample, in this case 5.5 nm PbSe NCs with oleic acid caps on a TPD underlayer. The high degree of spatial periodicity of the sample enables clear imaging of individual NCs in the hcp colloidal crystal as depicted in Figure 5.4. The average grain size exceeds  $1 \mu\text{m}^2$ , with a high degree of two dimensional ordering over tens of thousands of repeat units.



**Figure 5.3** Effect of NC size distribution on the degree of packing order: AFM phase images demonstrating this effect. For broad size distributions (a, (CdSe)ZnS), the NCs assume random packing. As the size distribution is narrowed (b, red emitting bare CdSe, c, 5.5nm PbSe) the NCs clearly pack into hexagonal arrays. For monodisperse samples with  $\sigma_{SD} < 5\%$  (c), high degrees of order are achievable, with grain sizes larger than  $1 \mu\text{m}^2$ . The insets show the two dimensional spatial Fourier transforms of the images. For the perfect single grain (c), the Fourier transform reveals the expected six point pattern. These six points blur into a ring for the image containing a large number of grains (b), and shows no distinct features for the disordered film. Fourier analysis is an effective method of measuring the periodicity (NC center to center spacing) of the NC monolayers.

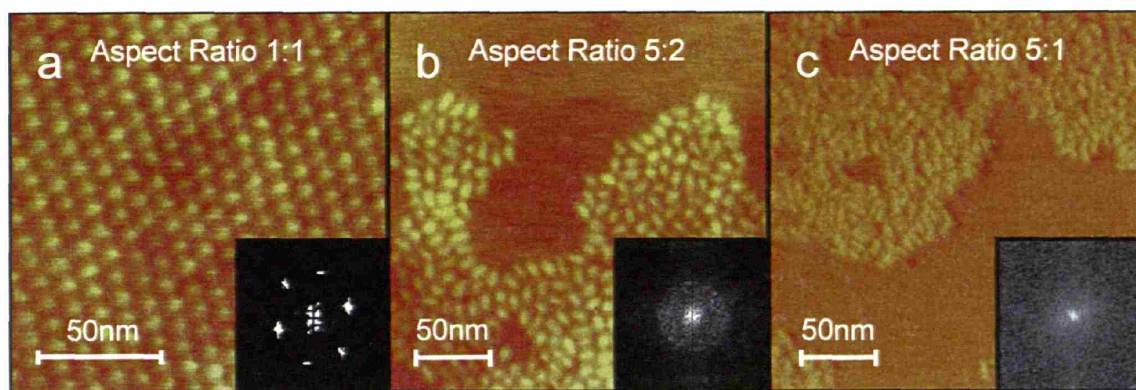
NC eccentricity, or size aspect ratio, also determines the degree of self-assembled order in these NCs monolayers<sup>[16]</sup>. Many of the II-VI colloidal semiconductors have a Wurtzite crystal structure, with a unique c-axis in the crystal unit cell. Recent work has exploited this asymmetry in the crystal structure to create growth anisotropy, yielding NCs with controllably tuned size eccentricity from  $R_A = 1.0$  (spherical) to several 100 (rod shaped NCs)<sup>[5]</sup>. Figure 5.5 demonstrates that the phase separation process is unaffected by changes in aspect ratio from  $R_A = 1$  to 5, but that the degree of ordering is



**Figure 5.4** Depiction of the effect of surface roughness on the resolution of Atomic Force Microscopy (AFM). The pervasive use of tapping mode AFM throughout this work as a primary method of analysis is chosen over other microscopy techniques due to its ease of use, resolution, and flexibility of substrate compatibility. In contrast, transmission electron microscopy (TEM) requires lengthy preparation techniques that would make the production of optimized devices prohibitive. Also, scanning electron microscopy (SEM) lacks the necessary resolution to easily image individual  $\sim 5$  nm particles. The AFM image resolution is in part determined by the probe tip radius, which was specified as  $<10$  nm for all the probes used for this work. The ability to resolve features that are smaller than this tip radius is due to the flatness of the samples (as in (a)). For exceptionally flat samples, imaging is done with the extreme tip of the probe, whereas the presence of any larger height variations (as when surface disorder is present) results in imaging with the entire tip diameter, setting the minimum resolvable feature size to  $\sim 20$  nm (as in (b)). Smooth surfaces allow for resolution below the size scale of the probe tip diameter.

reduced in samples made from more rod-like NCs. In these nanorod monolayers the minimum energy phase is likely liquid crystalline rather than the hcp structure we see for  $R_A = 1$  NCs.





**Figure 5.5** AFM images depicting the effect of NC aspect ratio on degree of ordering. For spheres with narrow size distributions the packing is highly ordered (a), while for samples with larger aspect ratios (b, c) packing is observed but ordering is nonexistent. This is due in part to the lack of size monodispersity on the length of the NCs, which is independent of the diameter monodispersity in these samples. The insets display the spatial Fourier transform of the images, highlighting the differences in order between the images. The NCs used in this study are (a) 7 nm PbSe NCs, (b) red emitting (CdSe)ZnS core-shell NCs (provided by Quantum Dot Corporation), and (c) CdSe nanorods.

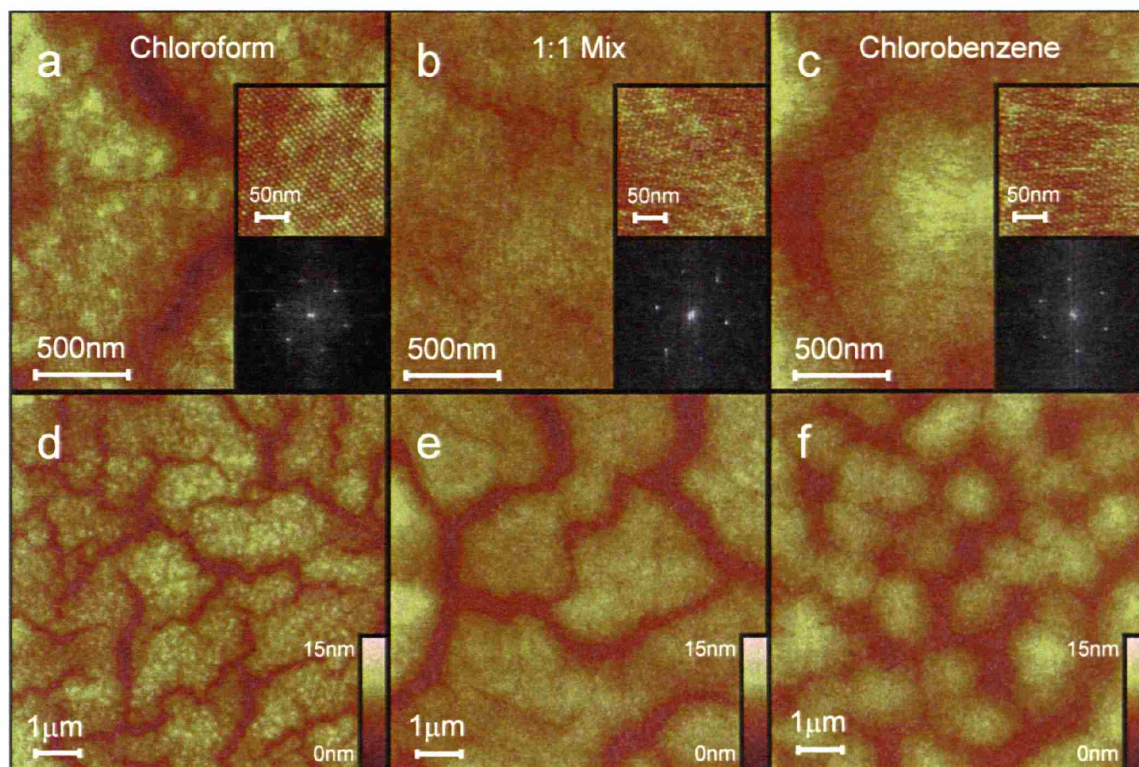
#### 5.2.4 Solvent

The crystallinity of the ordered domains is strongly affected by the solvent drying time during the spin-casting process. Solvent drying time is directly related to solvent vapor pressure, and as such a wide range of control is possible using only two miscible solvents. We chose to work with chloroform and chlorobenzene, as they have similar solubility properties (both solvate TPD and oleic acid capped NCs effectively), but very different vapor pressures (chloroform = 26.2 kPa, chlorobenzene = 1.6 kPa). Chloroform solutions dry in less than a second during the spin-coating process, while chlorobenzene solutions dry only after several seconds of spinning. A continuous range of solvent drying times could be achieved by mixing these two solvents in different ratios.

The equilibrium condition for monodisperse ( $\sigma_{SD} < 5\%$ ) NCs arranged into a two dimensional sheet is a single hcp grain. A trend towards equilibrium is demonstrated in

Figure 5.6, which depicts a series of spin-cast bilayer films that are made from the same QD sample and the same concentrations of both NCs and TPD. The solvent used is varied from 100% chloroform (fastest drying, Figures 5.6(a, d)) to 100% chlorobenzene (slowest drying, Figures 5.6(c, f)). The mean NC island size is maximized for the mixed solvent system. Small grain boundaries, however, are visible in the 8  $\mu\text{m}$  scan (Figure 5.6(e)) and are more clearly visible in the 2  $\mu\text{m}$  scan (Figure 5.6(b)) of the mixed solvent sample. Such grain boundaries, internal to an island, do not occur in the chlorobenzene sample, where almost every island is a single grain, in many cases larger than 1  $\mu\text{m}^2$ .

Cracking between the large area islands is likely due to the solvent drying process, as the optimal particle spacing for solvated NCs differs from the dry NC spacing<sup>[17]</sup>. In Figure 5.6(d) the cracks are of nearly fixed width, suggesting that adjacent islands were once joined together. While solvent is still surrounding the NCs during the spin-casting process, they pack into hcp arrays with some natural period corresponding to the spacing of solvent rich NCs. At this stage, the surface coverage is probably very close to 100%, and the NCs have some freedom to minimize their surface free energy. As the solvent continually evaporates, the NC spacing decreases, and the NCs in a given grain pack closer together. At some point the continuous NC layer must break to allow for the strain that results from this higher packing density. The breaking is most likely to occur at a grain boundary, as the van der Waals interactions that are holding the NCs to their neighbors are weakest at this point of the film. The result is the large scale cracking morphology that we observe in Figure 5.6(d), with the perimeters of adjacent islands tracking each other almost perfectly.



**Figure 5.6** Effect of solvent on grain size and structure: AFM height images of NC monolayers on TPD spun from identical concentration solutions of different solvents. (a) and (d) are images of the same film at different scan sizes, as are (b) and (e), and (c) and (f). In (f) each island is a single grain of colloidal crystal (sizes exceeding  $1 \mu\text{m}^2$ ), while in (d) and (e) the islands are composed of multiple grains separated by narrow grain boundaries that are observable in images (a) and (b). The insets in (a-c) are close up views of the individual NCs that make up the hcp grains, as well as spatial Fourier transform images showing the hexagonal periodicity of the NC self-assembled monolayers. The NCs in this figure are 6.5 nm diameter PbSe cores, prepared as described in Chapter 2, section 2.2.4.

For quickly drying solvents, the cracks seem to be more numerous, but smaller in width, while for slowly drying solvents the cracks are less frequent, but larger. In all cases, the total area of void is approximately constant (22%, 20%, and 27% respectively for chloroform, mixed, and chlorobenzene solutions). This implies that the QDs are packing into their equilibrium, dry packing distance in all situations, an effect confirmed by directly measuring the QD spacing on the AFM images (periods of 8.3 nm, 8.1 nm, and 8.3 nm were observed, respectively for chloroform, mixed, and chlorobenzene solutions). The tendency for slower drying solvents to yield larger cracks could be due to

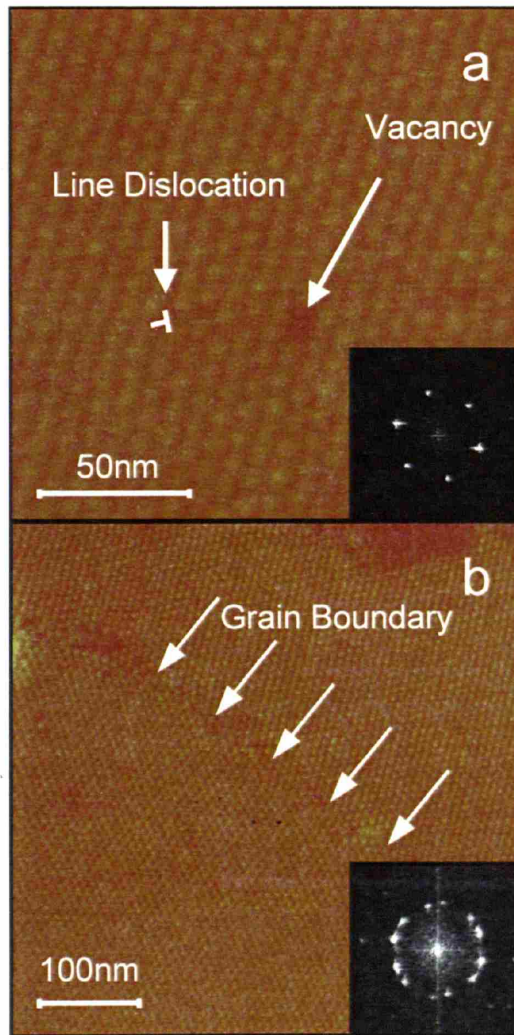


several factors. First, there are fewer grain boundaries available in this system, because of the larger mean grain size, and thus fewer sites where a crack could originate. The shrinking process is also occurring much slower in these films, allowing more time for the strain induced by shrinking to propagate to an existing crack, rather than nucleate a new one. Alternatively, the cracking could occur at many sites very early in the drying process, with the slower drying times allowing more time for the cracks to heal, and for islands to coalesce.

### **5.2.5 Observation of Two Dimensional Crystal Defects**

The creation of large area two dimensional super-lattices of NCs allows the direct observation of colloidal crystal defects. There are of course fundamental differences between this colloidal crystal system and a single crystalline semiconductor, or a molecular crystal. The size scale is larger, and therefore single elements of the crystal are more easily observed. In addition, we can tune this critical size by growing larger particles. Another major difference is that all of the units are not identical, with slightly different sizes, aspect ratios, and surface chemistry all affecting the process of crystallization. Finally, the energies involved are vastly different, with only van der Waals interactions playing a role. Crystal formation in the plane of a substrate in van der Waal bonded solids is not completely understood, indicating a potential benefit in using this system to study the kinetics of crystallization.

Figure 5.7 highlights crystal defects found in a NC self-assembled grain on an organic underlayer. Vacancies are manifested as dark spots in the AFM image of the hcp array (Figure 5.7(a)). Interstitial defects are imaged as a rare high spot in the AFM height scan, roughly one NC diameter higher than the remainder of the periodic pattern. Line



**Figure 5.7** Crystal defects in two-dimensional NC colloidal crystals: AFM images of (a) a single NC grain, with crystal defect points clearly visible and (b) the grain boundary between two large area colloidal crystal grains, allowing the study of the individual NCs that make up the grain edges. Insets are the spatial Fourier transforms of the two images, in (a) showing the three-fold symmetry (six points) of the hexagonal periodic array, and in (b) showing the six points of each of the two grains, resulting in 12 clearly distinguishable points on the same diameter circle. The NCs in this figure are 5.5 nm diameter PbSe cores, synthesized as described in Chapter 2, section 2.2.4.

defects, where two rows of NCs merge and become one row, are frequently observed (Figure 5.7(a)). Finally, the fine structure of the grain boundary itself is observable (Figure 5.7(b)). It is simultaneously possible to measure the grain angle deviation of two grains joining, and to identify the location of each NC that makes up the boundary.

### 5.2.6 Role of Organic Underlayer

Drying-mediated phase separation and self-assembly processes have recently received much attention in the literature,<sup>[7,18,19]</sup> though a detailed mechanism for the specific cases presented in this study are as yet unproven. During spin-casting, the organic/NC solution transitions from a homogeneous liquid mixture to a phase separated solid. It is unclear at exactly what point in time the separation occurs, a) early in the solvent drying, when the solute mass percent remains low or b) late in the process, when the solvent mass percent is low. The phase separation is driven by the minimization of interface surface energies. The organic small molecules are preferentially deposited on the substrate surface due to both their higher polarizability relative to NCs, and the higher contact area with a flat surface which they can achieve. The size of the NC units reduces both of these quantities relative to the small molecules.

Experiments in which the organic has been eliminated from the spin-casting solution demonstrate that one of the roles of the organic component is a simple surface modification; Neat NC solutions spun onto aromatic organic surfaces form monolayer films with hcp structure, while NC solutions spun onto silicon oxide form low coverage multilayers or sub-monolayers<sup>[20]</sup>. Another important effect of the organic is to slow down the evaporation of the solvent, allowing more time for the NCs to reach equilibrium on the surface. It is the combination of these two effects of the organic material that enable the monolayer formation and self-assembly to occur during the solvent drying time. Once phase separation has occurred, the NCs are mobile on the organic underlayer surface,<sup>[14,21]</sup> and self-assemble into hcp arrays as they seek their equilibrium

conformation, coarsening via a combination of Ostwald ripening<sup>[22,23]</sup> and cluster diffusion,<sup>[24]</sup> depending on the stage of coarsening and the initial NC concentration.

### 5.2.7 Experimental Details

A known quantity of the organic material is weighed out dry, solvated in the chosen solvent, and stirred until completely dissolved (typically 15-30 minutes). Some quantity of NC solution is then added, to yield both the desired organic to NC ratio, as well as overall concentration of solution. For example, in the bilayers used in Figure 5.4(a), the final solution contained 10mg/mL of N,N'-diphenyl-N,N'-bis(3-methylphenyl)-(1,1'-biphenyl)-4,4'-diamine (TPD), and 9mg/mL of NC sample solid dissolved in chloroform. For simplicity and reproducibility all of the NCs are handled as stock solutions. The final concentration of particles in the spin-casting solution is determined by accurately measuring out a volume of this NC stock into the already prepared solution of organic small molecules. This mixture is then spin-cast onto a substrate. The entire substrate surface must be wetted by the solution before spin casting begins. The separation process is observed for a wide range of spin-casting parameters such as speed, acceleration, spinning time, and atmosphere (gas, temperature, solvent content). For the best control and consistent reproducibility of bilayers, we use a single spin speed (3000 rpm), a maximum starting acceleration (10,000 rpm/s), and a long spinning time (60s) to insure complete evaporation of all solvent. Film properties can then be tuned by changing the solution composition.

The NC growth solution is purified by solvent precipitation twice before spin casting. A typical procedure is to a) crash the NCs out of growth solution using an incompatible solvent b) centrifuge c) pour off supernatant d) rinse with incompatible

solvent e) redisperse in compatible solvent f) crash out with incompatible solvent g) centrifuge h) decant supernatant i) rinse with incompatible solvent j) decant k) redissolve in compatible solvent l) filter m) pull vacuum on solution until completely dry n) redisperse in spin casting solvent to make stock solution.

The atomic force micrographs were taken using a Veeco Metrology Dimension 3000 stage with a Nanoscope 3A controller.

## 5.3 Near Infrared Emitting QD-LEDs\*

### 5.3.1 Introduction and Motivation

Large area ( $\text{mm}^2$  in size) infrared electroluminescent devices were made using colloiddally grown PbSe nanocrystals (NCs) or quantum dots (QDs) in organic host materials. By changing the NC size the electroluminescence was tuned from  $\lambda = 1.33$  to  $1.56 \mu\text{m}$  with a full width at half maximum of  $<160 \text{ nm}$  ( $<0.11 \text{ eV}$ ). This represents only a portion of the accessible NC tuning range, as the lowest energy optical absorption peak of our PbSe solutions can be tuned from  $1.1 \text{ eV}$  (corresponding to wavelength  $\lambda = 1.1 \mu\text{m}$  and  $2.6 \text{ nm}$  diameter NCs) to  $0.56 \text{ eV}$  ( $\lambda = 2.2 \mu\text{m}$ ,  $9.5 \text{ nm}$  diameter) (see Chapter 2, section 2.2.2). Our light emitting device fabrication combines the thin film processing techniques available to organic materials with the tunable optical properties of PbSe NCs. Formation of double heterojunction devices is enabled by material phase separation during the spin-coating step. Such large area emitters in the near infrared have been identified as technologically useful for chemical spectroscopy and sensing, night vision applications, and could be incorporated into on-chip optoelectronic integrated circuits.

---

\* Much of this section appeared in print (J. S. Steckel *et al*, *Adv. Mater.* **2003**, *15*, 1862)



Established technologies such as inorganic LEDs, lasers, photodetectors, and modulators have been developed and optimized in the near infrared (NIR) to address the needs of optical communications, chemical spectroscopy, and chemical sensing. These devices have high performance and long lifetimes, but the associated fabrication and material costs are high and therefore prohibitive for cost-constrained applications that require large area devices. New device paradigms that use less expensive fabrication processes and materials would enable the more widespread use of active NIR optoelectronic devices. Molecular and polymeric organics are among the materials that, in principle, meet these criteria, but as yet they are not readily available with efficient tunable emission beyond the wavelength of  $\lambda = 1\mu\text{m}$ , even when inorganic complexes are used as the emitter in doped organic structures<sup>[25,26]</sup>. In this work we generate NIR electroluminescence (EL) by using inorganic PbSe nanocrystals in solution processible organic structures. Although our efficiencies are low, the demonstrated QD-LEDs are controllably tuned across the NIR spectrum and have the potential to be further improved based on the high solution photoluminescence (PL) efficiencies of the starting materials and previous studies<sup>[1,11]</sup> of efficient CdSe QD-LEDs (see Chapter 1).

### 5.3.2 Device Fabrication

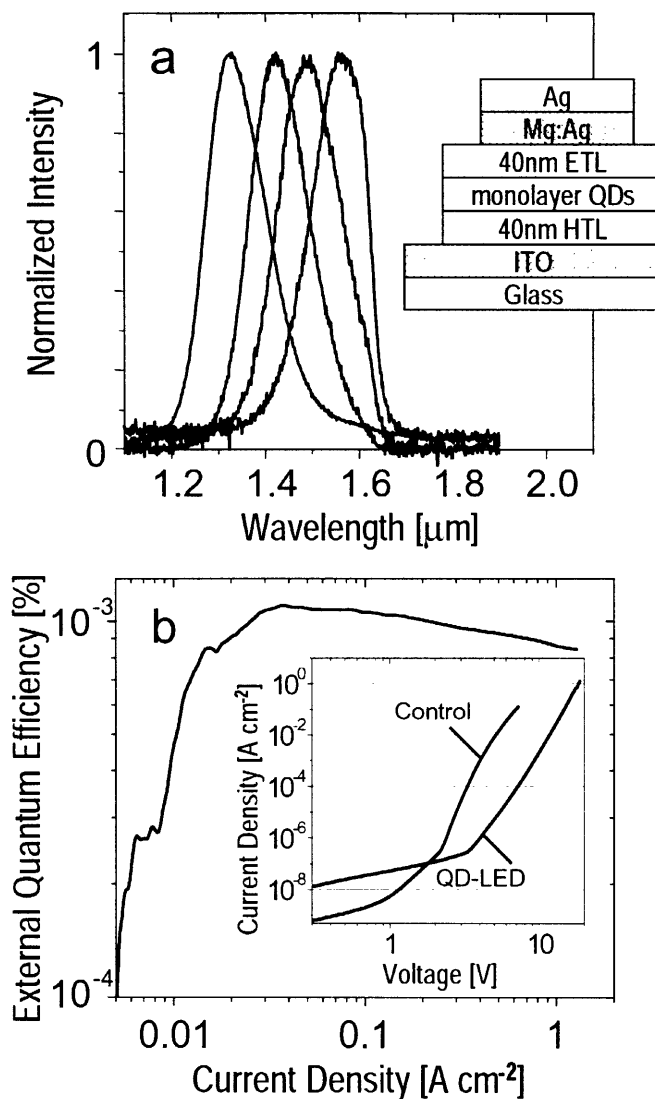
Device fabrication uses NCs processed air-free and dispersed in anhydrous chloroform in a nitrogen environment (<10 ppm O<sub>2</sub> and H<sub>2</sub>O). The NC solution is added to a chloroform solution of a hole transporting organic semiconductor, N,N'-diphenyl-N,N'-bis(3-methylphenyl)-(1,1'-biphenyl)-4,4'-diamine (TPD) or 4,4-bis[N-(1-naphthyl)-N-phenylamino]biphenyl ( $\alpha$ -NPD), and is spin cast onto a clean ITO coated glass substrate. The NCs phase separate into a monolayer (or sub-monolayer) on the

surface of the organic film as described in detail in section 5.2 of this chapter. The substrate is then transported into a thermal evaporator without exposure to air where the electron transporting layers (ETL), tris-(8 hydroxyquinoline)aluminum ( $\text{Alq}_3$ ) and/or bathocuproine (BCP), are deposited at  $<5 \times 10^{-6}$  torr. Finally the metal cathode (50 nm thick Mg:Ag, 50:1 by weight, 50 nm Ag cap) is thermally evaporated through a shadow mask to define 1 mm diameter devices. The assembled device structure is shown in the inset of Figure 5.8(a). High device yields and consistent LED performance are standard for devices fabricated in this manner.

Deposition of the hole transport layer (HTL) and the NC monolayer relies on phase separation during spin casting. The narrow size distribution of the PbSe NCs yields hexagonally packed layers with domain sizes on the order of  $10,000 \text{ nm}^2$  ( $\sim 300$  NCs per domain). From an atomic force microscopy (AFM) image, identical to those shown in Figure 5.6(a) and 5.6(d), we measured an average NC center-to-center distance of  $6.5 \pm 0.5 \text{ nm}$ . For this NC sample, which has a lowest energy peak absorption at  $\lambda = 1.4 \text{ }\mu\text{m}$ , TEM measurements of drop cast films showed a core diameter of  $4.7 \pm 0.4 \text{ nm}$ . Since the calculated length of fully extended oleic acid is  $1.8 \text{ nm}$ , the  $1.8 \pm 0.6 \text{ nm}$  spacing between NCs (edge to edge) is consistent with the interpenetration of oleic acid capping molecules on neighboring NCs.

### 5.3.3 Device Characterization

The NIR EL spectrum of QD-LEDs closely resembles the PL spectrum of the corresponding NC solution as expected. The tunability of QD-LED emission as a function of the NC diameter is shown in Figure 5.8(a), with EL spectral peaks at  $\lambda = 1.33 \text{ }\mu\text{m}$ ,  $1.42 \text{ }\mu\text{m}$ ,  $1.50 \text{ }\mu\text{m}$ , and  $1.56 \text{ }\mu\text{m}$ . The spectral FWHM of all four devices is  $<160 \text{ nm}$



**Figure 5.8** (a) Normalized electroluminescence spectra of a series of QD-LEDs tuned through the near infrared (emission peaks at  $\lambda = 1.33 \mu\text{m}$ ,  $1.42 \mu\text{m}$ ,  $1.50 \mu\text{m}$ , and  $1.56 \mu\text{m}$ ). The spectrum of the device emitting at  $1.56 \mu\text{m}$  is asymmetric due to the quantum efficiency of the cooled InGaAs detector dropping from 90% to below 10% for  $1.58 \mu\text{m} < \lambda < 1.62 \mu\text{m}$ . The inset shows the general QD-LED device structure; (b) External quantum efficiency and current-voltage plots for a PbSe QD-LED. The peak external quantum efficiency of 0.001% is obtained at  $37 \text{ mA/cm}^2$  and 13.3 V. The current-voltage characteristics are compared to a control device which is identical in structure except that the NC monolayer is omitted. This comparison exemplifies the increase in operating voltage that is typical of QD-LEDs.

(<0.11 eV). The devices also have an emission peak at  $\lambda = 530 \text{ nm}$  (not shown) due to exciton recombination within the  $\text{Alq}_3$  ETL (or  $\lambda = 405 \text{ nm}$  corresponding to TPD EL

when BCP is used as the ETL). We note that the InGaAs photodiode array used to record all of these spectra has low detection efficiency for  $\lambda > 1.6 \mu\text{m}$ , modifying the apparent shape of the  $\lambda = 1.56 \mu\text{m}$  emission peak.

The electrical characteristics of all the QD-LEDs of this study are similar, with a typical performance shown in Figure 5.8(b). The current density (J) versus voltage (V) plot shows a linear dependence for  $V < 3 \text{ V}$ , and power law dependence,  $J \propto V^9$ , when light is emitted. This is consistent with the properties of an Alq<sub>3</sub>/TPD device, though the operating voltage is higher, possibly due to NC charge trapping, realignment of interface dipoles, or charge screening by NCs. The PbSe QD-LED NIR external quantum efficiency ( $\eta_{\text{EL}}$ ) is measured to be 0.001 %, using a Silicon wafer to filter out visible emission from organic EL. The visible emission originates from Alq<sub>3</sub> and TPD (when BCP is used as the ETL) and has an external EL quantum efficiency of 0.1-0.3 %. These QD-LEDs demonstrate the feasibility of generating controllably tunable  $\lambda > 1.3 \mu\text{m}$  EL in a large area device, and provide a starting point in the creation of higher efficiency devices. Based on the absorption spectra shown in Figure 2.4 (in Chapter 2), we conclude that this device platform could be used to generate devices emitting in the spectral range of  $1.2 \mu\text{m} < \lambda < 2.2 \mu\text{m}$  (measurement of our EL spectra are limited to  $\lambda < 1.6 \mu\text{m}$  due to the detector cut-off).

PbSe QD-LEDs were also fabricated directly on a Si substrate instead of glass. This eliminated the need to use a Silicon wafer to filter out the visible emission from the organic EL as the substrate itself became the filter. Later studies using PbSe NCs with tighter size distributions (see Chapter 2, section 2.2.4) gave NIR emitting QD-LEDs with a 2-3 fold increase in external quantum efficiency and no visible light emission was seen

with our eyes from the organic EL. It is also worth mentioning that NIR emitting QD-LEDs made from NCs spun out of neat chloroform showed lower external quantum efficiencies (50 % less) compared to devices made by spinning the NC films out of chloroform doped with 20 % chlorobenzene. This is most likely due to the chlorobenzene, which has a lower vapor pressure than chloroform, providing more time during NC monolayer formation for the NCs to order into larger close packed grains (see section 5.2.4).

The low  $\eta_{EL}$  of our devices is the result of the lowered quantum efficiency of films of close packed NCs and a device design that is optimized for visible emission. While PbSe NCs have been shown to be very efficient NIR emitters in solution, the  $\eta_{PL}$  drops to 0.5 to 1.5 % in thin film form. This is due to a reduction in the number of available capping molecules to the NCs in thin film form, as well as exciton energy transfer within the NC film, both of which have been shown to reduce  $\eta_{PL}$  in semiconductor NC solids. Extrapolating from other NC material systems, it is reasonable to assume that the development of a core-shell PbSe NC would result in higher solid state  $\eta_{PL}$ . Our active layer thickness and choice of organic semiconductors was originally designed for visible emitting organic LEDs. For the long wavelength devices described in this paper, the optical mode overlap with the emissive NC layer is poor. Designs using a transparent highly conductive cathode would allow optimization of the distance between the metal and the emissive NC monolayer without incurring an increase in the operating voltage<sup>[27,28]</sup>. We further note that the choice of ITO as the anode in our devices is not ideal, since the transparency of the 150 nm film is only 70% at  $\lambda = 1.5 \mu\text{m}$ .

Previous work has suggested that Förster energy transfer and direct charge injection are both potential mechanisms for NC excitation within QD-LEDs.<sup>[11]</sup> We find that radiative excitation of the NCs by green Alq<sub>3</sub> EL (spectral peak at  $\lambda = 530$  nm) is a negligible source of NC NIR emission based on the following experiment: A  $\lambda = 532$  nm laser was used to excite a 1 mm spot on the device substrate, and its infrared emission monitored using a Germanium detector with a 500  $\mu\text{m}$  thick Silicon wafer filter. The laser power was adjusted using neutral density filters to match the green optical power emitted by our device at its maximum brightness operating point, 10  $\mu\text{W}$ . No optical signal was detected, allowing us to conclude that the Si filter effectively eliminates all trace of the Alq<sub>3</sub> emission from our EL device, and that the radiative excitation of the NCs from this Alq<sub>3</sub> emission is not sufficient to account for the measured NIR signal.

Exciton energy transfer should be possible for excitons created in the organic layer close to NCs despite the large capping group length ( $\sim 1.8$  nm). In contrast, photoconductivity experiments indicate that the 1.8 nm tunnel barrier is sufficient to reduce direct injection of charge carriers from the semiconducting organics into the NC core by several orders of magnitude relative to a NC capped with a shorter chain capping molecule<sup>[29]</sup>. For both mechanisms, however, shorter chain capping groups would serve to increase the likelihood of NC excitation. If we assume a Förster energy transfer process, the energy of the transferred exciton from Alq<sub>3</sub> molecules to NCs would initially be 2.4 eV (corresponding to the excited state of Alq<sub>3</sub>). The generated NC exciton would then lose  $\sim 1.6$  eV before occupying the lowest energy state from which NC emission originates. Since PbSe NC  $\eta_{\text{PL}}$  is constant over a wide range of excitation wavelengths,

PbSe QD-LEDs with higher power efficiency could be realized if organic transport materials with smaller optical gaps were utilized.

To accurately measure the efficiency and the EL spectrum of these QD-LEDs it is necessary to maximize the detected NIR emission and attenuate the emission signal of both organic and blackbody radiation by using appropriate spectral filters, detectors, and detection geometry<sup>[30]</sup>. In our quantum efficiency measurements, the NIR signal (1-50 nW) is maximized by using a minimum distance between the emitter and a large area detector (3 mm distance, 3 mm diameter Newport 818-IR-C/M Germanium detector). The spectral measurements were performed using an InGaAs photodiode array cooled to 173 K (Roper Scientific OMA V) and monochromator with a fiber bundle input. The fiber bundle was coupled to the device substrate to maximize the input signal. For both efficiency and spectral measurements, the visible emission is filtered out using a double sided polished, 500  $\mu\text{m}$  thick, Silicon wafer. The three lowest order diffraction peaks of  $\text{Alq}_3$  (at  $\lambda = 530 \text{ nm}$ ,  $1060 \text{ nm}$ , and  $1590 \text{ nm}$ ) that are otherwise detected by the spectrograph are completely eliminated when the Si filter is in place.

Finally, the possible detection of blackbody radiation must be accounted for. Our 1 mm diameter devices were run at currents as high as 10 mA and 20 V operating voltages, corresponding to 200 mW of peak input electrical power. The power efficiency of these devices is no better than 0.1 %, implying that 99.9 % of the input power is converted to heat<sup>[31]</sup>. While a large portion of this heat will be lost to the surrounding air by conduction and convection processes, there is no doubt that some device and substrate heating to above room temperature does occur. Blackbody radiation at 300 K to 350 K has the bulk of its emission in the  $\lambda = 17 \mu\text{m}$  range, but a measurable quantity of emission

is in the  $\lambda = 1.1 \mu\text{m}$  to  $1.7 \mu\text{m}$  detection window of Ge and InGaAs detectors. Our actual detected power in this spectral window was in all cases greater than 1 nW. A temperature rise of  $70^\circ\text{C}$  over the  $150 \text{ mm}^2$  area of our substrates would be required to generate 1 nW of power in the spectral detection window. Our device could not support such a rise as the glass transition temperature of TPD is  $65^\circ\text{C}$ <sup>[32]</sup>. Furthermore, substrate inspection indicates that QD-LEDs are not warm to the touch during operation. A temperature rise of less than  $10^\circ\text{C}$  corresponds to  $< 20 \text{ pW}$  of detectable radiated power, and thus a  $< 2\%$  error in measurement of QD-LED NIR  $\eta_{\text{EL}}$ . This analysis shows that the detected power is therefore not a result of either blackbody radiation or visible organic EL, and is in fact due to the band edge emission from the PbSe NCs.

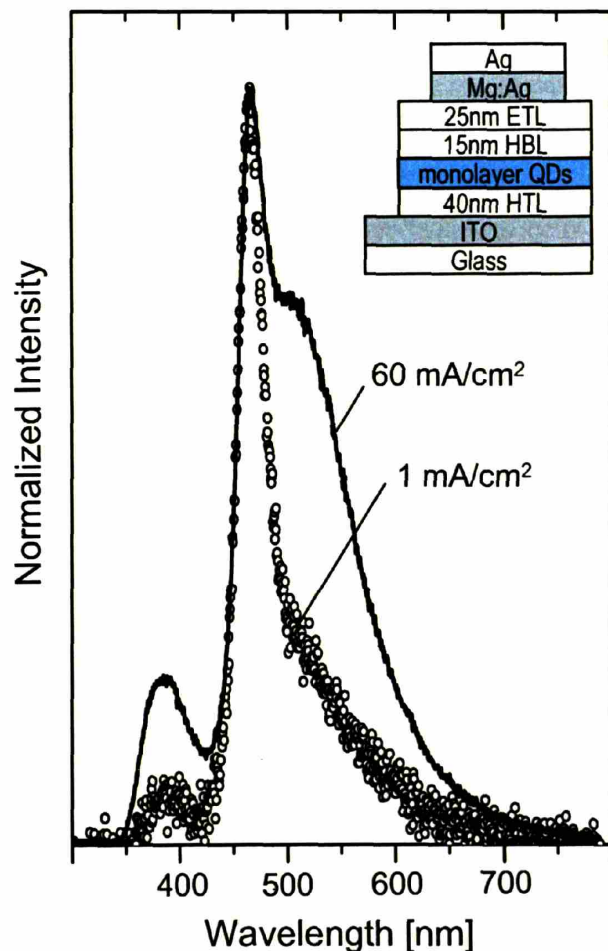
#### 5.4 Blue Emitting QD-LEDs\*

(CdS)ZnS core-shell NCs were isolated from growth solution by precipitating them out of solution twice with a miscible non-solvent (butanol and methanol), redispersing in chloroform, and filtered through a  $0.2 \mu\text{m}$  syringe filter before use in device fabrication. QD-LED fabrication consisted of first dissolving 5 mg of 4,4'-N,N'-dicarbazolyl-biphenyl (CBP) (hole transport layer (HTL)) in  $400 \mu\text{L}$  of chloroform and then adding  $100 \mu\text{L}$  of the (CdS)ZnS NC solution. Under air-free conditions this mixture was then spin cast (3000 rpm for 60 seconds) onto an indium tin oxide (ITO) coated glass substrate to create the 40 nm thick HTL with a densely packed monolayer of NCs on top of it via phase separation. The substrate was then transported into the thermal evaporator without exposure to air, where the hole blocking layer (HBL), 3-(4-biphenyllyl)-4-

---

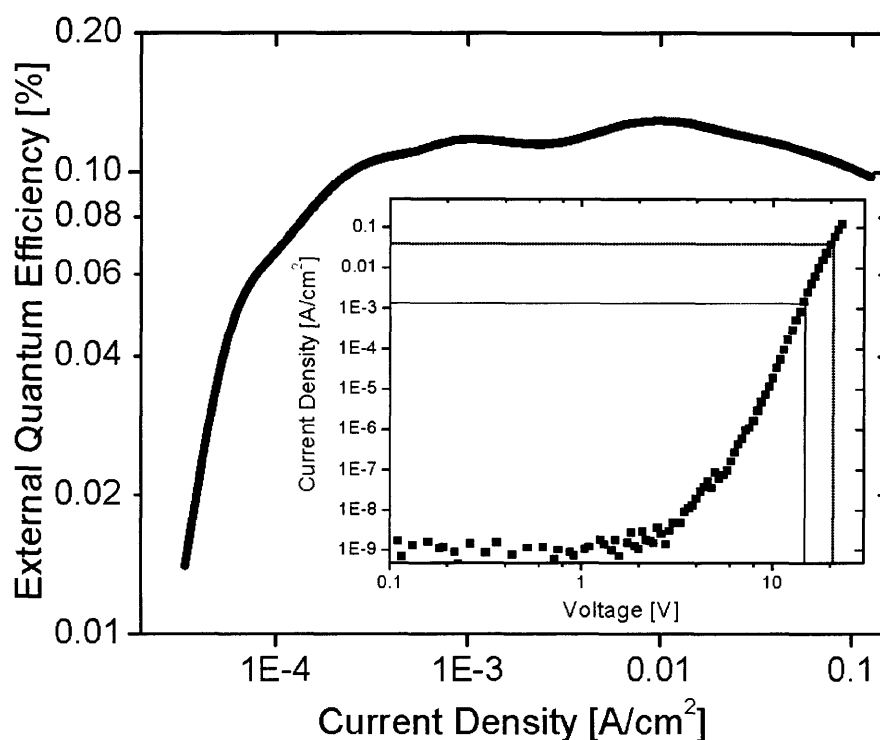
\* Much of this section has appeared in print (J. S. Steckel *et al*, *Angew. Chem. Ed. Int.* **2004**, *43*, 2154)





**Figure 5.9** The EL spectra, at two different current densities, of (CdS)ZnS core-shell nanocrystals embedded in a QD-LED. The layered device structure consists of ITO / CBP / (CdS)ZnS NC monolayer / TAZ / Alq<sub>3</sub> / Mg:Ag / Ag and exhibits an external quantum efficiency of 0.1 %. The inset shows a cross-section of the device.

phenyl-5-t-butylphenyl-1,2,4-triazole (TAZ) (15 nm thick), and then the electron transporting layer (ETL), tris-(8 hydroxyquinoline)aluminum (Alq<sub>3</sub>) (25 nm thick), were deposited. Finally the metal cathode (50 nm thick Mg:Ag, 50:1 by weight, 50 nm Ag cap) was thermally evaporated through a shadow mask to define 1mm diameter devices (see the inset in Figure 5.9 for a diagram of the assembled device structure).



**Figure 5.10** External quantum efficiency versus current density plot for the device: ITO / CBP / (CdS)ZnS QD monolayer / TAZ / Alq<sub>3</sub> / Mg:Ag / Ag. The inset shows the I-V curve with two dotted lines indicating the two different current densities (1mA/cm<sup>2</sup> at 14V and 60mA/cm<sup>2</sup> at 21V) to which the EL spectra in the inset of figure 5.9 correspond.

Figure 5.9 shows two electroluminescence (EL) spectra of a working (CdS)ZnS core-shell NC QD-LED. At low currents (circles, 1 mA/cm<sup>2</sup> at 14 V) the FWHM of the QD-LED spectral peak is 30 nm centered at 468 nm, while at higher currents (solid line, 60 mA/cm<sup>2</sup> at 21 V) the EL from organic layers begins to dominate (seen as the shoulders in the UV and the green regions of the spectrum). Organic and NC luminescence occur simultaneously in the working device and as more current is applied, the ratio of NC to organic emission changes. At high currents, excitons are created deeper in the organic transport layers, which causes the width of the exciton generation region to exceed the organic-NC Förster energy transfer radius, resulting in an increased contribution of organic luminescence to the EL spectrum<sup>[11]</sup> (see Chapter 1). These preliminary results

demonstrated the potential of (CdS)ZnS core-shell nanocrystals as blue emitters for display applications, but further optimization of the device and the materials was required, as can be seen in Chapter 6, to obtain saturated blue EL.

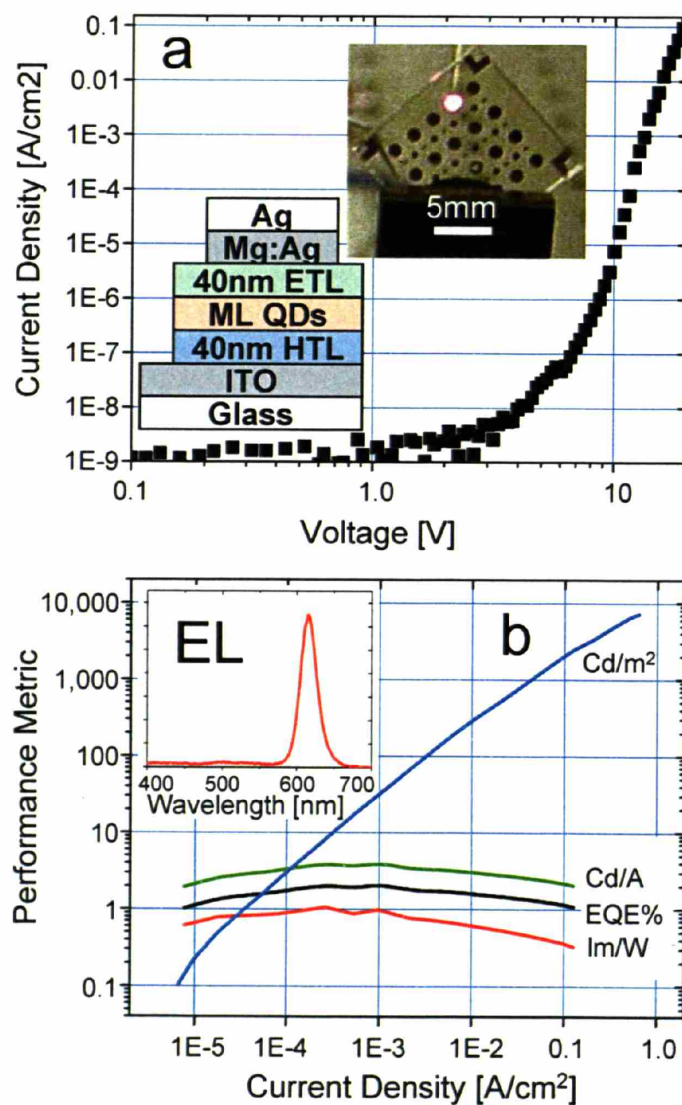
Figure 5.10 shows the plot of external quantum efficiency (EQE) versus current density as well as the I-V characteristics in the inset. The EQE of these devices was just over 0.1 %.

## 5.5 Red Emitting QD-LEDs\*

Figure 5.11 demonstrates the highest external quantum efficiency (>2%) QD-LED created to date. The NCs used to create this device were made by Quantum Dot Corporation. They were received in their growth solution and were precipitated out of solution three times before being used to make a QD-LED. The NCs were flocculated using isopropanol and methanol and after centrifuging were resuspended in hexane. After the NCs were dispersed in hexane for the first time after being precipitated out of growth solution, the hexane/NC solution was centrifuged to isolate a large quantity of white salt present in the solution. The supernatant, which contained the NCs suspended in hexane, was kept and the chunk of white salt was disposed of. The NCs were then precipitated out of solution another two times, dispersed in chloroform for device fabrication, and filtered using a 0.2  $\mu\text{m}$  syringe filter. The (CdSe)ZnS core-shell NCs had a peak absorption at 602 nm and a peak emission at 610nm with a FWHM of 21 nm. The solution PL quantum efficiency was measured to be 68 % after three precipitations (crashouts).

---

\* Much of this section has appeared in print (S. Coe-Sullivan *et al*, *Adv. Funct. Mater.* **2005**, *15*, 1117)



**Figure 5.11** Structure and performance of a red emitting QD-LED fabricated using the phase separation during spin-casting method. a) Current-Voltage characteristic of the device; a, inset) Cross-section of the QD-LED, and a photo of the operating 1 mm diameter device; b) Critical performance metrics of the QD-LED, with external quantum efficiency in excess of 2%, > 1 lm/W, and a maximum brightness of over 7,000 cd/m<sup>2</sup>; b, inset) Electroluminescence spectrum of the QD-LED, with saturated color red emission peaked at 615 nm, and FWHM of 27 nm. The NCs used to make this device were (CdSe)ZnS core-shell NCs provided by Quantum Dot Corporation.

These devices were made by dissolving the NCs and the hole transporting organic semiconductor, N,N'-diphenyl-N,N'-bis(3-methylphenyl)-(1,1'-biphenyl)-4,4'-diamine (TPD) in chloroform, which is spin cast onto a clean ITO coated glass substrate. The NCs phase separate into a monolayer (or sub-monolayer) on the surface of the organic film as described in detail in section 5.2 of this chapter (Figure 5.5(b) shows a zoomed in AFM image of a phase separated film of these NCs, which have an aspect ratio of 5:2). The NC coverage on the surface of the TPD in these devices was ~50 %. The substrate is then transported into the thermal evaporator without exposure to air where the hole blocking layer (HBL), 3-(4-biphenyl)yl-4-phenyl-5-t-butylphenyl-1,2,4-triazole (TAZ), and then the electron transporting layer (ETL), tris-(8 hydroxyquinoline)aluminum (Alq<sub>3</sub>) are deposited at  $<5 \times 10^{-6}$  torr. Finally the metal cathode (50 nm thick Mg:Ag, 50:1 by weight, 50 nm Ag cap) is thermally evaporated through a shadow mask to define 1 mm diameter devices as shown in the upper right inset in Figure 5.11. The layered device structure is shown in the lower left inset in Figure 5.11(a). The electroluminescence (EL) spectrum, shown in the inset in Figure 5.11(b) demonstrates that the emission is dominated by NC band edge emission. The external quantum efficiency is in excess of 2 %,  $> 1$  lm/W, with a maximum brightness of over 7,000 cd/m<sup>2</sup>.

QD-LED electroluminescence spectra were acquired with a Ocean Optics USB2000 Miniature Fiber Optic Spectrometer, while the QD-LED was turned on using a Tektronix 577 curve tracer. The current-voltage measurements and external quantum efficiency measurements were performed with a Hewlett Packard 4145B Semiconductor Parameter Analyzer and a Newport silicon photodiode (Model 818-UV) interfaced using LabView.

## 5.6 Conclusions

The fabrication of NC / organic bilayers via phase separation during spin-casting is a robust and general process. It has been shown to be a useful technique for the creation of new optoelectronic device structures, enabling the creation of high efficiency QD-LEDs. Large area NIR EL from PbSe QD-LEDs has been demonstrated. The LED emission is tuned from  $\lambda = 1.32$  to  $1.56 \mu\text{m}$  as the PbSe NC diameter is changed from 4 to 5 nm, without any modification to the device structure. Blue EL from (CdS)ZnS core-shell NCs as well as the highest efficiency QD-LED to date with red EL from (CdSe)ZnS core-shell NCs is demonstrated, all of which were enabled by use of phase separation during spin-casting. In addition to the creation of single monolayers of NCs on top of organic semiconductor contacts, this process enables the creation and study of large scale hcp crystal (super-lattice) domains of only two dimensions, which may be fabricated in seconds. The size scale of these domains is controllable, with a demonstrated maximum grain size in excess of a square micron. The upper limit of the grain sizes that could be formed certainly has not yet been reached. The facile assembly of large area arrays of nanoscale active elements, enabling the creation of macroscale devices from nanoscale materials, is an essential step to transitioning nanoscience into nanotechnology.

## 5.7 References

1. S. Coe, W.-K. Woo, M. Bawendi, V. Bulovic, *Nature* **2002**, *420*, 800.
2. C. B. Murray, D. J. Norris, M. G. Bawendi, *J. Am. Chem. Soc.* **1993**, *115*, 8706.
3. B. O. Dabbousi, J. Rodriguez-Viejo, F. V. Mikulec, J. R. Heine, H. Mattoussi, R. Ober, K. F. Jensen, M. G. Bawendi, *J. Phys. Chem. B* **1997**, *101*, 9463.
4. M. A. Hines, P. Guyot-Sionnest, *J. Phys. Chem.* **1996**, *100*, 468.
5. L. Manna, E. C. Scher, A. P. Alivisatos, *J. Am. Chem. Soc.* **2000**, *122*, 12700.
6. C. B. Murray, C. R. Kagan, M. G. Bawendi, *Science* **1995**, *270*, 1335.

7. X. M. Lin, H. M. Jaeger, C. M. Sorensen, K. J. Klabunde, *J. Phys. Chem. B* **2001**, *105*, 3353.
8. V. Santhanam, R. P. Andres, *Nano. Lett.* **2004**, *4*, 41.
9. B. O. Dabbousi, C. B. Murray, M. F. Rubner, M. G. Bawendi, *Chem. Mater.* **1994**, *6*, 216.
10. C. P. Collier, R. J. Saykally, J. J. Shiang, S. E. Henrichs, J. R. Heath, *Science* **1997**, *277*, 1978.
11. S. Coe-Sullivan, W. K. Woo, J. S. Steckel, M. Bawendi, V. Bulovic, *Organic Electronics* **2003**, *4*, 123.
12. J. S. Steckel, S. Coe-Sullivan, V. Bulovic, M. G. Bawendi, *Adv. Mater.* **2003**, *15*, 1862.
13. J. S. Steckel, J. P. Zimmer, S. Coe-Sullivan, N. E. Stott, V. Bulovic, M. G. Bawendi, *Angew. Chem. Int. Ed.* **2004**, *43*, 2154.
14. J. Tang, G. L. Ge, L. E. Brus, *J. Phys. Chem. B* **2002**, *106*, 5653.
15. A. Lo, R. T. Skodje, *J. Chem. Phys.* **2000**, *112*, 1966.
16. N. R. Jana, *Angew. Chem. Int. Ed.* **2004**, *43*, 1536.
17. S. Connolly, S. Fullam, B. Korgel, D. Fitzmaurice, *J. Am. Chem. Soc.* **1998**, *120*, 2969.
18. E. Rabani, D. R. Reichman, P. L. Geissler, L. E. Brus, *Nature* **2003**, *426*, 271.
19. H. Tanaka, *J. Phys.-Condens. Mat.* **2000**, *12*, R207.
20. M. Maillard, L. Motte, M. P. Pileni, *Adv. Mater.* **2001**, *13*, 200.
21. B. A. Korgel, D. Fitzmaurice, *Phys. Rev. Lett.* **1998**, *80*, 3531.
22. K. Morgenstern, G. Rosenfeld, G. Comsa, *Phys. Rev. Lett.* **1996**, *76*, 2113.
23. J. M. Wen, J. W. Evans, M. C. Bartelt, J. W. Burnett, P. A. Thiel, *Phys. Rev. Lett.* **1996**, *76*, 652.
24. G. L. Ge, L. E. Brus, *Nano Lett* **2001**, *1*, 219.
25. R. J. Curry, W. P. Gillin, A. P. Knights, R. Gwilliam, *Opt. Mater.* **2001**, *17*, 161.
26. Y. Kawamura, Y. Wada, M. Iwamuro, T. Kitamura, S. Yanagida, *Chem. Lett.* **2000**, *2000*, 280.
27. V. Bulović, V. B. Khalfin, G. Gu, P. E. Burrows, *Phys. Rev. B* **1998**, *58*, 3730.
28. R. R. Chance, A. Prock, R. Silbey, *J. of Chem. Phys.* **1974**, *60*, 2744.
29. C. A. Leatherdale, C. R. Kagan, N. Y. Morgan, S. A. Empedocles, M. A. Kastner, M. G. Bawendi, *Phys. Rev. B* **2000**, *62*, 2669.
30. S.R. Forrest, D.D.C. Bradley, M.E. Thompson, *Adv. Mater.* **2003**, *15*, 1043.
31. J. C. Sturm, W. Wilson, M. Iodice, *IEEE J. of Selected Topics in Quantum Electronics* **1998**, *4*, 75.
32. D. F. O'Brien, P. E. Burrows, S. R. Forrest, B. E. Koene, D. E. Loy, M. E. Thompson, *Adv. Mater.* **1998**, *10*, 1108.





# Chapter 6

## QD-LEDs Made Using Micro-Contact Printing

### 6.1 Introduction and Motivation

Colloidal NC lumophores are well suited for use in electroluminescent displays, with their saturated color emission, high photoluminescence efficiency and continuously tunable emission spectra<sup>[1,2]</sup>. Since multilayer NC solids have poor electrical transport properties in solid state devices, single monolayers of NCs are used in active devices so as to utilize their beneficial light emission properties while minimizing their impact on electrical performance<sup>[3]</sup> (see Chapter 1). Large area (several cm<sup>2</sup> in size) NC monolayers can be self assembled out of solution, either by spin-casting<sup>[2]</sup>, Langmuir-Blodgett techniques<sup>[4]</sup>, or drop-casting<sup>[5]</sup>. The use of Langmuir-Blodgett techniques and drop-casting for the creation of the active NC monolayer in QD-LEDs requires the device to be designed around the deposition technique, leading to non-ideal structures and inferior performance. Although the technique of phase separation during spin-casting, as discussed in Chapter 5, has provided the most efficient QD-LEDs to date via the formation of NC monolayers on top of an organic thin film, it is far from ideal for all experiments and device applications. Phase separation requires the co-deposition of the organic thin film with the NC monolayer, something which is not always desirable. Additionally, the organic underlayer must be homogeneous over the entire substrate, a constraint which limits the number of device designs which can be accessed. Also, only organic materials that are highly soluble can be used. While this is not necessarily a

limitation in the long term, currently the majority of organic small molecular semiconductors which have been studied are optimized for vapor phase deposition, not solubility. Finally, phase separation successfully assembles NC monolayers over entire surfaces, but does not allow the lateral patterning of red, green, and blue NC monolayers adjacent to each other, something which is clearly desirable for the fabrication of a full color QD-LED display.

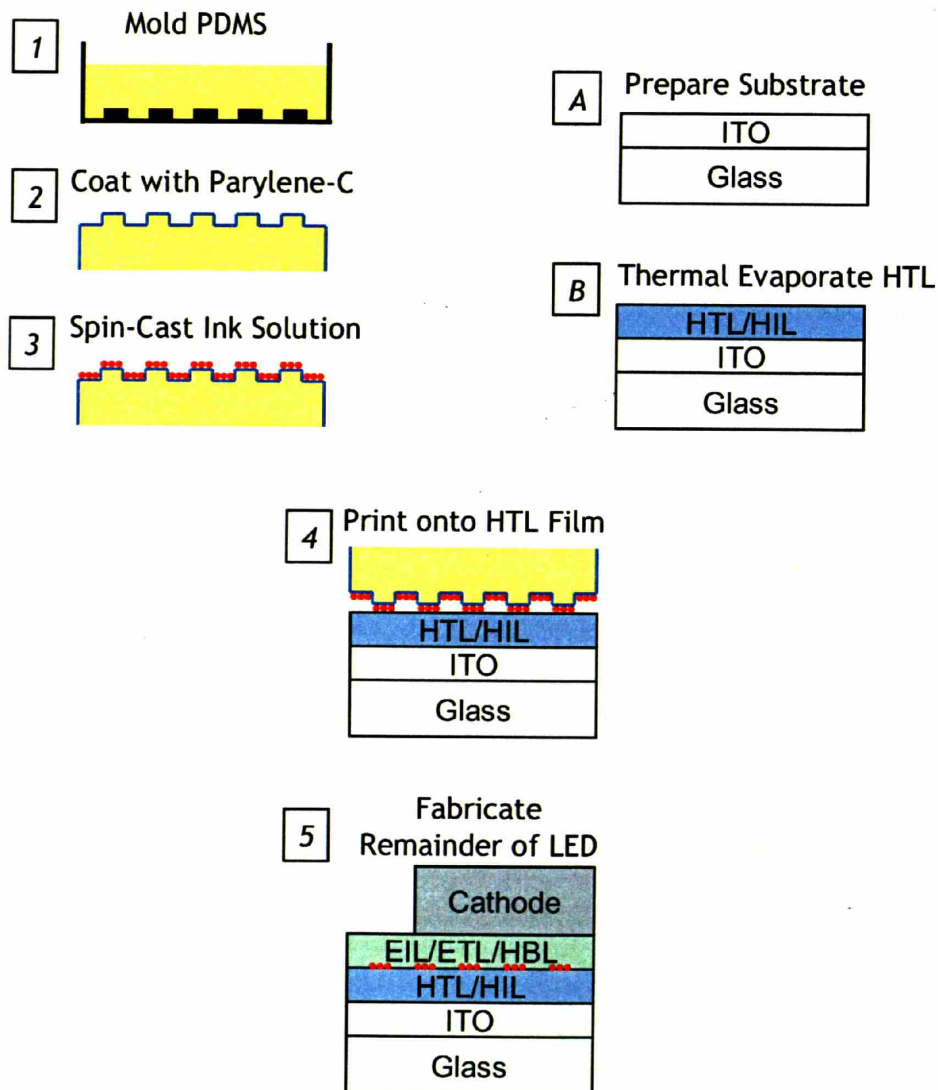
Thus a fabrication process that would allow for in plane patterning of NC monolayers is desirable, provided that it not place additional constraints on the materials or device designs that it can be used with. The ideal NC monolayer deposition technique for QD-LED fabrication would involve the dry (solvent free) application of an already patterned NC film to any substrate, removing all solubility and surface chemistry requirements on the substrate which are typical and to some extent assumed within the field. To satisfy this need, we have extended the method of micro-contact printing to NC monolayer deposition. This is a key milestone towards the development of pixelated QD-LEDs such as needed for flat panel display applications.

In this work we demonstrate that with the micro-contact printing method<sup>[6,7]</sup> we can deposit a patterned as well as a non-patterned, solvent-free NC monolayer to create QD-LEDs. Some initial work has been done on patterning of NC layers<sup>[7-11]</sup> as well, but has not been integrated into a device fabrication procedure. Using micro-contact printing we show for the first time the fabrication of saturated color red, green, and blue QD-LEDs, multiple QD-LEDs of different colors on a single substrate, and the patterning of QD-LED pixels on the micron scale (<100 $\mu$ m).

The critical step in the presented printing process is functionalizing the surface of the elastomer stamp by coating it with a thin film that is both a barrier to stamp swelling by the ink solvent (NCs in chloroform), and an adhesion/release layer for the NC monolayer. Chemical vapor deposited, aromatic organic polymers are a natural choice, resulting in a conformal coating of the shaped stamp and a chemical surface which is compatible with spreading of the chloroform-solvated inks. The stamp is inked via spin-casting with a NC solution and after the ink solvent evaporates the formed monolayer is transferred onto the substrate by contact printing. This work represents the first use of micro-contact printing of NCs in the creation of electroluminescent devices, a critical step towards the realization of pixelated, full color QD-LED displays.

## 6.2 Nanocrystal Micro-Contact Printing Process

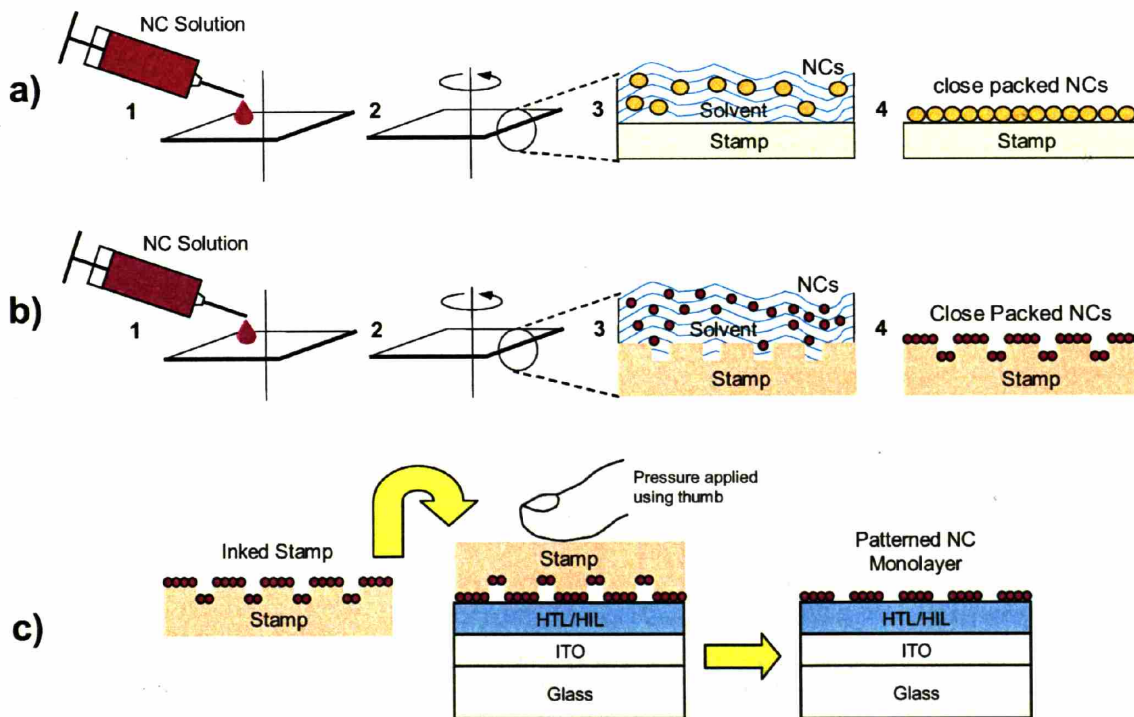
Figure 6.1 depicts a flow chart outlining the basic steps in the process. First, a silicon master is made using standard semiconductor processing techniques (alternatively, for a non-patterned deposition, a blank Si master can be used). Poly dimethyl Siloxane (PDMS, Sylgard 184) precursors are then mixed, degassed, poured onto the master, and degassed again, and allowed to cure at room temperature (or above room temperature, for faster cure times) (Figure 6.1, step 1). The PDMS rubber “stamp” is then freed from the master, and cut into the desired shape and size. This stamp is then coated with a chemical vapor deposited Parylene-C layer, anywhere from 0.1-2 $\mu$ m thick, depending on the pattern to be reproduced (Figure 6.1, step 2). This stamp is then inked through a simple spin-casting of neat NCs in a solution of chloroform (concentration 1-10mg/mL depending on desired outcome) (Figure 6.1, step 3). The inked stamp can then be



**Figure 6.1** A flow chart outlining the basic steps in the fabrication of QD-LEDs using micro-contact printing of NCs. First, a silicon master is transferred to PDMS (step 1). The PDMS rubber “stamp” is then coated with a chemical vapor deposited Parylene-C layer (step 2). The stamp is then inked through a simple spin-casting of neat NCs in a solution of chloroform (step 3) (detailed in Figure 6.2 (a) and (b)). The inked stamp is then inverted onto the ITO coated glass substrate (step A), which has already had hole transport and/or hole injection organic semiconductor layers thermally evaporated on top of it (step B). The ink (NCs) is transferred completely to the new substrate (step 4) (detailed in Figure 6.2 (c)) and the rest of the device (electron transport layer, electron injection layer, metal contacts) is then grown on top of the NCs (step 5).

inverted onto a substrate, and with gentle pressure applied for 30 seconds, the ink will transfer completely to the new substrate (Figure 6.1, step 4). Figure 6.2 shows in detail

step 3 and 4 of the process. Figure 6.1 (a,b) depicts an ITO coated glass substrate, which has already had hole transport and/or hole injection organic semiconductor layers (HTL and HIL respectively) thermally evaporated on top of it. The patterned NC monolayer is transferred to this HTL layer, and the rest of the device (electron transport layer (ETL), electron injection layer (EIL), metal contacts) can then be grown on top of the NCs (Figure 6.1, step 5).

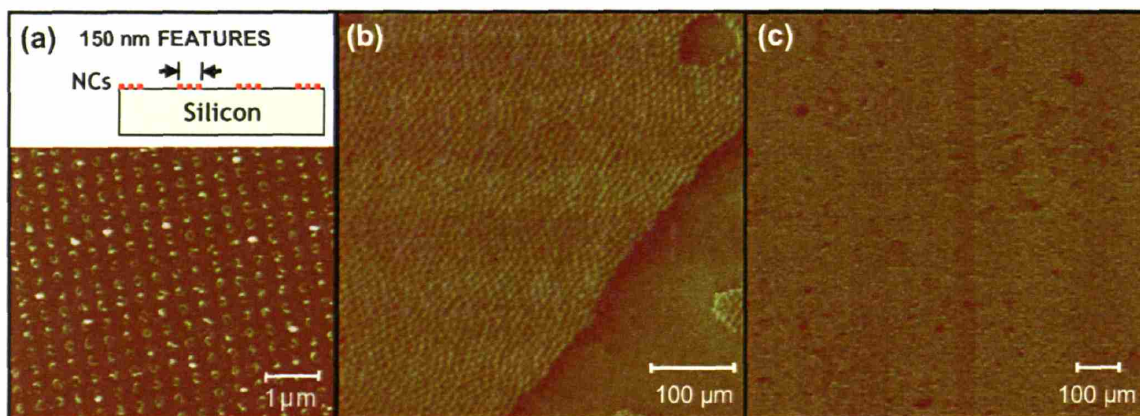


**Figure 6.2** Detailed flow diagram of steps 3 and 4 shown in Figure 6.1. Whether the stamp is planar (a) or patterned (b), the solution of NCs is dropped onto the stamp (1) and the stamp is set spinning (2) (3000 rpm for 60 seconds). During the solvent drying time, the NCs begin to order (3) and self-assemble into grains of hexagonally close packed spheres (4) on the surface of the stamp. In (c) the stamping process used to fabricate QD-LEDs is shown in detail, where a patterned stamp, for example, after being inked, is inverted onto the hole transporting/hole injecting layer and slight pressure with the thumb is applied for roughly a minute. The stamp is carefully removed and a monolayer of patterned NCs is left behind.

Figure 6.3 demonstrates the surface relief that is observable through atomic force microscopy (AFM) after the stamping process. Figure 6.3(a) shows the result of using



PbSe NCs with a patterned stamp (Figure 6.2 (b)). The master is created using interference lithography, yielding a two dimensional array of 150 nm features on a 300 nm period in both dimensions. This pattern is then replicated on the stamp, and finally on the NC layer transferred onto silicon. In the case of Figure 6.3 (b), (CdS)Cd<sub>x</sub>Zn<sub>1-x</sub>S core-shell NCs are deposited using a planar stamp (Figure 6.2 (a)) with submonolayer NC coverage, onto a TPD surface. The total peak to peak height in the corresponding AFM height image is less than 10 nm, indicating that the deposition is indeed only one monolayer high. Monolayers with film area coverages of greater than 90% are achieved by increasing the concentration of NCs in the original chloroform solution that is used to ink the stamp as shown in Figure 6.3 (c), where (Cd<sub>x</sub>Zn<sub>1-x</sub>Se)Cd<sub>y</sub>Zn<sub>1-y</sub>S core-shell NCs were stamped onto a thermally evaporated thin film of CBP (4-4'-N,N'-dicarbazolylbiphenyl).



**Figure 6.3** Atomic force microscopy (AFM) images of the surface relief that is observable after the completion of step 4 in Figure 6.1. a) Shows a partial PbSe NC monolayer resulting from transfer onto a Silicon surface using a patterned (150 nm circular features on a square grid) stamp. b) Shows a partial (CdS)Cd<sub>x</sub>Zn<sub>1-x</sub>S core-shell NC monolayer after transfer onto an organic semiconductor surface, using a planar (not patterned) stamp. c) Shows a monolayer of (Cd<sub>x</sub>Zn<sub>1-x</sub>Se)Cd<sub>y</sub>Zn<sub>1-y</sub>S core-shell NCs stamped (using a planar stamp) onto an organic surface with almost 100% film coverage.

## 6.3 Micro-Contact Printing of QD-LEDs

### 6.3.1 Red, Green, and Blue Emitting QD-LEDs

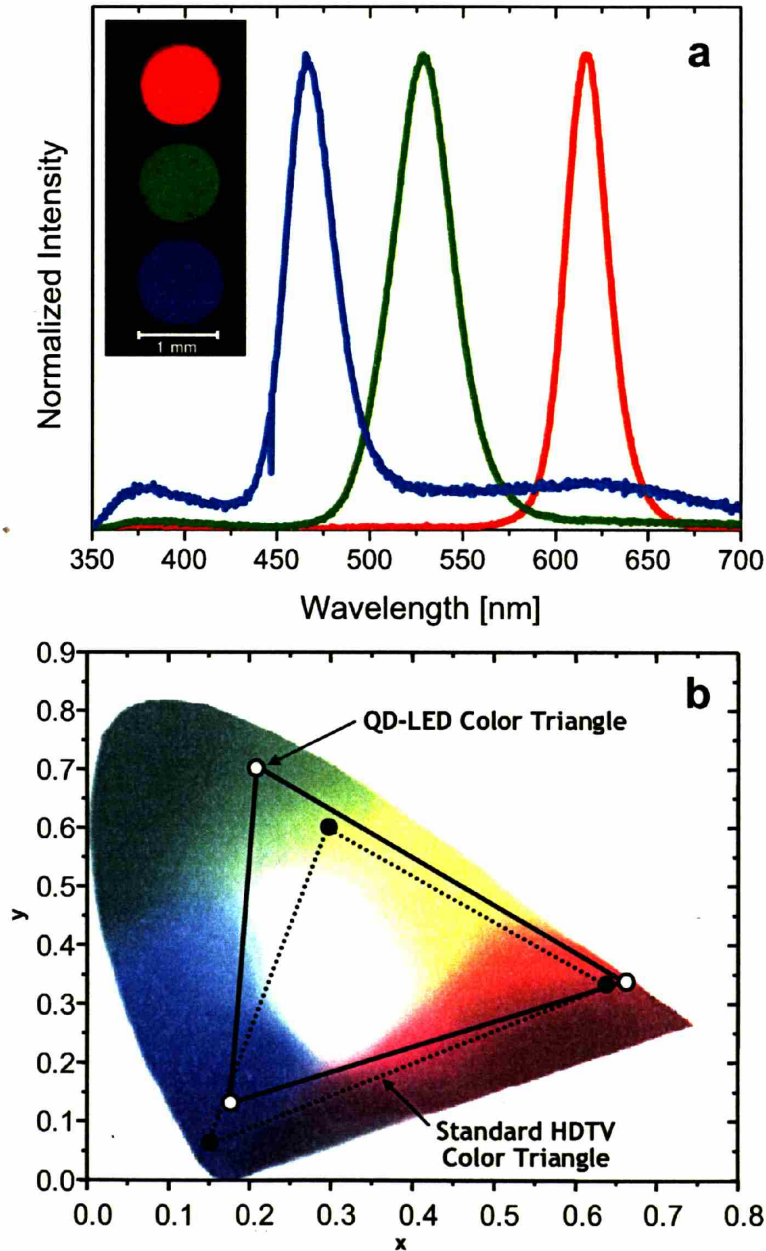
The three NC materials used to make saturated in color red, green, and blue QD-LEDs with peak emission wavelengths optimized for full color QD-LED displays were (CdSe)ZnS core-shell NCs from Quantum Dot Corporation (these NCs are discussed in Chapter 5, section 5.5),  $(\text{Cd}_x\text{Zn}_{1-x}\text{Se})\text{Cd}_y\text{Zn}_{1-y}\text{S}$  core-shell NCs (described in Chapter 4), and  $(\text{CdS})\text{Cd}_x\text{Zn}_{1-x}\text{S}$  core-shell NCs (described in Chapter 3, section 3.3), respectively. Before being used in device fabrication, the NC materials were isolated by precipitating them out of solution twice with a miscible non-solvent and then filtered through a 0.2  $\mu\text{m}$  syringe filter. Red, green, and blue emitting QD-LEDs were made by first thermally evaporating 35 nm of 4,4'-*N,N'*-dicarbazolyl-biphenyl (CBP) (hole transport layer (HTL)) onto an indium tin oxide (ITO) coated glass substrate at  $< 5 \times 10^{-6}$  torr. The NC monolayer, under air-free conditions, was then micro-contact printed onto the organic thin film of CBP using planar stamps (surface coverages for all three materials were roughly 80-95 %). The substrate was then transported back into the thermal evaporator without exposure to air, where the hole blocking layer (HBL), 3-(4-biphenyl)llyl)-4-phenyl-5-*t*-butylphenyl-1,2,4-triazole (TAZ) (20 nm thick), and then the electron transporting layer (ETL), tris-(8 hydroxyquinoline)aluminum ( $\text{Alq}_3$ ) (15 nm thick), were deposited. Finally the metal cathode (50 nm thick Mg:Ag, 50:1 by weight, 50 nm Ag cap) was thermally evaporated through a shadow mask to define 1mm diameter devices (see the inset in Figure 6.5(b) for a diagram of the assembled device structure).

The ability to now separate the deposition of the organic HTL/hole injection layer (HIL) from that of our NC monolayers allowed us to explore the use of other molecules

for the HTL/HIL and as a result led us to the wide band gap organic semiconductor, CBP. Our previous work (Chapter 5) on QD-LEDs mainly employed the use of N,N'-diphenyl-N,N'-bis(3-methylphenyl)-(1,1'-biphenyl)-4,4'-diamine (TPD) as the HTL, simply due to its good solubility in chloroform and chlorobenzene compared to many other HTL candidates. The wide band gap of CBP contributed to more efficient charge confinement and an improvement in color saturation of the QD-LEDs, yielding Commission International d'Eclairage (CIE) coordinates (0.18, 0.13), (0.21, 0.70), and (0.66, 0.34) for the blue, green, and red QD-LEDs, respectively (Figure 6.4(b)).

Color saturation refers to how pure a color appears to the human eye and is quantified in the CIE chromaticity diagram by calculating color coordinates based on the emission wavelength and bandwidth (full width at half maximum). For a gaussian emission spectrum with a full width at half maximum (FWHM) of 30 nm and a maximized perceived power, the optimal peak wavelength for display applications is  $\lambda = 610\text{-}620$  nm for red,  $\lambda = 525\text{-}530$  nm for green, and  $\lambda = 460\text{-}470$  nm for blue. For the red pixels, wavelengths longer than  $\lambda = 620$  nm become difficult for the human eye to perceive, while those shorter than  $\lambda = 610$  nm have coordinates that lie inside the standard NTSC/HDTV color triangle. Similar optimization applies for the blue pixels. Green pixels at  $\lambda = 525\text{-}530$  nm provide a red, green, and blue color triangle with the largest area on the CIE chromaticity diagram (and therefore the largest number of colors accessible by a display), but wavelengths longer than  $\lambda = 530$  nm start to cause the overall triangle made up by the red, green, and blue pixels to cut out some of the blue/green area of the triangle. Wavelengths shorter than  $\lambda = 525$  nm compromise the yellow display emissions.





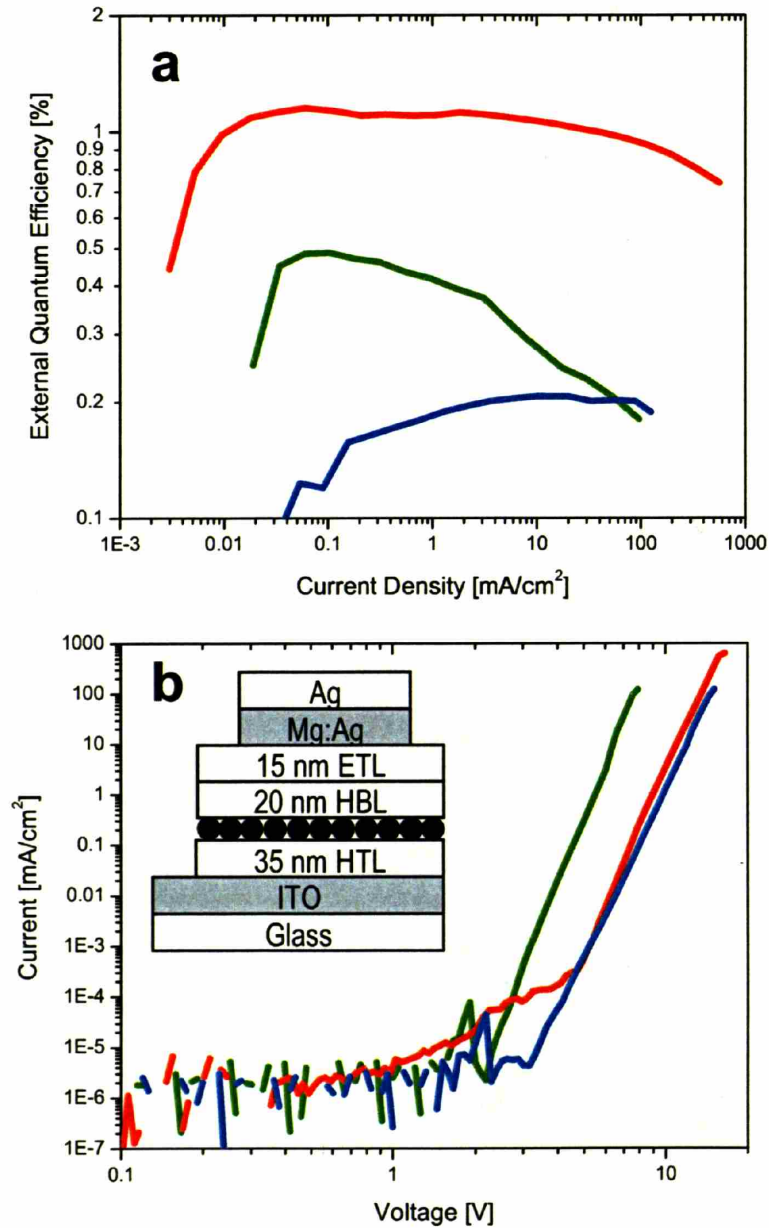
**Figure 6.4** Red, green, and blue QD-LED device luminescence characteristics. The red, green, and blue electroluminescence spectra are shown in (a) (the line color of each spectrum corresponds to the color that each device is emitting) with photographs of the working red, green, and blue QD-LED devices shown in the inset. The red device has a peak wavelength of emission at  $\lambda = 616$  nm with a FWHM = 24 nm, green  $\lambda = 527$  nm with a FWHM = 35 nm, and the blue device has peak emission at  $\lambda = 467$  nm with a FWHM = 27 nm. The red, green, and blue spectra were transformed into their corresponding CIE color coordinates and plotted on the CIE chromaticity diagram along with the HDTV color coordinates for comparison (b).

The red, green, and blue electroluminescence (EL) peaks of the QD-LEDs are shown in Figure 6.4(a) along with actual photographs of the working red, green, and blue devices. The red EL spectrum has a peak wavelength of  $\lambda = 616$  nm with a FWHM = 24 nm, green  $\lambda = 527$  nm with a FWHM = 35 nm, and the blue device has peak emission at  $\lambda = 467$  nm with a FWHM = 27 nm. Greater color saturation in these hybrid organic/inorganic QD-LEDs is defined by a decrease in the intensity of organic emission and an increase in intensity of NC emission, leading to a larger ratio between NC EL and organic EL. This could be attributed to the larger downhill energy transfer process now available with the use of CBP<sup>[10,12]</sup>, but could also be due to the higher photoluminescence (PL) quantum efficiencies of the NCs themselves. The superior color saturation of our red and green QD-LEDs is seen clearly by their position on the CIE chromaticity diagram relative to the current High Definition Television (HDTV) standard color triangle shown in Figure 6.4(b).

The blue QD-LED CIE color coordinates lie just inside the HDTV standard color triangle and is a result of the red tail seen in the blue QD-LED EL spectrum. This red tail we believe is the result of a mixed state between the two large band gap HTL and HBL (exciplex emission) in our device structure. An exciplex is a transient complex formed between the excited state of a donor molecule and the ground state of an adjacent acceptor molecule. This exciplex emission is not seen in the red QD-LED device most likely because those energy states from the exciplex are Förster energy transferred to the red emitting NCs. The green QD-LED exhibits only a very small amount of this exciplex emission probably due to the excellent film coverage of the monolayer of green emitting NCs, which separates the HTL from the HBL and therefore their interaction, as well as

the high PL quantum efficiency (40%) of the NCs themselves, which contributes to the large NC EL intensity relative to the organic exiplex EL. Another contributing factor is that when the devices are run at high currents ( $\sim 100$   $\mu\text{A}$ ) the exiplex emission peak shifts from  $\sim 620$  nm to  $\sim 520$  nm, which is right over the green emitting  $(\text{Cd}_x\text{Zn}_{1-x}\text{Se})\text{Cd}_y\text{Zn}_{1-y}\text{S}$  core-shell NC emission peak and is either covered completely by the green NC emission or is Förster energy transferred to the green emitting NCs. The blue QD-LED devices should improve as the blue emitting NC PL quantum efficiency increases (currently 20%) and more optimized films of NCs are deposited.

The small peak in the green and blue EL spectra at  $\lambda = 380$  nm is CBP emission, which for the green is only 2.6 % of the total emission from the device, while in the blue device it is a little more substantial. It appears that the amount of CBP EL relative to NC EL scales with the efficiency of the NCs in this case. Because the CBP peak lies to blue side (shorter wavelength emission than the NC EL) of the blue NC peak it does not influence the blue color saturation and in the green case, because the intensity of the CBP EL is so miniscule, its influence on color saturation is negligible. The QD-LED color triangle shown in Figure 6.4(b) demonstrates how using these saturated red, green, and blue QD-LEDs for a full color display would provide a significantly larger color triangle, which translates into a display with many more attainable colors as well as more saturated colors than an HDTV display can show. This large color gamut of QD-LEDs exceeds the performance of both LCD and organic LED (OLED) technologies, suggesting future use of QD-LEDs in high definition, accurate color flat panel displays and in general light sources.



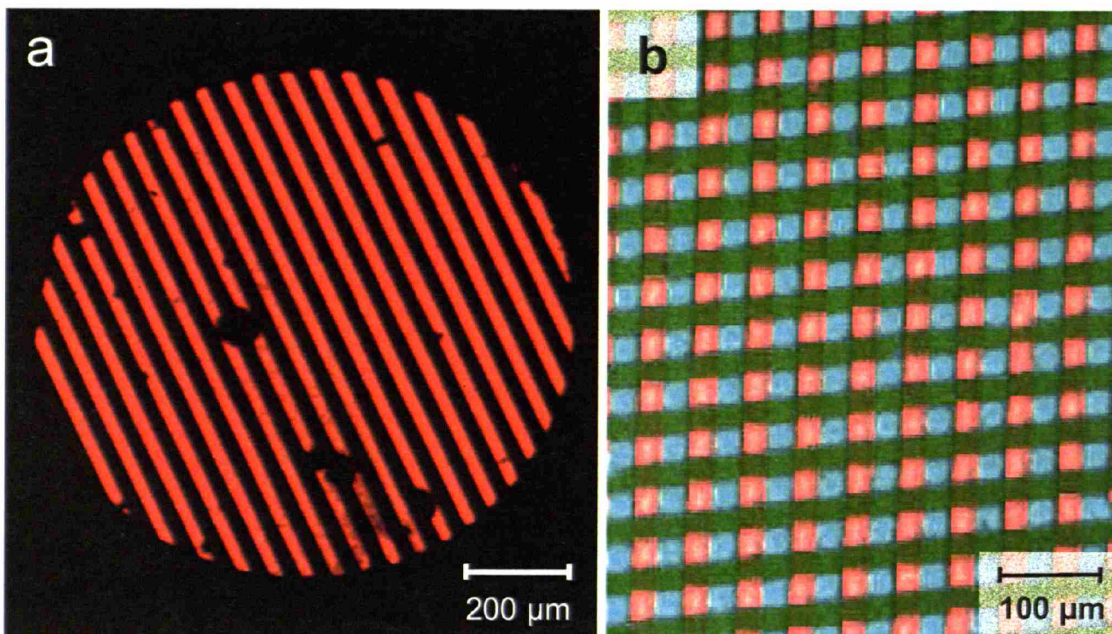
**Figure 6.5** Electrical performance data of the micro-contact printed QD-LED devices shown in Figure 6.4. The line color in each plot corresponds to the color of device emission. The plot of external quantum efficiency versus current density is shown in (a) for the red, green, and blue devices with peak efficiencies of 1.2 %, 0.5 %, and 0.2 % respectively. (b) shows the current-voltage curves for each device and the cross-section of these QD-LEDs is shown in the inset.

Figure 6.5(a) shows the external quantum efficiency (EQE) of the red, green, and blue QD-LEDs and demonstrates how the EQE of the devices scales with the PL quantum efficiency of the NCs. The red emitting QD-LED EQE is 1.2 % using (CdSe)ZnS core-shell NCs from Quantum Dot Corporation with PL quantum efficiencies of 70% after processing and preparing for device use (precipitated out of solution two times), the green emitting QD-LEDs have EQEs of 0.5 % using the  $(\text{Cd}_x\text{Zn}_{1-x}\text{Se})\text{Cd}_y\text{Zn}_{1-y}\text{S}$  core-shell NCs with PL quantum efficiencies of 40 %, and the blue EQE is 0.2 % using  $(\text{CdS})\text{Cd}_x\text{Zn}_{1-x}\text{S}$  core-shell NCs with PL quantum efficiencies of 20 % after being cleaned up for device use. All three color QD-LEDs have nice reproducible, stable, current-voltage (IV) characteristics as seen in Figure 6.5(b), with turn on voltages of 2-5 V and operating voltages of 8-12 V. Display brightness ( $100 \text{ cd/m}^2$ ) is achieved at  $\sim 2 \text{ mA/cm}^2$  and  $\sim 10 \text{ V}$  for these QD-LEDs.

### 6.3.2 Patterning of Nanocrystals, Towards QD-LED Displays

The most promising result of the NC micro-contact printing technique is the ability to place different color emitting NCs on the same substrate in a pattern towards pixilation for full color display applications. Sub-pixel dimensions for full color displays are typically on the order of 25-100  $\mu\text{m}$ . Here we demonstrate 25  $\mu\text{m}$  (1000 dpi) patterning of QD-LED pixels (Figure 6.6(a) and (b)), however, based on the results shown in Figure 6.3(a), much smaller features should be possible. Figure 6.6(a) shows a photograph of an operating 1 mm diameter QD-LED with 25  $\mu\text{m}$  wide patterned lines of red emitting NCs at a period of 50  $\mu\text{m}$ . The red emitting NCs were printed using a stamp that was patterned with lines having dimensions of 2  $\mu\text{m}$  in height and 25  $\mu\text{m}$  line widths on a 50 $\mu\text{m}$  pitch. In Figure 6.6(b), 25 $\mu\text{m}$  wide intersecting stripes of red and green NC

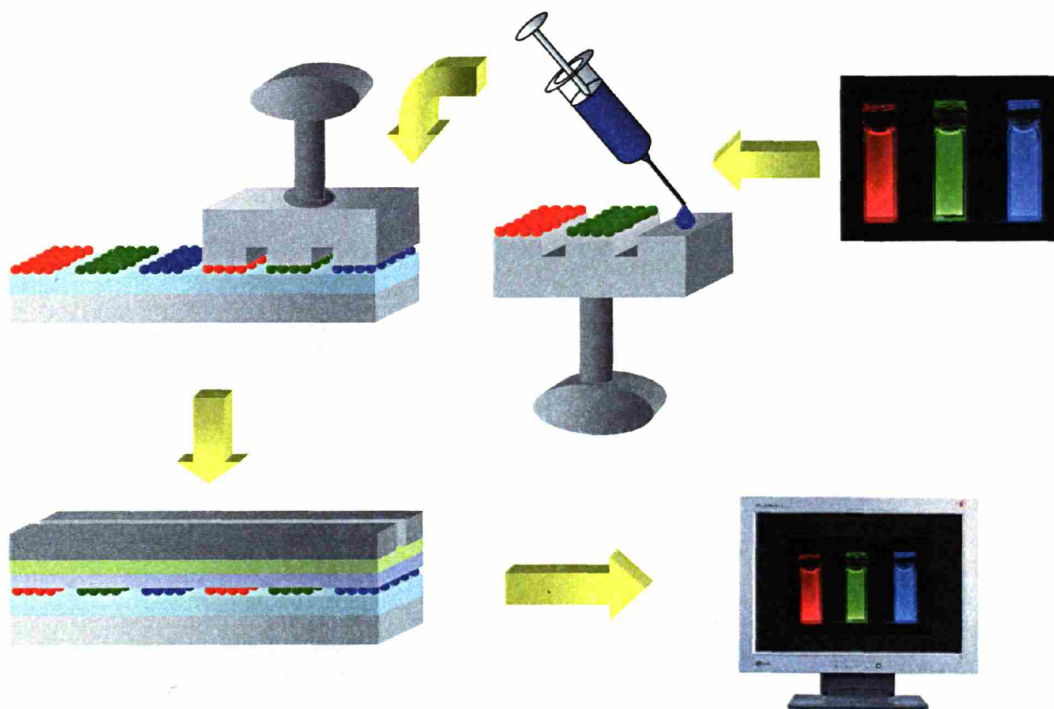




**Figure 6.6** Digital photographs of working QD-LED devices, where the emitting NC monolayers were patterned using micro-contact printing. (a) Photograph of an operating 1 mm diameter QD-LED with 25  $\mu\text{m}$  wide patterned lines of red emitting NCs at a period of 50  $\mu\text{m}$  (dark spots are most likely due to dust particles). (b) Photograph of a section of a QD-LED with 25  $\mu\text{m}$  wide intersecting patterned lines of red and green NCs at a period of 50  $\mu\text{m}$ . In the regions where no NCs were deposited blue organic LED emission (from TPD) is observed.

monolayers are stamped over each other in the QD-LED structure in which a TPD (40 nm) hole transporting layer replaced CBP. Electroluminescence of red and green NCs and blue TPD is simultaneously observed when the QD-LED is biased at 5V. A full color QD-LED display would require the printing of red, green, and blue NC monolayer stripes next to one another on the organic hole transport layer. The cartoon shown in Figure 6.7 illustrates in a very generic manner, how stripes of red, green, and blue NCs would need to be placed side by side to create a full color QD-LED display. The stamp (generically represented in the cartoon as a rubber stamp, but could also be a roller) would need to first be inked in some fashion (generically represented in the cartoon by the syringe), with the red, green, and blue NCs. The stamp would then be brought into

contact with the substrate, where the red, green, and blue stripes of dry NCs would be transferred over to the pre-deposited organic thin film. The rest of the organic layers would be deposited followed by a patterned cathode to complete the display.



**Figure 6.7** A cartoon illustrating in a very basic manner, how stripes of red, green, and blue NCs would be stamped side by side to create a full color QD-LED display. The syringe represents the inking of the stamp with red, green, and blue NCs from solution. The object that does the dry transferring of the stripes of red, green, and blue NC monolayers to the pre-deposited organic thin film is represented by the rubber stamp. When the stripes of red, green, and blue NCs are deposited side by side, the rest of the organic layers are laid down followed by the patterned cathode to complete the full color display.

## 6.4 Conclusions

In conclusion, we demonstrate red, green, and blue emitting QD-LEDs that are efficient and highly color saturated. The ability to deposit the NC monolayers for device fabrication via a dry transfer process (NC micro-contact printing) enabled the use of other organic hole transport materials and as a result an improvement in color saturation. The

NC materials that were used to fabricate red, green, and blue QD-LED devices with peak emission wavelengths optimized for full color QD-LED displays were (CdSe)ZnS core-shell NCs from Quantum Dot Corporation,  $(\text{Cd}_x\text{Zn}_{1-x}\text{Se})\text{Cd}_y\text{Zn}_{1-y}\text{S}$  core-shell NCs, and  $(\text{CdS})\text{Cd}_x\text{Zn}_{1-x}\text{S}$  core-shell NCs, respectively. We have shown that the NC monolayers can also be patterned towards pixilation for full color display applications when a patterned stamp is used during the micro-contact printing process. The micro-contact printing of NCs is inherently simpler than both inkjet printing and contact shadow masking. It has the potential to be efficient in materials usage and to scale easily to large area batches and continuous roll-to-roll processing. This work represents the first use of micro-contact printing of NCs in the creation of electroluminescent devices, a critical step towards the realization of pixelated, full color QD-LED displays.

## 6.5 References

1. V. L. Colvin, M. C. Schlamp, A. P. Alivisatos, *Nature* **1994**, 370, 354.
2. M. C. Schlamp, X. Peng, A. P. Alivisatos, *J. Appl. Phys.* **1997**, 82, 5837.
3. S. Coe, W.-K. Woo, M. Bawendi, V. Bulovic, *Nature* **2002**, 420, 800.
4. V. Santhanam, J. Liu, R. Agarwal, R. P. Andres, *Langmuir* **2003**, 19, 7881.
5. X. M. Lin, H. M. Jaeger, C. M. Sorensen, K. J. Klabunde, *J Phys Chem B* **2001**, 105, 3353.
6. A. Kumar, G. Whitesides, *Appl. Phys. Lett.* **1993**, 63, 2002.
7. V. Santhanam, R. P. Andres, *Nano Lett.* **2004**, 4, 41.
8. M. Islam, I. Herman, *Appl. Phys. Lett.* **2002**, 80, 3823.
9. S.-S. Bae, D. K. Lim, J.-I. Park, S. Kim, J. Cheon, W.-R. Lee, *J Phys Chem B* **2004**, 108, 2575.
10. C. R. Barry, N. Z. Lwin, W. Zheng, H. O. Jacobs, *Appl. Phys. Lett.* **2003**, 83, 5527.
11. X. M. Lin, R. Parthasarathy, H. M. Jaeger, *Appl. Phys. Lett.* **2001**, 78, 1915.
12. C. Adachi, R. C. Kwong, P. Djurovich, V. Adamovich, M. A. Baldo, M. E. Thompson, S. R. Forrest, *Appl. Phys. Lett.* **2001**, 79, 2082.



# Curriculum Vitae

JONATHAN S. STECKEL

Massachusetts Institute of Technology  
400 Main Street, 18-080  
Cambridge, MA 02139  
(617) 253-8594

231 Brookline St. Apt.3L  
Cambridge, MA 02139  
(857) 234-1664  
jonnys@mit.edu

---

## EDUCATION

- Ph.D. Chemistry, 2001-2006**  
Massachusetts Institute of Technology, Cambridge, Massachusetts  
Thesis: *The Synthesis of Inorganic Semiconductor Nanocrystalline Materials For the Purpose of Creating Hybrid Organic/Inorganic Light-Emitting Devices*. Thesis Advisor: Mounji G. Bawendi.
- B.A. Chemistry & Theater, 1996-2001**  
Oberlin College, Oberlin, Ohio  
Graduated with High Honors in Chemistry. Thesis: *Synthesis and Characterization of Mn-12 Multilayered Ultra-Thin Films* (43 pages). Thesis Advisor: Sarah L. Stoll. Cumulative GPA: 3.81; Chemistry GPA: 3.97, Theater GPA: 3.95.

## EXPERIENCE

**Co-Founder / Director of Chemistry**  
2005-present: QD Vision, Inc., Watertown, Massachusetts  
*Start-up company targeting the rapidly growing market for next generation flat panel displays.*  
Part-time consultant holding the position of Director of Chemistry while finishing PhD at MIT.

### Research Assistant

2001-2006: Massachusetts Institute of Technology, Cambridge, Massachusetts  
Chemistry Department: Inorganic/Physical

Developed colloidal synthesis for PbSe nanocrystals with tunable emission from  $\lambda = 1.1 \mu\text{m}$  to  $\lambda = 2.2 \mu\text{m}$ . Achieved record sample size distributions and produced self-assembled hexagonal close packed arrays of PbSe on the order of several microns squared. Incorporated PbSe nanocrystals into organic host materials to create infrared electroluminescent devices.

Invented novel procedure for the growth of (CdS)ZnS core-shell nanocrystals suitable for display applications that exhibit narrow, blue luminescence. Demonstrated for the first time blue electroluminescence from nanocrystals by embedding them in an organic thin film device.

Co-invented and developed a new procedure for the manufacture of quantum dot LEDs.

Co-developed and applied a new green emitting alloyed nanocrystal material to quantum dot LEDs to make the first highly saturated green quantum dot LED for display applications.

Worked out the chemical mechanism for nanocrystal formation in systems based on phosphorous containing molecules.

2000-2001: Oberlin College, Oberlin, Ohio  
Chemistry Department

Synthesized the manganese oxo-cluster (Mn-12) and created, using a layer-by-layer technique, self-assembled ultra-thin films made up of alternating layers of Mn-12 and poly(acrylic acid).

### **Teaching Assistant**

2001-2002: Massachusetts Institute of Technology, Cambridge, Massachusetts

Courses taught:

- *Advanced Chemical Experimentation and Instrumentation*
- *Introductory Chemical Experimentation*

1999-2001: Oberlin College, Oberlin, Ohio

Courses taught:

- *General Chemistry*
- *Inorganic Chemistry*
- *Organic Chemistry*

### **Presenter**

Spring 2003 & 2004: Massachusetts Institute of Technology, Cambridge, Massachusetts  
Chemistry Outreach Program. Presented chemistry demonstrations to students at local high schools to illustrate chemical principles.

### **Tutor**

1999-2001: Oberlin College, Oberlin, Ohio

Tutored first and second year students in General Chemistry and Italian.

## **HONORS AND AWARDS**

**Materials Research Symposium First Prize Poster Award Winner.** Title: *Tunable Quantum Dot Organic Light Emitting Devices from 540 nm to 1.55  $\mu$ m.* San Francisco, Spring 2003.

**Sigma Xi** - Scientific Research Honor Society, Oberlin College, 2001.

**Holmes Prize** - Awarded to senior chemistry majors for excellence in Chemistry, Oberlin College, 2001.

**Phi Beta Kappa** - Liberal Arts and Sciences Honor Society, Oberlin College, 2000 and 2001.  
**Baker Scholarship** - Awarded to one junior or senior Chemistry major to provide financial assistance, Oberlin College, 2000.

### MEMBERSHIPS

Material Research Society, 2002  
American Association for the Advancement of Science, 2002  
Sigma Xi Honor Society, 2001  
Phi Beta Kappa Honor Society, 2000

### SKILLS

*Languages:* Fluent in oral and written Italian.

*Computer:* Origin, SigmaPlot, SciFinder Scholar, WinSpec, NanoscopeIII.

*Specialized Skills:* Microscopy (Atomic Force Microscopy, Transmission Electron Microscopy), basic spectroscopic techniques, chemical analysis (Nuclear Magnetic Resonance, Thermal Gravimetric Analysis, X-ray Powder Diffraction), advanced air-free chemical synthesis techniques.

### ACADEMIC STUDY ABROAD

University of Bologna, Italy, 8/1997 to 7/1998. Brown in Bologna Program.  
Spent one year at the University of Bologna studying Italian Language, Italian History, Italian Literature, The History of Architecture, and The History of Photography.

### PUBLICATIONS

- **J. S. Steckel**, S. Coe-Sullivan, V. Bulović, M. G. Bawendi, "1.3  $\mu\text{m}$  to 1.55  $\mu\text{m}$  Tunable Electroluminescence from PbSe Quantum Dots Embedded within an Organic Device", *Advanced Materials*, **15**, 1862 (2003).
- S. Coe-Sullivan, W. Woo, **J. S. Steckel**, M. G. Bawendi, V. Bulović, "Tuning the Performance of Hybrid Organic/Inorganic Quantum Dot Light-Emitting Devices", *Organic Electronics*, **4**, 123 (2003).
- **J. S. Steckel**, J. P. Zimmer, S. Coe-Sullivan, N. Stott, V. Bulović, M. G. Bawendi, "Blue Luminescence from (CdS)ZnS Core-Shell Nanocrystals", *Angewandte Chemie International Edition*, **43**, 2154 (2004).
- Y. Chan, J. P. Zimmer, M. Stroh, **J. S. Steckel**, R. K. Jain, M. G. Bawendi, "Incorporation of Luminescent Nanocrystals into Monodisperse Core-Shell Silica Microspheres", *Advanced Materials*, **16**, 2092 (2004).

- **J. S. Steckel**, N. S. Persky, C. R. Martinez, C. L. Barnes, E. A. Fry, J. Kulkarni, J. D. Burgess, R. B. Pacheco, and S. L. Stoll, “Monolayers and Multilayers of [Mn12O12(O2CMe)16]”, *Nano Letters*, **4**, 399 (2004).
- Y. K. Olsson, G. Chen, R. Rapaport, D. T. Fuchs, and V. C. Sundar, **J. S. Steckel**, M. G. Bawendi, A. Aharoni, U. Banin, “Fabrication and optical properties of polymeric waveguides containing nanocrystalline quantum dots”, *Applied Physics Letters*, **18** 4469 (2004).
- D. T. Fuchs, R. Rapaport, G. Chen, Y. K. Olsson, V. C. Sundar, L. Lucas, and S. Vilan, A. Aharoni and U. Banin , **J. S. Steckel** and M. G. Bawendi, “Making waveguides containing nanocrystalline quantum dots”, *Proceedings of SPIE*, **5592**, 265 (2004).
- Y. Chan, **J. S. Steckel**, P. T. Snee, J.-Michel Caruge, J. M. Hodgkiss, D. G. Nocera, and M. G. Bawendi, “Blue semiconductor nanocrystal laser”, *Applied Physics Letters*, **86**, 073102 (2005).
- S. Coe-Sullivan, **J. S. Steckel**, W.-Keung Woo, M. G. Bawendi, and V. Bulovic, “Large-Area Ordered Quantum-Dot Monolayers via Phase Separation During Spin-Casting”, *Advanced Functional Materials*, **15**, 1117 (2005).
- S. Coe-Sullivan, **J. S. Steckel**, L. Kim, M. G. Bawendi, and V. Bulovic, “Method for fabrication of saturated RGB quantum dot light-emitting devices”, *Proceedings of SPIE Int. Soc. Opt. Eng.*, **108**, 5739 (2005).
- S. Coe-Sullivan, **J. S. Steckel**, L. Kim, P. Anikeeva, M. G. Bawendi, V. Bulović, “Micro-Contact Printing of Quantum Dot LEDs”, submitted.
- P. Anikeeva, S. Coe-Sullivan, C. Madigan, **J. S. Steckel**, M.G. Bawendi, V. Bulović, “Photoluminescence of CdSe/ZnS Core/Shell Quantum Dots Enhanced by Energy Transfer from a Phosphorescent Donor”, submitted.
- **J. S. Steckel**, P. Snee, S. Coe-Sullivan, J. P. Zimmer, J. E. Halpert, P. Anikeeva, L. Kim, M. G. Bawendi, and V. Bulovic, “Color Saturated Green Emitting QD-LEDs”, submitted.

## PATENTS

- Patent pending on novel chemistry to create blue luminescent nanocrystal material.
- Patent pending on novel chemistry to create near-infrared luminescent nanocrystal material.
- Patent pending on a method of growing semiconductor nanorods perpendicular to the substrate for the creation of a novel photovoltaic cell structure.
- Patent pending on method for depositing a monolayer of nanocrystals for the creation of quantum dot LEDs.
- Patent pending on the fabrication and materials for the creation of all inorganic quantum dot LEDs.

## CONFERENCE PRESENTATIONS

- J. S. Steckel, S. Coe-Sullivan, J. P. Zimmer, N. Stott, V. Bulović, M. G. Bawendi, "Blue Luminescence and Electroluminescence from (CdS)ZnS Core-Shell Nanocrystals," *Materials Research Society Meeting 2004*, Boston, Massachusetts (December 2004).
- J. S. Steckel, M. G. Bawendi, S. Coe, and V. Bulović, "Self-Assembling PbSe Nanocrystal Superlattices on an Organic Semiconductor Contact," *Materials Research Society Meeting, Spring 2004*, San Francisco, California (April 2004).
- J. S. Steckel, S. Stoll, B. Martin, T. E. Mallouk, "Synthesis and Characterization of Mn-12 Multilayer Ultrathin Films," *Cleveland Section, ACS Meeting-in-Miniature, Spring 2001*, John Carroll University, Cleveland, Ohio (March 2001).

## OTHER EXPERIENCE

**Teatro Comunale di Bologna**, Bologna, Italy. January 2000.

Assisted technical staff in light, sound, and scene design for the Opera "Pelleas et Melisand" directed by Pier'Alli.

**Independent Translation**, Bologna, Italy. January 1999.

Translated into English entire Italian theatrical play, *Questi Fantasmi*, written by Eduardo De Filippo, in fulfillment of independent winter term project through Oberlin College (61 pages).

**Pew Estate-Warwick Furnace**, Elverson, Pennsylvania. Summer 1997.

Worked as an unsupervised private gardener under the head gardener of the estate. Duties included mulching, planting, watering, and weeding.

**Longwood Gardens**, Kennett Square, Pennsylvania. Summer 1996.

Worked in the East conservatory maintaining plants, watering, weeding, planting, and trimming.

**Serv-I-Quip Inc.**, Downingtown, Pennsylvania. Summer 1994 & 1995.

Built refrigerant charging, reclamation, and leak test gas mixing systems used in the appliance, automobile, HVAC, agriculture, and truck industries. Responsibilities included electrical wiring, building and assembling custom units.

## Acknowledgements

The most important person in my life is my amazing wife and best friend Francesca. She was a part of my life long before my time at MIT and because of her wisdom, love, and support in everything, I find myself where I am today. I have shared everything with her in my time at MIT, high times and low times, and she has always loved and helped me along the way with her sweetness and wisdom. I need to thank her as well for tolerating my moodiness from day to day and for always accepting the long hours I put in during my time in graduate school.

My parents, Bill and Rose, have made significant sacrifices for my education from the beginning and for this I am truly grateful. Without their love and continual support in everything I have chosen in life I would not be who I am or where I am today.

The end of my first academic year, I left Oberlin College, as a theater major. When I returned from my year of study abroad in Italy I took the first semester of general chemistry to fulfill part of my science requirement and ended up loving it and feeling the desire to know more. I then took the second semester of general chemistry taught by Norman Craig. Norman Craig's love of chemistry, enthusiasm during teaching, and his ability to relate the chemistry subject matter to everyday life, inspired me and I became hooked on chemistry. Norman Craig advised and guided me through my entire undergraduate chemistry career and it is in large part because of him that I was able to continue my studies in chemistry at MIT. Two other very influential people at Oberlin that inspired me, advised me, and guided me in my chemistry studies were Sarah Stoll (undergraduate thesis advisor) and Manish Mehta. Certainly without both of their friendship, support, and enthusiasm I would not have had such a positive experience in my undergraduate chemistry studies and would not be where I am now.

I've learned so much about science and life from my advisor Mounji Bawendi. I've really enjoyed my time here at MIT in large part due to Mounji's style of advising. He always pushed me and demanded the best I could give in his own subtle way. He guided me and advised me in the laboratory in a most impressive manner and he also influenced my thinking and approach to many other aspects of graduate school and life.

Vladimir Bulović, my co-advisor, with his enthusiasm for science and life, his creative ideas, and his continual support, made my graduate career special. After speaking with Vladimir as a first year student I knew I had to be a part of his scientific effort. I'm so very thankful that I was able to continue a strong collaboration between the Bawendi and Bulović groups after Wing Woo left. Vladimir managed to always keep me so excited about what I was doing in the laboratory.

I collaborated with Seth Coe-Sullivan during my entire PhD. We were a unique team. We pushed and challenged each other in our respective ways and our collaboration thrived. We created a great working relationship in the laboratory and outside. My collaboration with Seth was the most fun, most fruitful, and the overall best I've ever had. I learned so much from Seth about science and every other thing associated with graduate school. I know I can always turn to him for help with anything. I always felt and still do feel that as a team there is nothing the two of us can't take on. I'm excited and thankful that we will continue to work together after MIT.

Justin Hodgkiss is not only one of my best friends with whom I've shared everything from the beginning, but he is an amazing person from whom I've learned so

much over these years at MIT. He has helped me in so many ways over these years, from preparing for orals to preparing this thesis. We have shared so much and my experience here at MIT and away from MIT over these past five years has been so great in large part due to him.

John Zimmer and I entered Mounqi's group as Inorganic students and remained inorganic students. This is our special bond, which grew strong after going through second and third year orals together. John and I have shared a great deal together over the past 5 years and he has helped me in so many ways. John was always there for me whether it was giving feedback on a rough draft, advice about something, or doing TEM. Through collaborations and discussions John has been intimately involved in my research and life and for this I am grateful. I could not have gotten through all of this without his continual help and advice these 5 years. If graduate school were a battle, which it kind of is, then John and I fought side by side from the beginning to the bitter end, came out alive and strong, and along the way he saved my life a couple of times. I've learned a lot from John over the years, had a blast with him in and outside of the lab, and I thank him for the crucial role he played during my time here at MIT.

Yinthai Chan and I, when teamed up on projects, really kicked some butt. Our collaborations were not only fun, but fruitful. Yinthai's questions, creative people naming, and unique personality have helped make my time here at MIT so enjoyable. I've had so many great discussions about science and every other imaginable topic over the years with Yinthai and have learned so much from him. Yinthai is one of the people who have contributed greatly to the shaping of my wonderful experience here at MIT.

Brian Yen is a brilliant person from whom I've learned a great deal. His clever humor has made our research collaboration and interactions in general a lot of fun. I really enjoyed working with him on my last project as a PhD student and am grateful for his kindness and help.

David Oertel and I were chemistry students at Oberlin College, where we got to know one another quite well. David is an extremely knowledgeable person from whom I've learned a great deal. He has always been very kind to me and has helped me in countless situations from when we were first years working on problem sets to now that we are 5th year students preparing to move on.

My thesis chair, Dan Nocera, taught me many good lessons about life and graduate school during my first year at MIT. He always showed me a good time and supported me throughout my PhD career.

I'd like to thank Joseph Sadighi for his insight into a question that arose during my second year oral exam and for all the extremely helpful discussions we had since then.

Jean-Michel Caruge has been here at MIT for as long as I have and he is like one of my classmates. He has always been there for me. I could always ask him for anything and he was willing and ready to spend an entire day or more with me. I was always struck by his brilliance in math and science. He's helped me a great deal with so many different things. Away from MIT we've had some great times as well, from watching and playing soccer together, to partying.

Preston Snee and I worked together in the lab a great deal. Both as collaborators as well as helping one another out by sharing results of past experiments and giving helpful advice. I've learned a great deal from Preston and he has always been very

helpful and kind to me. He helped make my experience in the lab a fun one, where we both made weird noises and gestures to get a strong laugh as the other walked by. His creativeness with chemical names and funny phrases will always make me laugh. We always had a blast outside the lab as well. 40's with straws stands out.

Wing Woo and Seth began the QD-LED project and the fruitful collaboration between the Bawendi and Bulović groups. Wing taught me a great deal and is still a friend. We always had a good laugh together. I also learned a great deal from Ken Shimizu and Vikram Sundar in the lab. We had some fun times outside the lab as well. They were always so helpful and willing to lend a hand.

Nathan Stott and I had a nice relationship in and outside of the lab. We worked together on the beginnings of the blue emitting particle project and I always enjoyed working with him. He taught me a great deal about nanoparticle synthesis and always had good creative suggestions for new things to try. He was always so willing to help or lend a hand when asked. He shared a lot with me about science and his life and for that I am grateful.

I shared an office with Dirk Weiss as well. Dirk helped me with many different things throughout my time at MIT. He always took the time to explain things to me and was always very supportive and interested in what I was working on and how it was going. I learned a great deal from Dirk and he helped me especially with preparing for my third year oral exam. We had many a good scientific and non-scientific discussion, which I enjoyed greatly.

I always had a great time with Brent Fisher. In the lab and in the office we laughed and joked around. I really enjoyed sharing an office with Brent. When appropriate he was quite and polite and when we both needed a break from concentrating we always had something funny to share or talk about.

Mirna Jarosz and I shared a hood for several years. We had some great discussions about science and life. She was always so kind and helpful and amazingly able to put up with my need for cleanliness without every complaining.

Venda Porter and I shared the hood after Mirna left. It was always a pleasure to talk with Venda, whether it was science related or not.

Jonathan Halpert has come on board and taken over the QD-LED project. Jonathan's positive and practical outlook on science and life has been great. We always have a good laugh together in the lab and outside the lab and he, like me, enjoys a good steak and a cigar.

Joe Tracy was always so willing to help me with anything. He helped me a great deal with learning the subject matter of a lab class I taught my first year as well as with many other little things throughout my time here at MIT.

Inhee Chung also resided in my office space and was always very kind and helpful in explaining things to me. We had our fair share of memorable conversations and laughs together as well.

Sungjee Kim was also always so helpful and kind to me. We had a brief collaboration together on IR emitting particles for imaging and he was always generous and supportive.

Hans Eisler during my first and second year could be found in the office or lab at any hour. He was always very helpful and kind to me as a new graduate student.



I'd like to acknowledge the following people that I did not mention specifically above for all they've given me in terms of experiences and help along the way: LeeAnn Kim, Alexi Arango, Polina Anikeeva, Conor Madigan, Jonathan Tischler, Jennifer Yu, Hao Huang, Numpon Insin, Jane Rempel, Wenchao Sheng, Juwell Wu, Pallavi Rao, Hideyuki Kamii, August Dorn, Xavier Brokmann, Heather Tavernier, Ryan Rieth, Amrit Sinha, Charles Hamilton, David Laitar, Greg Sirokman, and Adam Hock. Each person has played a special role in making my experience here at MIT a really great one.

I would also like to acknowledge Libby Shaw for her kindness and help with AFM, NIR absorption measurements, and XPS; Bob Edwards for his help with flame atomic absorption spectrometry; Mike Frongillo for his help with HRTEM and his unique personality that kept things interesting and fun down in the microscopy facility, and David Bray and Jeff Simpson for help and good conversations in the NMR facility.



Room 14-0551  
77 Massachusetts Avenue  
Cambridge, MA 02139  
Ph: 617.253.5668 Fax: 617.253.1690  
Email: docs@mit.edu  
<http://libraries.mit.edu/docs>

## **DISCLAIMER OF QUALITY**

Due to the condition of the original material, there are unavoidable flaws in this reproduction. We have made every effort possible to provide you with the best copy available. If you are dissatisfied with this product and find it unusable, please contact Document Services as soon as possible.

Thank you.

**Some pages in the original document contain color pictures or graphics that will not scan or reproduce well.**